DISCLAIMER:

This document does not meet the
current format guidelines of
the Graduate School at
The University of Texas at Austin.

It has been published for
informational use only.

The Dissertation Committee for Sunshine Zhou Certifies that this is the approved version of the following dissertation:

Engineering Block Copolymers for Advanced Lithography

Committee:

Christopher J. Ellison, Co-Supervisor

Carlton G. Willson, Co-Supervisor

Deji Akinwande

Benny D. Freeman

Donald R. Paul

Engineering Block Copolymers for Advanced Lithography

by

Sunshine Zhou, B.S.C.E, B.S. Physics

Dissertation

Presented to the Faculty of the Graduate School of

The University of Texas at Austin

in Partial Fulfillment

of the Requirements

for the Degree of

Doctor of Philosophy

The University of Texas at Austin

December 2016

Dedication

To my family and friends who have supported me throughout this journey, for their endless love and support.

Acknowledgements

To paraphrase Tolstoy, all triumphant graduate journeys are alike; each tumultuous graduate journey is challenging in its own way. As someone whose journey fell into the latter category, I have a multitude of people to thank for supporting me through the past five years.

First and foremost, I would like to thank my advisor, Dr. Christopher J. Ellison, for his tireless inspiration, motivation, and guidance throughout my graduate school career. He has provided with me with a myriad of opportunities, and he has been a constant source of encouragement for me. More importantly, he also knew when to dispense tough love. I am extremely grateful and fortunate to have had an advisor who cared to be honest with me through both good and bad times, and I have learned many invaluable life lessons in addition to advancing my scientific knowledge. Dr. Ellison's impact on my development during my graduate school career cannot be overstated, and I am infinitely grateful to him.

Next, I would like to thank my co-advisor, Dr. C. Grant Willson, for his support and willingness to share his font of knowledge with me. Dr. Willson always had an idea or a possible experiment to try, and I have benefited enormously from his advice. I would also like to thank every member of my committee: Dr. Paul for teaching the most thorough polymer course I have had the pleasure of taking, Dr. Freeman for his upbeat personality and enthusiasm, and Dr. Akinwande for his advice and collaboration on a graphene project.

I am fortunate to have conducted my graduate research studies at a university like UT Austin that has a plethora of indispensable staff that helped me throughout my time here. Angela Spangenberg and Steve Sorey of the NMR labs on campus have been a tremendous help, and they have run probably hundreds of ^{13}C NMR samples for me. They

have also helped me interpret many NMR spectra, and I am very grateful to them. Dwight Romanovic helped train me on the SEM machine on campus, and his sunny and cheerful demeanor has boosted my spirits more than once when the SEM did not reveal what I had hoped was there. Kevin Haynes, Jim Smitherman, Tammy McDade, Carrie Brown, and Kate Baird of the chemical engineering department have all helped me through many tight spots, and I thank them for keeping the department running seamlessly.

I am grateful to have worked with a fantastically inspiring group of graduate students during my time here. I would like to thank the BCP subgroup, including Dr. Michael Maher, Greg Blachut, Dr. Will Durand, Dr. Colin Hayes, Yusuke Asano, Dr. Christopher Bates, Dr. Julie Cushen, Dr. Dustin Janes, Kazunori Mori, Austin Lane, Yasunobu Someya, and Dr. Natsuko Ito, for helping me through every step of the process and for always providing feedback and positivity. I would especially like to thank Dr. Julie Cushen for helping me get started in grad school and for being a great friend, and Dr. Dustin Janes for always coming up with new ideas and helping me hone my writing and laboratory skills. I thank the past and present members of the Ellison group for making each day in the lab a great day, even if the experiments do not go the way I had hoped. Specifically, Dr. Josh Katzenstein was a great mentor, and I could not have asked for a better senior student to help guide me through my first years here. Dr. Heonjoo Ha is the most frighteningly efficient human being I have ever met, and I am grateful for all the fun and informative discussions we have had. Dr. Chae Bin Kim has supported me through my entire grad school career, and his jokes and enthusiasm for research have helped me through many difficult times.

Two members of the Ellison group in particular have become like sisters to me. I cannot properly convey how much I treasure my friendship with Yunping Fei and Reika Katsumata. These two women have supported me through my lowest lows, and they

motivate me each day to be a better friend, researcher, and person. Yunping is the happiest, most purely good person I have had the pleasure of meeting, and her infectious enthusiasm for and appreciation of every day inspires me to always look for the silver lining. Reika is the most passionate and dedicated person I have ever met, and she strives every day to put forth her best effort. Reika sees the full potential in everyone, and I endeavor to be the Sunshine that Reika thinks I am. Everyone should be so lucky as to have one friend such as Yunping or Reika, and I am privileged to have both of them in my life.

I must also thank my friends, near and far, for lending a shoulder or ear whenever I needed it. Joseph Cheng and Steven Blackwell have been pillars of support for me, no questions asked. Though separated by thousands of miles, Karen Li always knows when to send a much-needed text of encouragement, and I know that I can always call her for anything. Jing Li, Mengwen Zhang, and Ning Zhang are longtime friends who are also going through a lengthy graduate or medical program, and we can always commiserate with each other. Yini Shi is perpetually game for a lengthy phone call, and a long, rambling discourse about life with her is guaranteed to put me at peace.

Greg Blachut has been my best friend throughout everything. He has been my most ardent supporter, fiercest cheerleader, and sturdiest rock through all the ups and downs of this fantastic journey. His presence by my side makes every day more vivid and vibrant, and I could not imagine this experience without him.

Finally, my family has been my foundation through everything. I am so lucky to have been born to my mom and dad, and I am grateful for the sacrifices they have made to provide me with a happy, worry-free upbringing and the opportunities that have led me to where I am today. I am also thankful for Stephen, my younger brother, for being his happy, impish self and for motivating me to graduate soon so that he stops out-earning me so

egregiously. I also thank all four of my grandparents for believing in me and giving me so many wonderful, happy memories, and I hope to do their legacies justice.

Engineering Block Copolymers for Advanced Lithography

Sunshine Xu-Yang Zhou, Ph.D.

The University of Texas at Austin, 2016

Co-Supervisor: Christopher J. Ellison

Co-Supervisor: C. Grant Willson

Block copolymer (BCP) nanoimprint lithography is an attractive possible solution for manufacturing hard disk drives with information densities greater than 1 Tbit/in^2. At these densities, individual bits must be smaller than 10 nm, and BCPs can be engineered to spontaneously self-segregate into features on this size scale. In addition to small feature sizes, industrially relevant BCPs should have simple orientation strategies and possess good etch contrast and resistance.

Several silicon-containing BCPs were investigated due to the increased etch contrast and resistance imparted by silicon. The synthesis, characterization, and thin film studies of three silicon-containing BCPs are detailed. Due to the surface energy mismatch between the silicon-containing block and the organic block, solvent annealing and top coats were needed to perpendicularly orient these materials. While these materials possess many advantages, they each have shortcomings that prevent them from being ideal industrial materials.

A derivative of poly(styrene-*block*-methyl methacrylate) was engineered to take advantage of its simple orientation procedure while decreasing the smallest achievable feature size. The synthesis and characterization, including determination of the χ parameter, of this BCP are detailed. The thin film assembly of this BCP was also

successfully demonstrated, and this dissertation concludes with several ideas for future studies.

Table of Contents

List of Tables xv

List of Figures xvi

List of Illustrations xxxiii

Chapter 1: Block Copolymer Lithography 34

1.1 Introduction: Hard Disk Drives and the Superparamagnetic Effect 34

1.2 Overcoming the Superparamagnetic Effect 36

1.2.1 Two dimensional magnetic recording (TDMR) 37

1.2.2 Shingled magnetic recording (SMR) 38

1.2.3 Heat assisted magnetic recording (HAMR) 41

1.2.4 Bit patterned magnetic recording (BPMR) 42

1.3 Block Copolymer Lithography 44

1.3.1 BCP morphologies 47

1.3.2 Minimum feature sizes of BCPs 48

1.3.3 Perpendicular orientation of BCP thin films.....49

1.3.4 Etch resistance and etch selectivity.....50

1.3.5 Long range alignment 51

1.3.6 BCP lithography challenges.....53

1.4 References.....54

Chapter 2: Poly(trimethylsilyl styrene-*block*-lactide) (PTMSS-PLA) and Poly(trimethylsilyl styrene-*block*-isoprene) (PTMSS-PI) 60

2.1 Poly(trimethylsilyl styrene-*block*-lactide) (PTMSS-PLA) 61

2.1.2 Experimental Methods 62

2.1.2.1 TMSS monomer synthesis 62

2.1.2.2 TMSS monomer characterization 63

2.1.2.4 PTMSS-OH and PTMSS-PLA polymer synthesis 64

2.1.2.4 PTMSS-OH and PTMSS-PLA polymer characterization66

2.1.2.5 Small angle X-ray scattering (SAXS).....68

2.1.3 χ-Parameter Characterization 69

2.1.4 Thin Film Studies....70
2.1.5 Other Studies....74
2.1.6 Complications with PLA....74
2.2 Poly(trimethylsilyl styrene-block-isoprene) (PTMSS-PI)....75
2.2.1 Experimental Methods....76
2.2.1.1 Purification....76
2.2.1.2 Anionic polymerization....76
2.2.2 Results and Discussion....77
2.3 Conclusions....83
2.4 References....84
Chapter 3: Poly(pentamethyldisilyl styrene-*block*-ethyl glycolide) (PDSS-PEGL)86
3.1 Top Coat Orientation Strategy....86
3.2 Experimental Methods....89
3.2.1 PDSS-OH synthesis....89
3.2.2 PDSS-OH characterization....89
3.2.3 PDSS-PEGL synthesis....91
3.2.4 PDSS-PEGL characterization....92
3.2.5 PEGL homopolymer synthesis....95
3.2.6 Thin film island/hole test methods....96
3.3 Thin Film Experiments....96
3.3.1 Using I/H tests to determine interface neutrality....97
3.3.2 Control tests: is PEGL more robust than PLA?....99
3.3.1 Substrate neutralization....101
3.3.2 Top interface neutralization....103
3.4 Conclusions....124
6.5 References....125
Chapter 4: Using Intrablock Interactions to Increase χ of Poly(styrene-*block*-methyl methacrylate) (PS-PMMA)....127
4.1 Introduction....127
4.2 Experimental....129

4.2.1 Materials synthesis....129
4.2.2 Material characterization....131
4.2.3 Substrate neutralization....132
4.2.4 Thin film processing....133
4.2.5 Small angle X-ray scattering....133
4.2.6 Scanning electron microscopy (SEM)....134
4.3 Results and Discussion....134
4.3.1 Synthesis and characterization....134
4.3.2 χ parameter....144
4.3.3 Thin film processing....153
4.4 Conclusions....156
4.5 References....156
Chapter 5: Vinylnaphthalene Degradation during Light Exposure....162
5.1 Introduction....162
5.2 Experimental Methods....163
5.2.1 SAXS data collection for χ....163
5.2.2 Polyvinylnaphthalene (PVN) free radical polymerization....163
5.2.3. Poly(styrene-*random*-vinylnaphthalene) (PSVN) anionic polymerization....164
5.2.4 UV-Vis spectroscopy....164
5.2.5 UV light exposure....164
5.3 Results and Discussion: Poly((styrene-*random*-vinylnaphthalene)-*block*-methyl methacrylate) (PSVN-PMMA)....165
5.3.1 PSVN-PMMA sample damage during SAXS experiments....165
5.3.2 Modified χ data collection methodology....168
5.3.3 NMR study of PSVN degradation during SAXS....171
5.4 Results and Discussion: Light Exposure Tests for PSVN and PVN Homopolymers....173
5.4 Conclusions....182
5.5 Acknowledgements....183
5.6 References....183

Chapter 6: Future Works.....185
6.1 Directed Self-Assembly.....186
6.2 Increasing Etch Contrast and Resistance of PSVN-PMMA.....187
6.3 Doping Small Molecules into PSVN-PMMA.....189
6.4 Introducing Self-Interaction in the PMMA Block of PSVN-PMMA...190
6.5 References.....192
References.....194

List of Tables

Table 3.1 Characterization data for PDSS-OH. 91

Table 3.2. Characterization of PDSS-PEGL BCPs.....93

Table 3.3. Series of TC with varying ratios of maleic anhydride and cyclohexyl maleimide copolymerized with *t*-butyl styrene.....115

Table 3.4. Series of TC with varying ratios of maleic anhydride and methyl maleimide copolymerized with styrene. 117

Table 4.1 Characterization of all BCPs reported in this work. 135

Table 4.2 A and B parameters for the χ parameters of PS-PMMA and two VN-containing BCPs.....149

Table 4.3 Annealing conditions for the samples shown in Figure 4.11.....155

List of Figures

Figure 1.1 (a) A schematic illustration of a read-write head writing bits into perpendicularly magnetized media. (b) A TEM image of individual magnetic grains. Red and blue regions indicate magnetic bits of opposite polarities. Image from [3], © 2008 IEEE. 34

Figure 1.2 ASTC roadmap of increasing areal storage density on hard disk drives. Image from [8], © 2014 IDEMA. 36

Figure 1.3 Schematic illustrating the principle behind two dimensional magnetic recording (TDMR). Each individual random grain can act as a bit, each bit can be detected using a two dimensional waveform. Schematic from [9], © 2010 IEEE. 38

Figure 1.4 (a) Schematic of how SMR works. Each successive track partially overwrites the previous adjacent track, allowing for thinner tracks. (b) A more detailed schematic explaining SMR. The left side portrays four traditional tracks numbered 1-4 with width w and distance g between tracks. The right side portrays six shingled tracks numbered 1-6 with width w', effective width r, and distance g between shingled groups. Schematic from [18]. 40

Figure 1.5 Schematic of HAMR technology. A laser attached to the write head heats a small spot on the recording media while information is written, thus skirting the superparamagnetic effect. Reprinted with permission from [21], © 2009 Nature Photonics. 41

Figure 1.6 Differences between conventional HDD magnetic media (left) and bit patterned magnetic media (right). In conventional HDD magnetic media, bit boundaries are determined by the read/write head. In bit patterned media, each magnetic bit's size and location are predetermined. Figure from [3], © 2008 IEEE.. 43

Figure 1.7 Etched BCP features on a silicon wafer. This demonstrates that BCP can be used to pattern small, well-ordered, periodic structures, although the size of each feature in this figure remain too large for its intended HDD application. Reprinted with permission from [28]. Copyright 2011American Chemical Society. 44

Figure 1.8 (a) Diblock copolymer with poly-A and poly-B blocks. (b) Triblock terpolymer with poly-A, poly-B, and poly-C blocks. Many other forms of multiblock copolymers exist, including copolymers with repeating blocks, such as an A-B-A triblock terpolymer.....45

Figure 1.9 To make a patterning template, a BCP solution is first spin-coated onto a silicon substrate coated with a neutral surface treatment. After BCP is oriented and aligned on the substrate, one block is selectively removed by reactive ion etching, and the remaining block becomes an etch mask for the substrate. Finally, the pattern is transferred to the substrate and the remaining polymer is washed off.....46

Figure 1.10 Different morphologies can be achieved using BCPs by varying the volume fraction of one block to the other. In this phase diagram, reprinted from, the morphologies that can be achieved for a diblock copolymer are illustrated. Reprinted with permission from [39]. Copyright 2006 American Chemical Society. 47

Figure 1.11 The importance of neutral surface energies on lamellae-forming BCP alignment in thin film. Starting from the top row, the substrate surface energy must be neutral for the BCP (neither block preferentially wetting the substrate). Next, as shown in the bottom row, the top interface must also be neutral. Only when both the top and bottom interfaces are neutral for the BCP will the desired line-and-space pattern be visible from a top down view. 49

Figure 1.12 An example chemoepitaxy flow. Chemoepitaxy uses patterned substrate surface lines that are chemically preferential to one block of the BCP to guide alignment over the patterned area. Each patterned line can be spaced at a multiple of the natural domain periodicity of the BCP, resulting in pattern density multiplication. In this schematic, 4x density multiplication is illustrated. Schematic from [56]. Copyright 2012 Society of Photo Optical Instrumentation Engineers. 52

Figure 1.13 Graphoepitaxy flow. Graphoepitaxy uses topographic relief features on the substrate to form trenches with walls that are preferential to one block of the block copolymer. When the substrate is coated with a neutral layer, the preferential block will wet the walls, and the alignment will propagate inwards to fill the trench. Schematic from [56]. Copyright 2012 Society of Photo Optical Instrumentation Engineers. 53

Figure 2.1 The three stereoisomers of lactide. Image adapted from [10]. 62

Figure 2.2 ^{1}H NMR of purified TMSS monomer in $CDCl_3$. The peak integrations agree well with the assigned hydrogens, indicating successful synthesis. The unlabeled peak at 1.6 ppm is water, and the unlabeled peak at 7.26 is protonated solvent. Reprinted with permission from [11]. Copyright 2012 American Chemical Society. 64

Figure 2.3 SEC traces of PTMSS-$OH_{5.5}$ macroinitiator and $PTMSS_{5.5}$-$PLA_{6.6}$, where the subscript represents the number average molecular weight of the macroinitiator or BCP in kg/mol. A leftward shift of the entire trace indicates PLA growth on every PTMSS-OH macroinitiator. Adapted with permission from [11]. Copyright 2012 American Chemical Society. 67

Figure 2.4 Representative ^{1}H NMR trace from $PTMSS_{5.5}$-$PLA_{3.7}$. Peaks f and b were used to determine the mole and volume fractions of the material. Number average molecular weight was calculated based on the mole fractions and molecular weight of the PTMSS-OH macroinitiator. Peak c is residual THF. Reprinted with permission from [11]. Copyright 2012 American Chemical Society. 68

Figure 2.5 A picture of the solvent annealing apparatus for PTMSS-PLA orientation experiments conducted in the lab. An open scintillation vial containing the solvent of choice is placed in a closed jar with the thin film sample, and the solvent vapor interacts with the BCP. 72

Figure 2.6 $PTMSS_{5.5}$-*b*-$PLA_{3.7}$ after annealing with cyclohexane for a) 1h, b) 2h, c) 4h, and d) 24h. Reprinted with permission from [15]. Copyright 2012 American Chemical Society. 73

Figure 2.7 Representative SEC traces for PTMSS-PI polymerization attempts. The blue traces are the PTMSS aliquots, which polymerized as expected. However, the isoprene block was never cleanly initiated from the first PTMSS block. The red traces are the resulting BCPs, which sometimes had a shoulder and sometimes had a second peak at the elution volume of the aliquot, indicating the presence of a large fraction of PTMSS homopolymer. 78

Figure 2.8 Representative SEC traces for PI-PTMSS polymerization attempts, wherein the PI block was polymerized first. The blue traces are the PI aliquots, which polymerized mostly as expected. As can be seen from the left trace, isoprene sometimes coupled during the reaction. The red traces are the resulting BCPs, which sometimes had a shoulder and sometimes had a second peak at the elution volume of the aliquot, indicating the presence of a large fraction of PI homopolymer. This is indicative of the isoprenyl ion being unable to initiate TMSS effectively. 80

Figure 2.9 Anionic polymerization of PTMSS-PI in THF at -78 °C. (**a**) The resulting SEC trace, where the blue trace is the aliquot taken just before adding isoprene and the red trace is the BCP. As indicated by SEC, the PTMSS block did not initiate any isoprene growth. (**b**) ^{1}H NMR of the BCP (the red trace in (**a**)), and the lack of a peak at 5.1 confirms that no isoprene growth was initiated from the PTMSS block. 82

Figure 2.10 SEC trace of PS-PI polymerized in cyclohexane using the same procedure, equipment, and reagents as for the failed PTMSS-PI and PI-PTMSS experiments. The blue trace is the PS aliquot, and the red trace is the PS-PI BCP. This control experiment indicates that there is not an intrinsic flaw to the procedure, glassware, or reagents; rather, the interaction between TMSS and isoprene caused the crossover failures. 83

Figure 3.1 Maleic anhydride (blue) can be ring-opened with aqueous trimethylamine, and the ring-opened form (red structure) can be dissolved in methanol. Upon heating the ring-opened form, maleic anhydride will revert back to a ring-closed, less polar form (green). Reprinted with permission from [7]. Copyright 2014 American Chemical Society. 88

Figure 3.2 Top coat process flow. The crosslinked or grafted SNT is applied and immobilized, and then the BCP thin film is spin coated on top. Next, the polar (ring-opened) top coat (TC) is spin coated out of a polar solvent that does not dissolve the BCP. Then, the film stack is annealed to ring close the TC making the top coat less polar and, ideally, rendering it neutral for the BCP. At the same time, the BCP is perpendicularly oriented. After, the TC is stripped off using an aqueous base, revealing the perpendicularly oriented BCP. One block of the BCP can then be selectively removed, leaving the remaining block as an etch mask. Adapted from [[8]]. 89

Figure 3.3 ^{1}H NMR spectrum for PDSS-OH$_{5.1}$, where the subscript refers to the number average molecular weight of the sample in kg/mol as determined by SEC. The peaks are assigned as shown. 90

Figure 3.5 SEC trace used to determine the molecular weight dispersity of PDSS$_{4.8}$-PEGL$_{8.9}$ (red line). The PEGL added cleanly to the PDSS-OH macroinitiator (black line) as indicated by the sharp red peak that shifted uniformly from the macroinitiator. 93

Figure 3.6 Thermogravimetric analysis of PDSS$_{4.8}$-PEGL$_{8.9}$ determined that the T_d of this BCP was 302 °C in air. 94

Figure 3.7 Differential scanning calorimetry data of PDSS$_{4.8}$-PEGL$_{8.9}$ used to determine the T_gs of each block. 95

Figure 3.8 I/H tests for a BCP thin film with an initial spin coated thickness of 1.25 L_0. Here, the nonpolar red block prefers to wet the top air interface, and the BCP exhibits either symmetric (substrate also prefers red block) or asymmetric (substrate prefers blue block) wetting behavior upon annealing. As demonstrated, knowing the wetting preference of the top interface and the initial film thickness, the relative surface energy of the substrate is known depending on whether islands or holes are formed. Figure adapted from [8]. 98

Figure 3.9 10x and 100x optical micrograph images of PDSS$_{4.8}$-PEGL$_{8.9}$ after methanol was spin coated on it. The uniform interference color across the two micrographs demonstrates that the thin film was not destroyed or deformed by methanol. The dark spot in the 100x micrograph is a dust particle.....100

Figure 3.10 $PDSS_{4.8}$-$PEGL_{8.9}$ after annealing at 165 °C for 10 minutes formed holes on silicon substrate (left). After rinsing with THF, the thin film was easily rinsed off, leaving nothing grafted to the silicon (middle). An image of the edge of the wafer shows no iridescent colors indicative of a thin film (right). 101

Figure 3.11 I/H test on a silicon wafer for $PDSS_{4.8}$-$PEGL_{8.9}$ confirmed that the BCP exhibits asymmetric wetting behavior. The top row is the film thickness of each sample, the second row is the equivalent L_0, and the third row is the type of features formed. 102

Figure 3.12 Using I/H tests to determine a neutral SNT for each PDSS-PEGL BCP. The initial film thickness of $PDSS_{4.8}$-$PEGL_{8.9}$ was about 2.3 L_0 and the initial film thickness of $PDSS_{5.1}$-$PEGL_{10.0}$ was about 1.7 L_0. Each sample was annealed at 165 °C in air for 5 mins before imaging...103

Figure 3.13 Cracking behavior for various TCs over $PDSS_{4.8}$-$PEGL_{8.9}$ annealed at 165 °C in air for 5 mins. All percentages are mole percent of the monomer in the TC. Di-*t*-BuSty is di-*tert*-butylstyrene and MA is maleic anhydride. Images are all optical micrographs taken at 10x magnification with dimensions of 1.2 mm x 1.6 mm. 104

Figure 3.14 Example of a TC exhibiting strange I/H behavior on a cracked sample. The TC was CB3-33 (48 mol% styrene, 52 mol% MA) on $PDSS_{4.8}$-$PEGL_{8.9}$ on bare silicon annealed at 165 °C in air for 5 mins. Image is an optical micrograph taken at 100x magnification with dimensions of 120 μm x 160 μm.....105

Figure 3.15 Optical micrograph of a cracked TC on PDSS-PEGL on crosslinked PS after annealing at 165 °C for 5 seconds. Micrograph is 1.2 mm x 1.6 mm. 106

Figure 3.16 AFM images and topography profiles of four samples of $PDSS_{4.8}$-$PEGL_{8.9}$ with varying thicknesses of TC (CB3-33, 52% MA, 48% Sty) after annealing in air 165 °C for 5 minutes. Each AFM image is 90 μm x 90 μm. The cracking behavior was unaffected by the TC thickness.108

Figure 3.17 AFM images and topography profiles of four samples of $PDSS_{4.8}$-$PEGL_{8.9}$ with CB3-33 (52% MA, 48% Sty) after annealing in air 165 °C for various times ranging from 10 sec to 3 mins. Cracking was evident in all samples regardless of annealing time. Each AFM image is 90 μm x 90 μm. 108

Figure 3.18 Optical micrographs of samples of $PDSS_{4.8}$-$PEGL_{8.9}$ with CB3-33 (52% MA, 48% Sty) spin coated out of either toluene or MIBK. The cracking behavior persisted regardless of the polarity of the BCP spin coating solvent. 10x micrographs are 1.2 mm x 1.6 mm and 100x micrographs are 120 μm x 160 μm. 109

Figure 3.19 **(a)** Optical micrograph after application of the BCP film and a 10 s 100 °C soft bake in air. **(b)** Optical micrograph of TC deposited on the film in (a) and soft baked at 100 °C for 10 s in air. **(c)** Optical micrograph of the film stack in (b) after 1 minute at 165 °C in air. Each micrograph is 1.2 mm x 1.6 mm. 110

Figure 3.20 SEC curves of BCP and TC after annealing in the DSC. **(a)** The black curve corresponds to the BCP annealed under nitrogen, an inert atmosphere. The purple curve corresponds to the BCP and the TC being annealed in air together, simulating the actual annealing conditions. The green curve corresponds to the BCP annealed under air, and the red curve corresponds to the BCP as received, before any annealing. **(b)** All four curves from (a) collapsed together shows that the BCP did not change under of the annealing conditions. 111

Figure 3.21 Lamellae-forming PTMSS-PLA spin coated out of toluene and MIBK. CB3-33 was the TC used, and the samples were annealed at 165 °C for 5 min in air. The optical micrographs, despite having microstructures, show no indication of cracking. 10x micrographs are 1.2 mm x 1.6 mm and 100x micrographs are 120 μm x 160 μm. 112

Figure 3.22 Optical micrographs of PDSS-PEGL as cast on silicon wafer, PDSS-PEGL annealed at 165 °C for 5 mins to wet the air interface with PDSS, TC (CB3-33) spin coated on top of annealed PDSS-PEGL, and annealed PDSS-PEGL with TC annealed at 165 °C for 5 mins. As shown the final film still cracked. 10x micrographs are 1.2 mm x 1.6 mm and 100x micrographs are 120 μm x 160 μm. 113

Figure 3.23 The interaction between PEGL homopolymer and CB3-33 was investigated. Neither of the PEGL homopolymers showed cracking while PDSS-PEGL did after annealing at 165 °C for 5 mins in air. Each optical micrograph is 10x magnification with dimensions of 1.2 mm x 1.6 mm. 114

Figure 3.24 Thin film studies of the TCs detailed in Table 3.3. Films were annealed at 165 °C for 5 mins in air. 10x micrographs are 1.2 mm x 1.6 mm and 100x micrographs are 120 μm x 160 μm. 115

Figure 3.25 Thermal expansion coefficients of **(a)** $PDSS_{4.8}$-$PEGL_{8.9}$ **(b)** MM3-189 (21% MA, 31% cyclohexyl maleimide, 48% *t*-butyl styrene) and **(c)** MM3-187 (40% MA, 10% cyclohexyl maleimide, 50% *t*-butyl styrene) as measured by ellipsometry. While the two TCs have identical thermal expansion coefficients, MM3-189 did not crack, while MM3-187 did. 116

Figure 3.26 Thin film studies of the TCs detailed in Table 3.4. Films were annealed at 165 °C for 5 min in air.10x micrographs are 1.2 mm x 1.6 mm, and 100x micrographs are 120 μm x 160 μm. 117

Figure 3.27. Optical micrographs of the effect of benzoic acid doped in BCP on TC thin films after annealing at 165 °C for 5 min in air. 10x micrographs are 1.2 mm x 1.6 mm and 100x micrographs are 120 μm x 160 μm. All thin film micrographs have benzoic acid doped into the starting materials.119

Figure 3.28 Optical micrographs of the effect of DBU doped in BCP on TC thin film behavior after annealing at 165 °C for 5 min in air. 10x micrographs are 1.2 mm x 1.6 mm and 100x micrographs are 120 μm x 160 μm....121

Figure 3.29 DBU doped in the TC solutions with no BCP present. The films were annealed at 165 °C for 5 min in air, then imaged. 10x micrographs are 1.2 mm x 1.6 mm and 100x micrographs are 120 μm x 160 μm....122

Figure 3.30 Annealed films of PTMSS-PLA with DBU doped in. 10x micrographs are 1.2 mm x 1.6 mm and 100x micrographs are 120 μm x 160 μm.123

Figure 3.31 Annealed films of PMOST-PTMSS with DBU doped in. MM4-251 (50% MA, 34% di-*t*-BuSty, 16% Sty) was previously determined to be a neutral TC for this BCP. 10x micrographs are 1.2 mm x 1.6 mm and 100x micrographs are 120 μm x 160 μm. 124

Figure 4.1 $P(S_{85}VN_{15})_{21.7}$-$PMMA_{28.0}$ (a) before and (b) after washing with hot (50 °C) cyclohexane to remove the soluble PSVN fraction. 131

Figure 4.2 Quantitative ^{13}C NMR was used to determine the relative concentration of VN to styrene in the PVN block. A system of equations was set up using the peak assignments shown to solve for x. 137

Figure 4.3 A representative ^{1}H NMR spectrum used to determine the volume fraction of each block of PSVN-PMMA. The integrated area of the downstream aromatic region was normalized by the average number of aromatic protons for each unit of the PSVN block (5x + 7y, where x and y are the fractional composition of styrene and VN in the block, respectively), and the region between 3.5-4.0 ppm (from the MMA block) was normalized by the number of methyl protons (3). The ratio between the two normalized integrations is the mole ratio, and this was used to determine the volume ratio. 138

Figure 4.4 Reactor solution color changes throughout the polymerization process. **(a)** Immediately after adding a drop of styrene-VN monomer solution, the reactor solution turns a dark green. **(b)** After a few seconds, the VN monomers are all consumed, and the solution takes on a brown/orange tinge. The solution will stay this color until the next drop of styrene-VN monomer solution is added, at which point it will revert back to the color in (a). **(c)** DPE is added to the reactor after all the styrene-VN monomer had been added, and the reactor turns a deep red color. **(d)** For reference, the color of pure styrene is an orange color. 140

Figure 4.5 DSC scans of three PSVN samples containing various mol % of VN. As the concentration of VN increased, the glass transition temperature increased. The T_g (defined as the onset of the transition) was 95 °C for a sample with 0 mol % VN (i.e., PS only) (top blue curve), 105 °C for a sample with 15 mol % VN (middle green curve), and 113 °C for a sample with 30 mol % VN (bottom red curve). 141

Figure 4.6 Small angle x-ray scattering (SAXS) profiles for all ordered BCPs. Even order scattering peaks are absent from all but two samples, indicating all but $P(S_{75}VN_{25})_{12.6}$-$PMMA_{18.3}$ and $P(S_{80}VN_{20})_{15.1}$-$PMMA_{20.9}$ are volumetrically symmetric.[43] 143

Figure 4.7 **(a)** Domain spacing 'd' of each BCP as a function of its molecular weight and VN incorporation. As VN incorporation increases, the domain spacing increases for polymers of a similar molecular weight, implying an increase in the χ parameter. The regression lines represent the scaling implied by Equation 1 with a constant χ parameter for each composition, $d \sim N^{2/3}$. **(b)** Rearranging Equation 1 gives a proportionality factor for the χ parameter, which is calculated from averaged values from (a). When plotted against VN incorporation, the increasing trend implies that the χ parameter increases as more VN is included. 145

Figure 4.8 SAXS profiles for a representative sample, $P(S_{83}VN_{17})$-$PMMA_{Dis}$, near the first order peak. Scattering profiles were collected at several temperatures for the same sample, and best-fit lines were obtained by changing χ as one of the adjustable parameters using Leibler's mean-field theory.[18,46] 146

Figure 4.9 A comparison of the χ parameter of two VN-containing polymers to PS-PMMA. **(a)** A comparison of the χ parameter as a function of temperature shows that the VN-containing BCP's have much higher χ's as compared to PS-PMMA, which results in **(b)** smaller attainable features. 148

Figure 4.10 Representative AFM images of **(a)** PS and **(b)** PVN films dewetting from a crosslinked PMMA surface. Both films were annealed under vacuum at 160 °C for 96 hours. Isolated droplets of various sizes were selected to provide a comprehensive data set. A python code was written to determine the height and width of each droplet, and representative data for **(c)** PS and **(d)** PVN are shown. Dewetting contact angles were calculated by assuming spherical caps and using the equation $\cos\theta = 1 - 2(h/r)^2$, where h is the height of the droplet and r is half the width of the droplet. 152

Figure 4.11 Top-down SEM images of lightly etched **(a)** $P(S_{85}VN_{15})_{17.1}$-$PMMA_{19.1}$ with a film thickness of 1.7 L_0, **(b)** $P(S_{80}VN_{20})_{15.1}$-$PMMA_{20.9}$ with a film thickness of 1.0 L_0, **(c)** $P(S_{75}VN_{25})_{12.6}$-$PMMA_{18.3}$ with a film thickness of 1.7 L_0, and **(d)** $P(S_{65}VN_{35})_{7.7}$-$PMMA_{9.7}$ with a film thickness of 1.7 L_0. All images are 1 μm x 1 μm.....154

Figure 5.1 Photograph of PSVN-PMMA BCP sample after heating *in situ* during SAXS data collection for χ determination. The air bubbles developed during the data collection period and were not present before insertion into the SAXS sample chamber. The yellow color is from the Kapton tape. 166

Figure 5.2 SEC traces of a PSVN-PMMA BCP before (blue line) and after (orange dashed line) a typical SAXS experiment for χ with *in situ* heating.166

Figure 5.3 SAXS data collected at four temperatures for χ determination (open markers). χ is typically extracted from the curves fit to the collected data (colored lines), but the atypical peak heights and peak orders indicate that any extracted χ is likely inaccurate. 167

Figure 5.4. When the high temperature annealing step and SAXS data collection step were separated, the BCP sample did not show any signs of degradation. The yellow color is from the Kapton tape.....169

Figure 5.5 SEC trace of $P(S_{80}VN_{20})_{15.1}$-$PMMA_{20.9}$ before and after heating at 200 °C on a hot plate for 1 hour. The identical elution time and peak shape indicates that no chain scission or crosslinking occurred during the annealing process. 170

Figure 5.6 SEC trace of $P(S_{80}VN_{20})_{15.1}$-$PMMA_{20.9}$ before and after exposure to X-rays at room temperature for 60 minutes in a SAXS experiment setup. The identical elution time and peak shape indicates that no chain scission or crosslinking occurred during the data collection process.171

Figure 5.7 ^{1}H NMR spectra of a PSVN-PMMA sample (a) before and (b) after a typical SAXS run to collect data for χ, which involved heating the sample *in situ*. The integration of the aromatic region for both spectra have been set at 5.00. A relative increase in the methoxy integration centered at around 3.6 ppm after the experiment indicates that the PSVN block lost aromaticity during simultaneous SAXS and heating. 172

Figure 5.8 Chemical structures and UV-Vis absorption spectra data for benzene, naphthalene, and anthracene. As the size of the conjugated system increases, so does the wavelength of the absorption peak. Reproduced from [7].....174

Figure 5.9 UV-Vis data for a PVN homopolymer sample before exposure (red line) and after various doses of UV light. The arrow indicates the trend of the peak as dose increased. 175

Figure 5.10 Photo of the quartz wafer used for UV-Vis studies after soaking in THF bath for 2 days and sonicating for 1 hour. The cloudy portion is the crosslinked PVN film.....176

Figure 5.11 SEC trace of PSVN homopolymer before (blue) and after (orange) UV light exposure without heating.....176

Figure 5.12 UV-Vis data for a PVN thin film after exposure to 10 mJ/cm^2 of light exposure and subsequent heating at 160 C for up to 2 hours. The spectrum shape was not drastically changed after 2 hours of heating, suggesting that the PVN thin film did not undergo any further changes. In turn, this indicates that the crosslinking observed in the PVN thin film was not due to photodimerization of the naphthalene units.....178

Figure 5.13 UV-Vis data for a PVN homopolymer sample before exposure (red line) and after various doses of light exposure under a nitrogen atmosphere. 179

Figure 5.14 Contrast curve for PS and PVN homopolymers under ambient conditions. For PVN, the gel fraction increased until a maximum of about 60% after 20 W/cm^2 of exposure [1], then decreased afterwards [2]. It is hypothesized that PVN is crosslinking in section [1], and chain scission is occurring in section [2].....181

Figure 6.1 Water contact angle images of as cast PVN thin film, exposed PVN thin film, and exposed PVN thin film with grafted (a) trimethylchlorosilane and (b) APTES.....188

Figure 6.2 Proposed BCP that incorporates self-interaction into both blocks. 190

List of Illustrations

Scheme 2.1 Synthesis of TMSS monomer by a Grignard reaction. 63

Scheme 2.2 Synthesis of PTMSS-*b*-PLA by a combination of anionic and ring-opening polymerization. Reprinted with permission from [11]. Copyright 2012 American Chemical Society. 65

Scheme 2.3 Synthesis of PTMSS-PI using anionic synthesis in cyclohexane.77

Scheme 3.1 Synthesis of PDSS-PEGL from PDSS-OH macroinitiator. 92

Scheme 4.1 Synthesis of PSVN-PMMA block copolymer by anionic polymerization. 135

Scheme 5.1 Synthesis of PVN using free radical polymerization. 164

Scheme 5.2 (a) Reversible photodimerization of anthracene. Irradiation by 365 nm light can dimerize anthracene, and the photodimer can be reversed by either heat or by irridation by 303 nm light. (b) Proposed dimerization reaction by vinylnaphthalene. 177

Chapter 1: Block Copolymer Lithography

1.1 Introduction: Hard Disk Drives and the Superparamagnetic Effect

Consumer microelectronic devices have steadily become lighter, faster, less costly, and more powerful. This continuing pace of technological advancement has been powered by a rapid rate of component miniaturization described by an empirical phenomenon driven by Intel co-founder Gordon Moore's "Moore's Law."[1] In the hard disk drive (HDD) industry, "Kryder's Law" analogously describes the rapid areal storage density increase observed from 100 Mbit/in^2 in 1995 to 110 Gbit/in^2 in 2005, over a 1,000-fold increase[2]. The current hard drive technology utilizes granularly defined magnetic films where groups of magnetic grains representing individual bits directly neighbor one another, as shown in **Figure 1.1**.

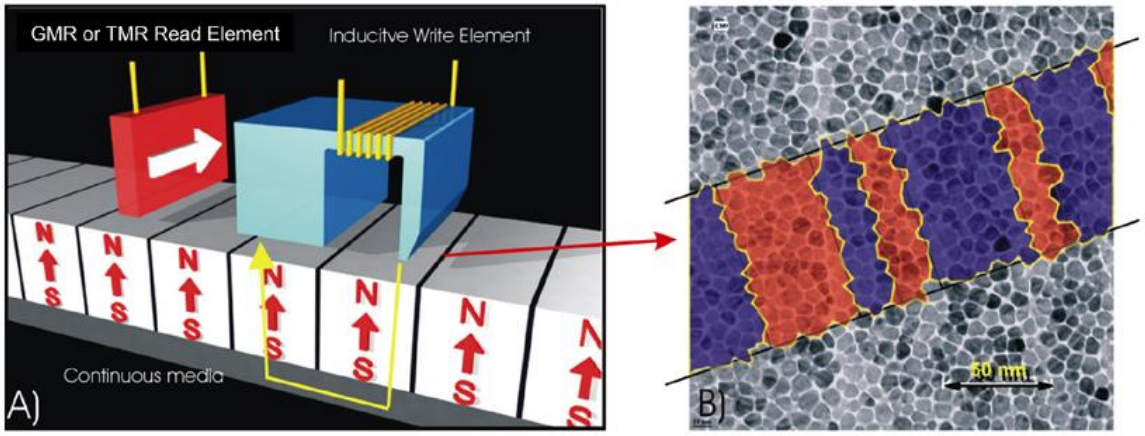

Figure 1.1 (a) A schematic illustration of a read-write head writing bits into perpendicularly magnetized media. (b) A TEM image of individual magnetic grains. Red and blue regions indicate magnetic bits of opposite polarities. Image from [3], © 2008 IEEE.

For many years, areal density has increased by simply shrinking the bit size (i.e., the total disk surface domain size whose magnetic polarity defines stored data) by

decreasing the number of magnetic grains that make up one bit. However, continual reduction of the number of grains in a bit eventually leads to intolerable signal-to-noise ratio (SNR). When the number of grains per bit is decreased, the bit boundary shape becomes increasingly distorted, as illustrated in **Figure 1.1(b)**. The SNR of the data stored on the HDD is inversely proportional to the number of grains in a bit:

$$SNR \propto \frac{W_{bt}}{V_g} \qquad \textbf{Equation 1.1}$$

where W_{bt} is the volume of a bit and V_g is the volume of a grain.[4] Therefore, decreasing the grain volume will allow the bit size to decrease while maintaining an acceptable SNR. However, if the grain volume is reduced too much, the magnetization becomes unstable and can spontaneously flip at room temperature, a phenomenon known as the superparamagnetic effect. Magnetization reversal can happen spontaneously when the anisotropy energy ($E_A = K_u V_g$) becomes comparable to the thermal energy ($E_T = k_B T$), where K_u is the anisotropy energy per unit volume, k_B is the Boltzmann constant, and T is the absolute temperature.[5] K_u is an intrinsic material property of the magnetic medium; therefore, continuous grain volume reduction will eventually lead to data corruption. Spontaneous magnetic switching manifests itself as an unacceptable loss of data integrity in a HDD.

For conventional perpendicular magnetic media currently used in the industry, 800-900 Gbit/in^2 HDD's are being shipped, and Toshiba recently unveiled a HDD with 1 Tbit/in^2 information density.[6] However, 1 Tbit/in^2 is approximately the limit for perpendicular magnetic media described above, and new recording technologies[7] are required to keep the HDD industry on pace with the Advanced Storage Technology Consortium (ASTC) roadmap shown in **Figure 1.2**.

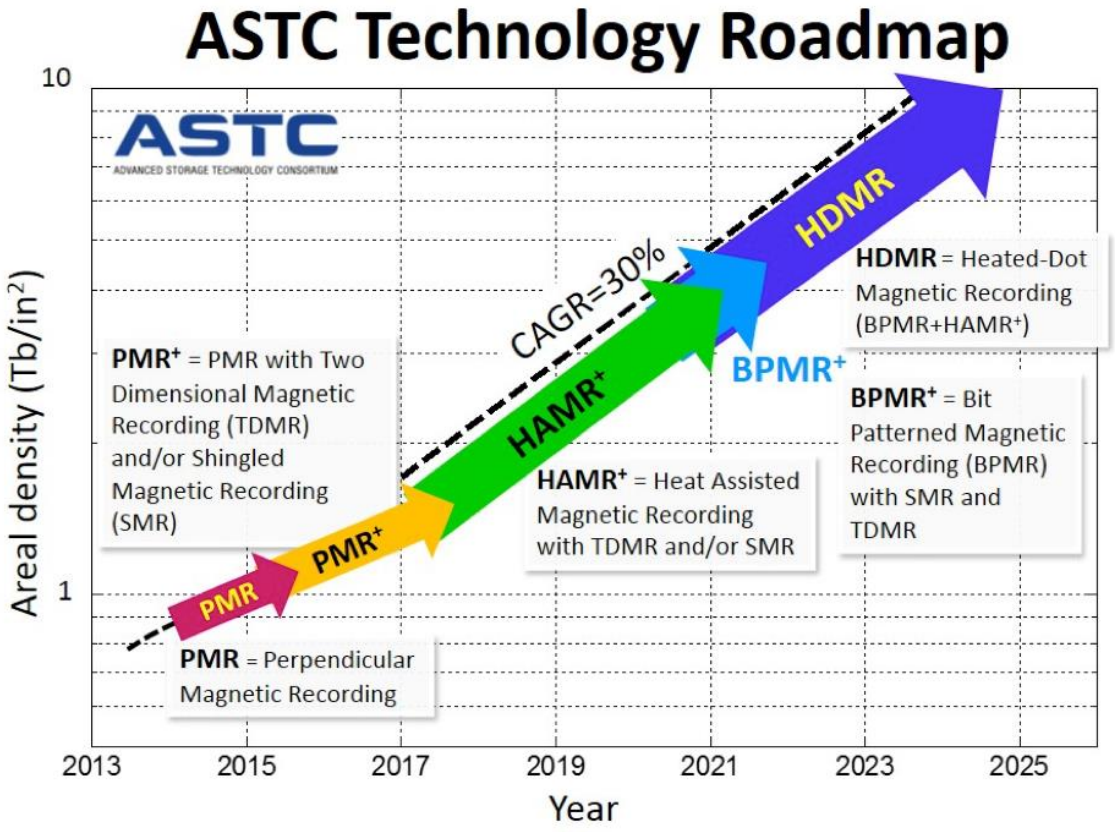

Figure 1.2 ASTC roadmap of increasing areal storage density on hard disk drives. Image from [8], © 2014 IDEMA.

1.2 Overcoming the Superparamagnetic Effect

Developing new recording technologies to move past the information density limit imposed by the superparamagnetic effect has been a priority for the HDD industry for many years, and several promising candidates have emerged. As shown in **Figure 1.2**, two dimensional magnetic recording (TDMR), shingled magnetic recording (SMR), heat assisted magnetic recording (HAMR), and bit patterned magnetic recording (BPMR) are expected to increase areal density to over 10 Tbit/in^2 and carry the HDD industry through 2025. This section will give a brief overview, including advantages and disadvantages, of each recording strategy.

1.2.1 Two dimensional magnetic recording (TDMR)

TDMR relies on using a complex algorithm to process a two dimensional wave signal instead of the typical one-dimensional signal (magnetization polarity), which can theoretically reduce bit sizes down to a single grain,[9] as shown in **Figure 1.3**. With each grain as a separate bit, information densities of up to 10 Tb/in^2 can be realized.[10] However, major drawbacks include read/write heads being too large to read or write at such a small scale and still-nascent processing algorithms.[11–13] While it is unlikely that this recording technology will be implemented on its own in the near future,[13] TDMR can offer numerous processing advantages when used in conjunction with other strategies.

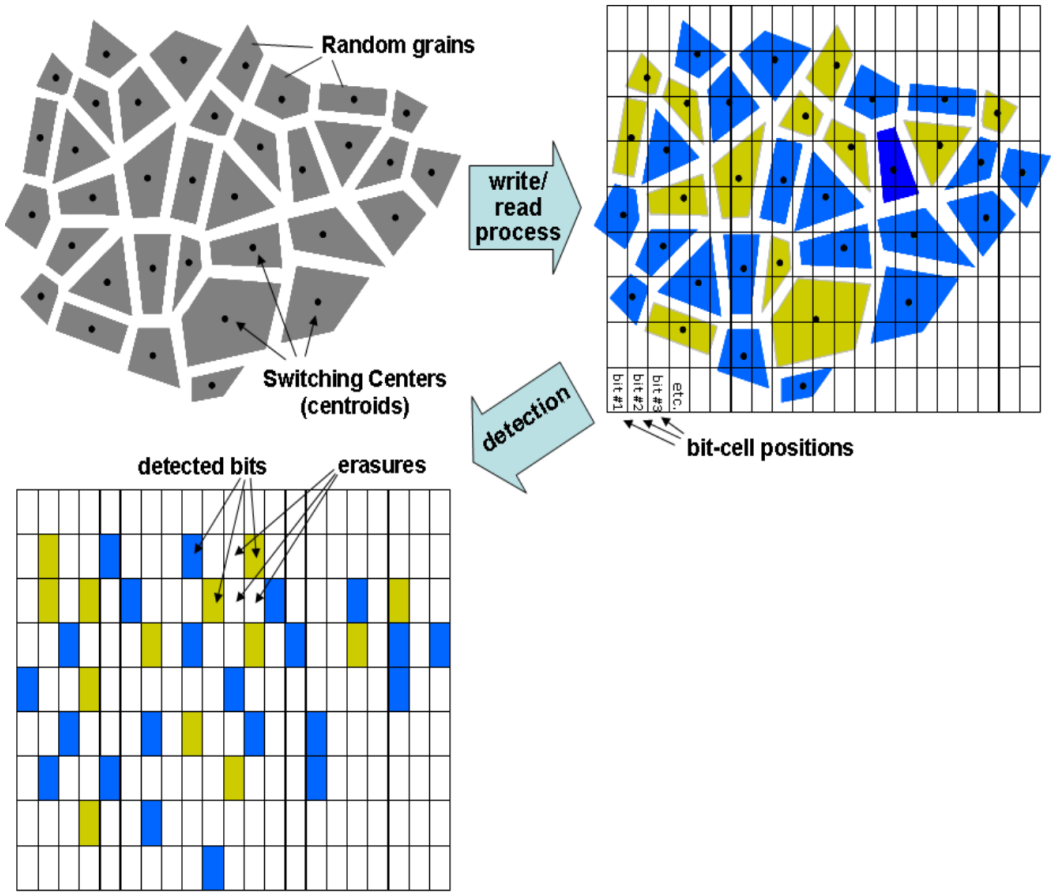

Figure 1.3 Schematic illustrating the principle behind two dimensional magnetic recording (TDMR). Each individual random grain can act as a bit, each bit can be detected using a two dimensional waveform. Schematic from [9], © 2010 IEEE.

1.2.2 Shingled magnetic recording (SMR)

SMR is a recording technology that uses much of the existing HDD read-write architecture and media and improves areal density by partially overwriting adjacent tracks, much like shingles on a roof (**Figure 1.4**). It is easier to read thinner tracks than to write thinner tracks, and the main advantage of this approach is that it can improve areal density up to 2.25x without equipment innovation.[14] The widths of the written tracks are not greatly reduced; therefore, the strength of the magnetic polarization is strong enough to prevent

the superparamagnetic effect.[14] The main challenge to this approach is rewriting information without damaging the information contained on neighboring tracks and the associated slow HDD response times.[15] Despite these challenges, Seagate announced its first SMR HDD in September 2013,[16] followed by HGST in September 2014.[17]

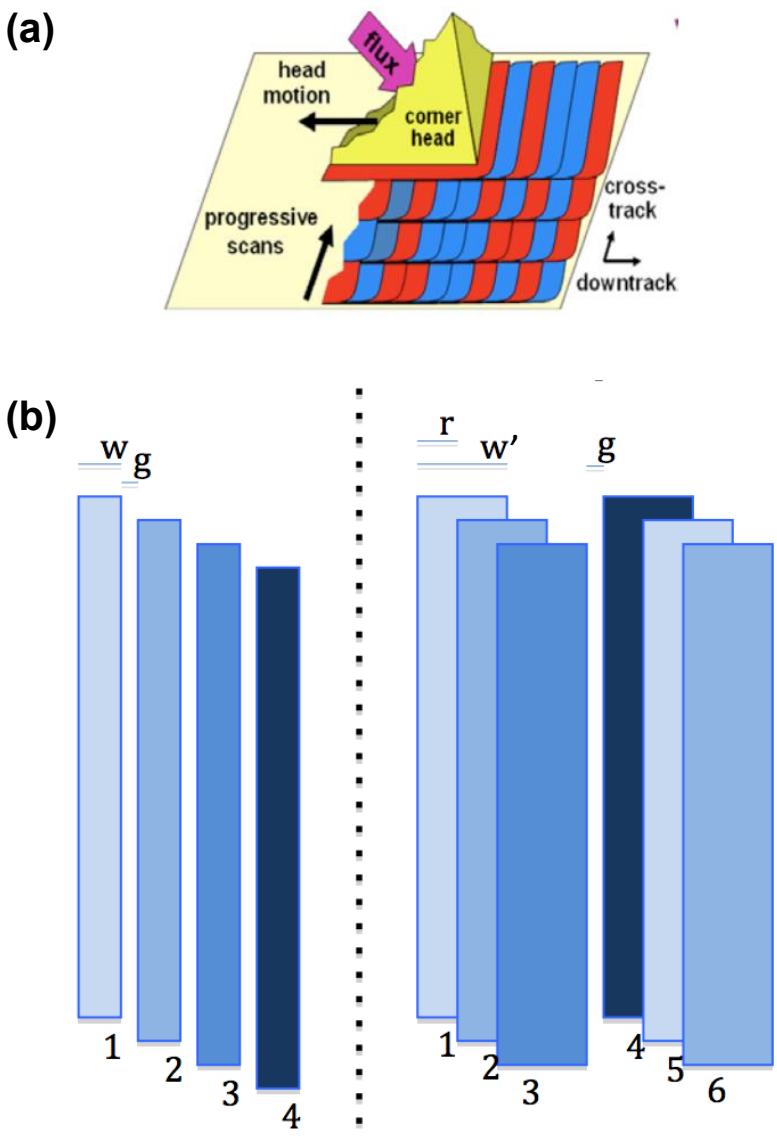

Figure 1.4 (a) Schematic of how SMR works. Each successive track partially overwrites the previous adjacent track, allowing for thinner tracks. (b) A more detailed schematic explaining SMR. The left side portrays four traditional tracks numbered 1-4 with width w and distance g between tracks. The right side portrays six shingled tracks numbered 1-6 with width w', effective width r, and distance g between shingled groups. Schematic from [18].

1.2.3 Heat assisted magnetic recording (HAMR)

HAMR exploits the temperature dependence of a magnetic property called coercivity: as temperature increases, coercivity decreases. When magnetic coercivity is higher, magnetic polarization is more stable, but the magnetic media is more difficult to write. As bit size decreases, so does magnetic coercivity, and there exists a size at which the superparamagnetic effect becomes a destabilizing factor. However, if a magnetic medium with a higher coercivity is employed and a laser is used to locally heat the small portion of the medium that is being written, the data can be written at low coercivity.[19] Soon after the laser and write head moves to the next area, the previously heated area cools rapidly, regaining the high coercivity desired for stable data storage (**Figure 1.5**).[20]

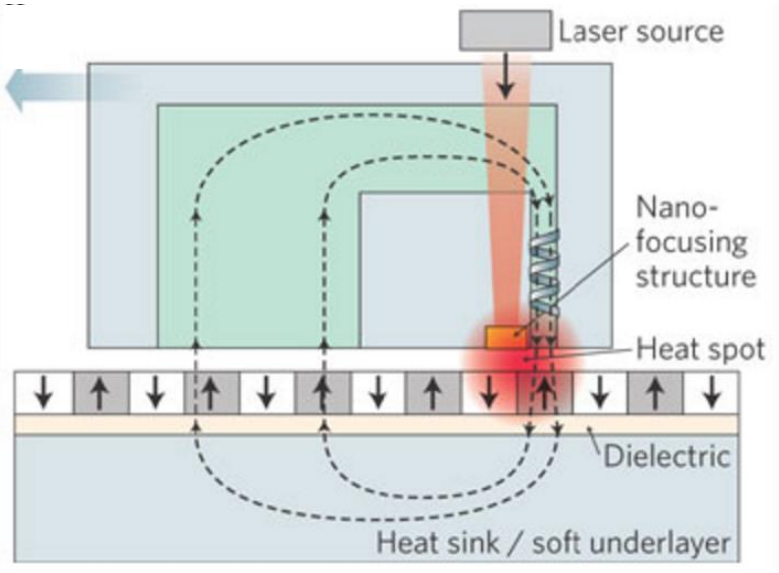

Figure 1.5 Schematic of HAMR technology. A laser attached to the write head heats a small spot on the recording media while information is written, thus skirting the superparamagnetic effect. Reprinted with permission from [21], © 2009 Nature Photonics.

The major technological challenge to this approach is manufacturing a write head with an attached laser powerful enough to heat the magnetic media to the required writing

temperature.[22] Due to this challenge, commercial HDD's with HAMR technology have not yet been commercially manufactured.[23]

1.2.4 Bit patterned magnetic recording (BPMR)

BPMR shifts the media paradigm away from continuous magnetic media to discrete magnetic islands in an "insulating" matrix, as shown in **Figure 1.6**. By magnetically isolating each bit, the effect of surrounding magnetic polarizations is diminished, leading to higher SNR. The smallest bit size is now limited by the patterning of each bit and the ability of the read/write head to register the bits.[24] Theoretically, bit sizes can shrink down to several nanometers in size, thereby increasing areal density up to 5 Tb/in^2 or more.[25]

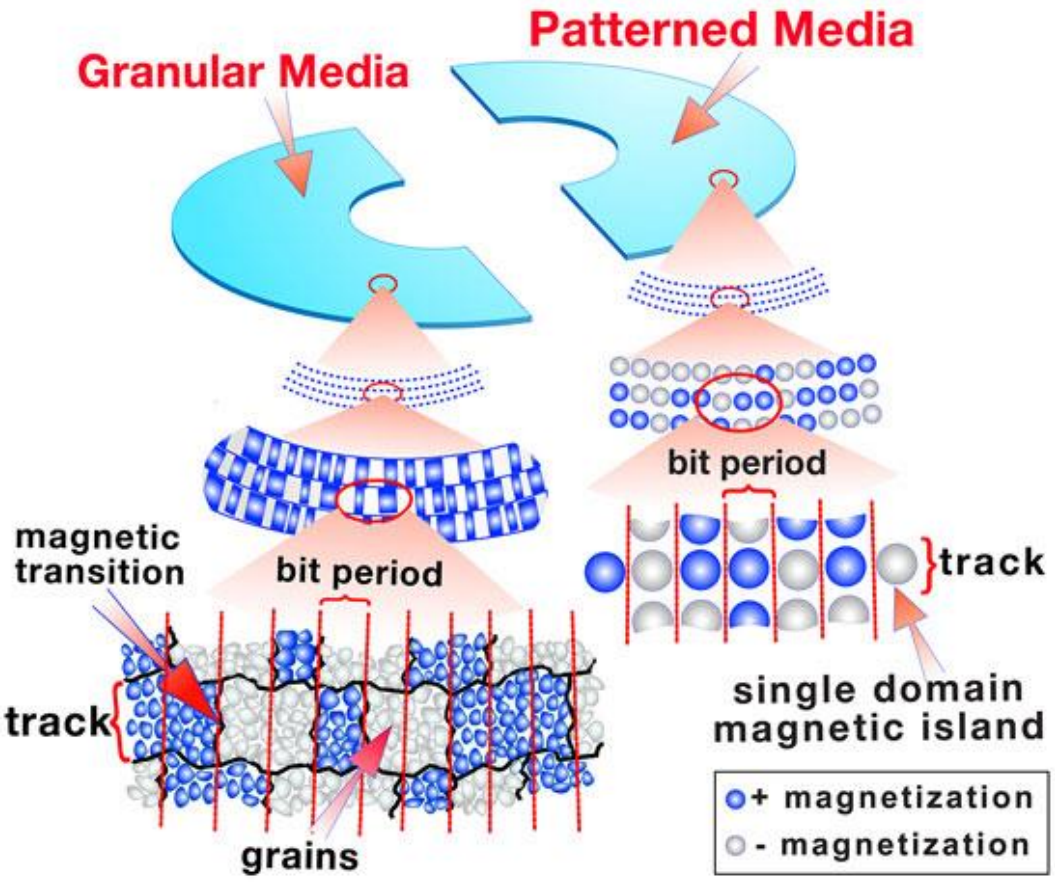

Figure 1.6 Differences between conventional HDD magnetic media (left) and bit patterned magnetic media (right). In conventional HDD magnetic media, bit boundaries are determined by the read/write head. In bit patterned media, each magnetic bit's size and location are predetermined. Figure from [3], © 2008 IEEE..

The challenge to implementing BPMR is developing a technique for placing the small magnetic islands in precisely controlled locations and then manufacturing disks containing such structures on a commercial scale. Nanoimprint lithography, wherein a master template can be used to create replicate disk patterns, is a potential solution to this problem,[26] but a master template must first be manufactured. Because each bit is so small, conventional patterning techniques are either inadequate or prohibitively expensive and time consuming.[27]

This dissertation focuses on the use of block copolymers (BCP) to pattern nanoimprint templates to enable BPMR for the HDD industry. Several promising preliminary results, such as that shown in **Figure 1.7**, have demonstrated that BCPs can be used to fabricate ordered, well-aligned features.[28,29] However, shrinking the size of each bit to below 10 nm and ensuring perfect pattern alignment over a 3.5-inch disk are challenges yet to be addressed.

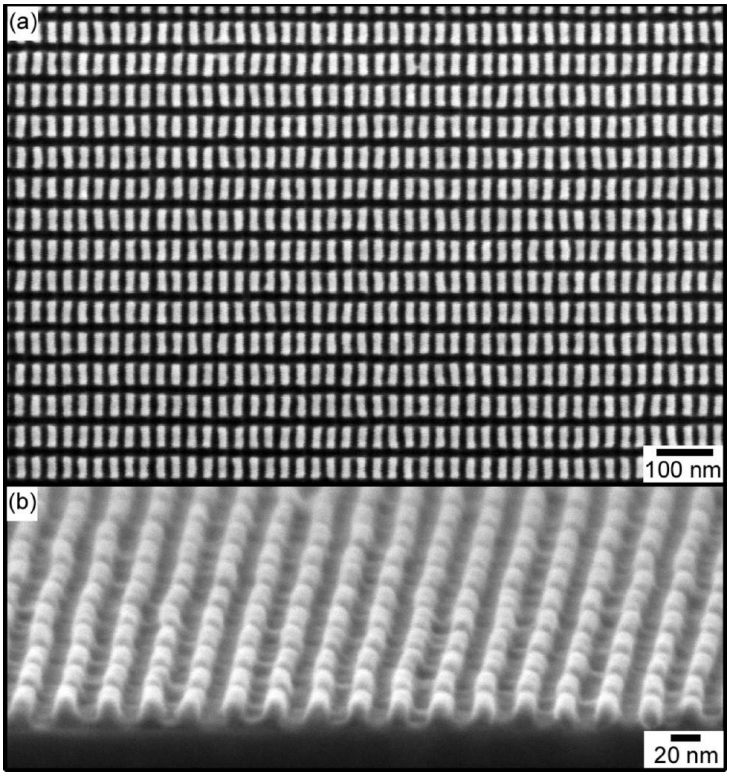

Figure 1.7 Etched BCP features on a silicon wafer. This demonstrates that BCP can be used to pattern small, well-ordered, periodic structures, although the size of each feature in this figure remain too large for its intended HDD application. Reprinted with permission from [28]. Copyright 2011American Chemical Society.

1.3 BLOCK COPOLYMER LITHOGRAPHY

A key step to implementing BPMR is developing a methodology for patterning the individual bits. Because the bits must be on the size scale of single nanometers to achieve

the projected areal densities,[24] the patterning process must be able to accurately and precisely produce features of 10 nm or smaller.

Photolithography, the use of light to pattern features, is the patterning process currently used in high volume semiconductor manufacturing. However, the attainable feature size is limited by the wavelength of light used, and the current technology can pattern half pitches down to approximately 40 nm with 193 nm radiation, far larger than the 10 nm target for BPMR.[30] Advanced light sources with smaller wavelengths, such as extreme ultraviolet lithography machines, are currently being developed, but these new machines are prohibitively expensive and wildly behind high-throughput production schedule.[31]

BCP lithography is a promising approach for fabricating magnetically isolated bits at this size range[31–34] in a high throughput manner. In this dissertation, BCP will refer exclusively to diblock copolymers (**Figure 1.8(a)**), a subgroup of multiblock copolymers (**Figure 1.8(b)**). Diblock copolymers consist of two chemically distinct homopolymers that are covalently joined at one terminus of each.

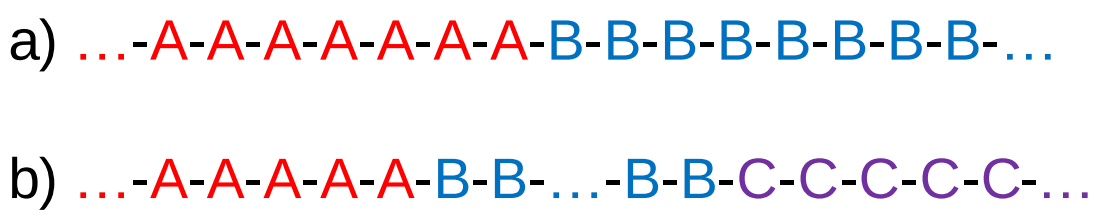

Figure 1.8 (a) Diblock copolymer with poly-A and poly-B blocks. (b) Triblock terpolymer with poly-A, poly-B, and poly-C blocks. Many other forms of multiblock copolymers exist, including copolymers with repeating blocks, such as an A-B-A triblock terpolymer.

Because the two blocks are usually immiscible, BCPs often microphase separate upon annealing to form periodic structures with a characteristic length scale ranging from 5-100 nm.[35–37] The process flow by which a BCP can be used to pattern a silicon substrate is shown in **Figure 1.9**. Once the appropriate molecular architecture is chosen, the BCP is deposited as a thin film onto the substrate. The BCP must then be oriented in such a way that features are visible from the top down, which is usually perpendicular to the substrate. Once the desired features are present, one block is selectively removed, and the remaining block acts as an etch mask for the underlying substrate. The etched silicon substrate can then be used as a patterning template for nanoimprint lithography.

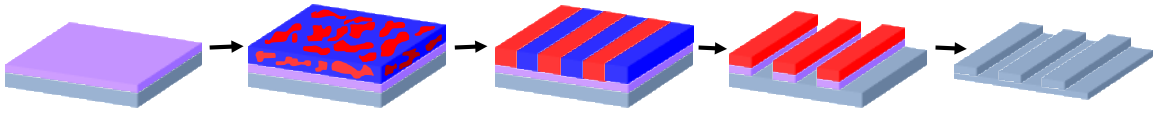

Figure 1.9 To make a patterning template, a BCP solution is first spin-coated onto a silicon substrate coated with a neutral surface treatment. After BCP is oriented and aligned on the substrate, one block is selectively removed by reactive ion etching, and the remaining block becomes an etch mask for the substrate. Finally, the pattern is transferred to the substrate and the remaining polymer is washed off.

In order for a BCP to be lithographically useful, it should satisfy the following criteria:

1. Form a lithographically useful morphology
2. Form features that are small enough to be useful for the application
3. Perpendicular orientation in thin films
4. Etch selectivity and resistance for ease of pattern transfer
5. Ability to be aligned over large areas

Judicious selection of the two blocks can help satisfy most, if not all, of the above criteria, which will each be explained in more detail in the following subsections.

1.3.1 BCP morphologies

A variety of chemical strategies can be employed to tailor BCPs to the processing needs of specific applications. Different self-assembled morphologies can be accessed by manipulating the volume ratios of the two blocks. As shown in **Figure 1.10**, morphologies from cubic packed spheres to hexagonally packed cylinders to lamellae can be achieved. Cubic spheres may be useful for templating graphene nanodots,[38] while hexagonal cylinders and lamellae can be useful for the HDD industry.

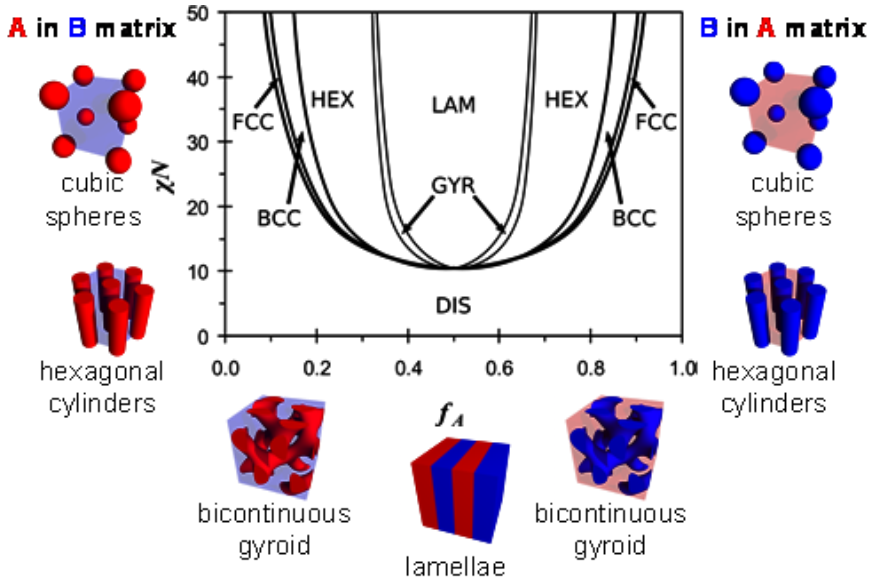

Figure 1.10 Different morphologies can be achieved using BCPs by varying the volume fraction of one block to the other. In this phase diagram, reprinted from, the morphologies that can be achieved for a diblock copolymer are illustrated. Reprinted with permission from [39]. Copyright 2006 American Chemical Society.

1.3.2 Minimum feature sizes of BCPs

The size of the features formed is governed by the BCP's degree of polymerization (N) and the Flory-Huggins interaction parameter (χ) between the two components of the BCP.[40] The product χN is a direct measure of the thermodynamic incompatibility between two blocks, with a higher χN designating more chemically incompatible blocks, providing a quantitative means to evaluate the smallest possible features accessible by a given chemical structure. The domain spacing (d) for symmetric, lamella-forming BCP's scales with χ and N by the following relationship[41]:

$$d = a\chi^{1/6}N^{2/3} \qquad \textbf{Equation 1.2}$$

showing that smaller periodic structures are achieved by reducing N. However, below a critical threshold value of $\chi N \sim 10.5$, volumetrically symmetric diblock copolymers no longer microphase separate but become miscible in one another, as illustrated by the disordered region (DIS) in **Figure 1.10**.[41]

It is clear that so called "high χ" block copolymers are needed to access smaller d values, and therefore smaller features, to take advantage of the weaker χ dependence relative to N in **Equation 1.2** and still be above the miscibility threshold. χ was originally defined to represent the energetic penalty for removing one repeat unit from a lattice of its peers and placing it in a new lattice where it is surrounded by a different chemical constituent. Therefore, χ in a BCP can be increased by making the blocks more chemically dissimilar or by enhancing intramolecular interactions between identical blocks. In addition, based on the phase diagram shown in **Figure 1.10**, the smallest ordered features for a specific BCP can be accessed only when the volume fractions of A and B are 50:50 in the lamellae morphology. Therefore, the majority of the work presented in this dissertation is focused on symmetric lamellae-forming BCPs.

1.3.3 Perpendicular orientation of BCP thin films

In addition to having the ability to form smaller features, a lithographically useful BCP must also be able to be process-able using current industrial equipment. Processing, when applied to BCP lithography, means orienting the BCP in a thin film into lithographically useful features oriented perpendicular to the substrate. This way, both blocks can be seen from a top down view, as shown in **Figure 1.11**. Thereafter, one of the blocks can be selectively removed, and the remaining block can be used as an etch mask.[42]

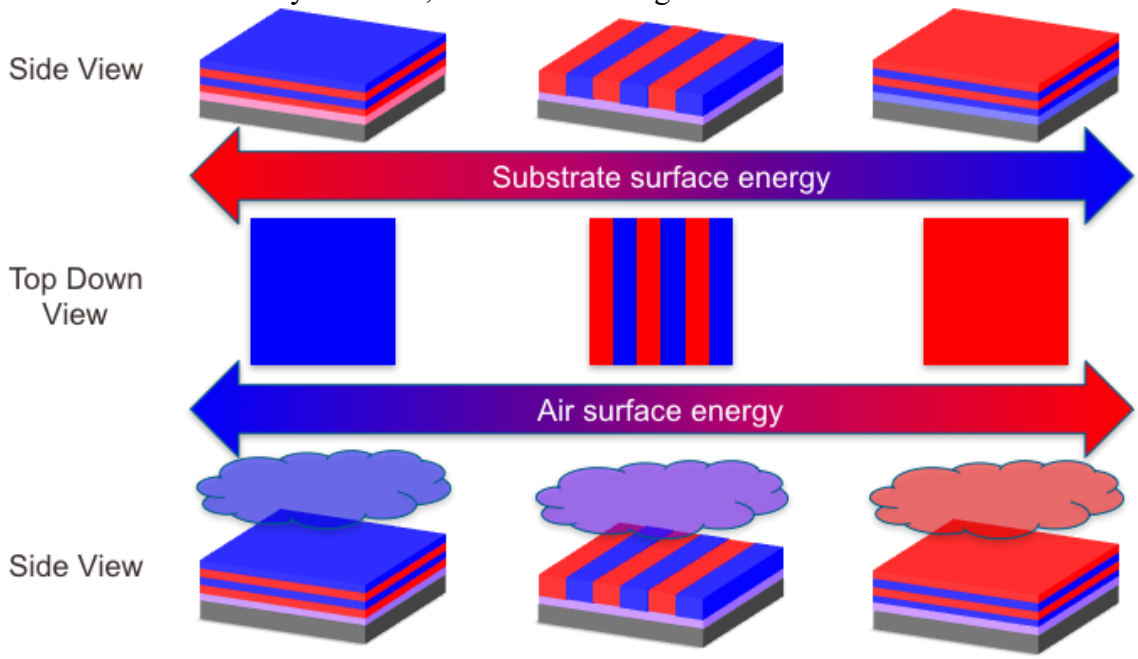

Figure 1.11 The importance of neutral surface energies on lamellae-forming BCP alignment in thin film. Starting from the top row, the substrate surface energy must be neutral for the BCP (neither block preferentially wetting the substrate). Next, as shown in the bottom row, the top interface must also be neutral. Only when both the top and bottom interfaces are neutral for the BCP will the desired line-and-space pattern be visible from a top down view.

In order for a BCP to orient itself perpendicular to a substrate, the surface energies of the materials below the BCP (the substrate) and above the BCP must be 'neutral' relative

to the BCP. In other words, the substrate and the top interface must both possess a surface energy in between the surface energies of the two blocks of the BCP such that neither block prefers to wet either interface.[43] The substrate surface energy can be easily tuned using a crosslinked or grafted surface neutralization treatment,[44] but controlling the top interface surface energy is more challenging in practice.

Solvent annealing,[35,43,45] polymeric top coats,[46–48] thermal annealing, electric fields, and shear alignment have all been used to perpendicularly align BCP's, among many other orientation strategies. Among these strategies, polymeric top coats and thermal annealing are the most attractive. Polymeric top coats require careful selection of an appropriate top coat, but once selected, it easily integrates into existing process flows with simple spin coating and thermal annealing track equipment. Thermal annealing is the simplest and most easily integrated annealing strategy in terms of processing. Because surface energy can also vary with temperature, for certain BCPs whose blocks' surface energies are slightly different, there may exist a temperature at which their surface energies are the same below their degradation temperatures.[49] In these cases, a simple one-step thermal annealing process, which only requires a hot plate, can perpendicularly orient the BCP microdomains (e.g., poly(styrene-*block*-methyl methacrylate) (PS-PMMA) fits into this category).

1.3.4 Etch resistance and etch selectivity

After the desired perpendicular structure is achieved in a thin film, the structure must be translated into the underlying inorganic substrate through an etch step. The governing parameter during this step is etch selectivity, or the relative etch rate between the two blocks of the BCP.[50] For an ideal BCP, one block would be highly resistant to the etch while the other would be minimally resistant, resulting in complete removal of one block and leaving behind high aspect ratio features comprised of the other block.[51] After

etching away one block, the remaining block acts as an etch mask for the underlying substrate. Etching into the substrate typically requires a different etch recipe, and in general, tall, high-aspect ratio etch mask features simplify processing.

1.3.5 Long range alignment

For BCPs to be useful for the HDD industry, it must produce bits that are aligned and evenly spaced over a large area, such as a standard 3.5-inch HDD. For this reason, simply having perpendicular features is not enough; the features must be located at precise intervals relative to each other such that a read/write head can determine the location of adjacent bits based on one bit. For this, long range alignment of the BCP is necessary which is often achieved using directed self-assembly (DSA) strategies.[52]

Chemoepitaxy (**Figure 1.12**) and graphoepitaxy (**Figure 1.13**) are two approaches to the DSA of BCP's. Chemoepitaxy relies on using substrate surface patterns that are chemically preferential to one block of the BCP to "guide" the BCP to the desired pattern.[53,54] Graphoepitaxy uses physical trenches with preferential walls to guide the alignment of BCPs.[55] The BCPs best suited to DSA are those with two very chemically disparate blocks so that one block will strongly preferentially interact with either a guide stripe or a trench wall. However, the BCP must also be perpendicularly oriented in both chemoepitaxy and graphoepitaxy, and a high-χ BCP typically requires a more complicated orientation strategy due to the often significant surface energy mismatch between the two blocks.

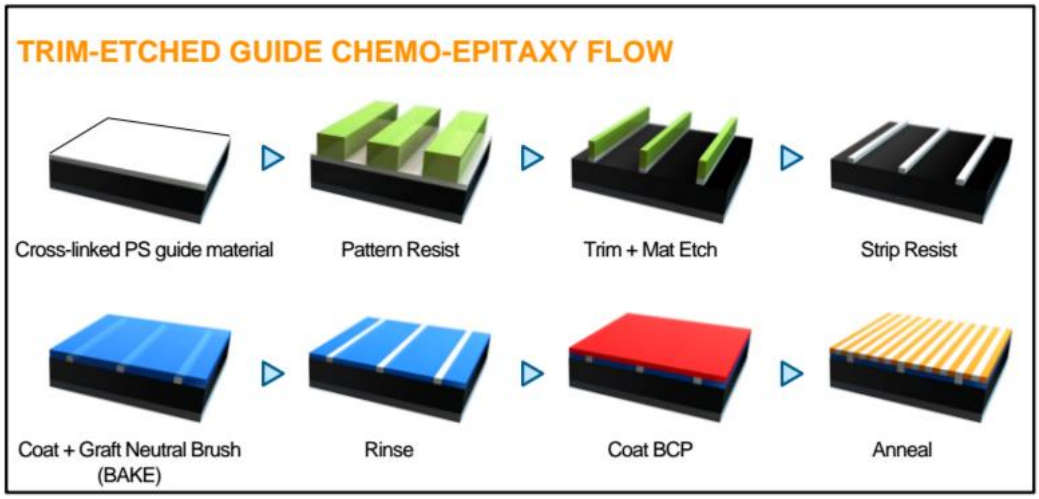

Figure 1.12 An example chemoepitaxy flow. Chemoepitaxy uses patterned substrate surface lines that are chemically preferential to one block of the BCP to guide alignment over the patterned area. Each patterned line can be spaced at a multiple of the natural domain periodicity of the BCP, resulting in pattern density multiplication. In this schematic, 4x density multiplication is illustrated. Schematic from [56]. Copyright 2012 Society of Photo Optical Instrumentation Engineers.

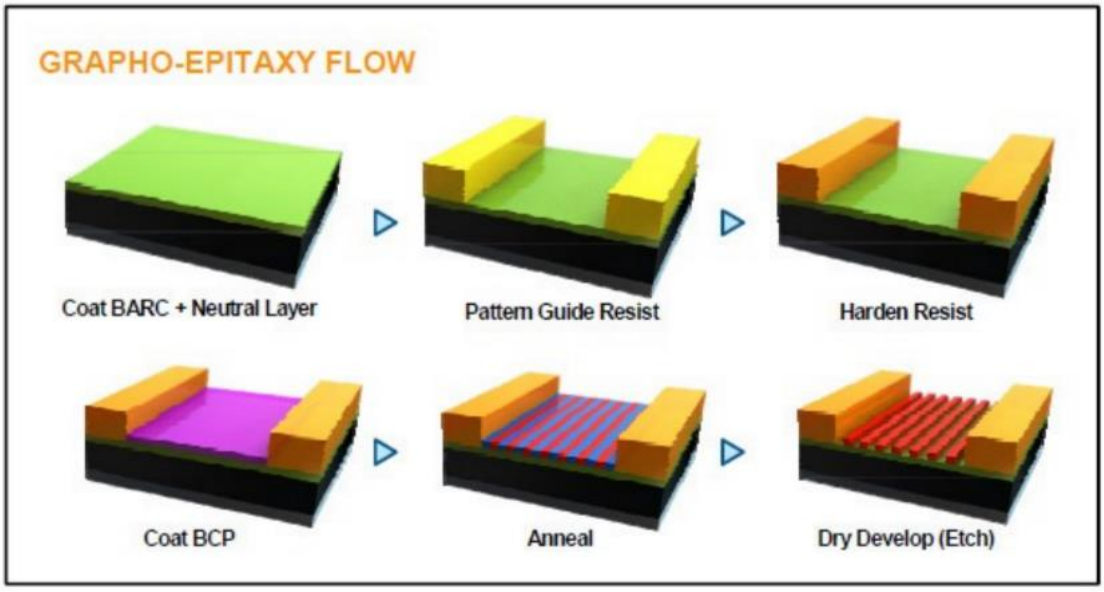

Figure 1.13 Graphoepitaxy flow. Graphoepitaxy uses topographic relief features on the substrate to form trenches with walls that are preferential to one block of the block copolymer. When the substrate is coated with a neutral layer, the preferential block will wet the walls, and the alignment will propagate inwards to fill the trench. Schematic from [56]. Copyright 2012 Society of Photo Optical Instrumentation Engineers.

1.3.6 BCP lithography challenges

Bit patterned magnetic recording represents a paradigm shift from the continuous magnetic media to bit patterned media, which brings with it a host of technological challenges. Two main challenges are adapting the current read/write procedure to bit patterned media and managing the defects of the BCP nanopattern to create the nanoimprint mask.

First, the read/write procedure must be modified to account for each discrete dot, and spatial error tolerances are on the order of 1 nm.[24] Instead of creating the bit boundaries based on the area of the read/write head, the equipment and software must be altered to recognize discrete magnetic islands.[3] In addition, the small bit sizes necessitate either writing with stronger magnetic field strengths or reading with greater sensitivity.[57]

Next, the individual bits must be arranged precisely for the read/write head to recognize them, which means the BCP nanopattern must be aligned perfectly across the area of the HDD. This requires precise control over alignment and orientation of the BCP thin film, and the etch process must transfer the patterns in the BCP to the underlying substrate with great fidelity. Despite these challenges, BPMR remains a promising technology to lead the HDD industry to greater areal densities. While there are many BCPs that already fulfill some of the five criteria listed in Section 1.2,[32,48,58,59] there does not yet exist a BCP that can fulfill all five criteria.

The following chapters in this dissertation present four BCPs that were studied for their potential use in making the nanoimprint masks needed for the HDD industry to implement BPMR. Chapter 2 discusses the synthesis and thin film studies of two silicon-containing BCPs, poly(trimethylsilyl styrene-*block*-lactide) (PTMSS-PLA) and poly(trimethylsilyl styrene-*block*-isoprene) (PTMSS-PI), wherein a silicon-containing block was incorporated into the BCP to enhance both etch contrast and χ. Chapter 3 focuses on another silicon-containing BCP, poly(pentamethydisilyl styrene-*block*-ethyl glycolide) (PDSS-PEGL) by further increasing the chemical dissimilarity between the two blocks relative to PTMSS-PLA. Chapter 4 focuses on the synthesis, thin film studies, and χ characterization for the BCP poly((styrene–*random*-vinylnaphthalene)-*block*-methyl methacrylate) (PSVN-PMMA), a BCP that simplifies the perpendicular orientation process, and Chapter 5 details the photochemistry of PSVN-PMMA. This dissertation concludes with some future works, found in Chapter 6.

1.4 References

(1) Moore, G. E. Cramming More Components onto Integrated Circuits. *Electronics* **1965**, *38* (5), 114–117.

(2) Walter, C. Kryder's Law. *Scientific American*. 2005.

(3) Dobisz, E. A.; Bandić, Z. Z.; Wu, T. W.; Albrecht, T. Patterned Media: Nanofabrication Challenges of Future Disk Drives. *Proc. IEEE* **2008**, *96* (11), 1836–1846.

(4) Wood, R. The Feasibility of Magnetic Recording at 1 Terabit per Square Inch. *IEEE Trans. Magn.* **2000**, *36* (1), 917–923.

(5) Weller, D.; Moser, A. Thermal Effect Limits in Ultrahigh-Density Magnetic Recording. *IEEE Trans. Magn.* **1999**, *35* (6), 4423–4439.

(6) Alcorn, P. Toshiba Achieves Record Areal Density in 2.5-Inch HDDs.

(7) Ross, C. A. Patterned Magnetic Recording Media. *Annu. Rev. Mater. Res.* **2001**, *31*, 203–235.

(8) ASTC. ASTC Technology Roadmap.

(9) Wood, R. *Shingled Magnetic Recording and Two-Dimensional Magnetic Recording*; 2010.

(10) Krishnan, A. R.; Radhakrishnan, R.; Vasic, B. Read Channel Modeling for Detection in Two-Dimensional Magnetic Recording Systems. *IEEE Trans. Magn.* **2009**, *45* (10), 3679–3682.

(11) Chan, K. S.; Radhakrishnan, R.; Eason, K.; Elidrissi, M. R.; Miles, J. J.; Vasic, B.; Krishnan, A. R. Channel Models and Detectors for Two-Dimensional Magnetic Recording. *IEEE Trans. Magn.* **2010**, *46* (3 PART 1), 804–811.

(12) Hwang, E.; Negi, R.; Kumar, B. V. K. V. Signal Processing for Near 10 Tbit/in<formula Formulatype="inline"> <img src="/images/tex/732.gif" alt="^{2}"> </formula> Density In<newline/> Two-Dimensional Magnetic Recording (TDMR). *IEEE Trans. Magn.* **2010**, *46* (6), 1813–1816.

(13) Wood, R.; Williams, M.; Kavcic, A.; Miles, J. The Feasibility of Magnetic Recording at 10 Terabits per Square Inch on Conventional Media. *IEEE Trans. Magn.* **2009**, *45* (2), 917–921.

(14) Amer, A.; Holliday, J.; Long, D. D. E.; Miller, E. L.; Pâris, J. F.; Schwarz, T. Data Management and Layout for Shingled Magnetic Recording. *IEEE Trans. Magn.* **2011**, *47* (10), 3691–3697.

(15) Hall, D.; Marcos, J. H.; Coker, J. D. Data Handling Algorithms for Autonomous Shingled Magnetic Recording HDDs. *IEEE Trans. Magn.* **2012**, *48* (5 PART 1), 1777–1781.

(16) Shimpi, A. L. Seagate to Ship 5TB HDD in 2014 using Shingled Magnetic Recording http://www.anandtech.com/show/7290/seagate-to-ship-5tb-hdd-in-2014-using-shingled-magnetic-recording/.

(17) Gasior, G. Shingled platters breathe helium inside HGST's 10TB hard drive.

(18) Gibson, G.; Ganger, G. *Principles of Operation for Shingled Disk Devices*; 2011.

(19) Rottmayer, R. E.; Batra, S.; Buechel, D.; Challener, W. A.; Hohlfeld, J.; Kubota, Y.; Li, L. L. L.; Lu, B. L. Bin; Mihalcea, C.; Mountfield, K.; Pelhos, K.; Peng, C. P. C.; Rausch, T.; Seigler, M. A.; Weller, D.; Yang, X. Y. X. Heat-Assisted Magnetic Recording. *IEEE Trans. Magn.* **2006**, *42* (10), 2417–2421.

(20) Kryder, M. H.; Gage, E. C.; McDaniel, T. W.; Challener, W. A.; Rottmayer, R. E.; Ganping Ju; Yiao-Tee Hsia; Erden, M. F. Heat Assisted Magnetic Recording. *Proc. IEEE* **2008**, *96* (11), 1810–1835.

(21) Pan, L.; Bogy, D. B. Data Storage: Heat-Assisted Magnetic Recording. *Nat. Photonics* **2009**, *3* (4), 189–190.

(22) Stipe, B. C.; Strand, T. C.; Poon, C. C.; Balamane, H.; Boone, T. D.; Katine, J. a.; Li, J.-L.; Rawat, V.; Nemoto, H.; Hirotsune, A.; Hellwig, O.; Ruiz, R.; Dobisz, E.; Kercher, D. S.; Robertson, N.; Albrecht, T. R.; Terris, B. D. Magnetic Recording at 1.5 Pb m−2 Using an Integrated Plasmonic Antenna. *Nat. Photonics* **2010**, *4* (7), 484–488.

(23) Shilov, A. Hard Disk Drives with HAMR Technology Set to Arrive in 2018 http://www.anandtech.com/show/9866/hard-disk-drives-with-hamr-technology-set-to-arrive-in-2018.

(24) Shiroishi, Y.; Fukuda, K.; Tagawa, I.; Iwasaki, H.; Takenoiri, S.; Tanaka, H.; Mutoh, H.; Yoshikawa, N. Future Options for HDD Storage. *IEEE Trans. Magn.* **2009**, *45* (10), 3816–3822.

(25) Richter, H. J.; Dobin, A. Y.; Gao, K.; Heinonen, O.; Van De Veerdonk, R. J.; Lynch, R. T.; Xue, J.; Weller, D. K.; Asselin, P.; Erden, M. F.; Brockie, R. M. Recording on Bit-Patterned Media at Densities of 1Tb/in2 and beyond. *INTERMAG 2006 - IEEE Int. Magn. Conf.* **2006**, *42* (10), 721.

(26) Yang, X.; Xu, Y.; Seiler, C.; Wan, L.; Xiao, S. Toward 1Tdot ⁄ in.2 Nanoimprint Lithography for Magnetic Bit-Patterned Media: Opportunities and Challenges. *J. Vac. Sci. Technol. B* **2008**, *26* (2008), 2604–2610.

(27) Ruiz, R.; Kang, H.; Detcheverry, F. A.; Dobisz, E.; Kercher, D. S.; Albrecht, T. R.; de Pablo, J. J.; Nealey, P. F. Density Multiplication and Improved Lithography by Directed Block Copolymer Assembly. *Science (80-.).* **2008**, *321* (5891), 936–939.

(28) Ruiz, R.; Dobisz, E.; Albrecht, T. R. Rectangular Patterns Using Block Copolymer Directed Assembly for High Bit Aspect Ratio Patterned Media. *ACS Nano* **2011**, *5* (1), 79–84.

(29) Wan, L.; Ruiz, R.; Gao, H.; Patel, K. C.; Lille, J.; Zeltzer, G.; Dobisz, E. a.; Bogdanov, A.; Nealey, P. F.; Albrecht, T. R. Fabrication of Templates with Rectangular Bits on Circular Tracks by Combining Block Copolymer Directed

Self-Assembly and Nanoimprint Lithography. *J. Micro/Nanolithography, MEMS, MOEMS* **2012**, *11* (3), 031405–1.

(30) Pease, B. R. F.; Chou, S. Y. Lithography and Other Patterning Techniques for Future Electronics. *Proc. IEEE* **2008**, *96* (2).

(31) Neisser, M.; Wurm, S. ITRS Lithography Roadmap: 2015 Challenges. *Adv. Opt. Technol.* **2015**, *4* (4), 235–240.

(32) Bates, C. M.; Maher, M. J.; Janes, D. W.; Ellison, C. J.; Willson, C. G. Block Copolymer Lithography. *Macromolecules* **2014**, *47* (1), 2–12.

(33) Ji, S.; Liu, C.-C.; Liu, G.; Nealey, P. F. Molecular Transfer Printing Using Block Copolymers. *ACS Nano* **2010**, *4* (2), 599–609.

(34) Stoykovich, M. P.; Nealey, P. F. Block Copolymers and Conventional Lithography. *Mater. Today* **2006**, *9* (9), 20–29.

(35) Cushen, J. D.; Otsuka, I.; Bates, C. M.; Halila, S.; Fort, S.; Rochas, C.; Easley, J. A.; Rausch, E. L.; Thio, A.; Borsali, R.; Willson, C. G.; Ellison, C. J. Oligosaccharide/silicon-Containing Block Copolymers with 5 Nm Features for Lithographic Applications. *ACS Nano* **2012**, *6* (4), 3424–3433.

(36) Park, S.; Lee, D. H.; Xu, J.; Kim, B.; Hong, S. W.; Jeong, U.; Xu, T.; Russell, T. P. Macroscopic 10-Terabit-per-Square-Inch Arrays from Block Copolymers with Lateral Order. *Science* **2009**, *323* (February), 1030–1033.

(37) Kennemur, J. G.; Yao, L.; Bates, F. S.; Hillmyer, M. A. Sub‐5 Nm Domains in Ordered Poly(cyclohexylethylene)- Block - Poly(methyl Methacrylate) Block Polymers for Lithography. **2014**.

(38) Lee, J.; Kim, K.; Park, W. I.; Kim, B.-H.; Park, J. H.; Kim, T.-H.; Bong, S.; Kim, C.-H.; Chae, G.; Jun, M.; Hwang, Y.; Jung, Y. S.; Jeon, S. Uniform Graphene Quantum Dots Patterned from Self-Assembled Silica Nanodots. *Nano Lett.* **2012**, *12* (12), 6078–6083.

(39) Cochran, E. W.; Garcia-Cervera, C. J.; Fredrickson, G. H. Stability of the Gyroid Phase in Diblock Copolymers at Strong Segregation. *Macromolecules* **2006**, *39* (7), 2449–2451.

(40) Fredrickson, G. H.; Bates, F. S. Dynamics of Block Copolymers: Theory and Experiment. *Annu. Rev. Mater. Sci.* **1996**, *26* (1), 501–550.

(41) Matsen, M. W.; Bates, F. S. Unifying Weak- and Strong-Segregation Block Copolymer Theories. *Macromolecules* **1996**, *29* (4), 1091–1098.

(42) Park, M. Block Copolymer Lithography: Periodic Arrays of 1011 Holes in 1 Square Centimeter. *Science (80-.).* **1997**, *276* (5317), 1401–1404.

(43) Albert, J. N. L.; Epps III, T. H. Self-Assembly of Block Copolymer Thin Films. *Mater. Today* **2010**, *13* (6), 24–33.

(44) Mansky, P. Controlling Polymer-Surface Interactions with Random Copolymer Brushes. *Science (80-.).* **1997**, *275* (5305), 1458–1460.

(45) Park, S.; Kim, B.; Xu, J.; Hofmann, T.; Ocko, B. M.; Russell, T. P. Lateral Ordering of Cylindrical Microdomains Under Solvent Vapor. *Macromolecules* **2009**, *42* (4), 1278–1284.

(46) Maher, M. J.; Bates, C. M.; Blachut, G.; Sirard, S.; Self, J. L.; Carlson, M. C.; Dean, L. M.; Cushen, J. D.; Durand, W. J.; Hayes, C. O.; Ellison, C. J.; Willson, C. G. Interfacial Design for Block Copolymer Thin Films. *Chem. Mater.* **2014**, *26* (3), 1471–1479.

(47) Bates, C. M.; Seshimo, T.; Maher, M. J.; Durand, W. J.; Cushen, J. D.; Dean, L. M.; Blachut, G.; Ellison, C. J.; Willson, C. G. Polarity-Switching Top Coats Enable Orientation of Sub-10-Nm Block Copolymer Domains. *Science (80-.).* **2012**, *338* (6108), 775–779.

(48) Durand, W. J.; Blachut, G.; Maher, M. J.; Sirard, S.; Tein, S.; Carlson, M. C.; Asano, Y.; Zhou, S. X.; Lane, A. P.; Bates, C. M.; Ellison, C. J.; Willson, C. G. Design of High-χ Block Copolymers for Lithography. *J. Polym. Sci. Part A Polym. Chem.* **2015**, *53* (2), 344–352.

(49) Wu, S. Surface and Interfacial Tensions of Polymer Melts. II. Poly (Methyl Methacrylate), Poly (N-Butyl Methacrylate), and Polystyrene. *J. Phys. Chem.* **1970**, *I* (1960).

(50) Asakawa, K.; Hiraoka, T.; Hieda, H.; Sakurai, M.; Kamata, Y.; Naito, K. Nano-Patterning for Patterned Media Using Block-Copolymer. *J. Photopolym. Sci. Technol.* **2002**, *15* (3), 465–470.

(51) Jung, Y. S.; Ross, C. A. Orientation-Controlled Self-Assembled Nanolithography Using a Polystyrene-Polydimethylsiloxane Block Copolymer. *Nano Lett.* **2007**, *7* (7), 2046–2050.

(52) Stoykovich, M. P.; Kang, H.; Daoulas, K. C.; Liu, G.; Liu, C. C.; De Pablo, J. J.; Müller, M.; Nealey, P. F. Directed Self-Assembly of Block Copolymers for Nanolithography: Fabrication of Isolated Features and Essential Integrated Circuit Geometries. *ACS Nano* **2007**, *1* (3), 168–175.

(53) Yang, X. M.; Peters, R. D.; Nealey, P. F.; Solak, H. H.; Cerrina, F. Guided Self-Assembly of Symmetric Diblock Copolymer Films on Chemically Nanopatterned Substrates. *Macromolecules* **2000**, *33* (26), 9575–9582.

(54) Kim, S. O.; Solak, H. H.; Stoykovich, M. P.; Ferrier, N. J.; De Pablo, J. J.; Nealey, P. F. Epitaxial Self-Assembly of Block Copolymers on Lithographically Defined Nanopatterned Substrates. *Nature* **2003**, *424* (6947), 411–414.

(55) Bita, I.; Yang, J. K. W.; Jung, Y. S.; Ross, C. a; Thomas, E. L.; Berggren, K. K. Graphoepitaxy of Self-Assembled Block Copolymers on Two-Dimensional Periodic Patterned Templates. *Science* **2008**, *321* (5891), 939–943.

(56) Somervell, M.; Gronheid, R.; Hooge, J.; Nafus, K.; Delgadillo, P. R.; Thode, C.; Younkin, T.; Matsunaga, K.; Rathsack, B.; Scheer, S.; Nealey, P. Comparison of Directed Self-Assembly Integrations. *Adv. Resist Mater. Process. Technol. XXIX* **2012**, *8325*, 83250G (14 pp.).

(57) Albrecht, T. R.; Bedau, D.; Dobisz, E.; Gao, H.; Grobis, M.; Hellwig, O.; Kercher, D.; Lille, J.; Marinero, E.; Patel, K.; Ruiz, R.; Schabes, M. E.; Wan, L.; Weller, D.; Wu, T.-W. Bit Patterned Media at 1 Tdot/in<formula Formulatype="inline"><tex Notation="TeX">^{2}</tex></formula> and Beyond. *IEEE Trans. Magn.* **2013**, *49* (2), 773–778.

(58) Cheng, J. Y.; Ross, C. A.; Thomas, E. L.; Smith, H. I.; Vancso, G. J. Fabrication of Nanostructures with Long-Range Order Using Block Copolymer Lithography. *Appl. Phys. Lett.* **2002**, *81* (19), 3657–3659.

(59) Wang, J.; Chen, W.; Russell, T. P. Ion-Complexation-Induced Changes in the Interaction Parameter and the Chain Conformation of PS-B-PMMA Copolymers. *Society* **2008**, 4904–4907.

Chapter 2: Poly(trimethylsilyl styrene-*block*-lactide) (PTMSS-PLA) and Poly(trimethylsilyl styrene-*block*-isoprene) (PTMSS-PI)

A multitude of BCPs have been studied as candidates for enabling BCP lithography. The most widely studied BCP, poly(styrene-*block*-methyl methacrylate) (PS-PMMA), has been used to pattern well-aligned, ordered lamellae, cylinders, and non-linear, device-useful patterns. However, the smallest etch-transferable features accessible by PS-PMMA is about 12 nm,[1] which limits the usefulness of the BCP to about one generation of bit patterned magnetic recording hard disk drives (BPMR HDDs). In addition, although PS-PMMA has been successfully used as an etch mask for a hard substrate, etch contrast between PS and PMMA is about 1:2-1:7 depending on the etching conditions.[2,3] Also, the PS domain that remains after etch removal of the PMMA domain is not a very robust etch mask material as compared to metal,[4] and pattern transfer to the underlying substrate could be challenging, even with a high aspect ratio PS structure. The BCP would be more commercially useful if the feature size could be decreased, the etch contrast between the two blocks increased, and the block acting as an etch mask engineered to be more robust.

In this chapter, two alternative candidate BCPs, poly(trimethylsilyl styrene-*block*-*D,L*-lactide) (PTMSS-PLA) and poly(trimethylsilyl styrene-*block*-isoprene) (PTMSS-PI), were investigated in an effort to identify a lithographically useful BCP with smaller features and better etch properties as compared to PS-PMMA. In both BCPs, the nonpolar block is PTMSS, a silicon-containing styrene derivative. PTMSS was chosen because it is relatively easy to synthesize, has an accessible T_g, and imparts many advantageous properties to the BCP. The inclusion of silicon as TMS increases the hydrophobicity of the nonpolar block relative to polystyrene, which should also increase the χ parameter of the BCP. In addition, the inclusion of the metalloid silicon in the nonpolar block increases the etch resistance of that block since silicon produces nonvolatile compounds in the presence

of oxygen plasma,[5] in contrast to the volatile products formed by organics in oxygen plasma.

2.1 POLY(TRIMETHYLSILYL STYRENE-*BLOCK*-LACTIDE) (PTMSS-PLA)

The viability of PLA as a BCP component was first studied by my mentor, Julie Cushen, and the work was carried out as a joint collaboration between Julie, myself, and HGST (now Western Digital). This was the first project I was involved with in my graduate career, and I synthesized many of the samples used in this section. In addition, I helped with the solvent annealing of the resulting polymer films. Finally, this project was the inspiration for the project discussed in the second part of this chapter on PTMSS-PI.

PLA was chosen as the repeat unit for the polar block because of its high oxygen content which leads to high polarity, cost effectiveness as a "green," renewable and biodegradable material,[6] and the availability of a straightforward polymerization route. Most importantly, the χ parameter of poly(styrene-*block*-lactide) (PS-PLA) had already been measured to be 0.25 at 25 °C,[7] which is many times higher than that of PS-PMMA at the same temperature. By pairing this monomer with a more hydrophobic silico-containing styrenic counterpart, the increase in χ should be even more dramatic.

Lactide has three stereoisomers *D*-lactide, *L*-lactide, and *meso*-lactide (**Figure 2.1**), which all form crystalline homopolymers due to their stereoregularity. Therefore, to avoid the high melting points associated with crystalline polymers,[8] *D,L*-lactide, a physical mixture of the *D*- and *L*- isomers, was chosen as the monomer for PTMSS-PLA. Due to the inclusion of two different stereoisomers which promote irregularity in the repeat unit structure, the crystallinity is suppressed.[9]

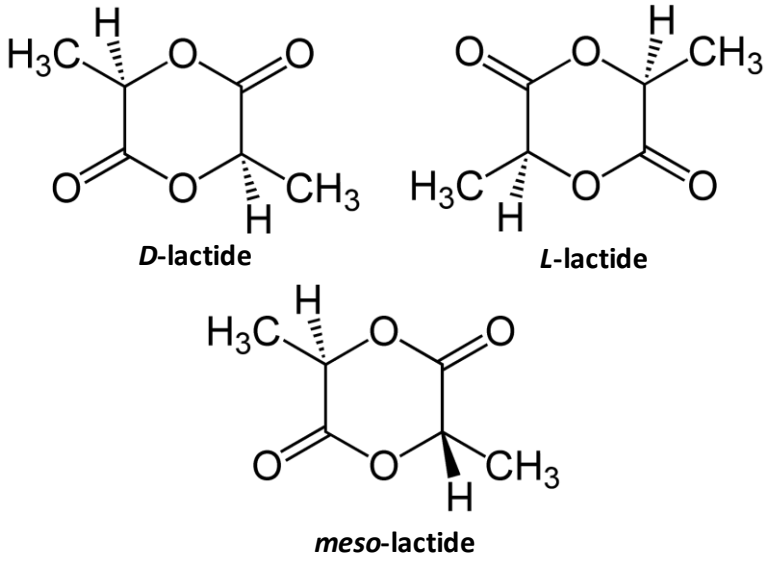

Figure 2.1 The three stereoisomers of lactide. Image adapted from [10].

2.1.2 Experimental Methods

2.1.2.1 TMSS monomer synthesis

The trimethylsilyl styrene (TMSS) monomer was not commercially available, so it was synthesized using a Grignard reaction shown in **Scheme 2.1**. Magnesium shavings were freshly ground using a mortar and pestle then immediately added to a rubber septa-capped 500 mL flame dried 3-neck round bottom flask equipped with a reflux column, which was placed in a 70 °C oil bath. Dry THF from a column-based solvent purification/dispensing system was cannulated to the reaction flask. Three drops of dibromoethane were added to the reactor, and a few minutes passed before the reaction started bubbling. Then, chlorostyrene was added to the reactor drop by drop via an airtight syringe. If the reaction became too exothermic, the chlorostyrene was added more slowly. After all the chlorostyrene was added, the reactor vessel was moved from the oil bath to an ice bath. Next, chlorotrimethylsilane was added dropwise to the reactor using a syringe. The reaction was allowed to proceed overnight, and it was quenched by adding

isopropanol, methanol, water, and finally weak acid to the reactor. The TMSS monomer product was isolated by extraction with ether and purified by fractional distillation.

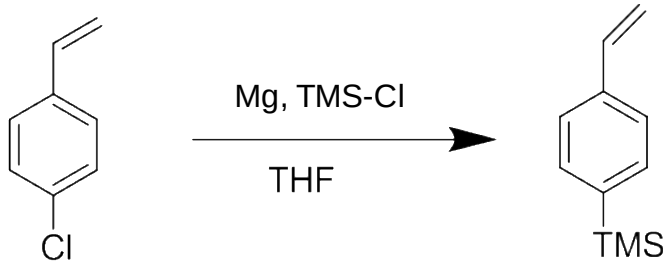

Scheme 2.1 Synthesis of TMSS monomer by a Grignard reaction.

2.1.2.2 TMSS monomer characterization

Hydrogen nuclear magnetic resonance (^{1}H NMR) was used to confirm the purity of the TMSS monomer, as shown in **Figure 2.2**. The integration of the peaks matched well with the number of assigned hydrogens, indicating that TMSS was successfully synthesized with little to no precursor molecules remaining.

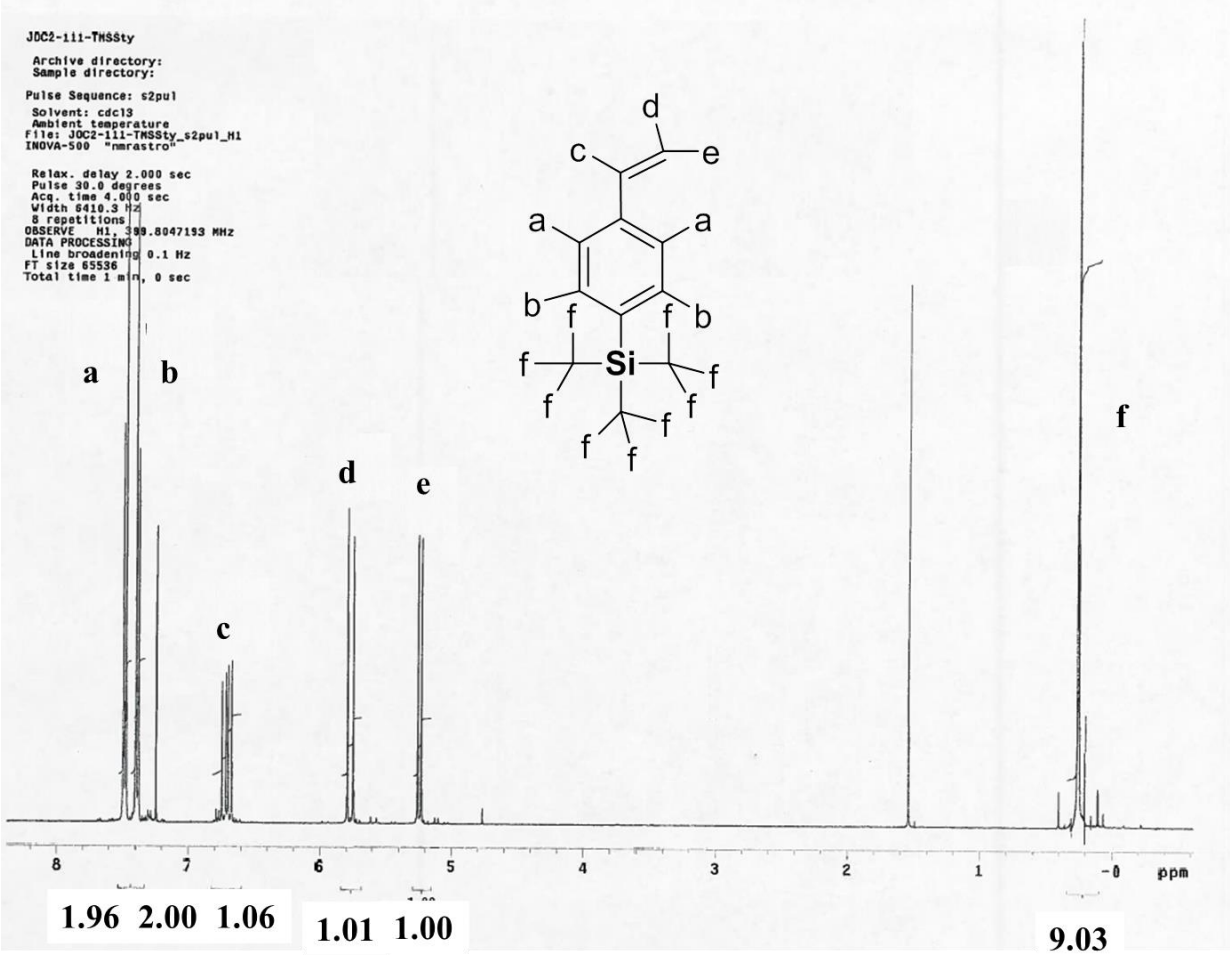

Figure 2.2 ^{1}H NMR of purified TMSS monomer in $CDCl_3$. The peak integrations agree well with the assigned hydrogens, indicating successful synthesis. The unlabeled peak at 1.6 ppm is water, and the unlabeled peak at 7.26 is protonated solvent. Reprinted with permission from [11]. Copyright 2012 American Chemical Society.

2.1.2.4 PTMSS-OH and PTMSS-PLA polymer synthesis

PTMSS-PLA was synthesized by a combination of anionic and ring-opening polymerization, as shown in **Scheme 2.2**. Hydroxyl-terminated PTMSS was first synthesized by anionic polymerization. An appropriate amount of *sec*-butyl lithium was used to initiate the reaction in cyclohexane at 40 °C from the column-based solvent

purification/dispense system. After stirring for 45 minutes, TMSS monomer was added dropwise with an airtight glass syringe. The reaction was allowed to proceed overnight. The hydroxyl end-cap was installed by adding a 10x molar excess of purified ethylene oxide (distilled twice over butyl magnesium chloride), and this reaction was again allowed to proceed overnight. Finally, degassed methanol was added to the reactor to quench the reaction. The PTMSS-OH polymer was precipitated in methanol and dried *in vacuo*, and it later functioned as a macroinitiator for the PLA block.

D,L-lactide was recrystallized from ethyl acetate to remove impurities from the monomer and stored in the dry box. A carefully measured amount of PTMSS-OH was taken into a dry box, where purified toluene (distilled twice over calcium hydride to remove water) was added to the macroinitiator. Triethylaluminium was then added to the PTMSS-OH solution and allowed to stir for 2 hours, forming an aluminum alkoxide initiator. The lactide was then added to the solution, and the round bottom flask was capped with a rubber septum and brought out of the dry box. The reactor was immediately submerged in a 90 °C oil bath and stirred for 6 hours before it was quenched with a few drops of a 1 N HCl solution. The BCP was precipitated in a 1:1 methanol:water mixture and dried *in vacuo*.

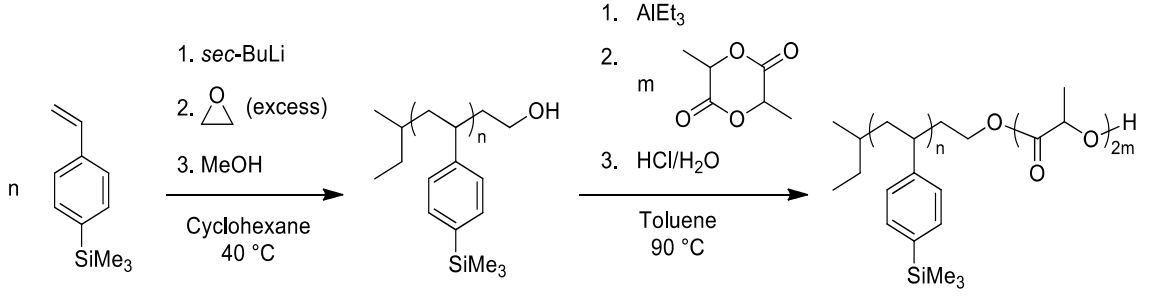

Scheme 2.2 Synthesis of PTMSS-*b*-PLA by a combination of anionic and ring-opening polymerization. Reprinted with permission from [11]. Copyright 2012 American Chemical Society.

2.1.2.4 PTMSS-OH and PTMSS-PLA polymer characterization

Absolute molecular weight and dispersity for the PTMSS-OH macroinitiator were determined using size exclusion chromatography (SEC) (measured dn/dc of PTMSS-OH in THF at 30 ºC was 0.138). The dispersity for the BCP was determined using SEC, and the clean shift of the SEC trace from PTMSS-OH to PTMSS-PLA (i.e., no shoulder or additional peak in the trace at the PTMSS-OH elution volume) indicated that 1) nearly every PTMSS polymer chain was successfully hydroxyl-terminated and 2) the PLA block was added to each PTMSS-OH macroinitiator (**Figure 2.3**). The molecular weight of the BCP was calculated from a ^{1}H NMR spectrum (**Figure 2.4**) based on the molecular weight of the PTMSS-OH block and the mass densities of PTMSS (0.963 g/cm^3) and PLA (1.15 g/cm^3). Volume and mole fractions for PTMSS-PLA were also calculated from the ^{1}H NMR spectrum.

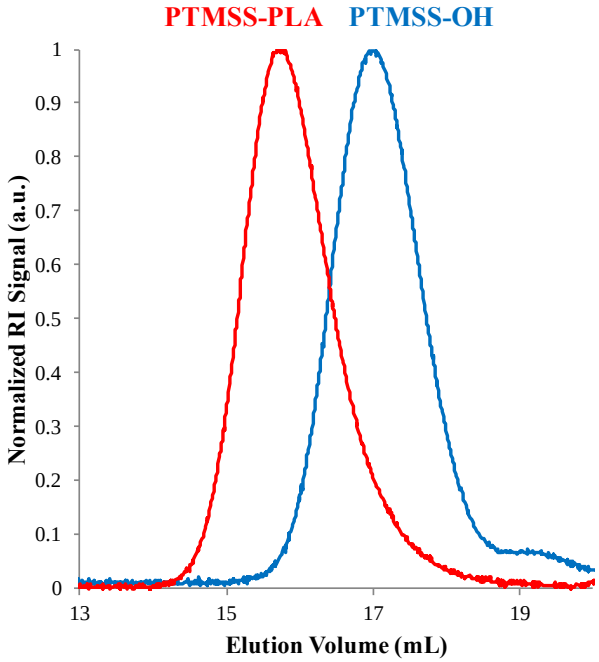

Figure 2.3 SEC traces of PTMSS-$OH_{5.5}$ macroinitiator and $PTMSS_{5.5}$-$PLA_{6.6}$, where the subscript represents the number average molecular weight of the macroinitiator or BCP in kg/mol. A leftward shift of the entire trace indicates PLA growth on every PTMSS-OH macroinitiator. Adapted with permission from [11]. Copyright 2012 American Chemical Society.

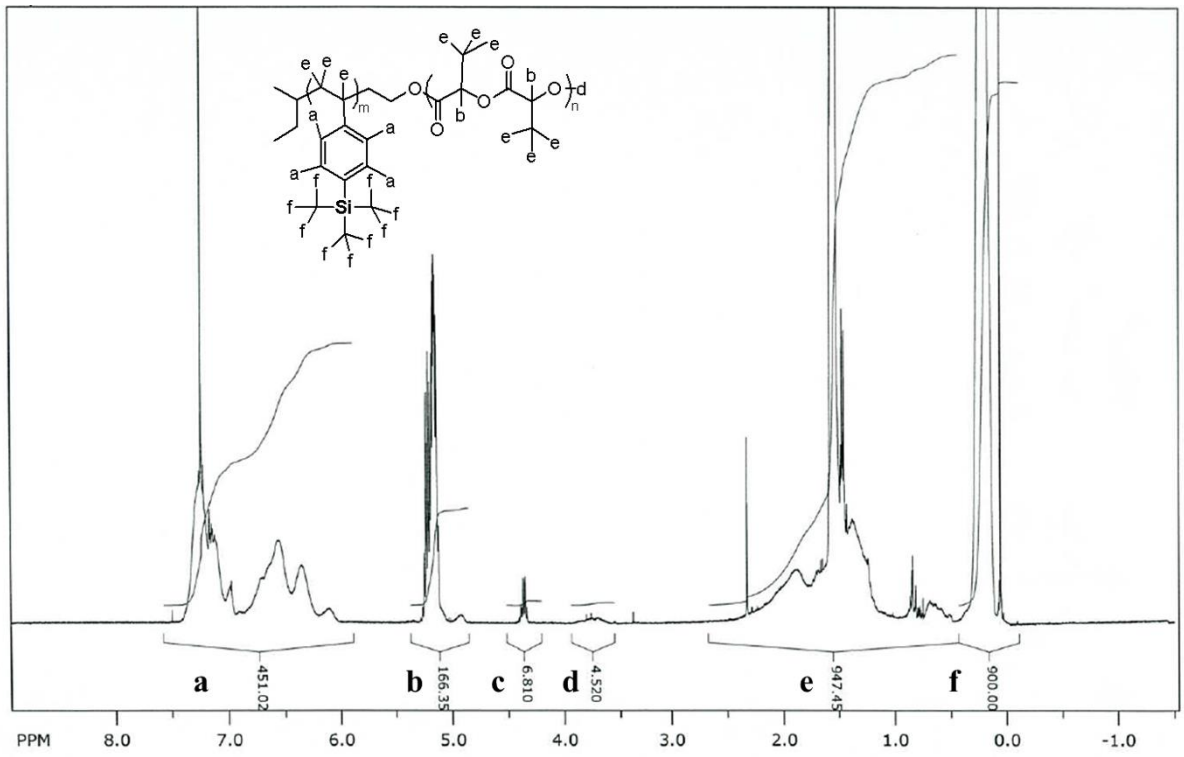

Figure 2.4 Representative ^{1}H NMR trace from $PTMSS_{5.5}$-$PLA_{3.7}$. Peaks f and b were used to determine the mole and volume fractions of the material. Number average molecular weight was calculated based on the mole fractions and molecular weight of the PTMSS-OH macroinitiator. Peak c is residual THF. Reprinted with permission from [11]. Copyright 2012 American Chemical Society.

Of the PTMSS-PLA samples I synthesized and characterized, the most useful one was $PTMSS_{5.5}$-$PLA_{3.7}$, where the subscripts represent the molecular weight of each block in kg/mol. This BCP was necessary for proving that small cylinders could be perpendicularly oriented in thin films. However, many additional PTMSS-PLA samples were synthesized and studied, and full details can be found in Julie Cushen's dissertation.[12]

2.1.2.5 Small angle X-ray scattering (SAXS)

SAXS data was taken on the PTMSS-PLA samples to determine whether the sample was ordered, and, if so, the bulk morphology and domain size/spacing of the

samples. The BCP samples were placed in an o-ring sandwiched by Kapton tape, and the samples were annealed at 160 °C for 30 minutes in air on a hot plate to give the BCP ample kinetic mobility and time to assemble in bulk. As determined by SAXS, $PTMSS_{5.5}$-$PLA_{3.7}$ formed cylinders in bulk with a domain spacing of 12.1 nm. Given that the volume fraction of the PLA block was 36%, the expected structure is cylinders of PLA in a PTMSS matrix.

2.1.3 χ-Parameter Characterization

The chief area of interest in the characterization phase of this BCP was whether its χ parameter would be increased as compared to PS-PLA or PS-PMMA, and if so, by how much. Therefore, Julie synthesized a disordered, symmetric sample of PTMSS-PLA to determine the χ parameter using absolute scattering SAXS data fit to a modified version of Liebler's mean field theory that accounts for polydispersity and segmental asymmetry. χ was an adjustable parameter in the fitting, and the best fit from data obtained at four temperatures produced the following temperature-dependent expression for χ:

$$\chi = 51.3/T + 0.29 \qquad \textbf{Equation 2.1}$$

Further details on the methodology and results can be found in Chapter 6 of Julie Cushen's dissertation.[12]

Importantly, the χ parameter of PTMSS-PLA is significantly higher than that of PS-PLA, as hypothesized. At 25 °C, the χ parameter of PTMSS-PLA (0.46) is almost double that of PS-PLA (0.25), which is already much greater than the χ of PS-PMMA at the same temperature (0.046). The high χ of PTMSS-PLA relative to PS-PMMA implies that it can access features smaller than 10 nm, near the limit for forming PS-PMMA features; this makes PTMSS-PLA especially attractive as a potential material for BCP lithography. However, measuring the bulk feature size via χ does not guarantee that the

BCP will be useful as an etch mask or well-behaved in thin films; therefore, thin film studies were performed to further assess the industrial usefulness of PTMSS-PLA.

2.1.4 Thin Film Studies

After synthesizing and characterizing the PTMSS-PLA samples, thin film studies were conducted to further evaluate their usefulness for patterning applications. As mentioned in Chapter 1, BCP lithography requires that the BCP act as an etch mask for the substrate underneath. For the best etch transfer results, BCPs should form perpendicular features in thin films first.

There are many ways to perpendicularly orient BCPs in thin films, and two of the most popular and straightforward methods are thermal annealing and solvent annealing. Due to disparate length-scales in thin films, interfacial effects dominate the orientation of BCPs. Interfaces that are non-preferential to either BCP block are essential to perpendicular orientation, so thermal annealing is a great option for BCPs whose two block surface energies differ by a small amount, such as PS-PMMA. However, because PTMSS-PLA has a much higher χ parameter than PS-PMMA, which is partially due to the increased chemical dissimilarity between the two blocks, thermal annealing PTMSS and PLA was not an option for this BCP. Therefore, we chose solvent annealing as the orientation strategy for this BCP. Top coats are another option for PTMSS-PLA, but at the time of these studies, the top coat orientation methodology was still being finalized. However, top coats later proved to be another method of perpendicularly orienting PTMSS-PLA.[13]

In solvent annealing, solvent vapor can be used to mitigate the surface energy differences of the two blocks. If the correct annealing conditions are chosen, the solvent vapor creates an essentially non-preferential top surface and neutralizes the surface energies of the BCP at the free-interface, allowing for perpendicular orientation. There are

many parameters that can be varied in solvent annealing: annealing time and temperature, identity of solvent, vapor pressure, mixtures of multiple solvents, etc. The science (or art) of solvent annealing is an ongoing study both experimentally and computationally,[14] but currently is still not well understood. The plethora of parameters available in a solvent annealing process results in a trial-and-error method to finding the best annealing conditions for a given BCP.

Our initial solvent annealing strategy consisted of placing small scintillation vials of different solvents in a larger capped jar with the sample, which was PTMSS-PLA spin-coated onto standard silicon wafers with a 2 nm native oxide layer (**Figure 2.5**). Later on these results were translated to more sophisticated solvent annealing equipment, but the jar method was a satisfactory method with which to screen a variety of solvent annealing conditions.

Figure 2.5 A picture of the solvent annealing apparatus for PTMSS-PLA orientation experiments conducted in the lab. An open scintillation vial containing the solvent of choice is placed in a closed jar with the thin film sample, and the solvent vapor interacts with the BCP.

Many solvents were tested in this manner, including tetrahydrofuran, dimethylformamide, acetone, cyclohexane, chloroform, toluene, dichloromethane, methanol, benzene, anisole, pentane, *n*-hexane, acetic acid, isopropanol, mixtures of cyclohexane and acetone, and mixtures of tetrahydrofuran and water. These solvents were chosen to span a spectrum of polarities. The polar solvents, such as dimethylformamide, methanol, and water, were anticipated to preferentially swell the PLA block, while the nonpolar solvents, such as cyclohexane and pentane, were anticipated to preferentially swell the hydrophobic PTMSS. Lastly, good solvents for both blocks, such as acetone and tetrahydrofuran, were chosen to swell both blocks simultaneously. For every solvent except cyclohexane, the films dewet from the substrate within minutes. Serendipitously, the

cyclohexane samples not only did not dewet, but also annealed well, and a thin film evaluation of the BCP was possible.

Once a suitable solvent was selected, the annealing time was varied to get a rough idea of the kinetics of orientation. $PTMSS_{5.5}$-$PLA_{3.7}$ formed PLA cylinders in a PTMSS matrix, and it took about 4 hours for the sample to transition from parallel cylinders to perpendicular cylinders, as shown in **Figure 2.6**. Perpendicular structures are preferable for ease of etch transfer, but etch transfer with parallel cylinders is possible.[4] However, these samples were only imaged with top-down imaging techniques, so it was not possible to know whether the top interface orientation persists through the film from these images alone.

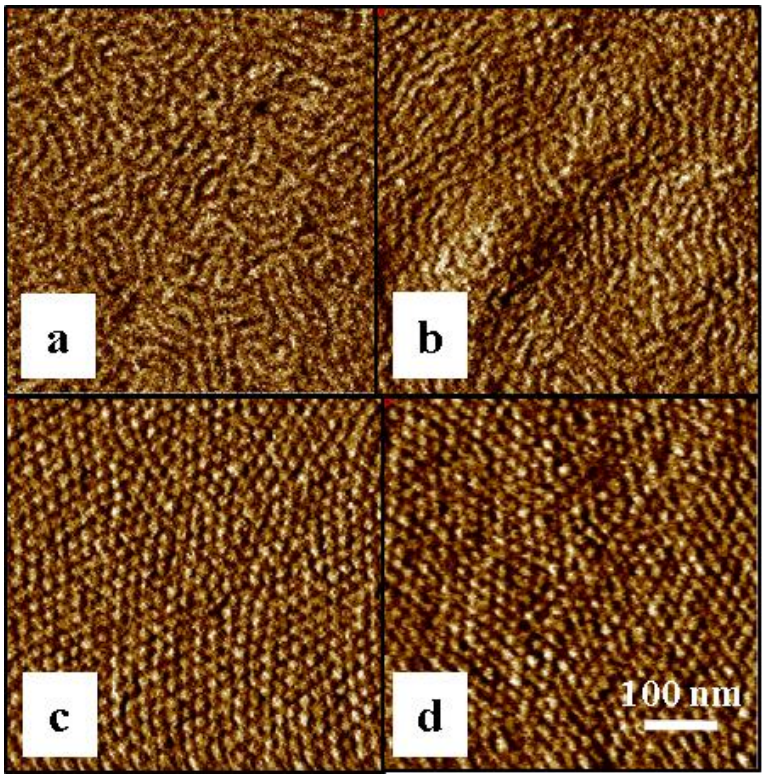

Figure 2.6 $PTMSS_{5.5}$-*b*-$PLA_{3.7}$ after annealing with cyclohexane for a) 1h, b) 2h, c) 4h, and d) 24h. Reprinted with permission from [15]. Copyright 2012 American Chemical Society.

2.1.5 Other Studies

Material synthesis, characterization, and thin film studies were my major contributions to the PTMSS-PLA project. Julie Cushen conducted many more detailed studies into this BCP, including island/hole and terracing studies to determine the through-film BCP behavior, optimizing the solvent annealing conditions with a solvent annealing chamber during an internship at HGST, and demonstrating that solvent annealing had an unforeseen effect in increasing the effective χ parameter of the BCP.[12,14] She also proved that directed self-assembly techniques could be applied to PTMSS-PLA, demonstrating 2x and 3x density multiplication, as well as pattern transfer to the underlying substrate.[12]

2.1.6 Complications with PLA

Although PTMSS-PLA is an attractive BCP for many reasons enumerated heretofore, the PLA block brings with it many complications. First, PTMSS-PLA must be stored in a humidity-controlled environment. Due to the synthesis method, the PLA block is end-capped by a hydroxyl group, which can cause hydrolytic degradation.[16] Next, the high degree of polarity in PTMSS-PLA causes it to swell in methanol, which is the preferred spin coating solvent for the polarity-switching top coats developed by my collaborators. Therefore, while the top coat strategy does work to orient PTMSS-PLA, it is not an ideal solution. Finally, the hydroxyl end group means that the polymer can potentially graft to native oxide, even through a polymer brush. Therefore, thermal annealing, such as the type that is required for implementing a top coat orientation strategy, is more complicated due to the necessity of selecting an appropriate crosslinked substrate surface mat that does not allow the BCP to graft through it.

2.2 POLY(TRIMETHYLSILYL STYRENE-BLOCK-ISOPRENE) (PTMSS-PI)

Due to the complications of the PLA block detailed in the preceding section, we hoped to find a replacement block to pair with PTMSS while retaining the high χ parameter of PTMSS-PLA. At around the same time that we were discovering the difficulties with PLA, Kim et al. published an interesting study on the effect of epoxidation of the isoprene block of poly(styrene-*block*-isoprene) (PS-PI) on surface energy and effective χ. Their study demonstrated that while the effective χ of partially epoxidized PS-PI changed in a non-linear fashion based on the percent epoxidation, the surface energy of the PI block changed linearly with regard to percent epoxidation.[17] This suggests that any BCP that contains isoprene as a block has some adjustability to both its χ parameter and the window in which the two blocks will have similar surface energies, which also increases the chance of using thermal annealing as an orientation strategy.

Drawing inspiration from the PS-PI study, we opted to replace the PS block with PTMSS in that system. From our studies with PTMSS-PLA, we saw that replacing the nonpolar block with an even more nonpolar block dramatically increased the χ parameter, and we hoped that the same would hold true for PTMSS-PI. In addition, by replacing the labile PLA group, we hoped that thermal annealing with or without top coats could be used to orient the BCP.

However, the polymerization of PTMSS-PI had unforeseen complications. As will be explained in detail below, the crossover from the first to the second block never occurred cleanly, and a PTMSS-PI BCP with the characteristic low dispersity of a living polymerization was never produced.

2.2.1 Experimental Methods

2.2.1.1 Purification

Isoprene was purified by distilling twice over *n*-butyl lithium. TMSS was either synthesized as detailed earlier in this chapter or provided by Nissan Chemical (using the same synthesis procedure). TMSS was fractionally separated then distilled twice over *di*-butylmagnesium. Cyclohexane was purified by distilling twice over *n*-butyl lithium (the column-based solvent dispense/purification system was being regenerated at the time).

2.2.1.2 Anionic polymerization

The synthesis of PTMSS-PI was attempted using anionic polymerization (**Scheme 2.3**), as polymers and BCPs of both materials have been prepared with this technique (although the BCP of the two has never been reported). The initiation steps and synthesis of the PTMSS block proceeded in the same manner as for PTMSS-OH, but without end-capping with ethylene oxide. Instead, an aliquot was taken from the reactor after letting the PTMSS block propagate overnight. The freshly purified isoprene monomer was then added to the reactor. The reactor steadily lost the orange color over the next 3-4 hours, but it was still faintly colored 7-8 hours after adding the isoprene block. The isoprene block was allowed to propagate overnight, and by the next morning, the reaction was clear, the expected color of the isoprene carbanion. Degassed methanol was added to the reactor to terminate the reaction.

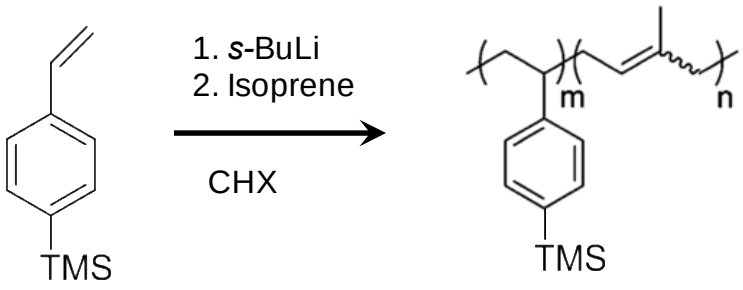

Scheme 2.3 Synthesis of PTMSS-PI using anionic synthesis in cyclohexane.

2.2.2 Results and Discussion

The crossover from PTMSS to PI was not successful, as shown in **Figure 2.7**. The first block, PTMSS, was able to be initiated and propagated as expected, as evidenced by the single narrow peak in the SEC trace. However, the BCP produced from this good first polymer had a very high dispersity index of over 1.3 on every synthesis attempt. In addition, the shoulder or in some cases second peak in the SEC trace showed that a large fraction of the PTMSS block did not initiate the isoprene block at all. The high dispersity and large component of PTMSS homopolymer in the resulting BCP would have affected the bulk and thin film behavior of the BCP significantly, making it impossible to make accurate comparisons between PTMSS-PI and the other polymers studied by the group. Therefore, these polymers were ultimately abandoned as a candidate for making templates for BPMR.

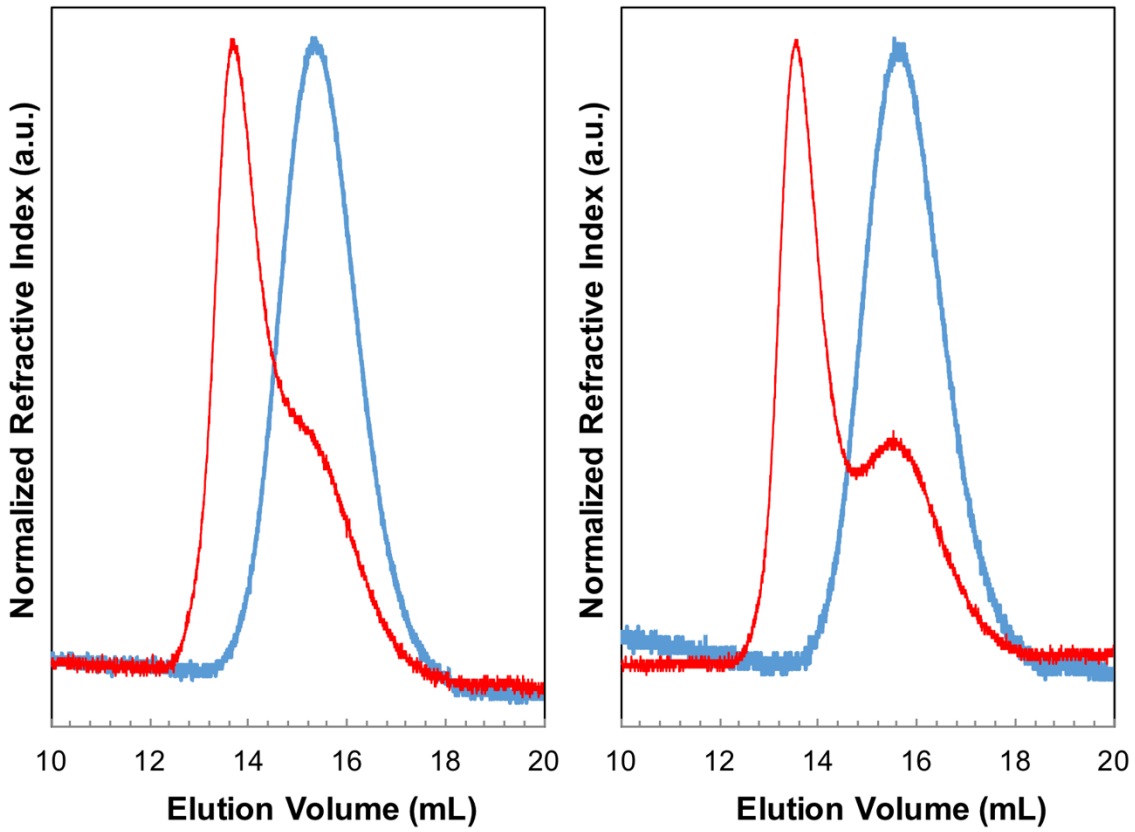

Figure 2.7 Representative SEC traces for PTMSS-PI polymerization attempts. The blue traces are the PTMSS aliquots, which polymerized as expected. However, the isoprene block was never cleanly initiated from the first PTMSS block. The red traces are the resulting BCPs, which sometimes had a shoulder and sometimes had a second peak at the elution volume of the aliquot, indicating the presence of a large fraction of PTMSS homopolymer.

My hypothesis for this crossover failure is that the TMSS anion is not reactive enough to initiate the isoprene block. Because the TMS group acts as an electron withdrawing group, its anion is more stable and less reactive than that of styrene.[18] In addition, isoprene has been shown to be slow to initiate in cyclohexane, even by a reactive butyl lithium anion.[19] The main reason anionic polymerization results in low dispersity polymers is because the initiation step is typically designed to take place almost

instantaneously compared to the rate of polymerization. The slow isoprene initiation accounts for the dispersity observed in the BCP. This hypothesis is qualitatively reinforced by the observation that the orange color indicative of the TMSS anion fades slowly over several hours after the addition of isoprene. If the initiation of isoprene is slow enough, it is likely that some TMSS polymers do not initiate any isoprene growth before the propagating chains consume the isoprene monomer, resulting in PTMSS homopolymer recovered after the reaction is terminated.

After being unable to synthesize PTMSS-PI by growing the PTMSS block first, the experiment was conducted where the PI block was first synthesized, followed by PTMSS addition. Isoprene has a similar pKa value to styrene, so polyisoprenyllithium could potentially be more reactive than TMSS and initiate this polymerization. Therefore, the isoprene anion should be able to initiate the TMSS block more cleanly and effectively than vice versa. However, as shown in **Figure 2.8**, this method also did not work.

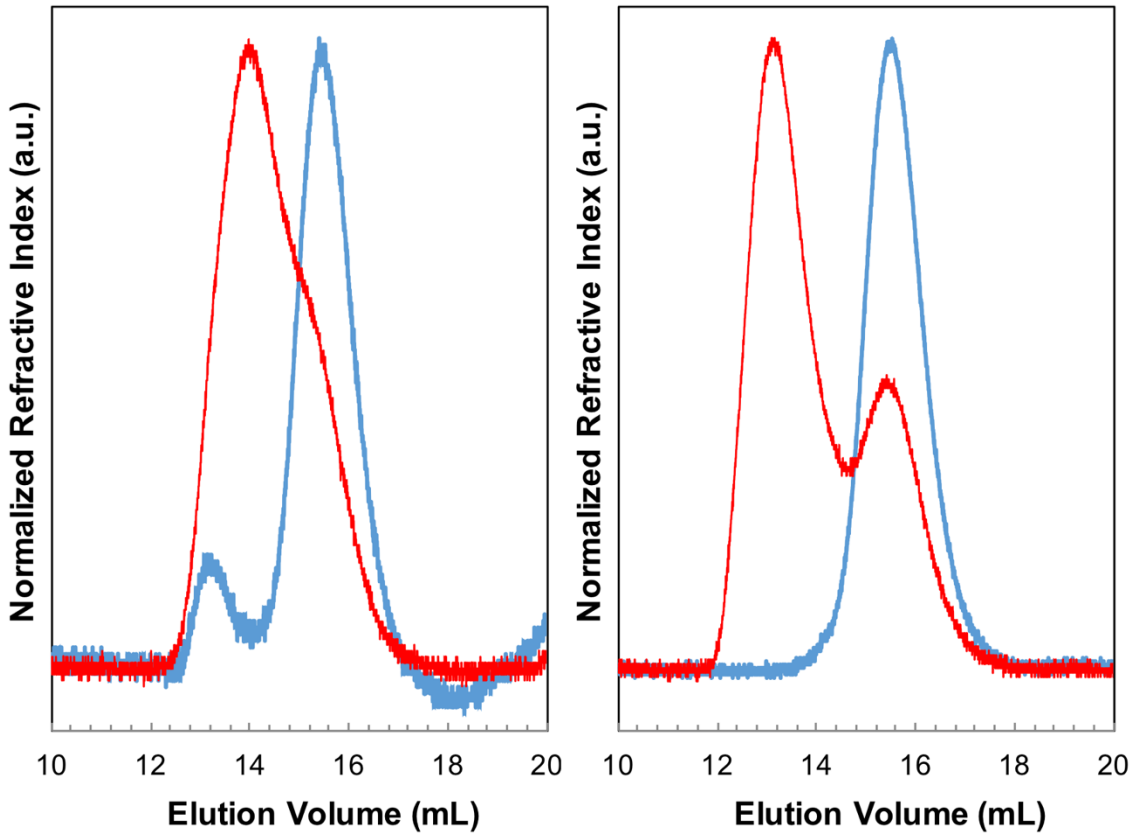

Figure 2.8 Representative SEC traces for PI-PTMSS polymerization attempts, wherein the PI block was polymerized first. The blue traces are the PI aliquots, which polymerized mostly as expected. As can be seen from the left trace, isoprene sometimes coupled during the reaction. The red traces are the resulting BCPs, which sometimes had a shoulder and sometimes had a second peak at the elution volume of the aliquot, indicating the presence of a large fraction of PI homopolymer. This is indicative of the isoprenyl ion being unable to initiate TMSS effectively.

The crossover from the PI block to TMSS did not occur as expected, either. From my observations of the reactor as the TMSS was added, some degree of TMSS initiation proceeded readily. The reactor changed from clear to an orange color immediately when the TMSS monomer was added. However, the orange color faded steadily over the next few hours. This suggests that either trace impurities remaining in the TMSS monomer

eventually terminated the living ends (unlikely since PTMSS was readily made via the same method), or some side-reactions occurred in this system. The polymerization was also attempted in THF (purified by distilling twice over *n*-butyllithium) to try a different reaction system, but these attempts were also unsuccessful, as shown in **Figure 2.9**. As a final control test, PS-PI was polymerized using the exact same procedure, equipment, and reagents in cyclohexane. As shown in **Figure 2.10**, this classic reaction was able to proceed as expected. Therefore, the cause of the polymerization failure is inherent in the TMSS and isoprene interaction. Rather than attempting to elucidate the cross-over failure mechanisms, attention was focused on other candidate BCP polymers, which will be detailed in the following chapters.

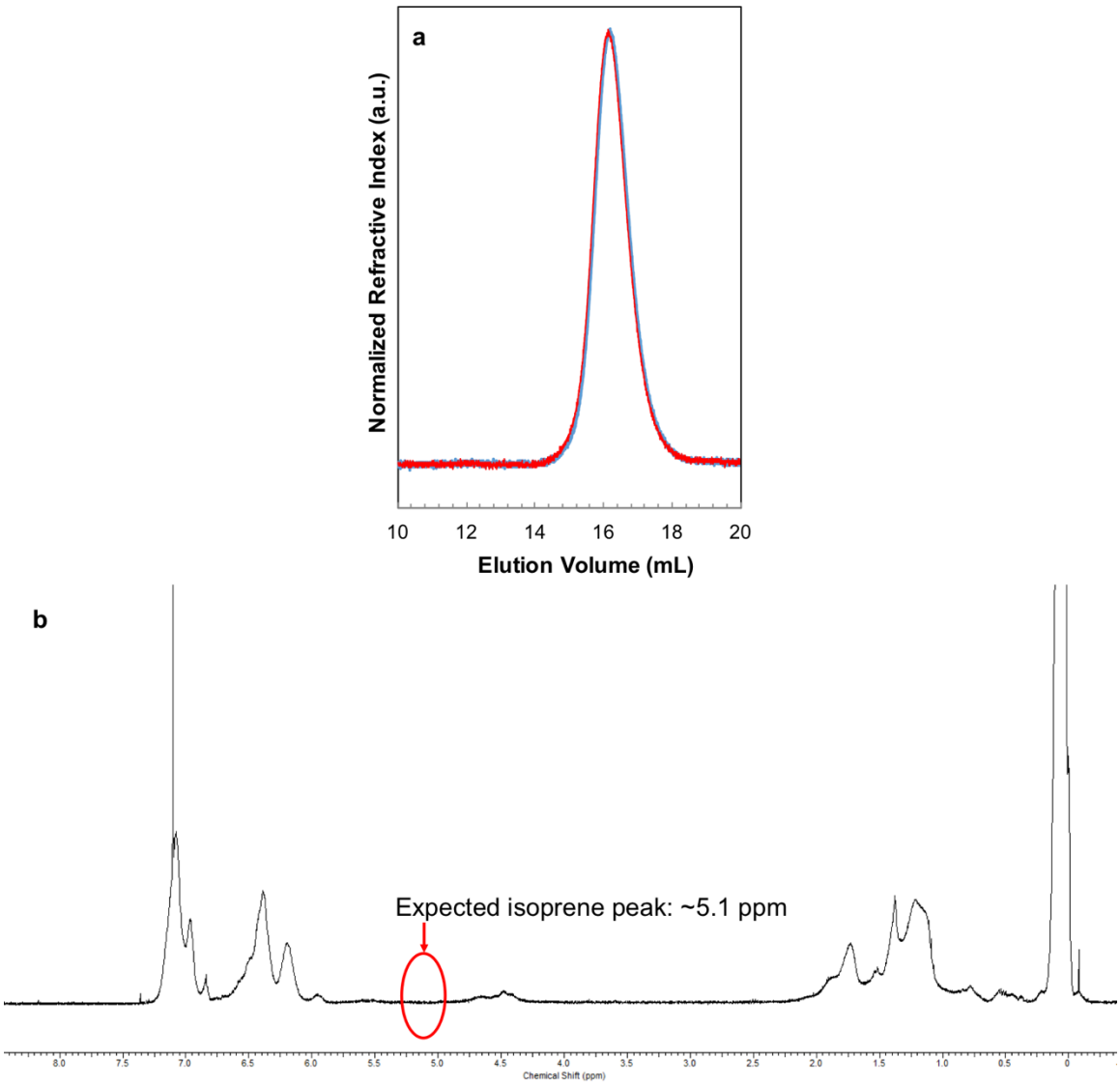

Figure 2.9 Anionic polymerization of PTMSS-PI in THF at -78 °C. (**a**) The resulting SEC trace, where the blue trace is the aliquot taken just before adding isoprene and the red trace is the BCP. As indicated by SEC, the PTMSS block did not initiate any isoprene growth. (**b**) ^{1}H NMR of the BCP (the red trace in (**a**)), and the lack of a peak at 5.1 confirms that no isoprene growth was initiated from the PTMSS block.

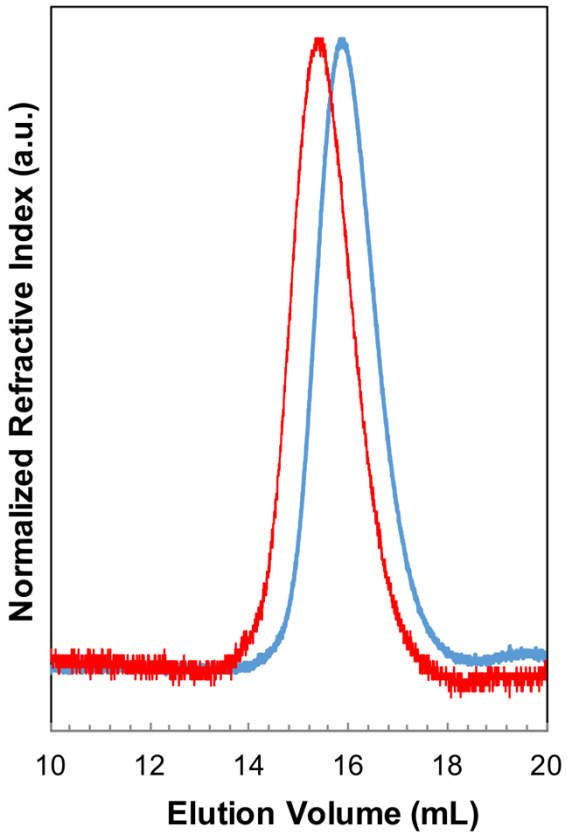

Figure 2.10 SEC trace of PS-PI polymerized in cyclohexane using the same procedure, equipment, and reagents as for the failed PTMSS-PI and PI-PTMSS experiments. The blue trace is the PS aliquot, and the red trace is the PS-PI BCP. This control experiment indicates that there is not an intrinsic flaw to the procedure, glassware, or reagents; rather, the interaction between TMSS and isoprene caused the crossover failures.

2.3 Conclusions

PTMSS-PLA offers many lithographic advantages over PS-PMMA, and its usefulness as a candidate for BPMR was demonstrated. However, the PLA block suffers from polymer instability due to the reactive hydroxyl terminus, which precludes most thermal annealing routes. Inspired by this work and work in the field, PTMSS-PI was investigated as another possible silicon-containing BCP that does not contain a reactive

end group. The possibility of epoxidation of PTMSS-PI was especially attractive because it allows for control over the surface energy of the BCP, thereby increasing the chance that some form of epoxidized PTMSS-PI could be oriented through thermal annealing. However, despite its theoretical promise, the synthesis of PTMSS-PI was ultimately not successful, so no thin film studies were possible. In the next chapter, another BCP similar to PTMSS-PLA, poly(pentamethydisilyl styrene-*block*-ethyl glycolide) (PDSS-PEGL) is introduced. The BCP was chosen for its wildly different surface energies which enables high χ and small feature sizes, but ultimately proved difficult to work with, presumably due to residual synthesis reagents.

2.4 REFERENCES

(1) Wan, L.; Ruiz, R.; Gao, H.; Patel, K. C.; Albrecht, T. R.; Yin, J.; Kim, J.; Cao, Y.; Lin, G. The Limits of Lamellae-Forming PS- B -PMMA Block Copolymers for Lithography. *ACS Nano* **2015**, *9* (7), 7506–7514.

(2) Ting, Y.-H.; Park, S.-M.; Liu, C.-C.; Liu, X.; Himpsel, F. J.; Nealey, P. F.; Wendt, A. E. Plasma Etch Removal of Poly(methyl Methacrylate) in Block Copolymer Lithography. *J. Vac. Sci. Technol. B Microelectron. Nanom. Struct.* **2008**, *26* (5), 1684.

(3) Liu, C. C.; Nealey, P. F.; Ting, Y. H.; Wendt, A. E. Pattern Transfer Using Poly(styrene-Block-Methyl Methacrylate) Copolymer Films and Reactive Ion Etching. *J. Vac. Sci. Technol. B* **2007**, *25* (6), 1963–1968.

(4) Jung, Y. S.; Ross, C. A. Orientation-Controlled Self-Assembled Nanolithography Using a Polystyrene-Polydimethylsiloxane Block Copolymer. *Nano Lett.* **2007**, *7* (7), 2046–2050.

(5) Chiang, W.-Y.; Lin, Y.-C. Synthesis and Characterization of Novel Copolymers with the Trimethylsilyl Group for Deep-UV Photoresists. *J. Appl. Polym. Sci.* **2002**, *83* (13), 2791–2798.

(6) Vert, M.; Schwach, G.; Engel, R.; Coudane, J. Something New in the Field of PLA / GA Bioresorbable Polymers? *J. Control. Release* **1998**, *53* (May 1997), 85–92.

(7) Zalusky, A. S.; Olayo-Valles, R.; Wolf, J. H.; Hillmyer, M. a. Ordered Nanoporous Polymers from Polystyrene-Polylactide Block Copolymers. *J. Am. Chem. Soc.* **2002**, *124* (43), 12761–12773.

(8) Cushen, J. D.; Otsuka, I.; Bates, C. M.; Halila, S.; Fort, S.; Rochas, C.; Easley, J. A.; Rausch, E. L.; Thio, A.; Borsali, R.; Willson, C. G.; Ellison, C. J. Oligosaccharide/silicon-Containing Block Copolymers with 5 Nm Features for Lithographic Applications. *ACS Nano* **2012**, *6* (4), 3424–3433.

(9) Dechy-Cabaret, O.; Martin-Vaca, B.; Bourissou, D. Controlled Ring-Opening Polymerization of Lactide and Glycolide. *Chem. Rev.* **2004**, *104* (12), 6147–6176.

(10) Wikimedia Commons. Lactide Stereoisomers Structural Formulae.

(11) Cushen, J. D.; Bates, C. M.; Rausch, E. L.; Dean, L. M.; Zhou, S. X.; Willson, C. G.; Ellison, C. J. Thin Film Self-Assembly of Poly(trimethylsilylstyrene- B - D , L -Lactide) with Sub-10 Nm Domains. *Macromolecules* **2012**, *45* (21), 8722–8728.

(12) Cushen, J. D. High Interaction Parameter Block Copolymers for Advanced Lithography, University of Texas at Austin, 2013.

(13) Bates, C. M.; Seshimo, T.; Maher, M. J.; Durand, W. J.; Cushen, J. D.; Dean, L. M.; Blachut, G.; Ellison, C. J.; Willson, C. G. Polarity-Switching Top Coats Enable Orientation of Sub-10-Nm Block Copolymer Domains. *Science (80-.).* **2012**, *338* (6108), 775–779.

(14) Cushen, J. D.; Wan, L.; Pandav, G.; Mitra, I.; Stein, G. E.; Ganesan, V.; Ruiz, R.; Willson, C. G.; Ellison, C. J. Ordering Poly(trimethylsilyl Styrene-Block- D,L -Lactide) Block Copolymers in Thin Films by Solvent Annealing Using a Mixture of Domain-Selective Solvents. *J. Polym. Sci. Part B Polym. Phys.* **2014**, *52* (1), 36–45.

(15) Cushen, J. D.; Bates, C. M.; Rausch, E. L.; Dean, L. M.; Zhou, S. X.; Willson, C. G.; Ellison, C. J. Thin Film Self-Assembly of Poly(trimethylsilylstyrene-B-D,L-Lactide) with Sub-10 Nm Domains. *Macromolecules* **2012**, *45* (21), 8722–8728.

(16) De Jong, S. J.; Arias, E. R.; Rijkers, D. T. S.; Van Nostrum, C. F.; Kettenes-Van den Bosch, J. J.; Hennink, W. E. New Insights into the Hydrolytic Degradation of Poly(lactic Acid): Participation of the Alcohol Terminus. *Polymer (Guildf).* **2001**, *42* (7), 2795–2802.

(17) Kim, S.; Nealey, P. F.; Bates, F. S. Decoupling Bulk Thermodynamics and Wetting Characteristics of Block Copolymer Thin Films. *ACS Macro Lett.* **2012**, *1* (1), 11–14.

(18) Hirao, A.; Loykulnant, S.; Ishizone, T. Recent Advance in Living Anionic Polymerization of Functionalized Styrene Derivatives. *Prog. Polym. Sci.* **2002**, *27* (8), 1399–1471.

(19) Worsfold, D. J.; Bywater, S. ANIONIC POLYMERIZATION OF ISOPRENE. *Can. J. Chem.* **1964**, *42* (12), 2884–2892.

Chapter 3: Poly(pentamethyldisilyl styrene-*block*-ethyl glycolide) (PDSS-PEGL)

As mentioned in **Chapter 2**, the lactide block was not an ideal component of a silicon-containing BCP due to the processing difficulties it introduced. In this chapter, a potentially improved version of PTMSS-PLA is reported, poly(pentamethyldisilyl styrene-*block*-ethyl glycolide) (PDSS-PEGL). Poly(ethyl glycolide) is more stable than poly(lactide) and no hydrolysis has been observed or reported within this polymer. In addition, pentamethyldisilyl styrene (DSS) possesses one more silicon atom per repeat unit compared to TMSS, which should further increase etch resistance favorably. In combination, I hoped that this BCP would perform equally as well or better than PTMSS-PLA.

This chapter will detail the synthesis and characterization of PDSS-PEGL and evaluate its candidacy for perpendicular orientation using a top coat strategy. Within the first few thin film experiments, it was obvious that this BCP interacted unexpectedly with top coats, causing unprecedented cracks to form in the top coat upon thermal annealing. The majority of this chapter will be spent describing and elucidating the cause behind the cracks, including multiple control experiments to rule out possible causes. In the end, the interaction between a small molecule used in the synthesis of the BCP, the BCP, and the maleic anhydride content of the top coat was pinpointed as the cause of the cracks.

3.1 Top Coat Orientation Strategy

A major drawback to PTMSS-PLA was its thin film processing challenges. While solvent annealing was effective in orienting the BCP in thin films, it is not an ideal orientation strategy in manufacturing. First, the use of solvents should be minimized in

industrial fabrication processes due to concerns of contamination and toxicity, and the expense of recovering volatilized solvent. Secondly, optimizing a solvent annealing strategy is most often an empirical process, although more fundamental understanding of this kind of processing is emerging every day. Thirdly, commercial scale solvent annealing processing equipment does not presently exist. Therefore, it is preferable if a non-solvent dependent annealing process can be used.

However, high χ BCPs, which are required to form the smallest features, typically combine two highly chemically incompatible blocks,[1–3] which poses a challenge for perpendicular orientation in thin films. Perpendicular orientation requires that the two blocks equally prefer both the top and bottom interfaces such that one block does not preferentially wet either interface. Substrate (bottom) interface neutralization is relatively straight-forward, and selecting a polymeric mat or brush random copolymer composed of the two components of the BCP can usually result in a neutral surface. Substrate neutralization is trivial because the surface neutralization treatment (SNT) is spin coated onto a bare substrate and either crosslinked or grafted prior to applying the BCP layer.[4,5] Therefore, when the BCP solution is spin coated, the solvent in which the BCP is solvated cannot also dissolve the underlying SNT.

My collaborators developed a strategy, so-called top coats, that can neutralize the air interface and allow the same principle to be applied to the top interface.[6] Before this innovation, attempts to use a SNT on top of the BCP thin film failed because the same solvents that deposited the neutral top interface would necessarily also dissolve the BCP thin film. This is because a "neutral" material necessarily has a surface energy between that of the two blocks of a BCP and consequently "neutral" materials are usually dissolvable in solvents that also dissolve the BCP, preventing formation of discrete layers. The innovative top coat strategy developed by my collaborators utilizes a ring-opening

monomeric compound, maleic anhydride (MA), which can switch upon heating from a polar, ring-opened form that can be dissolved in methanol or aqueous base to a less polar, ring-closed form (**Figure 3.1**). Because the ring-opened form can be dissolved in methanol or aqueous base, in which our BCPs of interest do not dissolve, the top coat can be applied directly on top of an existing BCP film. By judiciously choosing the alternating copolymer composition with the maleic anhydride component, the surface energy of the ring-closed form can be tailored to be neutral for a BCP.

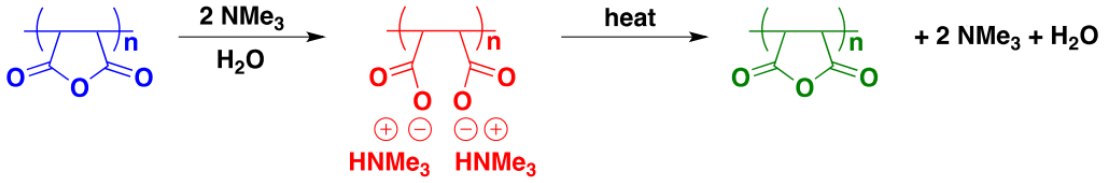

Figure 3.1 Maleic anhydride (blue) can be ring-opened with aqueous trimethylamine, and the ring-opened form (red structure) can be dissolved in methanol. Upon heating the ring-opened form, maleic anhydride will revert back to a ring-closed, less polar form (green). Reprinted with permission from [7]. Copyright 2014 American Chemical Society.

The top coat (TC) orientation process, shown in **Figure 3.2**, is an extension of thermal annealing.[6,7] With the addition of a few more spin coating and heating steps, solvent annealing can be entirely foregone. The optimization process is simplified with top coats because there are specific parameters that may be tuned to achieve perpendicular orientation, such as adjusting the copolymer composition.

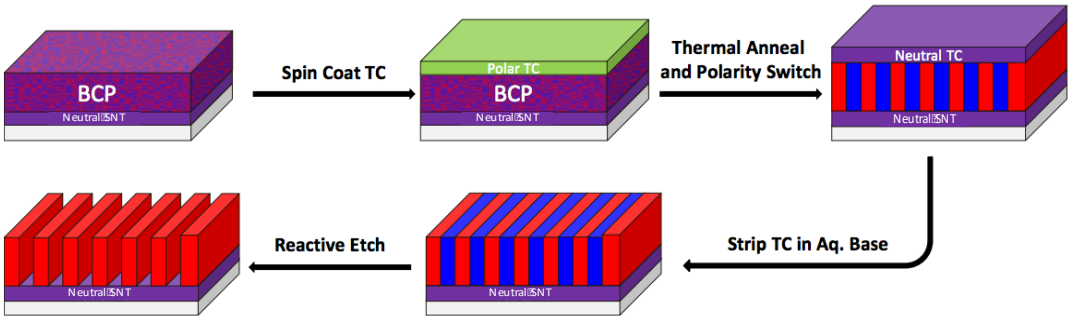

Figure 3.2 Top coat process flow. The crosslinked or grafted SNT is applied and immobilized, and then the BCP thin film is spin coated on top. Next, the polar (ring-opened) top coat (TC) is spin coated out of a polar solvent that does not dissolve the BCP. Then, the film stack is annealed to ring close the TC making the top coat less polar and, ideally, rendering it neutral for the BCP. At the same time, the BCP is perpendicularly oriented. After, the TC is stripped off using an aqueous base, revealing the perpendicularly oriented BCP. One block of the BCP can then be selectively removed, leaving the remaining block as an etch mask. Adapted from [8].

3.2 Experimental Methods

3.2.1 PDSS-OH synthesis

PDSS-PEGL was synthesized in a two-step reaction in the same manner as PTMSS-PLA. DSS monomer was synthesized through a Grignard reaction and purified by distillation twice over *di*-butylmagnesium by Yusuke Asano. PDSS-OH was synthesized by anionic polymerization in -78 °C THF. PDSS-OH was initiated by *sec*-butyllithium and end-capped by ethylene oxide. The resulting macroinitiator was precipitated in methanol and characterized by size exclusion chromatography (SEC), nuclear magnetic resonance (NMR), and matrix-assisted laser desorption/ionization time-of-flight mass spectrometry (MALDI).

3.2.2 PDSS-OH characterization

The molecular weight of PDSS-OH was determined through three methods: SEC, NMR (**Figure 3.3**), and MALDI (**Figure 3.4**). Of the three methods used to determine

molecular weight, the most accurate theoretically is MALDI, and the least accurate is NMR. SEC data was collected after determining dn/dc for each sample separately to generate absolute molecular weights. SEC and MALDI data agree well, and each sample is named as PDSS-OH_{MW} where the subscript is the number average molecular weight in kg/mol as determined by SEC. Molecular weight dispersity, Đ, was determined from SEC and MALDI. Two PDSS-OH samples were synthesized, and their characterization details are listed in **Table 3.1**.

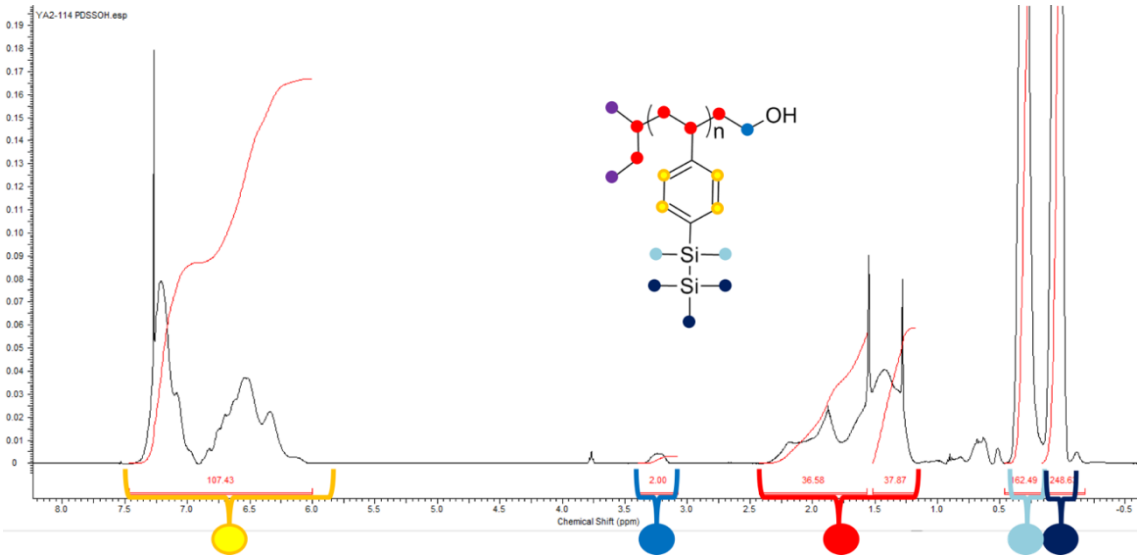

Figure 3.3 ^{1}H NMR spectrum for PDSS-$OH_{5.1}$, where the subscript refers to the number average molecular weight of the sample in kg/mol as determined by SEC. The peaks are assigned as shown.

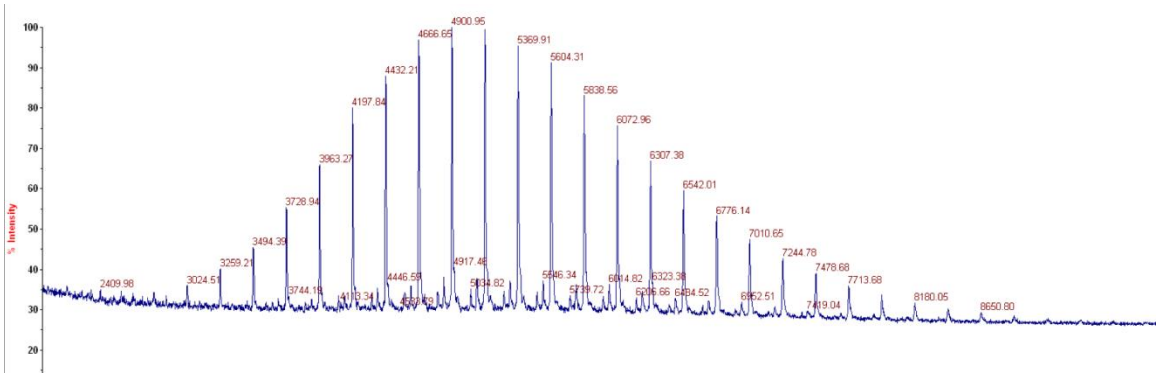

Figure 3.4 MALDI data for PDSS-$OH_{5.1}$.

		SEC	NMR	MALDI
PDSS-$OH_{5.1}$	Mn (kg/mol)	5,100	6,100	5,300
	Mw (kg/mol)	5,300	---	5,600
	Đ	1.04	---	1.05
PDSS-$OH_{4.8}$	Mn (kg/mol)	4,800	5,800	4,900
	Mw (kg/mol)	5,100	---	5,200
	Đ	1.06	---	1.05

Table 3.1 Characterization data for PDSS-OH.

3.2.3 PDSS-PEGL synthesis

The PEGL block was added to the PDSS-OH macroinitiator by my collaborator at the University of Minnesota, Leo Oquendo from the Hillmyer group. The synthesis scheme is shown below as **Scheme 3.1**. PDSS-OH (0.4 g, 0.075 mmol) was placed in an oven-dried Schlenk flask equipped with a magnetic stir bar. The flask was flame dried 3 times and the polymer was allowed to be under vacuum overnight. The next day the flask was brought in the glove box. Ethyl glycolide (0.62 g, 3.58 mmol), dry dichloromethane (3 mL) and DBU (0.075 mL, 0.0755 mmol) were added to the flask containing PDSS-OH. The

reaction was stirred at room temperature for 1 hour, then 0.5 mL of a 0.3 M solution containing benzoic acid in dichloromethane was added. The polymer was precipitated in cold methanol (3 times), filtered, and dried at room temperature under vacuum for 48 hours.

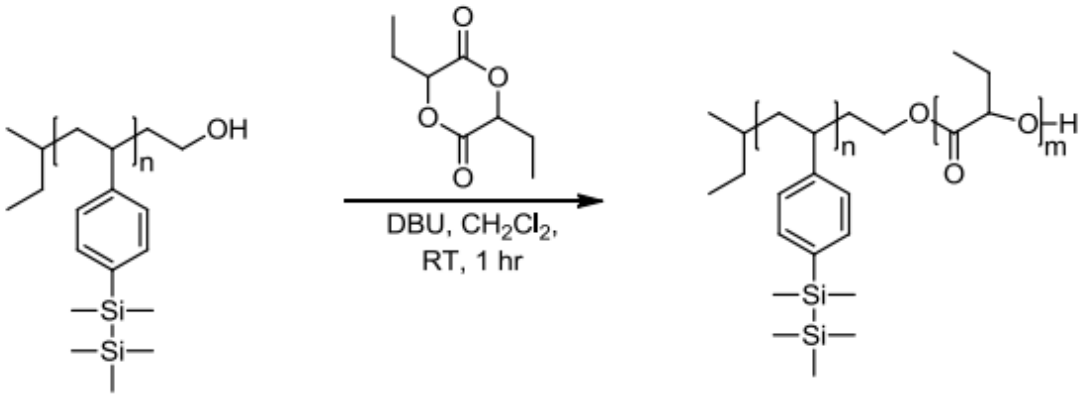

Scheme 3.1 Synthesis of PDSS-PEGL from PDSS-OH macroinitiator.

3.2.4 PDSS-PEGL characterization

The characterization of two PDSS-PEGL BCPs was performed at the University of Minnesota and is included below in **Table 3.2**. The volume fraction and number average molecular weight of the PEGL block and the BCP were determined by ^{1}H NMR relative to the absolute molecular weight of PDSS-OH using the mass densities of 0.91 g/cm^3 for PDSS and 1.09 g/cm^3 for PEGL. Molecular weight dispersity was determined by SEC (**Figure 3.5**). The decomposition temperature, T_d, was defined as the temperature at which 5% of the original polymer mass was lost (**Figure 3.6**). Glass transition temperatures, T_g, were recorded from the second heat at 5 °C/min on a differential scanning calorimeter (DSC) (**Figure 3.7**). Due to the small amount of BCP synthesized at Minnesota (under 500 mg each), SAXS studies for L_0 characterization were not performed.

BCP	M_n, PDSS (kg/mol)	M_n, PEGL (kg/mol)	M_n, BCP (kg/mol)	f_{PDSS}	Đ	T_d (°C)	T_g, PDSS (°C)	T_g, PEGL (°C)
$PDSS_{4.8}$-$PEGL_{8.9}$	4.8	8.9	13.7	0.55	1.02	302	63	20
$PDSS_{5.1}$-$PEGL_{10.0}$	5.1	10.0	15.1	0.52	1.01	324	67	20

Table 3.2. Characterization of PDSS-PEGL BCPs.

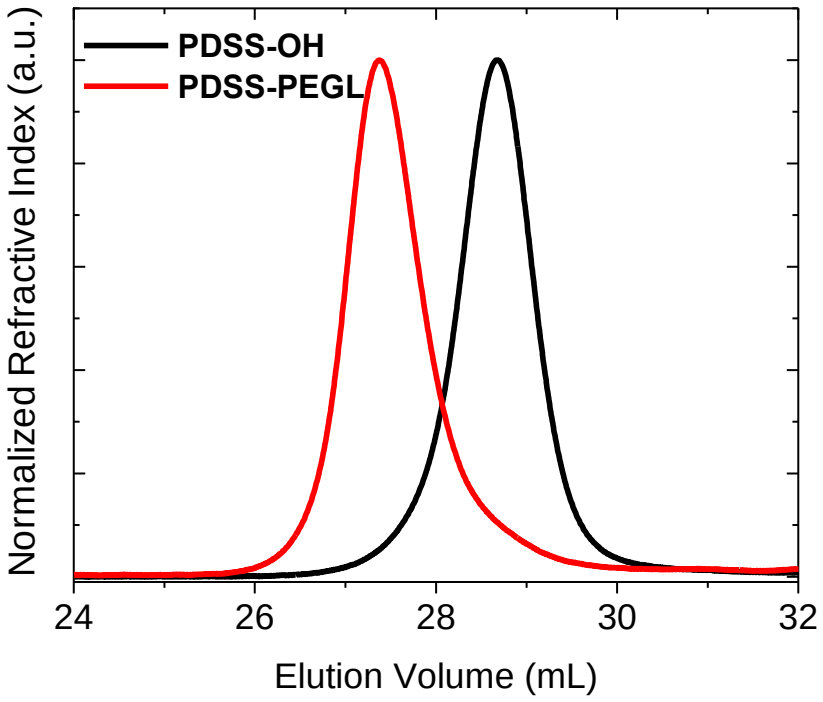

Figure 3.5 SEC trace used to determine the molecular weight dispersity of $PDSS_{4.8}$-$PEGL_{8.9}$ (red line). The PEGL added cleanly to the PDSS-OH macroinitiator (black line) as indicated by the sharp red peak that shifted uniformly from the macroinitiator.

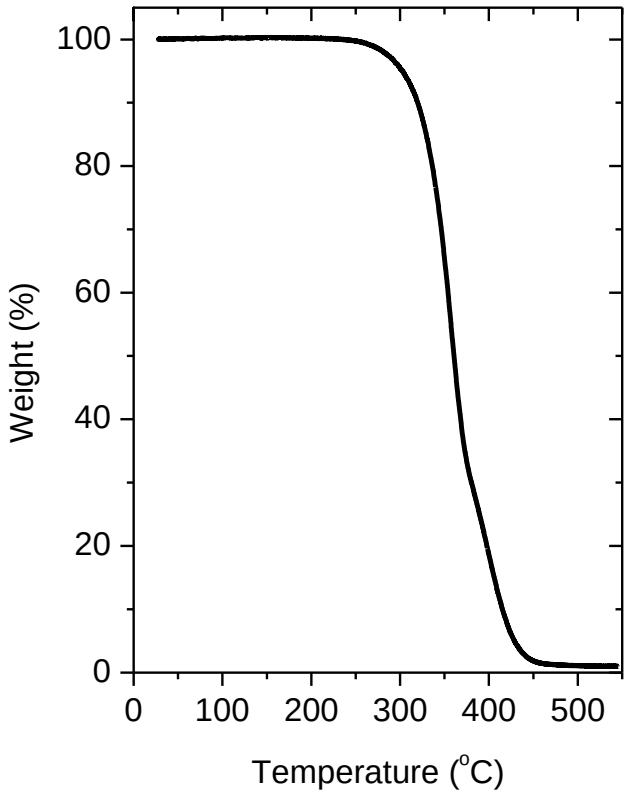

Figure 3.6 Thermogravimetric analysis of $PDSS_{4.8}$-$PEGL_{8.9}$ determined that the T_d of this BCP was 302 °C in air.

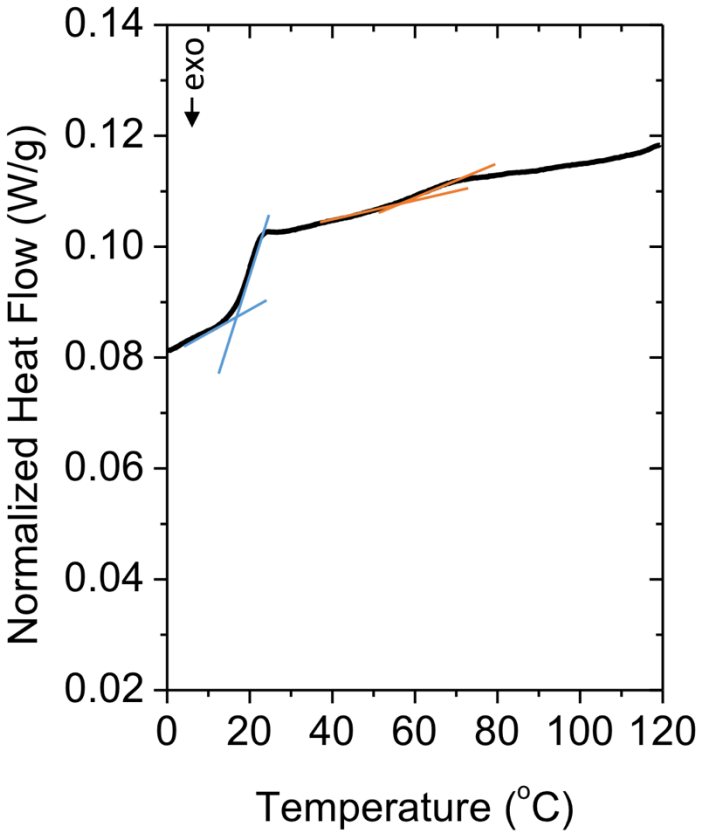

Figure 3.7 Differential scanning calorimetry data of $PDSS_{4.8}$-$PEGL_{8.9}$ used to determine the T_gs of each block.

3.2.5 PEGL homopolymer synthesis

PEGL homopolymer was also synthesized at the University of Minnesota. Ethyl glycolide (1g, 6 mmol) was added to a flame-dried Schlenk flask equipped with a magnetic stir bar and brought inside the dry box. Dry toluene (7 mL) and tin(II) 2-ethylhexanoate (8 mg, 0.02 mmol) were added to the flask. The flask was sealed and removed from the dry box, placed into a preheated oil bath (130 °C), and left under continuous stirring for 40 min. After this time, the system was removed from heating, and the polymer was precipitated 3 times into methanol to remove residual monomer and catalyst. The polymer was dried under vacuum for 2 days at room temperature.

3.2.6 Thin film island/hole test methods

Thin film experiments to select for suitable SNTs were conducted by first spin coating the SNT on a silicon substrate. The vast SNT library available was synthesized by various members of the group, and many combinations of random copolymers are available. For the experiments detailed here, a series of poly(*t*-butylstyrene-*random*-methyl methacrylate-*random*-vinylbenzyl azide) P(*t*-BuSty-MMA-VBzAz) random copolymers was used, each containing 5-6 mol% vinylbenzyl azide and varying concentrations of t-BuSty and MMA. The azide acted as a crosslinking group, and each SNT was annealed at 250 °C for 5 mins to form the crosslinked mat. The BCP of interest was then spin coated on top of the SNT mat and annealed in air at 175 °C for 5 mins, and the sample was imaged with optical microscopy.

Thin film experiments to select for suitable TCs were conducted in a similar manner. As with the SNTs, a vast library of TC options exists. There are many "families" of TCs with different chemical components, so each TC used will be detailed as it is introduced. A BCP thin film was spin coated on a substrate, and the TC was spin coated on top. The film stack was annealed at a temperature between the T_gs of both blocks of the BCP and the T_g of the TC for 5 mins to ensure that the BCP had enough kinetic mobility to assemble into islands or holes without fear of mixing with a liquefied TC, the importance of which will be discussed in the next section.

3.3 Thin Film Experiments

After synthesis and characterization, thin film studies were performed to identify an appropriate SNT and TC that would enable the perpendicular orientation of each BCP. As mentioned before, a major advantage of the TC method for BCP domain orientation lies in the systematic approach that can be taken when selecting neutral conditions. For solvent annealing, each set of parameters can only be analyzed after completing the

experiment, and each evaluation result only reports that the conditions worked or did not work. With the TC method, island/hole (I/H) tests[9] can be performed to select the neutral SNT and TC separately, and I/H tests direct subsequent experiments (such as increasing or decreasing the polarity of the surface being tested). In addition, I/H tests can be conducted simply with a spin coater and hot plate, and the features can be easily observed using an optical microscope.

3.3.1 Using I/H tests to determine interface neutrality

In the absence of neutral interfaces, BCP thin films will reorganize upon thermal annealing to adopt a thickness commensurate with its L_0, or natural bulk domain periodicity.[10] When a BCP thin film of incommensurate thickness (i.e., a film not n or ($0.5 + n$) L_0 thick) is spin coated on a preferential substrate, the BCP film will develop into quantized $0.5nL_0$ thicknesses upon annealing, as shown in **Figure 3.8**. If the majority of the annealed film is at nL_0 with a minority of the film at $(n+1)L_0$, then islands are formed. Conversely, if a minority of the film is at $(n-1)L_0$, then holes are formed. It is important to note that I/H features only form when one interface exhibits preferential wetting, driving parallel orientation. These island and hole features can be easily identified using an optical microscope, where raised regions (islands) appear darker in color and depressed regions (holes) appear lighter in color.

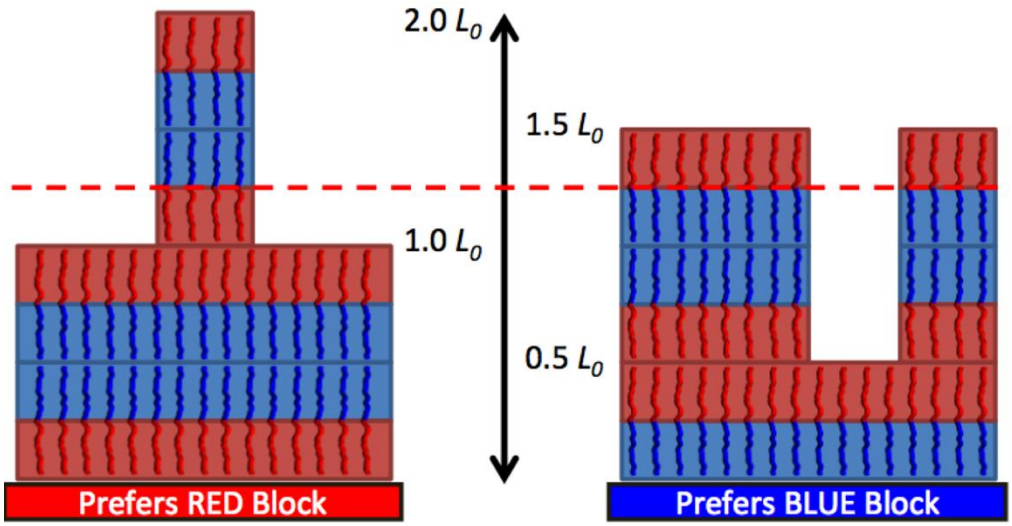

Figure 3.8 I/H tests for a BCP thin film with an initial spin coated thickness of 1.25 L_0. Here, the nonpolar red block prefers to wet the top air interface, and the BCP exhibits either symmetric (substrate also prefers red block) or asymmetric (substrate prefers blue block) wetting behavior upon annealing. As demonstrated, knowing the wetting preference of the top interface and the initial film thickness, the relative surface energy of the substrate is known depending on whether islands or holes are formed. Figure adapted from [8].

A SNT can be systematically determined by knowing the wetting behavior of the top interface. When air is the top interface, the nonpolar block of the BCP is assumed to wet the surface of the BCP upon thermal annealing. Thus, knowing the spin coated thin film thickness, the L_0 of the BCP, and the presence of islands or holes dictates which block is wetting the substrate. This information indicates whether the substrate SNT is too polar or nonpolar, and SNT composition adjustments can be made accordingly. If a subsequent SNT exhibits the opposite behavior, then the SNT composition has been adjusted too far in the other direction, and the neutral state lies somewhere in between. In this manner, a SNT can be selected with a minimum of trial and error.

In an analogous manner, a TC can be selected for each BCP system. An interesting phenomenon is that TCs can deform to "stretch" over underlying islands and holes, despite the annealing temperature being below the T_g of the TC. In this case, if the wetting behavior of the bottom interface is known, the wetting behavior of the TC can be deduced. A neutral TC can be identified by testing a series of TCs with slightly varied compositions and looking for a switch between islands and holes.

After a neutral SNT and TC are identified, the two can be used together to perpendicularly orient the BCP using the process flow in **Figure 3.2**. Atomic force microscopy (AFM) or scanning electron microscopy (SEM) can be used to confirm orientation.

3.3.2 Control tests: is PEGL more robust than PLA?

Two control tests were performed with $PDSS_{4.8}$-$PEGL_{8.9}$ to ensure that PEGL did not have the same drawbacks as PLA. As mentioned in the previous chapter, the methanol used to dissolve the TCs swelled the PLA block. To test whether methanol had the same effect on PDSS-PEGL, the BCP was spin coated on a silicon substrate, and its film thickness was measured using spectroscopic ellipsometry to be approximately 20 nm. Afterwards, methanol was spin coated on the BCP, and the film thickness was again measured. No appreciable film thickness difference (always less than 0.2 nm) was observed for the three samples tested in this manner, confirming that methanol did not swell the BCP. The optical micrographs in **Figure 3.9** corroborate that no deformation of the BCP thin film had occurred.

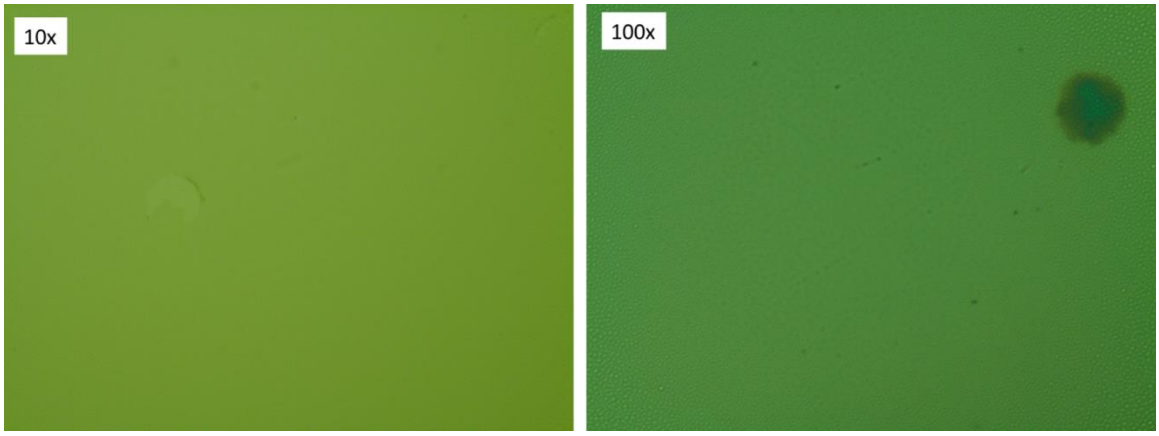

Figure 3.9 10x and 100x optical micrograph images of $PDSS_{4.8}$-$PEGL_{8.9}$ after methanol was spin coated on it. The uniform interference color across the two micrographs demonstrates that the thin film was not destroyed or deformed by methanol. The dark spot in the 100x micrograph is a dust particle.

Another concern was whether the PEGL group would graft to the silicon substrate like PLA. To test this, a 23.7 nm film of $PDSS_{4.8}$-$PEGL_{8.9}$ was spin coated on a silicon substrate and heated at 165 °C for 10 minutes, double the usual annealing time. As confirmed by optical microscopy (**Figure 3.10**), holes developed in the thin film. After this thin film was rinsed with THF, the film thickness was measured to be 0 nm by ellipsometry, and optical microscopy also confirmed that the smooth silicon substrate was recovered.

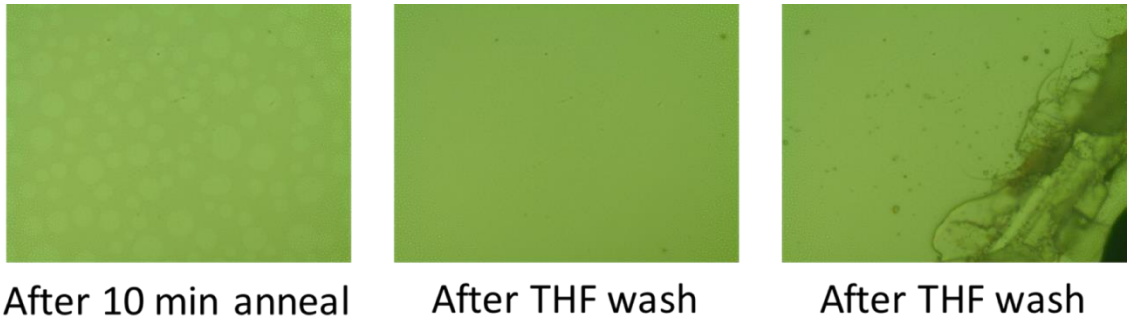

Figure 3.10 $PDSS_{4.8}$-$PEGL_{8.9}$ after annealing at 165 °C for 10 minutes formed holes on silicon substrate (left). After rinsing with THF, the thin film was easily rinsed off, leaving nothing grafted to the silicon (middle). An image of the edge of the wafer shows no iridescent colors indicative of a thin film (right).

3.3.1 Substrate neutralization

Although I was not able to determine the bulk domain spacing, L_0, from SAXS due to lack of suitable material quantities, the islands and holes formed during I/H testing are for the most part quantized to 1 L_0. From AFM scans of the I/H tests, the smaller sample, $PDSS_{4.8}$-$PEGL_{8.9}$, formed 11 nm I/H and the larger sample, $PDSS_{5.1}$-$PEGL_{10.0}$, formed 12.5 nm I/H, signifying that the domain spacings (L_0) of these BCPs are 11 nm and 12.5 nm, respectively. It is necessary to establish L_0 for each BCP first because specific thicknesses are targeted during I/H tests.

Next, the wetting behavior of PDSS-PEGL at both the air and silicon interfaces was determined. As shown in **Figure 3.11**, PDSS-PEGL exhibited asymmetric wetting when the island-hole test was performed on a silicon substrate with the nonpolar block, PDSS, wetting the air interface and the polar block, PEGL, wetting the silicon interface.

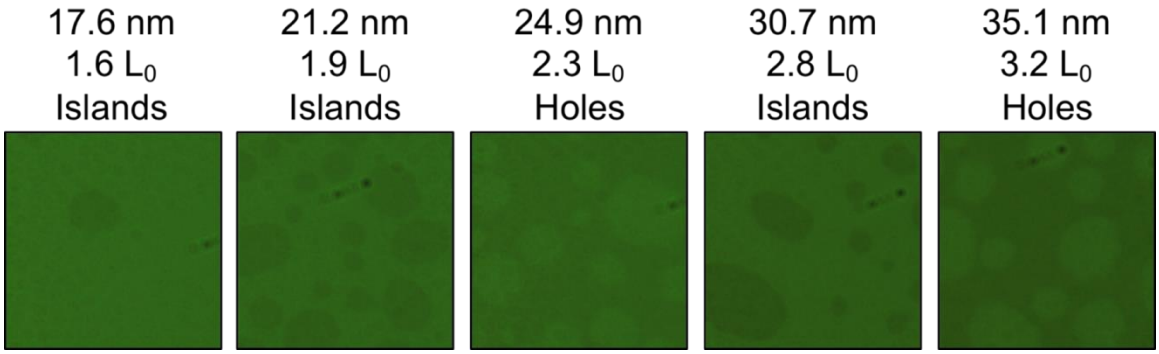

Figure 3.11 I/H test on a silicon wafer for $PDSS_{4.8}$-$PEGL_{8.9}$ confirmed that the BCP exhibits asymmetric wetting behavior. The top row is the film thickness of each sample, the second row is the equivalent L_0, and the third row is the type of features formed.

Next, neutral SNTs were found for each BCP. Each BCP was spin coated on a series of SNTs containing varying amounts of *t*-BuSty (as specified in **Figure 3.12**), with 5-6 mol% VBzAz as crosslinker, and MMA making up the balance of the SNT. As the SNT surface energy changes, the wetting behavior of the bottom interface eventually changes from asymmetric to symmetric wetting. At the crossover from asymmetric to symmetric wetting is a neutral SNT that produces a flat film or a film with islands and holes that are the height of 0.5 L_0, which shows up on optical micrographs as lighter colored features.

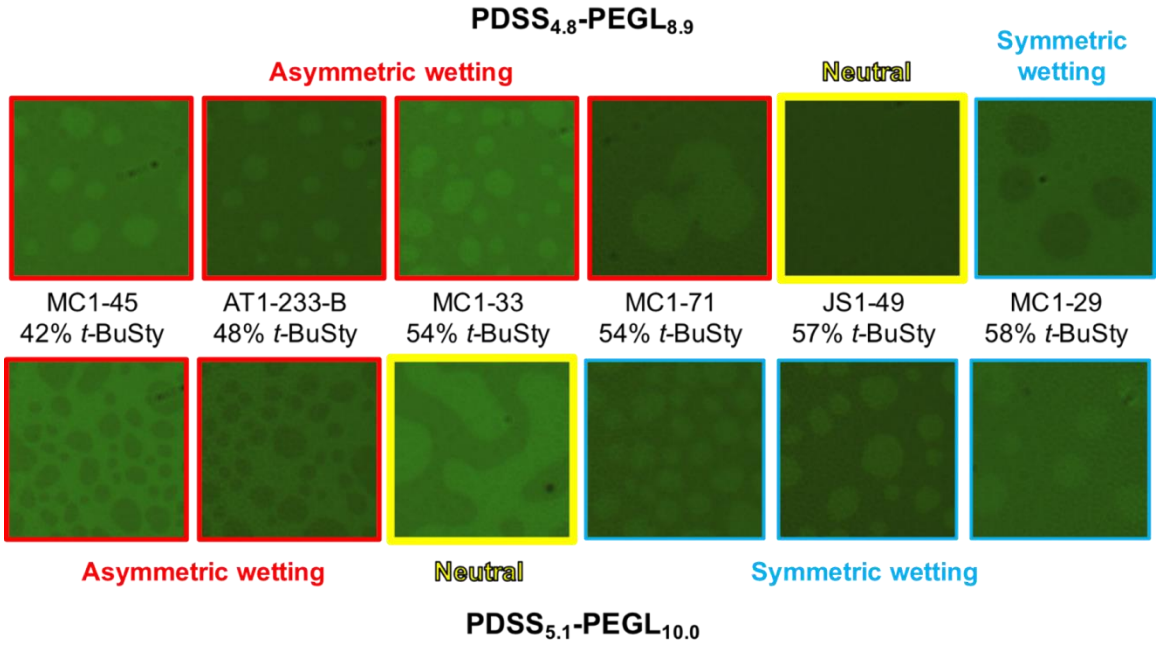

Figure 3.12 Using I/H tests to determine a neutral SNT for each PDSS-PEGL BCP. The initial film thickness of $PDSS_{4.8}$-$PEGL_{8.9}$ was about 2.3 L_0 and the initial film thickness of $PDSS_{5.1}$-$PEGL_{10.0}$ was about 1.7 L_0. Each sample was annealed at 165 °C in air for 5 mins before imaging.

3.3.2 Top interface neutralization

After identifying neutral SNTs for the two BCPs, the next step was to identify neutral TCs. Knowing that the PEGL block will preferentially wet the silicon substrate allows for identification of the TC in an analogous manner to the SNT. It should be noted that TCs will not form islands and holes on all BCPs for reasons that are still not clear, but it fortuitously happened to do so for PDSS-PEGL. From here on in this chapter, the BCP used is $PDSS_{4.8}$-$PEGL_{8.9}$ unless otherwise stated.

Due to the vast array of TCs available for testing, the first few were chosen at random to provide an initial survey. However, in addition to observing islands and holes, a mysterious "cracking" behavior was exhibited for all the TCs, as shown in **Figure 3.13**. Aside from being unprecedented, this cracking behavior is deleterious because it is difficult

to ascertain how the BCP underneath is changing in thickness. Without knowledge of the BCP film thickness, it is impossible to analyze the I/H data. In many samples, there were patches of both islands and holes, as shown in **Figure 3.14**, seeming to indicate that the BCP thin film was no longer uniform in thickness.

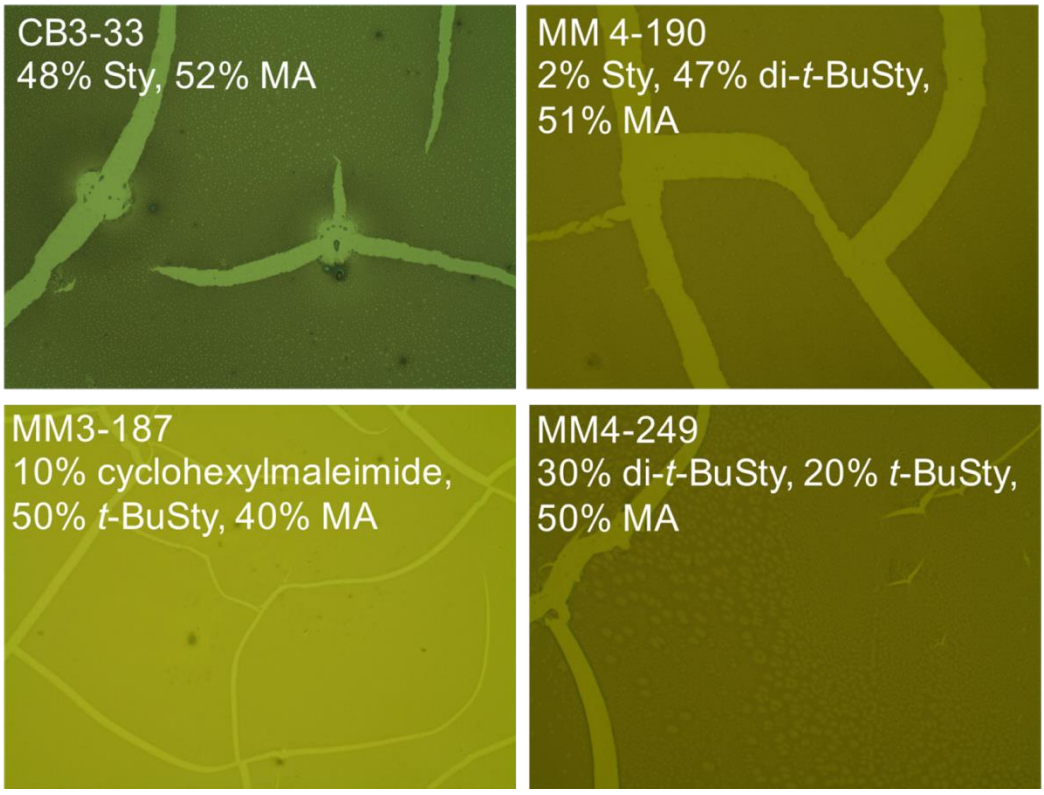

Figure 3.13 Cracking behavior for various TCs over $PDSS_{4.8}$-$PEGL_{8.9}$ annealed at 165 °C in air for 5 mins. All percentages are mole percent of the monomer in the TC. Di-*t*-BuSty is di-*tert*-butylstyrene and MA is maleic anhydride. Images are all optical micrographs taken at 10x magnification with dimensions of 1.2 mm x 1.6 mm.

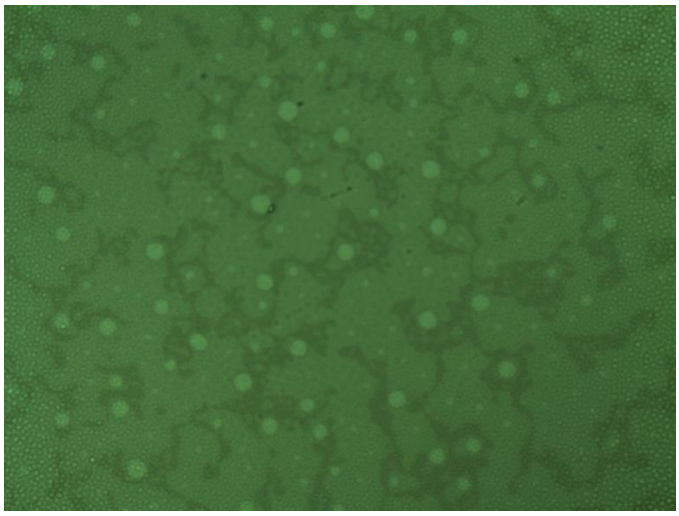

Figure 3.14 Example of a TC exhibiting strange I/H behavior on a cracked sample. The TC was CB3-33 (48 mol% styrene, 52 mol% MA) on $PDSS_{4.8}$-$PEGL_{8.9}$ on bare silicon annealed at 165 °C in air for 5 mins. Image is an optical micrograph taken at 100x magnification with dimensions of 120 μm x 160 μm.

It is interesting to note that when the BCP was spin coated on top of any TC and annealed, no cracking was observed. However, this is not a solution to the cracking problem because there needs to be a TC on top of the BCP to mitigate the top interface surface energy. In addition, there is much greater uncertainty about the thickness of the BCP film when it is spin coated on top of a TC, and a few nanometers can make a crucial difference in the interpretation of I/H data when the L_0 is so small. For example, for $PDSS_{4.8}$-$PEGL_{8.9}$, a measurement of 21 nm would be just under 2 L_0, while a measurement of 23 nm would be just over 2 L_0, and observed holes at 21 nm would indicate the opposite wetting behavior as observed holes at 23 nm. However, because having the TC underneath mitigated the cracking, it was hypothesized that having an organic layer underneath PDSS-PEGL might prevent cracking. Unfortunately, as shown in **Figure 3.15**, a film stack of TC on BCP on SNT on silicon still resulted in cracking. This sample was annealed at 165 °C for a mere 5 seconds.

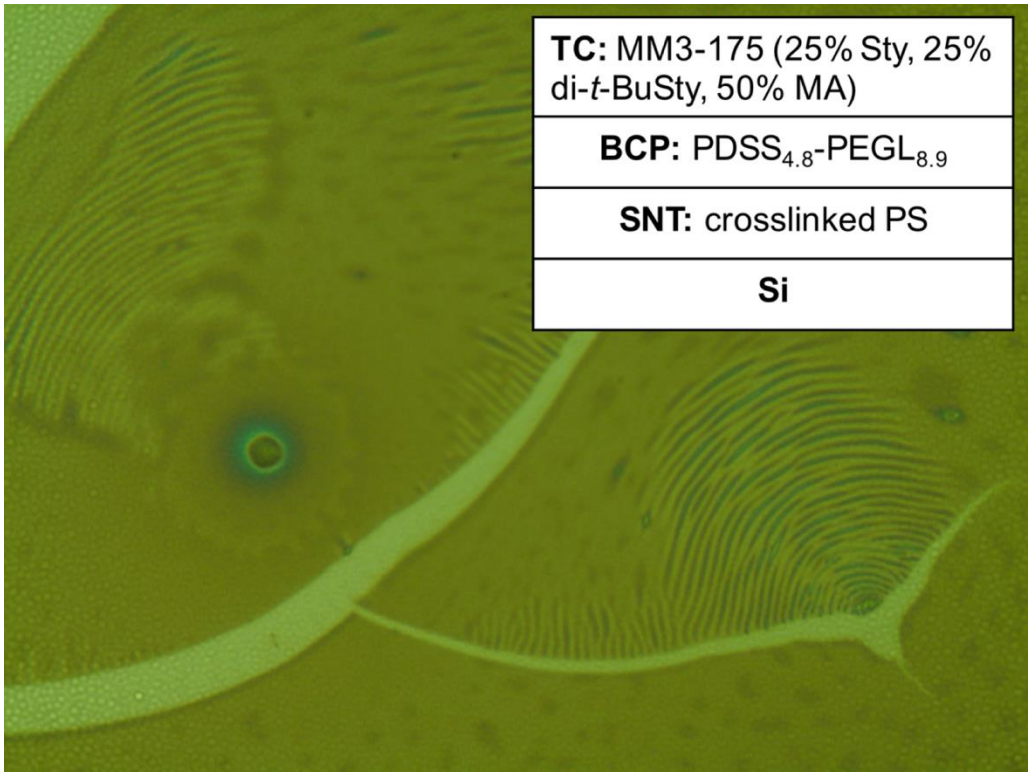

Figure 3.15 Optical micrograph of a cracked TC on PDSS-PEGL on crosslinked PS after annealing at 165 °C for 5 seconds. Micrograph is 1.2 mm x 1.6 mm.

After this, a variety of control experiments were performed to probe many variables including the effects of TC thickness, annealing time, spin coating solvent, soft bake, and whether the annealing process was causing the BCP to graft to each other or to the TC. To keep results consistent and comparable, $PDSS_{4.8}$-$PEGL_{8.9}$ and the TC CB3-33 (52% MA, 48% Sty) were used for all control experiments. **Figure 3.16** shows the effect of TC thickness on the cracking behavior in a series of AFM scans. As shown, the islands on the ledges (light grey areas) and the holes in the cracks (dark grey and black regions) did not change with changing TC thickness. **Figure 3.17** shows the effect of annealing time on crack behavior when annealed in air at 165 °C. Once again, there was no effect on the cracking behavior. **Figure 3.18** shows thin film behavior of two different casting solvents

for the BCP, toluene (an aromatic solvent) and methyl isobutyl ketone (MIBK) (a ketone). While there are some qualitative differences in the way the spin coated films looked, the cracking behavior persisted regardless of the solvent. **Figure 3.19** shows the results from applying a soft bake to the film stack before more aggressive annealing to relieve any stress that may exist in the films. Again, the cracking behavior was present after a soft bake. Finally, DSC and SEC experiments were performed to rule out the possibility of BCP crosslinking and BCP reacting with TC. To perform these experiments, DSC aluminum pans were filled with BCP and TC and annealed in either air or nitrogen at 165 °C for 10 minutes, twice the length of the typical annealing time. After removal from the DSC, the samples were dissolved in THF and run through the SEC. As shown in the SEC traces in **Figure 3.20**, the lack of a shoulder on the left side of each trace means that the SEC was unable to detect any crosslinking or grafting. In summary, TC cracking occurred in all of the basic control experiments.

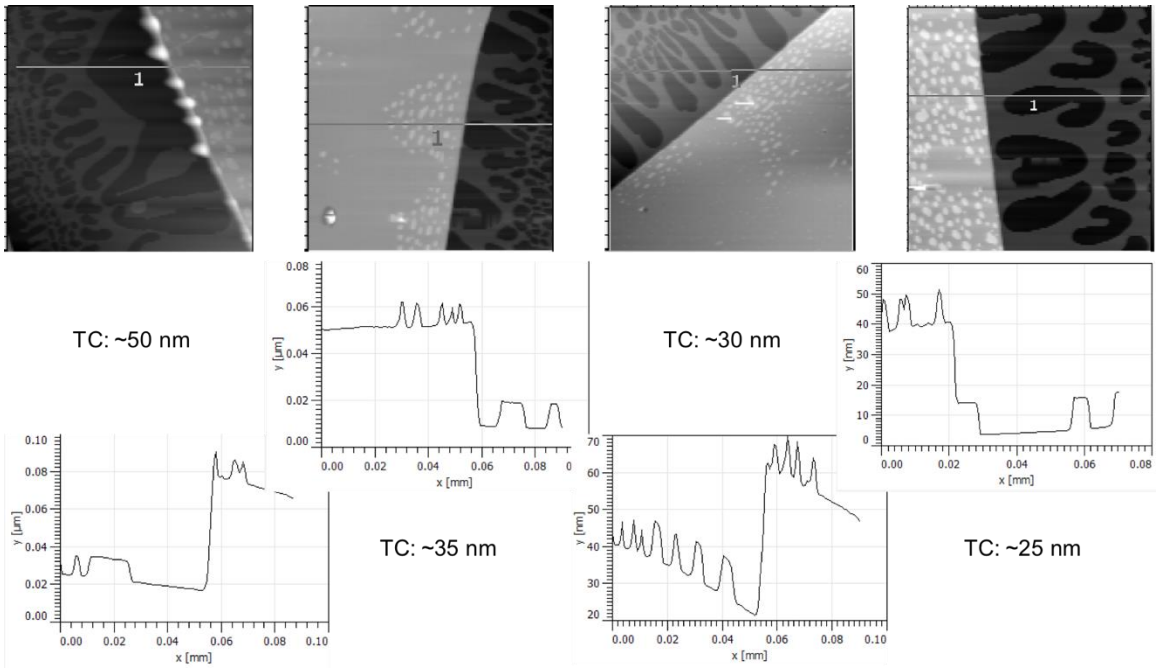

Figure 3.16 AFM images and topography profiles of four samples of $PDSS_{4.8}$-$PEGL_{8.9}$ with varying thicknesses of TC (CB3-33, 52% MA, 48% Sty) after annealing in air 165 °C for 5 minutes. Each AFM image is 90 µm x 90 µm. The cracking behavior was unaffected by the TC thickness.

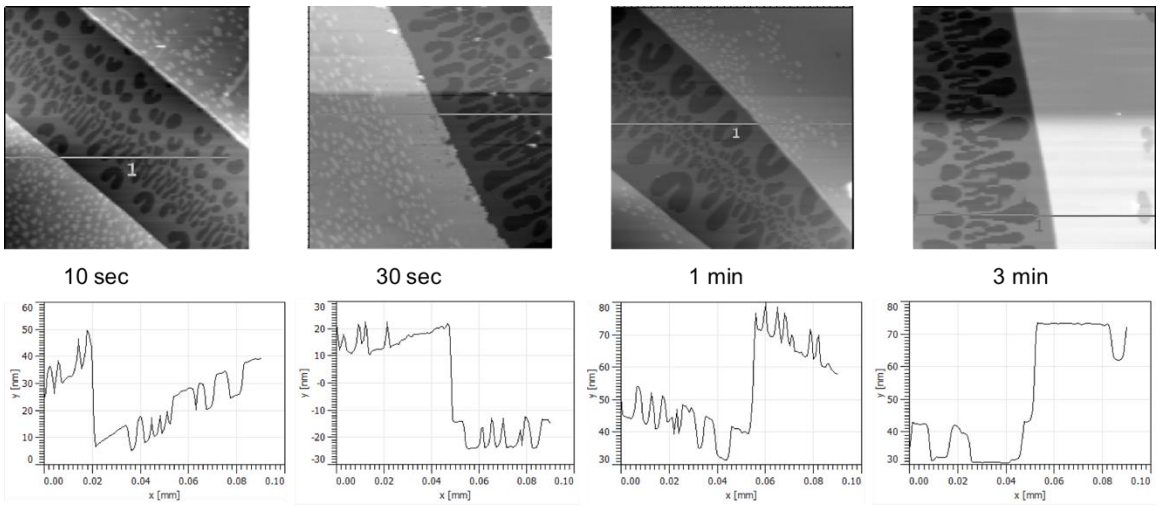

Figure 3.17 AFM images and topography profiles of four samples of $PDSS_{4.8}$-$PEGL_{8.9}$ with CB3-33 (52% MA, 48% Sty) after annealing in air 165 °C for various times ranging from 10 sec to 3 mins. Cracking was evident in all samples regardless of annealing time. Each AFM image is 90 µm x 90 µm.

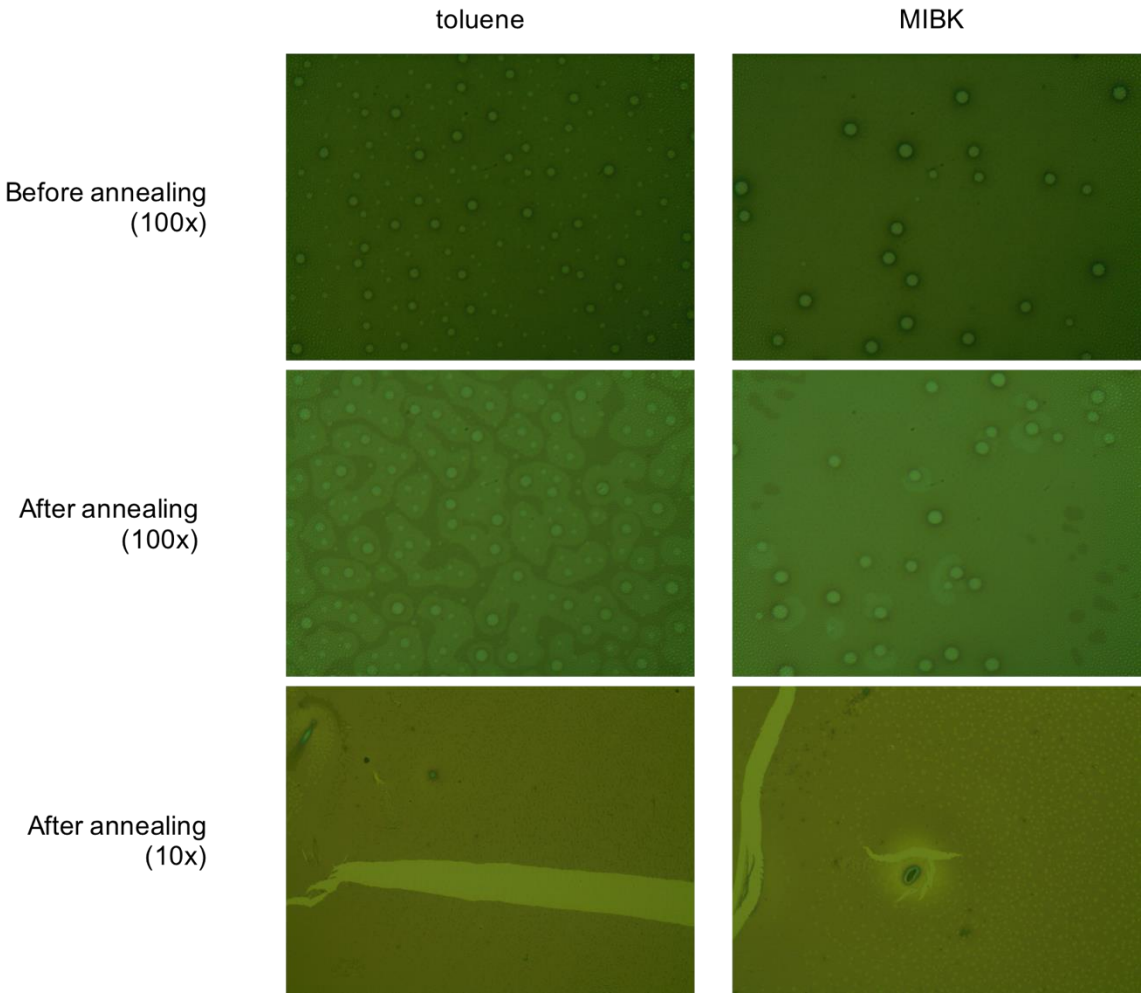

Figure 3.18 Optical micrographs of samples of $PDSS_{4.8}$-$PEGL_{8.9}$ with CB3-33 (52% MA, 48% Sty) spin coated out of either toluene or MIBK. The cracking behavior persisted regardless of the polarity of the BCP spin coating solvent. 10x micrographs are 1.2 mm x 1.6 mm and 100x micrographs are 120 μm x 160 μm.

Figure 3.19 **(a)** Optical micrograph after application of the BCP film and a 10 s 100 °C soft bake in air. **(b)** Optical micrograph of TC deposited on the film in (a) and soft baked at 100 °C for 10 s in air. **(c)** Optical micrograph of the film stack in (b) after 1 minute at 165 °C in air. Each micrograph is 1.2 mm x 1.6 mm.

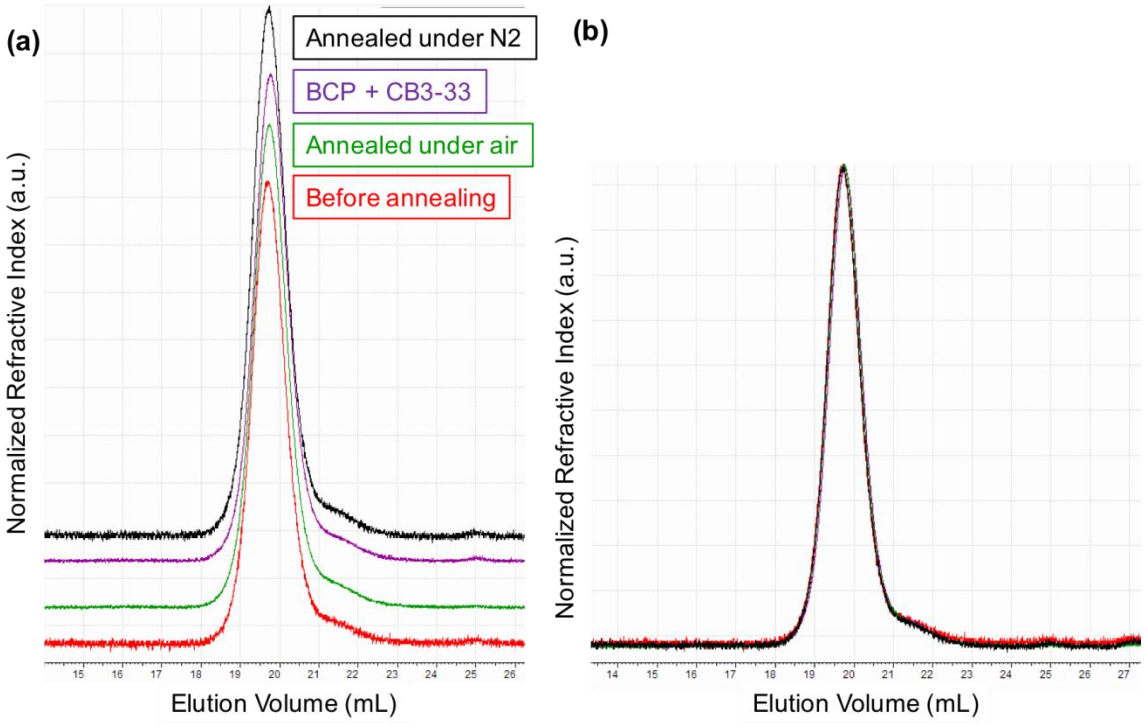

Figure 3.20 SEC curves of BCP and TC after annealing in the DSC. **(a)** The black curve corresponds to the BCP annealed under nitrogen, an inert atmosphere. The purple curve corresponds to the BCP and the TC being annealed in air together, simulating the actual annealing conditions. The green curve corresponds to the BCP annealed under air, and the red curve corresponds to the BCP as received, before any annealing. **(b)** All four curves from (a) collapsed together shows that the BCP did not change under of the annealing conditions.

After exhausting those control tests, I looked back to PTMSS-PLA, the BCP that inspired PDSS-PEGL. PTMSS-PLA was the closest analogue available to us, and I was curious as to whether the cracking behavior is due to the lactide-like block. This was unlikely because PTMSS-PLA had been oriented using TCs before, but these experiments were carried out to confirm these new TCs behaved as expected. As shown below in **Figure 3.21**, PTMSS-PLA indeed did not exhibit any cracking behavior after annealing with a TC.

The TC used in this study was also CB3-33 (52% MA, 48% Sty), the same TC used for the control experiments above.

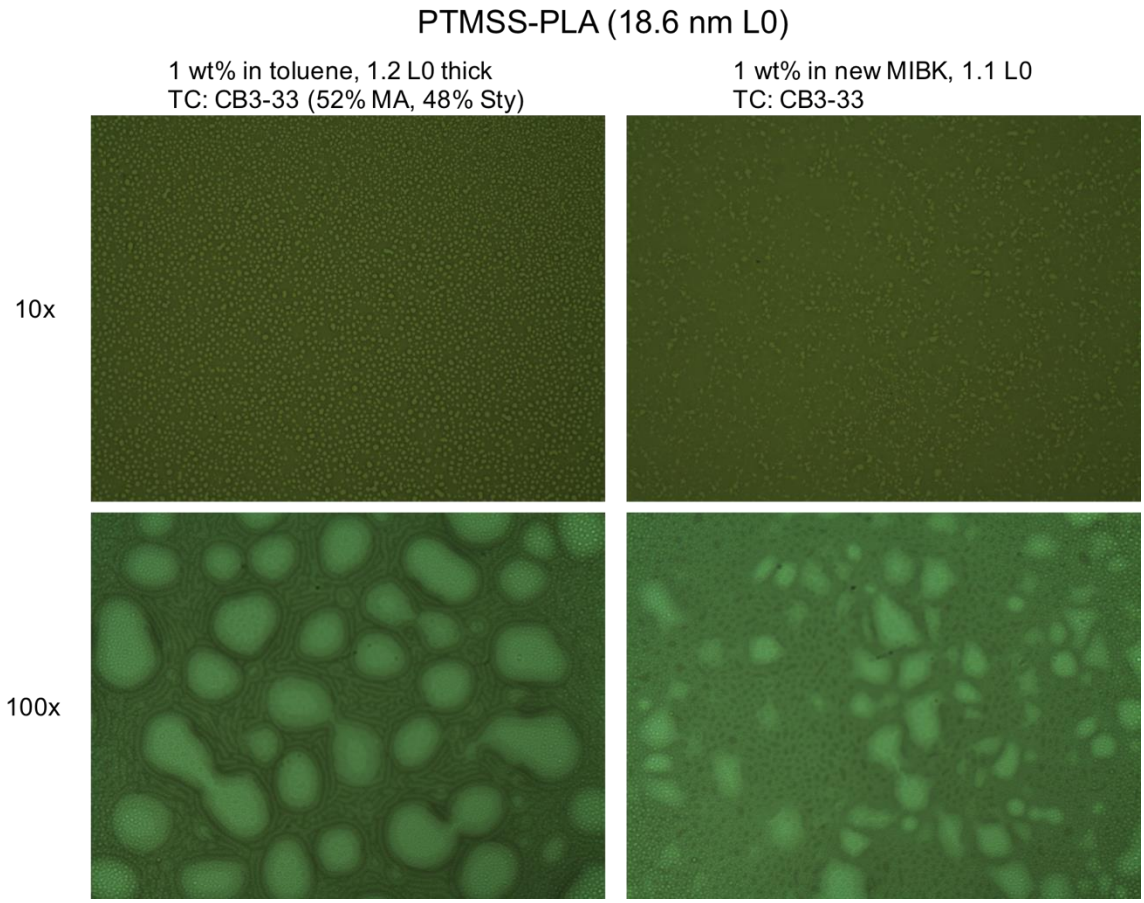

Figure 3.21 Lamellae-forming PTMSS-PLA spin coated out of toluene and MIBK. CB3-33 was the TC used, and the samples were annealed at 165 °C for 5 min in air. The optical micrographs, despite having microstructures, show no indication of cracking. 10x micrographs are 1.2 mm x 1.6 mm and 100x micrographs are 120 μm x 160 μm.

The PTMSS-PLA results suggest that the culprit is inherent either in the PDSS-PEGL BCP or in the BCP's interaction with TCs. The PDSS block should not be a problem

because TCs have been used to perpendicularly orient many other PDSS-containing BCPs.[3] To verify this, I spin coated TC on top of PDSS-PEGL annealed in air. As mentioned in the previous section, the PDSS block selectively wets the top interface when annealed in air, so annealing before applying TC means that the TC should only be in contact with the PDSS block. As shown in **Figure 3.22**, the film still cracked. One hypothesis is that the PDSS block was too thin to screen the effects of the underlying PEGL block from the TC,[11] so the next test involved TC on PEGL homopolymer.

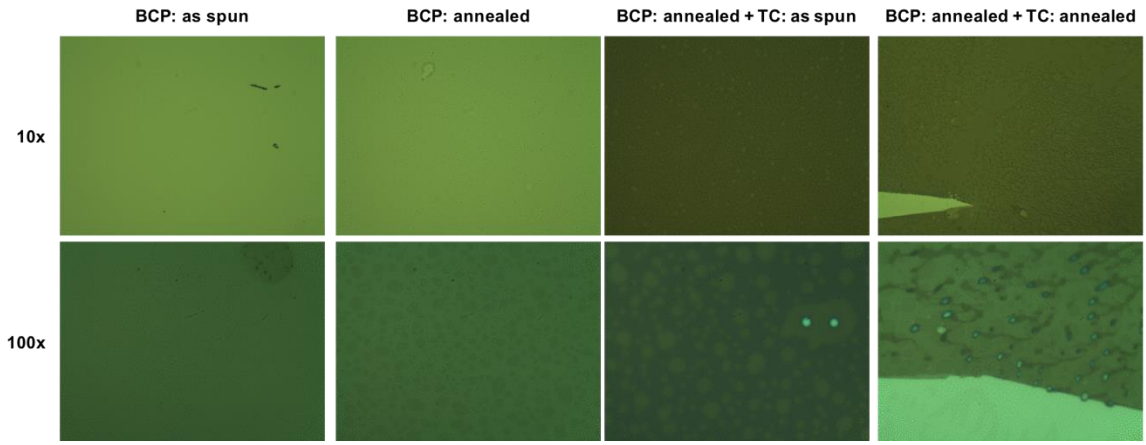

Figure 3.22 Optical micrographs of PDSS-PEGL as cast on silicon wafer, PDSS-PEGL annealed at 165 °C for 5 mins to wet the air interface with PDSS, TC (CB3-33) spin coated on top of annealed PDSS-PEGL, and annealed PDSS-PEGL with TC annealed at 165 °C for 5 mins. As shown the final film still cracked. 10x micrographs are 1.2 mm x 1.6 mm and 100x micrographs are 120 μm x 160 μm.

The interaction between PEGL homopolymer and CB3-33 was investigated next. Two PEGL homopolymers with varying molecular weights (8.6 kg/mol and 25.8 kg/mol) were supplied to us by the University of Minnesota. As shown in **Figure 3.23**, the PEGL homopolymers remarkably did not crack with TC on top. However, the BCP did crack under identical conditions.

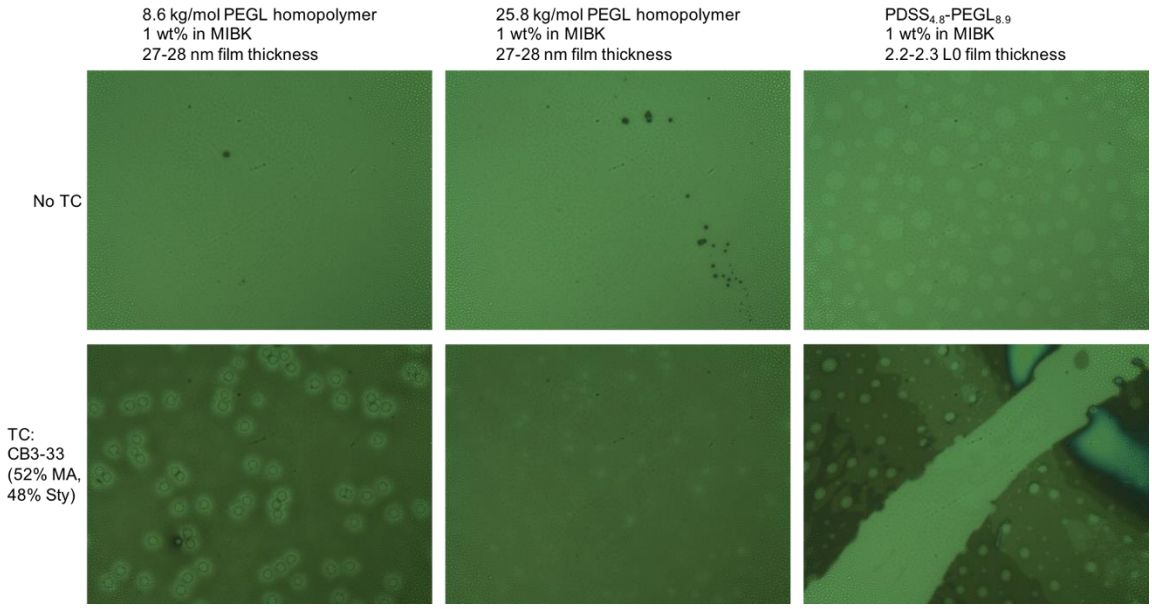

Figure 3.23 The interaction between PEGL homopolymer and CB3-33 was investigated. Neither of the PEGL homopolymers showed cracking while PDSS-PEGL did after annealing at 165 °C for 5 mins in air. Each optical micrograph is 10x magnification with dimensions of 1.2 mm x 1.6 mm.

After ruling out that both the PDSS and PEGL blocks could not be the source of the problem, I turned to the TC to look for clues. Most of the TCs in the group's library have 50 mol% maleic anhydride while the other 50 mol% is composed of various styrenic moieties because maleic anhydride and styrene undergo essentially alternating copolymerization. Thus, all of the TCs used so far have been roughly 50 mol% MA. To test the effect of MA on the thin film behavior, I looked at series of TCs with varying amounts of MA, as detailed in **Table 3.3**. These TCs are still composed of approximately 50 mol% of a styrene-based moiety, *t*-butyl styrene, and the balance is cyclohexyl maleimide. As shown in **Figure 3.24**, both MM3-188 and MM3-189, the two TCs with the lowest amounts of MA, did not crack upon annealing. Because MM3-189 had fewer defects after annealing, this TC was used in subsequent experiments and is referred to as the "good" TC.

TC	MA	Cyclohexyl maleimide	*t*-BuSty
MM 3-187	40%	10%	50%
MM 3-188	31%	21%	49%
MM 3-189	21%	31%	48%

Table 3.3. Series of TC with varying ratios of maleic anhydride and cyclohexyl maleimide copolymerized with *t*-butyl styrene.

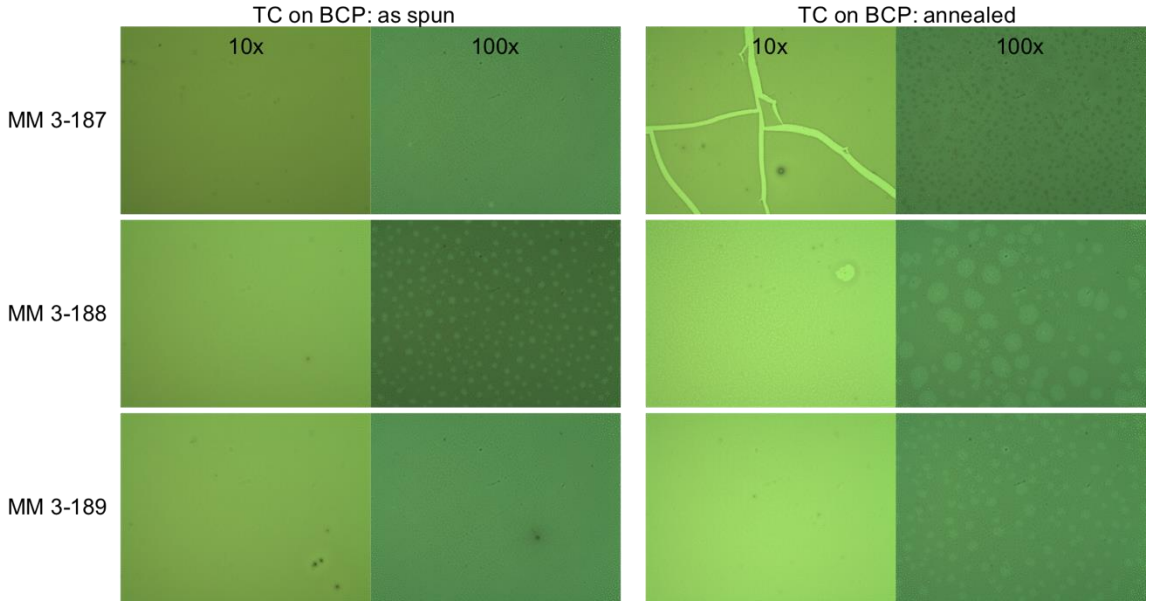

Figure 3.24 Thin film studies of the TCs detailed in Table 3.3. Films were annealed at 165 °C for 5 mins in air. 10x micrographs are 1.2 mm x 1.6 mm and 100x micrographs are 120 μm x 160 μm.

One possible physical explanation for the apparent MA content dependency is that different concentrations of MA led to very different thermal expansion coefficients (TEC), and drastically mismatched TECs between the BCP and TC would lead to cracking.[12,13] Reika Katsumata performed ellipsometric experiments to determine the TEC for PDSS-PEGL, MM3-189 (the "good" TC), and MM3-187 (a TC that cracked) for temperatures between 100 °C and 190 °C. In this temperature range, PDSS-PEGL is above its T_g while both TCs are below their T_gs, which explains the order of magnitude difference in TEC

between the BCP and the TCs shown in **Figure 3.25**. The two TCs had identical TECs to within the tolerances of the measurement, which means that physical stress on the thin films was not the cause for the cracks.

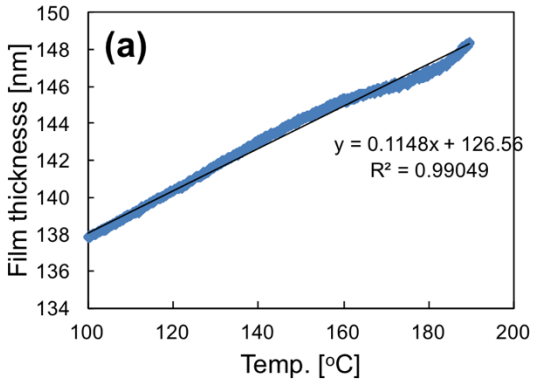

BCP: 0.1148 nm/°C

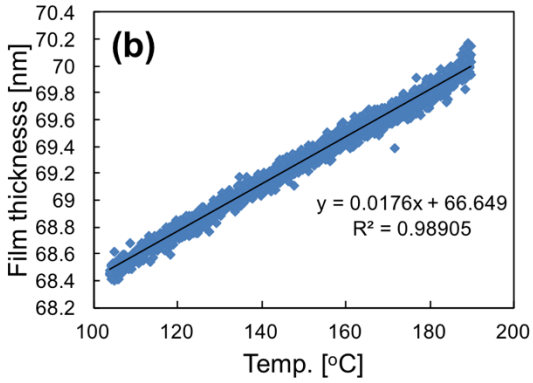

MM3-189: 0.0176 nm/°C

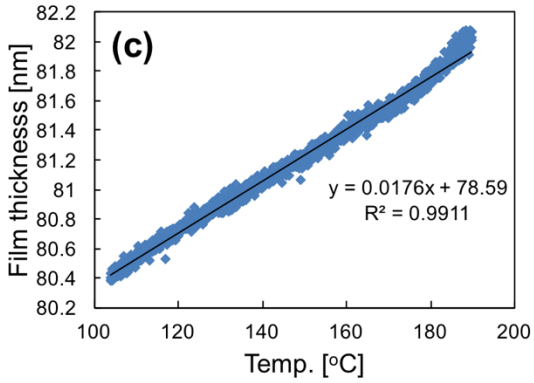

MM3-187: 0.0176 nm/°C

Figure 3.25 Thermal expansion coefficients of **(a)** $PDSS_{4.8}$-$PEGL_{8.9}$ **(b)** MM3-189 (21% MA, 31% cyclohexyl maleimide, 48% *t*-butyl styrene) and **(c)** MM3-187 (40% MA, 10% cyclohexyl maleimide, 50% *t*-butyl styrene) as measured by ellipsometry. While the two TCs have identical thermal expansion coefficients, MM3-189 did not crack, while MM3-187 did.

To test the hypothesis that the MA content was the main contributor to cracking, another series with varying MA content was tested. The TCs detailed in **Table 3.4** contain styrene instead of *t*-butyl styrene, and the balance is methyl maleimide instead of cyclohexyl maleimide. When this series of TCs were tested, every sample cracked, including those with MA content comparable to MM3-189, as shown in **Figure 3.26**. This result may be due to many factors: 1. The alternative maleimide species may be the deciding factor, 2. Styrene versus *t*-butyl styrene may be critical, or 3. A combination thereof. While none of these are satisfactory explanations, the lack of other TC series with varied MA content makes it difficult to verify or disprove any of the hypotheses.

TC	MA	Methyl maleimide	Styrene
MM 3-257	0.23	0.32	0.46
MM 3-267	0.25	0.29	0.46
MM 3-268	0.3	0.23	0.47
MM 3-269	0.35	0.19	0.47
MM 3-270	0.38	0.14	0.48

Table 3.4. Series of TC with varying ratios of maleic anhydride and methyl maleimide copolymerized with styrene.

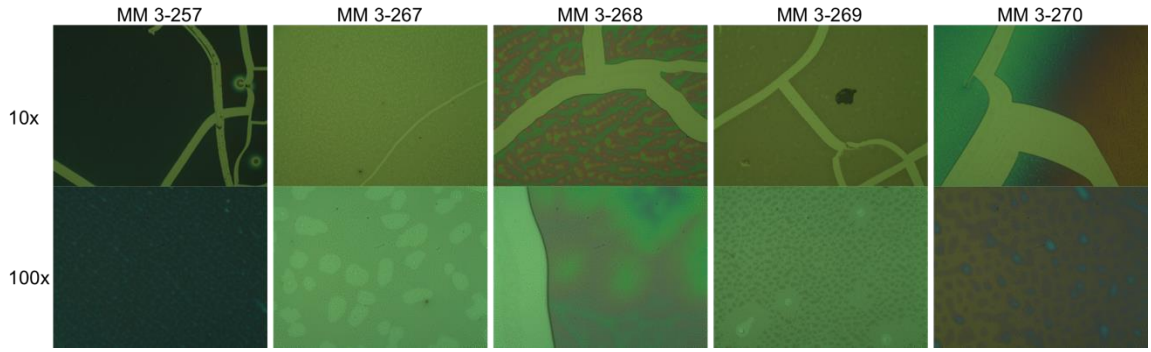

Figure 3.26 Thin film studies of the TCs detailed in Table 3.4. Films were annealed at 165 °C for 5 min in air.10x micrographs are 1.2 mm x 1.6 mm, and 100x micrographs are 120 μm x 160 μm.

Finally, I turned to the synthesis procedures used at the University of Minnesota to see whether any of the reagents used could be left in the BCP and cause the cracking. By comparing and contrasting the synthesis procedures for PEGL homopolymer and PDSS-PEGL, I found that two reagents were used in the BCP synthesis that were not used in the homopolymer synthesis, benzoic acid and 1,8-diazabicycloundec-7-ene (DBU). Due to the observed cracking with the BCP and the lack thereof with the homopolymer, I focused on the effect of these two small molecules on TC cracking.

I started by testing the effect of benzoic acid on TC behavior. First, I added in one drop of benzoic acid to about 1 mL of 1 wt% PDSS-PEGL solution and sonicated for 30 minutes to ensure even dispersion. Then, the BCP and TC were spin coated onto a silicon wafer according to standard procedure and annealed at 165 °C for 5 minutes. As shown in **Figure 3.27**, benzoic acid did not affect the behavior of the BCP. The BCP formed holes without TC on top, cracked with MM3-187 on top, and formed holes with MM3-189 on top. Therefore, I concluded that benzoic acid was not the cause of the cracking.

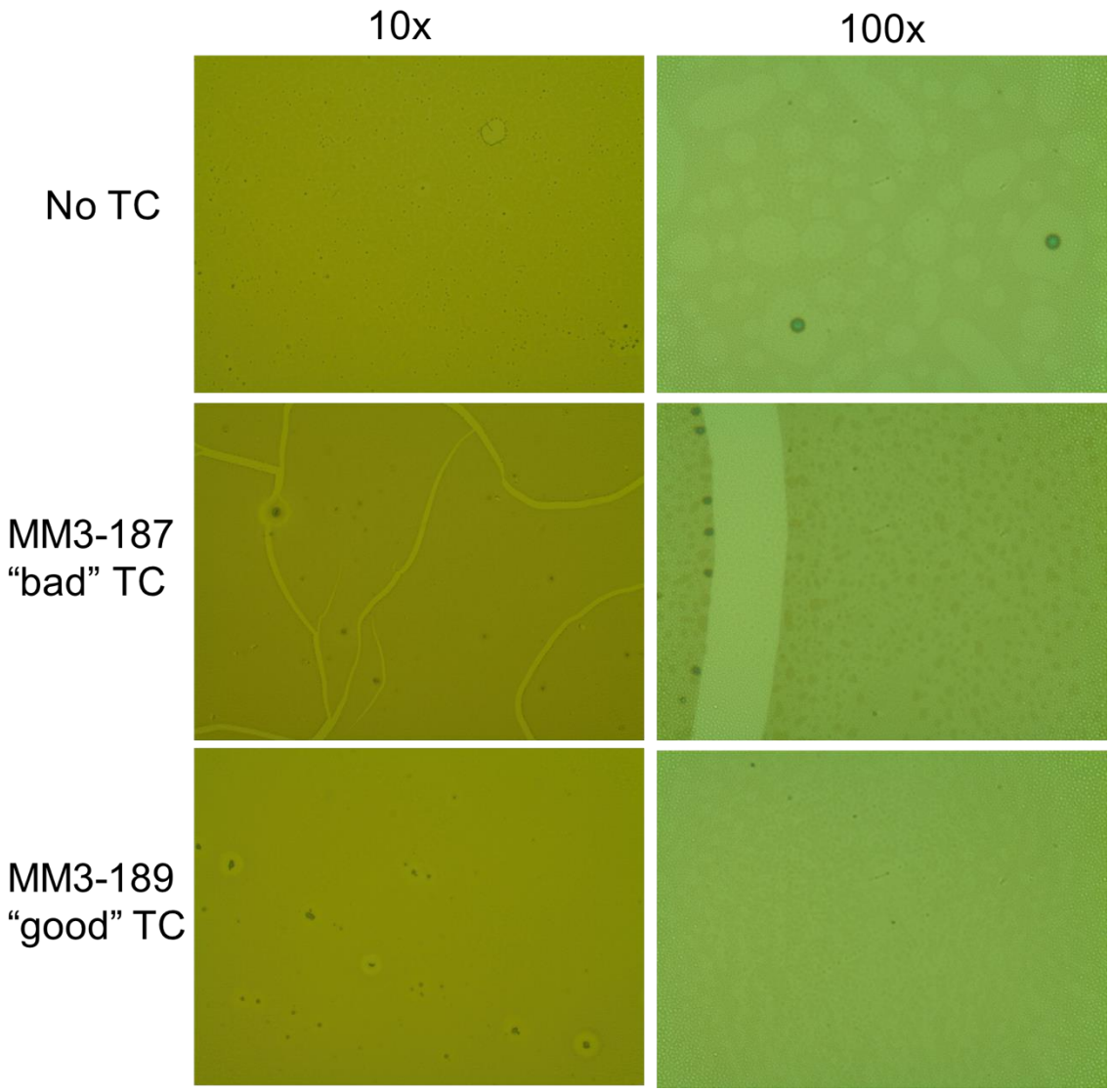

Figure 3.27. Optical micrographs of the effect of benzoic acid doped in BCP on TC thin films after annealing at 165 °C for 5 min in air. 10x micrographs are 1.2 mm x 1.6 mm and 100x micrographs are 120 μm x 160 μm. All thin film micrographs have benzoic acid doped into the starting materials.

Next, I conducted the same experiment with DBU. Following the same procedure, I mixed one drop of DBU into about 1 mL of 1 wt% BCP solution and spin coated on silicon wafer. As shown in the images of the annealed films in **Figure 3.28**, the effect was

dramatic. The DBU had a deleterious effect on the BCP film even without TC, but no cracks were formed. When a TC was added on top, the cracking behavior was dramatic. Most importantly, the “good” TC, MM3-189, which had not cracked with CB3-33 or with benzoic acid doped in, cracked when DBU was doped into the BCP solution. This result suggests that residual amounts of DBU left in the BCP after synthesis interacted with the TC in some manner, perhaps reacting with the MA. As evidenced by the lack of cracking in MM3-189 (the “good” TC) with the normal BCP solution, the trace amounts of DBU in the BCP seem to be compatible with smaller concentrations of MA in the TC.

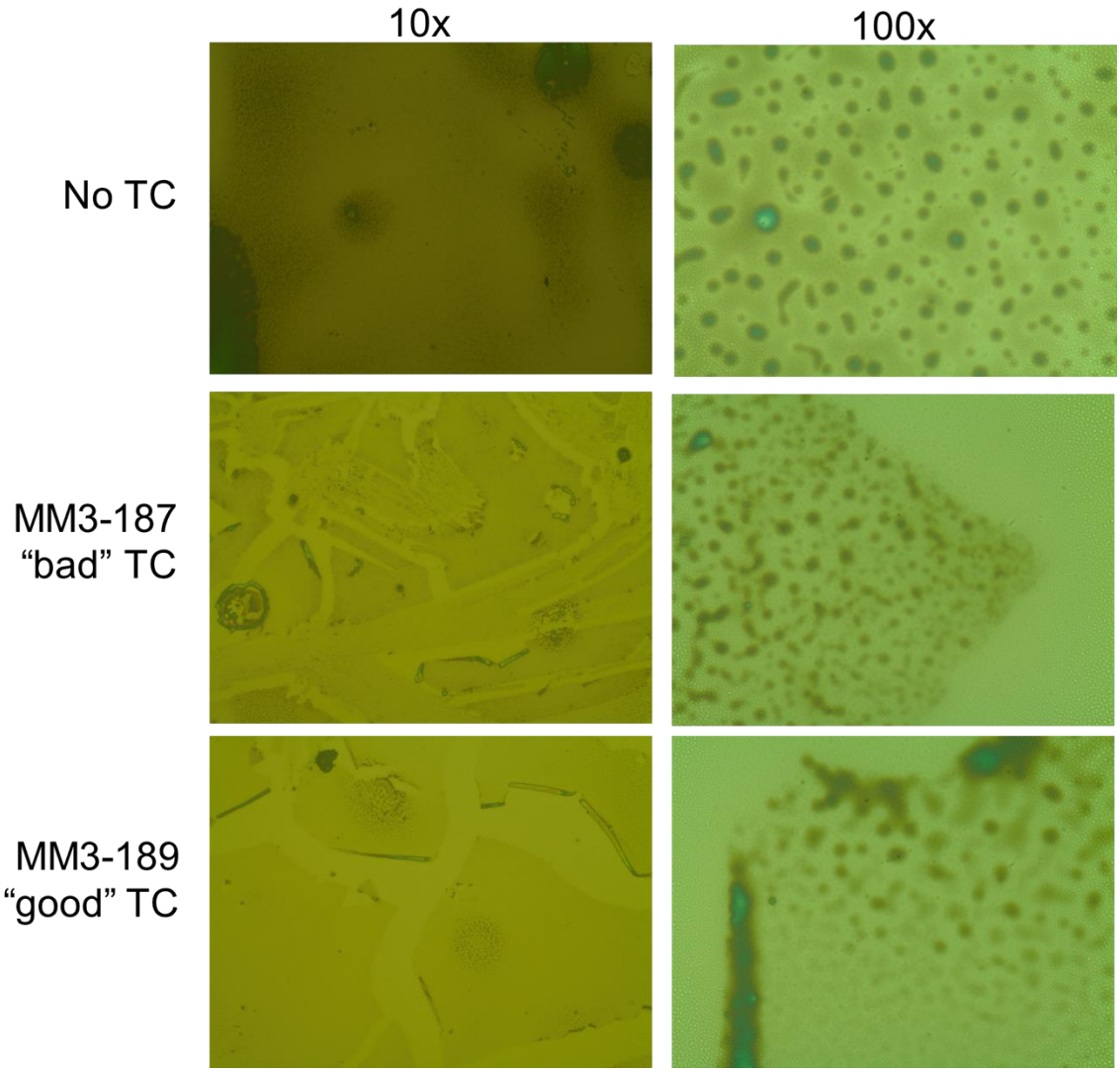

Figure 3.28 Optical micrographs of the effect of DBU doped in BCP on TC thin film behavior after annealing at 165 °C for 5 min in air. 10x micrographs are 1.2 mm x 1.6 mm and 100x micrographs are 120 μm x 160 μm.

I then ran the control of adding DBU to the TC solution. For the micrographs shown in **Figure 3.29**, the DBU-doped TCs were spin coated directly onto a silicon wafer with no BCP. As shown, none of the samples cracked. This suggests that the presence of DBU is causing a strange interaction between the BCP and TC.

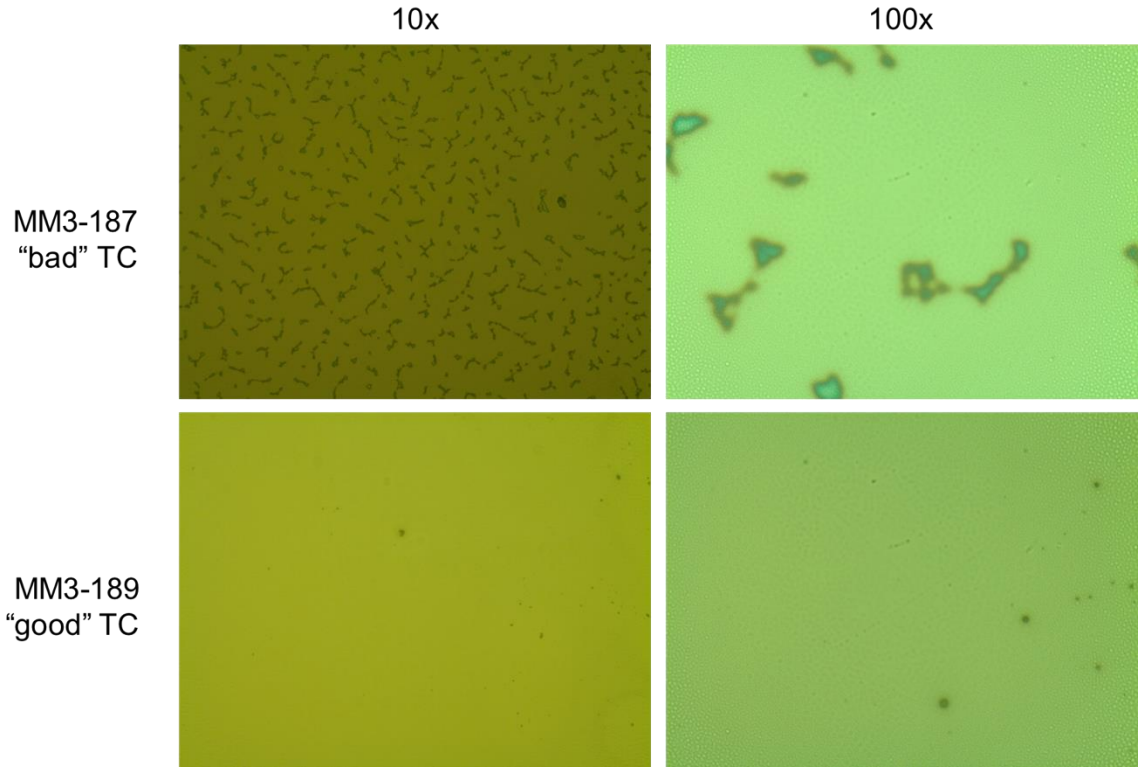

Figure 3.29 DBU doped in the TC solutions with no BCP present. The films were annealed at 165 °C for 5 min in air, then imaged. 10x micrographs are 1.2 mm x 1.6 mm and 100x micrographs are 120 μm x 160 μm.

Finally, I wanted to test the theory that the DBU is disrupting the interaction between the BCP and TC on some other BCP systems. PTMSS-PLA and poly(methoxystyrene-*b*-trimethylsilyl styrene) (PMOST-PTMSS) were tested in the same manner; one drop of DBU was added to approximately 1 mL of BCP solution. As shown in **Figure 3.30** for PTMSS-PLA and **Figure 3.31** for PMOST-PTMSS, the film cracked in all cases where BCP, DBU, and TC were present. When one or more of the three were missing, the film did not crack.

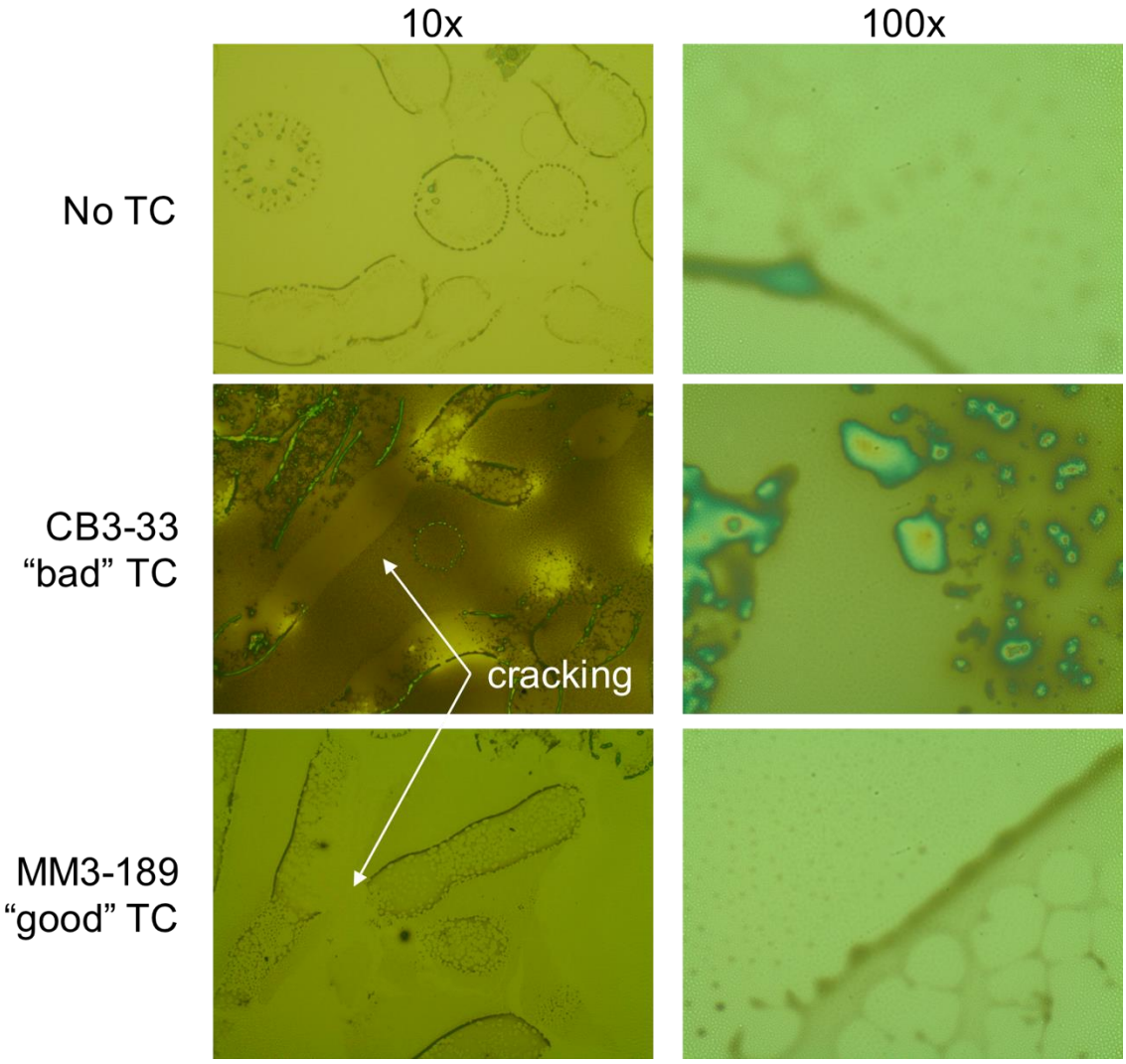

Figure 3.30 Annealed films of PTMSS-PLA with DBU doped in. 10x micrographs are 1.2 mm x 1.6 mm and 100x micrographs are 120 μm x 160 μm.

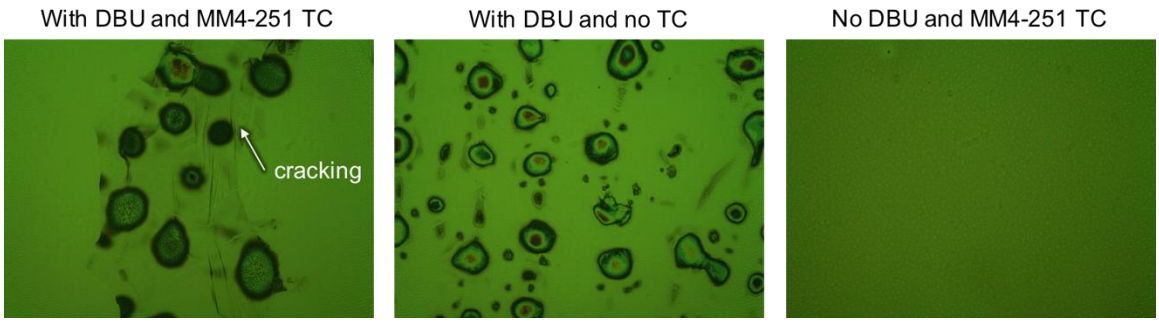

Figure 3.31 Annealed films of PMOST-PTMSS with DBU doped in. MM4-251 (50% MA, 34% di-*t*-BuSty, 16% Sty) was previously determined to be a neutral TC for this BCP. 10x micrographs are 1.2 mm x 1.6 mm and 100x micrographs are 120 μm x 160 μm.

3.4 CONCLUSIONS

PDSS-PEGL was investigated as an alternative BCP which possessed all the advantages of PTMSS-PLA without the issues of the lactide block. However, through the course of the thin film investigation, severe issues arose in the compatibility between the BCP and TC. After exhaustive tests, the cause of the problem was determined to be trace amounts of DBU remaining from synthesis interacting with the maleic anhydride in the TC. Because of the small amount of BCP left (about 100 mg for each sample) and the limited number of TCs containing less than 50% MA, further tests to verify this hypothesis are not possible.

Several options exist to ascertain that the DBU is causing the problem. The best control test would be altering the PEGL block synthesis procedure to not include DBU at all. If PDSS-PEGL synthesized in this manner does not crack with TC, then DBU is certainly the cause of the cracking. Next, if a greater amount of the BCP were available now, columns could be run to remove the trace amount of DBU from the BCP.

With the current BCP, it might still be possible to perpendicularly orient the BCP by synthesizing a new series of TCs. In this chapter, I have shown that MM3-189 (48 mol%

t-butyl styrene, 21% MA, 31% cyclohexyl maleimide) does not crack when annealed on top of the BCP stack. In addition, normal I/H features can be observed through that TC. Therefore, if the MA and cyclohexyl maleimide concentrations are kept constant and the surface energy is tuned by varying the ratio of styrene to *t*-butyl styrene as is standard for many other series of TCs, a neutral TC might be identified even with the trace amounts of DBU in the BCP. The neutral TC can then be combined with the already-identified neutral SNTs to perpendicularly align PDSS-PEGL.

In the next chapter, I step away from the silicon-and-lactide systems described in these two chapters to focus on a different strategy of obtaining smaller features with a more straightforward annealing procedure. I chose to decrease the accessible feature size of a very well-studied BCP, PS-PMMA, by adding in a self-interacting vinyl naphthalene moiety to produce poly((styrene-*random*-vinylnaphthalene)-*block*-methyl methacrylate), which can be perpendicularly oriented with simple thermal annealing without a TC.

6.5 References

(1) Zhang, J.; Clark, M. B.; Wu, C.; Li, M.; Trefonas, P.; Hustad, P. D. Orientation Control in Thin Films of a High-χ Block Copolymer with a Surface Active Embedded Neutral Layer. *Nano Lett.* **2016**, *16* (1), 728–735.

(2) Cushen, J. D. High Interaction Parameter Block Copolymers for Advanced Lithography, University of Texas at Austin, 2013.

(3) Durand, W. J.; Blachut, G.; Maher, M. J.; Sirard, S.; Tein, S.; Carlson, M. C.; Asano, Y.; Zhou, S. X.; Lane, A. P.; Bates, C. M.; Ellison, C. J.; Willson, C. G. Design of High-χ Block Copolymers for Lithography. *J. Polym. Sci. Part A Polym. Chem.* **2015**, *53* (2), 344–352.

(4) Mansky, P. Controlling Polymer-Surface Interactions with Random Copolymer Brushes. *Science (80-.).* **1997**, *275* (5305), 1458–1460.

(5) Han, E.; Stuen, K. O.; La, Y. H.; Nealey, P. F.; Gopalan, P. Effect of Composition of Substrate-Modifying Random Copolymers on the Orientation of Symmetric and Asymmetric Diblock Copolymer Domains. *Macromolecules* **2008**, *41* (23), 9090–9097.

(6) Bates, C. M.; Seshimo, T.; Maher, M. J.; Durand, W. J.; Cushen, J. D.; Dean, L. M.; Blachut, G.; Ellison, C. J.; Willson, C. G. Polarity-Switching Top Coats Enable Orientation of Sub-10-Nm Block Copolymer Domains. *Science (80-.).* **2012**, *338* (6108), 775–779.

(7) Maher, M. J.; Bates, C. M.; Blachut, G.; Sirard, S.; Self, J. L.; Carlson, M. C.; Dean, L. M.; Cushen, J. D.; Durand, W. J.; Hayes, C. O.; Ellison, C. J.; Willson, C. G. Interfacial Design for Block Copolymer Thin Films. *Chem. Mater.* **2014**, *26* (3), 1471–1479.

(8) Durand, W. J. Design, Synthesis, and Engineering of Advanced Materials for Block Copolymer Lithography, 2015.

(9) Huang, E.; Pruzinsky, S.; Russell, T. P.; Mays, J.; Hawker, C. J. Neutrality Conditions for Block Copolymer Systems on Random Copolymer Brush Surfaces. *Macromolecules* **1999**, *32* (16), 5299–5303.

(10) Koneripalli, N.; Singh, N.; Levicky, R.; Bates, F. S.; Gallagher, P. D.; Satija, S. K. Confined Block Copolymer Thin Films. *Macromolecules* **1995**, *28*, 2897–2904.

(11) Rafiee, J.; Mi, X.; Gullapalli, H.; Thomas, A. V.; Yavari, F.; Shi, Y.; Ajayan, P. M.; Koratkar, N. a. Wetting Transparency of Graphene. *Nat. Mater.* **2012**, *11* (3), 217–222.

(12) Ma, S. J.; Mannino, S. J.; Wagner, N. J.; Kloxin, C. J. Photodirected Formation and Control of Wrinkles on a Thiol − Ene Elastomer. *ACS Macro Lett.* **2013**, *2*, 474–477.

(13) Stafford, C. M.; Harrison, C.; Beers, K. L.; Karim, A.; Amis, E. J.; VanLandingham, M. R.; Kim, H. C.; Volksen, W.; Miller, R. D.; Simonyi, E. E. A Buckling-Based Metrology for Measuring the Elastic Moduli of Polymeric Thin Films. *Nat. Mater.* **2004**, *3* (8), 545–550.

Chapter 4: Using Intrablock Interactions to Increase χ of Poly(styrene-*block*-methyl methacrylate) (PS-PMMA)

4.1 Introduction

Poly(styrene-*block*-methyl methacrylate) (PS-PMMA) is the most widely-studied candidate material for block copolymer (BCP) lithography,[1–3] and it is produced commercially at pilot-scale.[4] Use of PS-PMMA is advantageous because the substrate is readily neutralized with crosslinked mats or grafted polymers,[5,6] and the similarity in surface energy between the two blocks of PS-PMMA at elevated temperature permits the microdomains to be oriented perpendicular to the substrate via simple one-step hot-plate annealing.[7–9] This thin-film morphology is practically desirable for the subsequent etch step, and the processing is fully compatible with existing nanofabrication tools.[10,11]

Unfortunately, the smallest lithographically-useful features using PS-PMMA are about 11 nm wide due to thermodynamically-driven mixing between the two blocks for smaller features and shorter BCP chains,[1] and this size scale is still too large to shift the paradigm from photolithography to BCP lithography. Polymer chemists are designing new BCP lithography candidate materials that are capable of self-assembling into ever-smaller features (5-10 nm) such that BCP lithography, if implemented, will be viable for several miniaturization cycles.[12–15] These materials are colloquially referred to as "high- χ" BCPs because the Flory-Huggins interaction parameter, χ, has been increased relative to PS-PMMA. In a tradeoff demonstrated in **Equation 4.1**,[16] increasing χ allows for symmetric, diblock BCPs with lower molecular weight and smaller degree of polymerization N, to microphase separate, resulting in a smaller periodic width, d.

$$d = a\,\chi^{1/6}N^{2/3}$$ **Equation 4.1**

In this report, "feature size" will refer to the width of one lamella (one light *or* dark stripe in a top-down scanning electron microscope (SEM) image), and "domain size," d, will refer to one full periodic width (one light *and* one dark stripe). Thus, feature size is one half of the domain size.

An established route to creating high- χ BCPs is to choose blocks with increased chemical dissimilarity.[17,18] However, high- χ BCPs capable of self-assembling into features smaller than 10 nm often possess highly disparate surface energies between blocks, which preclude perpendicular orientation at the top surface via thermal self-assembly. Solvent annealing[19] and surface-energy-modifying top coats[20–22] have been shown to enable perpendicular orientation in these materials. But an alternate strategy is to design a material which has higher χ than PS-PMMA but still possesses similar surface energy between blocks such that perpendicular orientation can be obtained by thermal annealing alone. Two key examples of BCPs achieving these ends are the partially epoxidized poly(styrene-*block*-isoprene) system described by Kim et al.[23] and the addition of the ionic liquid, 1-ethyl-3-methylimidalzolium bis(trifluoromethanelsufonyl)amide (emim NTf_2), to PS-PMMA demonstrated by Bennett et al.[24] Hydrogen bonding interactions have been exploited by adding in a second BCP[25–27] or homopolymer,[28,29] and solvents have been used as small molecule additives to increase the effective χ.[30]

It is important to note that χ was defined by Flory to represent the energetic penalty for removing one repeat unit from a lattice of its peers and placing it in a new lattice where it is surrounded by different chemical constituents.[31] Therefore, increasing attractive self-interactions within blocks may be an equally viable strategy for increasing χ as compared to the more common approach of increasing chemical dissimilarity between blocks. To this end, we describe the synthesis and characterization of a new high- χ BCP in this material

class, poly((styrene-*random*-vinylnaphthalene)-*block*-methyl methacrylate) (PSVN-PMMA). By including a vinylnaphthalene (VN) comonomer into the PS block, which possesses increased self-interactions,[32] we demonstrate a two-fold improvement in χ in the absence of deleterious changes to block surface energy.

4.2 EXPERIMENTAL

4.2.1 Materials synthesis

All reagents were used as received unless otherwise noted. HPLC-grade tetrahydrofuran (THF) (J.T. Baker) for anionic polymerization was purified by passing through a Pure Solv MD-2 solvent purification system containing two activated alumina columns. 2-Vinylnaphthalene (VN) (Acros Organics) was purified by subliming twice under reduced pressure. Styrene (Sigma-Aldrich) was distilled twice over di-*n*-butylmagnesium. Methyl methacrylate (MMA) (Sigma-Aldrich) was distilled once over calcium hydride then distilled once over trioctylaluminum. Lithium chloride (LiCl) was stored in a vacuum oven kept at 170 °C and under 100 mTorr until ready to use. Diphenylethylene (DPE) was distilled twice over *n*-butyllithium using a cow-type distillation receiver with an insulated vigreux distillation head and stored in a drybox freezer.

PSVN-PMMA was synthesized by sequential addition of monomers in anionic polymerization. The reactor vessel was flame dried five times, and then an appropriate amount of dry LiCl from the vacuum oven was added. Purified THF was added to the reactor vessel and allowed to stir for 30 minutes at room temperature to facilitate the dissolution of LiCl. The reactor was then cooled to -78 °C, and the appropriate amount of *sec*-butyllithium was added to initiate the reaction. The SVN block was synthesized by first adding the required amount of liquid styrene monomer to solid vinylnaphthalene monomer

in the drybox and swirling the flask until the vinylnaphthalene completely dissolved in the styrene. The styrene-vinylnaphthalene monomer mix was then added to the reactor dropwise using an airtight glass syringe, resulting in a dark green solution that was stirred for 1 hour. DPE was then added in fivefold molar excess to the initiator, and the dark red solution was stirred for 1.5 hours before an aliquot was taken. A small amount of MMA was added to the reactor, and after the dark red solution turned completely clear, the rest of the MMA was added dropwise. The reaction was left to proceed for two hours after all MMA was added, and degassed methanol was used to terminate the reaction.

Some planning was required for PSVN-PMMA synthesis. First, VN monomer must be used as soon as possible after purification. Typically, VN monomer was purified on the first day of the reaction and stored in an aluminum foil-covered distillation flask in the dry box freezer (-20 °C) overnight. The monomer flask was only taken out of the freezer when it was ready to be used. Storage for more than one night compromised some polymerization reactions; the reaction solution would lose color about an hour after S/VN momoner introduction. Next, the *sec*-butyllithium should not be more than a few months old; older bottles of initiator have also led to anions "dying." Next, the reaction temperature should be below -65 °C at all times. From personal experience, while PS-PMMA and other polymers made with anionic polymerization can withstand temperatures of up to -50 °C, PSVN-PMMA is liable to terminate if the temperature gets too high during the polymerization. Thus, each monomer must be added slowly. Finally, DPE stored in the dry box freezer can be used for up to a few months after purification as long as it freezes into a solid. If the DPE is liquid in the freezer, then it should be distilled again.

The polymer was isolated by precipitating in methanol and then it was dried on a Schlenk line until baseline was achieved. On the occasions where a small fraction of the PSVN living block was terminated when drawing an aliquot, the BCP was selectively

precipitated in hot (50 °C) cyclohexane to remove the soluble PSVN fraction (see **Figure 4.1**).

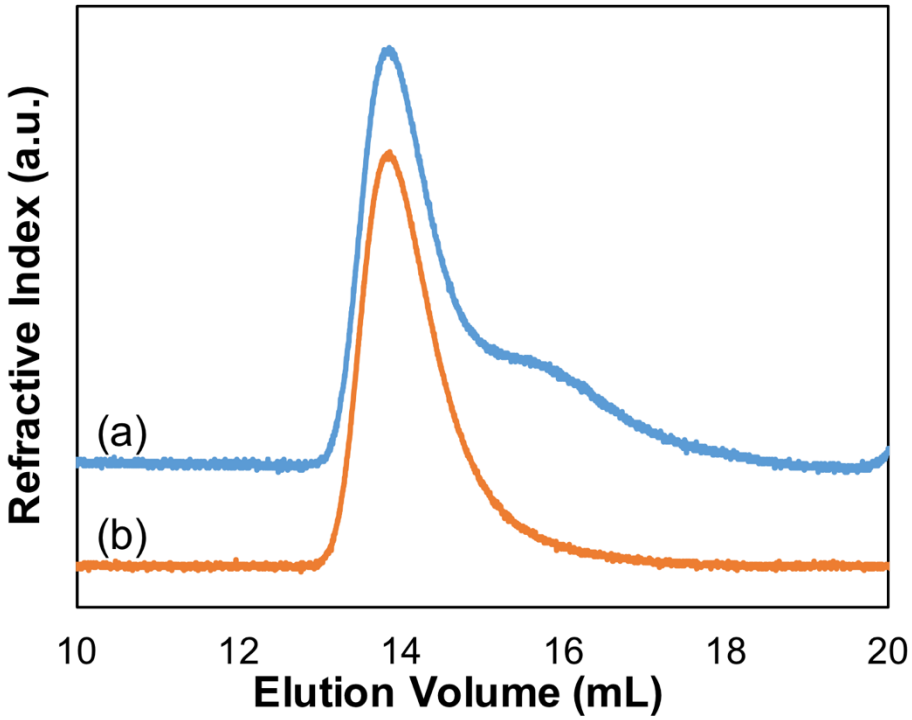

Figure 4.1 $P(S_{85}VN_{15})_{21.7}$-$PMMA_{28.0}$ (a) before and (b) after washing with hot (50 °C) cyclohexane to remove the soluble PSVN fraction.

Di-*n*-butylmagnesium, *n*-butyllithium, and *sec*-butyllithium are pyrophoric materials, and extreme caution should be taken when working with these materials. Flame retardant personal protective equipment should be worn at all times while handling these materials. These materials should be transferred using airtight glass syringes in a drybox or under an inert gas environment.

4.2.2 Material characterization

Size exclusion chromatography (SEC) measurements were taken on a Viscotek GPC Max VE 2001 size exclusion chromatograph equipped with a Viscotek Model 270

dual detector of viscometer/light scattering detector, a Viscotek VE 3580 refractive index detector, and two I-Series mixed bed low MW columns. THF was used as the eluent, and samples were run with a flow rate of 1.0 mL min^{-1}. Samples were prepared by dissolving the polymer in THF (2 mg mL^{-1}) beforehand. ^{1}H NMR spectra were recorded on a Varian Unity Plus 400 MHz and ^{13}C NMR spectra were recorded on a Varian DirectDrive 600 MHz with $CDCl_3$ as the solvent. Differential scanning calorimetry (DSC) experiments were performed on a Mettler Toledo DSC-1 under dynamic nitrogen at a heating rate of 10 °C min^{-1}. All reported data are from second heat after heating above all glass transition temperatures.

4.2.3 Substrate neutralization

Silicon wafers were purchased from NOVA Electronic Materials, LLC. Random copolymers of poly(styrene-*random*-methyl methacrylate-*random*-glycidyl methacrylate) were crosslinked on the Si wafers and acted as surface treatments to tune the surface energy of the underlying substrate; these layers are generally referred to as surface neutralization treatment or 'SNT' layers hereafter.[6] The ratio of styrene to MMA was empirically chosen such that neither block of PSVN-PMMA would preferentially wet the substrate, and 1 mol% glycidyl methacrylate was included to act as a crosslinking agent. All random copolymers will henceforth be referred to as GLxx, where xx represents the mole percent of styrene in the feed. GMA was used as received, and styrene, MMA, and toluene were purified by stirring over alumina and calcium hydride (0.1 g/mL each). The GL series was synthesized by conventional free radical polymerization (70 °C, toluene) with benzoyl peroxide as the initiator.[6] GL51 and GL57 were synthesized, and the number averaged molecular weights (M_n) relative to a polystyrene standard of GL51 and GL57 were 26.7 kDa (molecular weight dispersity, $Đ_M$ = 1.6, 71 mol% styrene) and 23.6 kDa ($Đ_M$ = 1.6, 77

mol% styrene), respectively. These random copolymers were precipitated in methanol and freeze dried prior to use. GL54 was made by dissolving equal masses of GL51 and GL57 together and freeze drying.

4.2.4 Thin film processing

Polymers were dissolved in toluene (1 wt%) and filtered with 200 nm Teflon filters (CHROMAFIL Xtra PTFE 20/25). Thin films were prepared by spin-coating the 1 wt% polymer solutions out of toluene for 40 s, and spin speeds were empirically chosen to produce films with about 1.2 L_0 film thickness. Thin film thicknesses were measured by a spectroscopic ellipsometer (J.A. Woollam M-2000D) with a fitting wavelength range of 400-1000 nm. Thin films were lightly etched in an oxygen plasma cleaner (HARRICK PDC-32G) for 45 sec with an oxygen partial pressure of 350 mTorr and power of 6.8 W applied to a radio frequency coil to enhance the imaging contrast between the two blocks.

4.2.5 Small angle X-ray scattering

Small-angle X-ray scattering (SAXS) measurements were conducted on a Molecular Metrology instrument equipped with a high brilliance rotating copper anode source using Cu Kα radiation (λ= 1.5418 Å) and a gas-filled two-dimensional 120 mm multiwire detector. Horizontal focus and wavelength selection were achieved using an asymmetric cut Si(111) monochromator, and vertical focus was achieved using a single-crystal germanium mirror. Silver behenate with a primary reflection peak at 1.076 nm^{-1} was used to calibrate the beam center.

SAXS data for calculating the χ parameter were generated by first annealing the BCP sample in an enclosed heating stage for 45 minutes, then immediately cooling in water for 1-2 sec then in liquid nitrogen for 1 min. The BCP sample was then loaded in the SAXS vacuum sample chamber. After waiting 1 h for the sample chamber to reach baseline

pressure, the SAXS data was collected. This procedure was repeated for all temperatures at which SAXS data was collected. This procedure is explained in more detail in Chapter 5.

4.2.6 Scanning electron microscopy (SEM)

A Zeiss Supra 40 VP SEM was used to capture top-down SEM micrographs using an in-lens detector with an accelerating voltage of 5 keV and a working distance of 5-10 mm.

4.3 Results and Discussion

4.3.1 Synthesis and characterization

PSVN-PMMA was synthesized by sequential addition of monomers in anionic polymerization, as illustrated in **Scheme 4.1**. A series of PSVN-PMMA with varied molecular weight and percent VN incorporation were synthesized. The volume fractions of the styrenic block and the MMA block were kept near 50% to ensure that all BCP's formed lamellar microstructures upon thermal self-assembly and to facilitate a direct comparison between different BCPs. **Table 4.1** summarizes the synthesized BCPs and provides relevant characterization information.

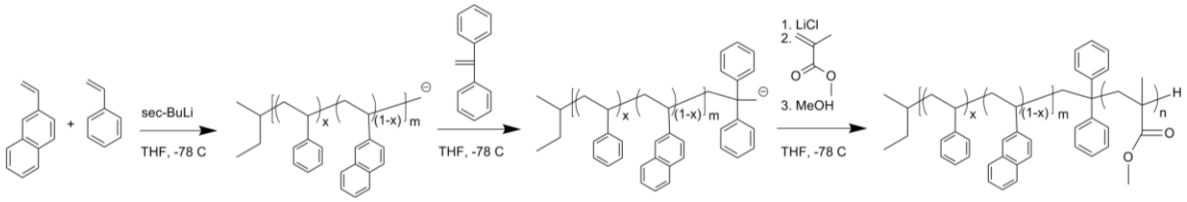

Scheme 4.1 Synthesis of PSVN-PMMA block copolymer by anionic polymerization.

Sample[a]	Mol% VN[b]	M_n (PSVN) (Da)	$Đ_M$ (PSVN)	M_n (BCP) (Da)	$Đ_M$ (BCP)	Vol% SVN[c]	d (nm)[d]
$P(S_{85}VN_{15})_{17.1}$-$PMMA_{19.1}$	15	17,100	1.08	36,200	1.02	50	20
$P(S_{85}VN_{15})_{21.7}$-$PMMA_{28.0}$	15	21,700	1.17	49,700	1.06	52	28
$P(S_{85}VN_{15})_{32.5}$-$PMMA_{54.2}$	15	32,500	1.11	86,700	1.07	45	40
$P(S_{80}VN_{20})_{15.1}$-$PMMA_{20.9}$	20	15,100	1.14	36,000	1.02	49	26
$P(S_{75}VN_{25})_{12.6}$-$PMMA_{18.3}$	25	12,600	1.04	30,900	1.09	44	26
$P(S_{75}VN_{25})_{13.7}$-$PMMA_{19.6}$	25	13,700	1.09	33,300	1.20	44	30
$P(S_{70}VN_{30})_{7.7}$-$PMMA_{7.7}$	30	7,700	1.25	15,400	1.32	53	28
$P(S_{70}VN_{30})_{11.0}$-$PMMA_{11.8}$	30	11,000	1.31	22,800	1.24	51	38
$P(S_{65}VN_{35})_{7.7}$-$PMMA_{9.7}$	35	7,700	1.37	17,400	1.26	51	34
$P(S_{83}VN_{17})$-$PMMA_{Dis}$	17	5,300	1.07	10,900	1.07	52	---
$P(S_{71}VN_{29})$-$PMMA_{Dis}$	29	5,400	1.12	11,700	1.13	49	---

Table 4.1 Characterization of all BCPs reported in this work.

a Sample names are written as $P(S_xVN_y)_n$-$PMMA_m$ where x and y are the mol % of styrene and VN in the styrenic block, respectively, and n and m are the M_n in kDa of the PSVN and PMMA blocks, respectively.

b Determined by quantitative ^{13}C NMR. Mol % VN refers to mol % VN in the PSVN block, not entire BCP.

c Densities used in this calculation were 1.13 g/mol for PVN, 1.05 g/mol for PS, and 1.18 g/mol for PMMA. Densities were measured using an AG204 Mettler Toledo Balance and Mettler Toledo Density Kit for XP/XS Precision Balances.[18] PSVN densities were calculated using a weighted average of the PS and PVN densities.

d Determined by SAXS.

The concentration of VN incorporated into the PSVN block was determined from quantitative ^{13}C NMR, and a representative spectrum and analysis are shown below (**Figure 4.2**). Absolute molecular weight was determined using SEC and NMR. First, SEC was used to determine dn/dc and, subsequently, molecular weight for each PSVN block, which was taken as an aliquot from the reactor vessel immediately before the addition of MMA monomer.[33] Using the molecular weight of the first block (PSVN), the total molecular weight and the volume fraction composition of the BCP (PSVN-PMMA) were calculated from ^{1}H NMR,[34] and a representative spectrum and calculation are shown below (**Figure 4.3**).

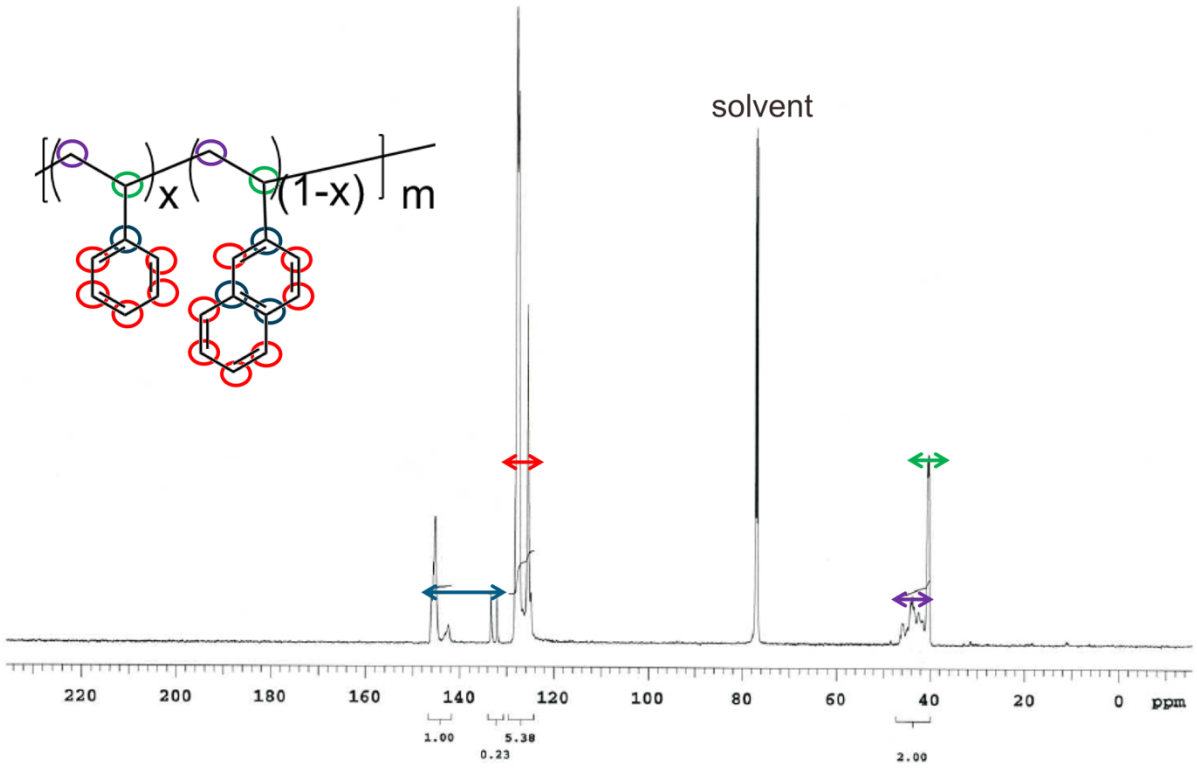

Figure 4.2 Quantitative ^{13}C NMR was used to determine the relative concentration of VN to styrene in the PVN block. A system of equations was set up using the peak assignments shown to solve for x.

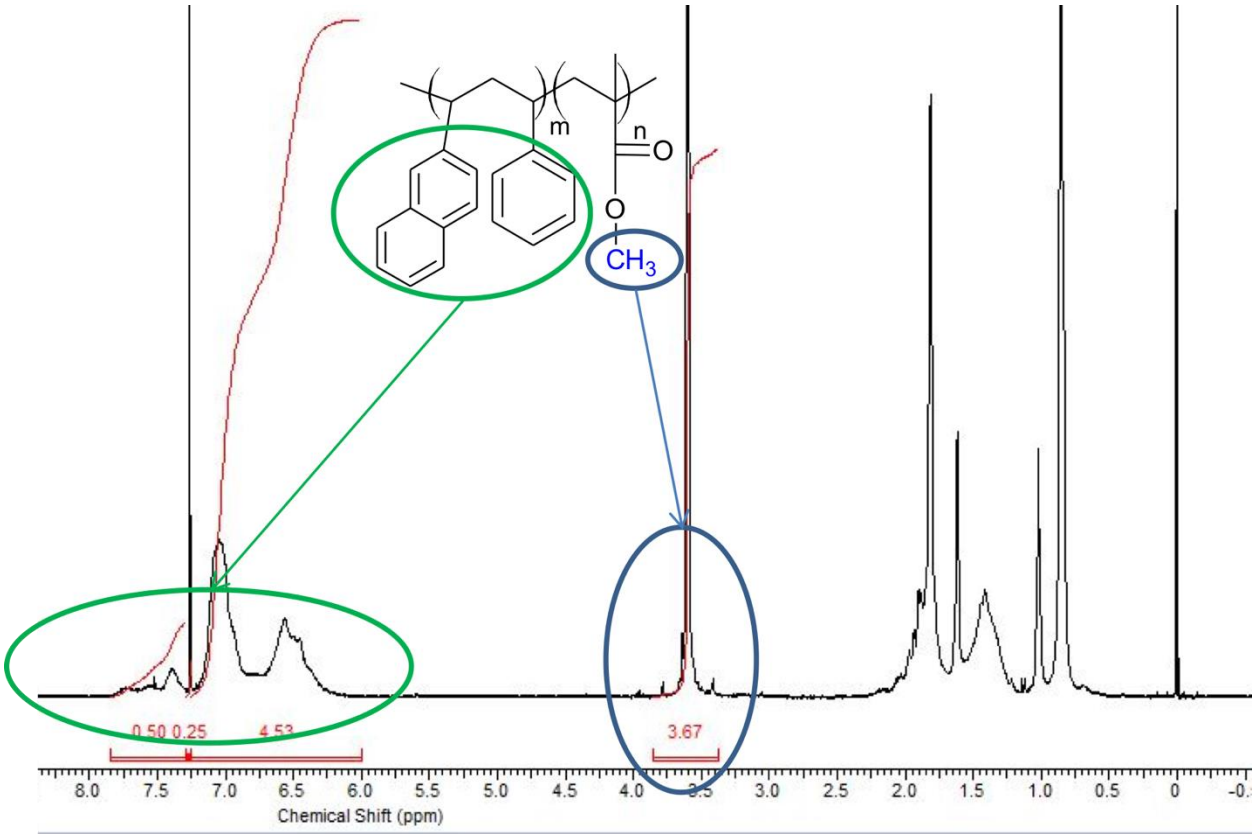

Figure 4.3 A representative ^{1}H NMR spectrum used to determine the volume fraction of each block of PSVN-PMMA. The integrated area of the downstream aromatic region was normalized by the average number of aromatic protons for each unit of the PSVN block (5x + 7y, where x and y are the fractional composition of styrene and VN in the block, respectively), and the region between 3.5-4.0 ppm (from the MMA block) was normalized by the number of methyl protons (3). The ratio between the two normalized integrations is the mole ratio, and this was used to determine the volume ratio.

The synthesis procedure was developed to ensure an even distribution of VN in the PSVN block, and the visual appearance of the reaction solution confirmed this as described in detail below. This precaution was taken to ensure that the results are a consequence of the chemical "modification" of the styrenic block, and not of other effects such as those that arise from gradient structure effects.[35,36] First, the VN was dissolved directly into the styrene monomer before addition to the reaction vessel. Second, the styrene-VN solution

was added to the reaction vessel dropwise in an effort to ensure that all available monomer had reacted before adding more. The reaction solution would slightly change color as each drop was added. When the drop was first added, the solution turned a deep, dark forest green, indicative of a VN anion. After a few seconds, the solution would take on a slight brown/orange tinge at the edges while remaining very dark in the middle, indicating that styrene, normally an orange anion under these conditions, replaced some VN units as the terminal anion. Waiting longer did not result in any further color change. Upon the addition of the next drop of styrene-VN solution, the solution turned dark green again. After all the monomer had been added, the reaction solution would continue to hold its dark color with brown/orange edges without change until the addition of diphenylethylene (dark red anion color). A previous study on the reactivity ratios of propagating styrene and VN anions in THF at room temperature showed that an alternating addition is favored.[37] Because the polymers synthesized in this study all contained more styrene units than VN units, each droplet of styrene-VN solution added would start off with alternating styrene and VN (dark green anion color) and end with a short run of styrene (orange anion color). This indicated that the VN was evenly distributed in the styrenic block. Representative photographs of the different anions described above are shown below in **Figure 4.4**.

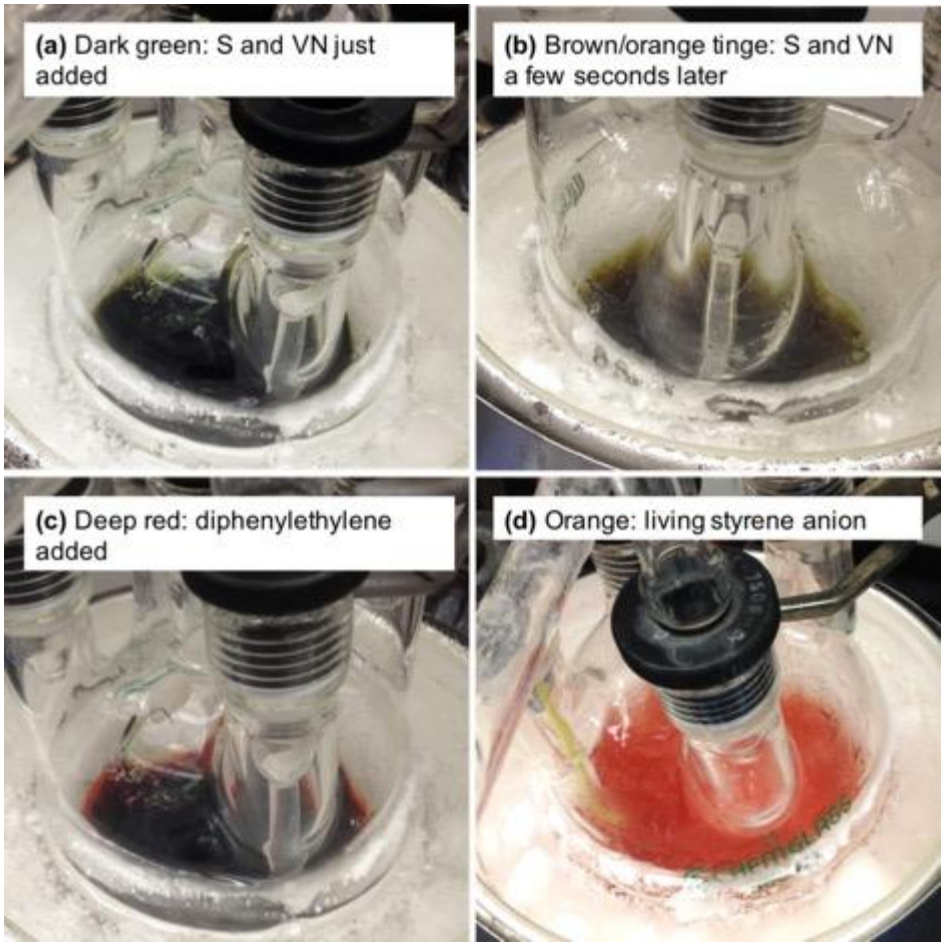

Figure 4.4 Reactor solution color changes throughout the polymerization process. **(a)** Immediately after adding a drop of styrene-VN monomer solution, the reactor solution turns a dark green. **(b)** After a few seconds, the VN monomers are all consumed, and the solution takes on a brown/orange tinge. The solution will stay this color until the next drop of styrene-VN monomer solution is added, at which point it will revert back to the color in (a). **(c)** DPE is added to the reactor after all the styrene-VN monomer had been added, and the reactor turns a deep red color. **(d)** For reference, the color of pure styrene is an orange color.

To further confirm the even distribution of VN in the styrenic block, the T_g's of polystyrene and several PSVN polymers (without the PMMA block) with various concentrations of VN were compared. As shown in **Figure 4.5,** the T_g of polystyrene is around 100 °C, while the T_g of polyvinylnaphthalene is expected at around 138 °C.[38] The

T_g's of the PSVN samples clearly increase progressively as more VN is added, and there is only one T_g for all PSVN samples. In addition, the breadth of the glass transition is similar for all samples. This suggests that there is little to no "blockiness" of styrene and vinylnaphthalene in the PSVN polymers, and that they are evenly distributed along the polymer chain.[39,40] One can note from **Table 4.1** that the molecular weight dispersity of the PSVN block increases up to 1.37 with 35% VN content, suggesting that synthetic control of anionically polymerized PVN is challenging. Indeed, our current methodology was not capable of directly synthesizing PVN-PMMA, and an alternate route is necessary to access that material. Nevertheless, an increase in molecular weight dispersity in one block does in no way preclude the ability of the resulting polymers to self-assemble into sharply defined, well-organized periodic structures.[41,42]

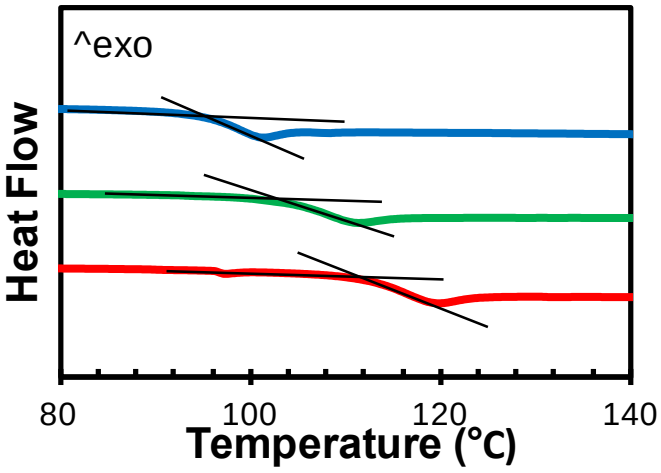

Figure 4.5 DSC scans of three PSVN samples containing various mol % of VN. As the concentration of VN increased, the glass transition temperature increased. The T_g (defined as the onset of the transition) was 95 °C for a sample with 0 mol % VN (i.e., PS only) (top blue curve), 105 °C for a sample with 15 mol % VN (middle green curve), and 113 °C for a sample with 30 mol % VN (bottom red curve).

Domain spacing for the BCP samples were determined using SAXS. The domain spacing, d, is defined by the primary scattering peak, q*, and is calculated by $d = 2\pi / q^*$. The presence of secondary scattering peaks, as shown in the SAXS patterns in **Figure 4.6**, indicates that all samples are ordered. Because the secondary scattering peaks for all samples are integer multiples of q* (2q*, 3q*, etc.), the morphology for all samples studied are lamellae.

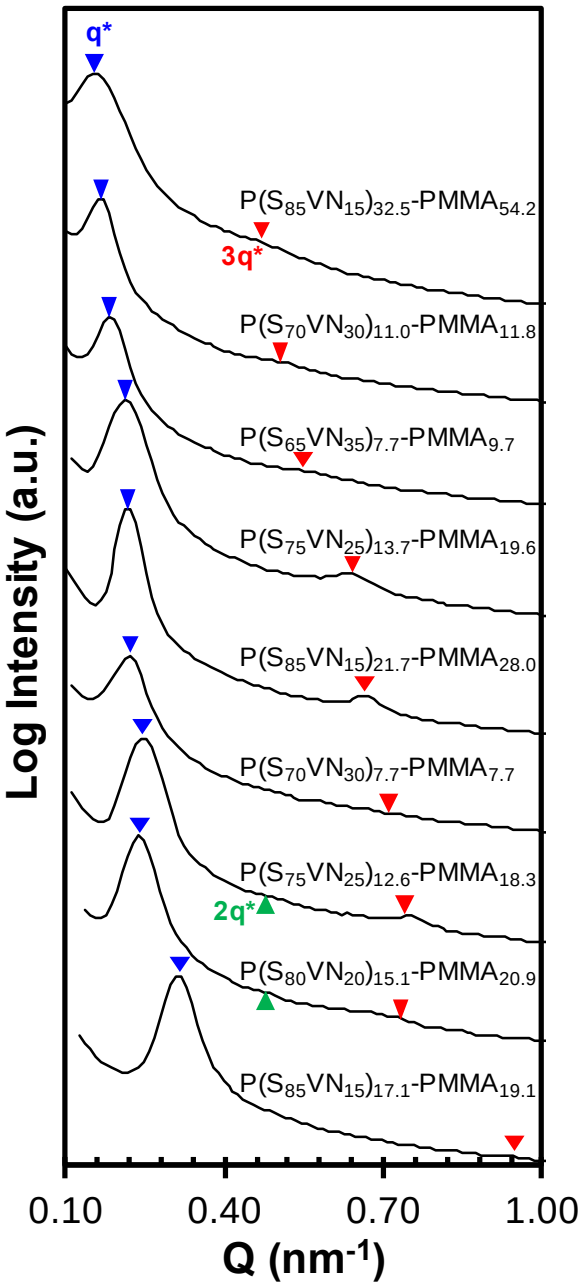

Figure 4.6 Small angle x-ray scattering (SAXS) profiles for all ordered BCPs. Even order scattering peaks are absent from all but two samples, indicating all but $P(S_{75}VN_{25})_{12.6}$-$PMMA_{18.3}$ and $P(S_{80}VN_{20})_{15.1}$-$PMMA_{20.9}$ are volumetrically symmetric.[43]

4.3.2 χ parameter

First, the effect of VN on the χ parameter was investigated. According to **Equation 4.1**, with knowledge of the molecular weight and the domain spacing of each sample, some preliminary conclusions can be drawn about the effect of VN incorporation on the χ parameter. In **Figure 4.7 (a)**, the ordered samples in **Table 4.1** are grouped based on their VN concentration, and their domain sizes are plotted as a function of molecular weight. The trend lines are curved because domain spacing scales as a function of the molecular weight to the 2/3 power. In this representation, the slope of each line is proportional to the χ parameter, and a steeper slope indicates a higher χ parameter.

Instead, if **Equation 1** is rearranged as:

$$\chi^{1/6} \propto \frac{d}{N^{2/3}} \qquad \textbf{Equation 4.2}$$

then $dN^{-2/3}$ can be plotted against concentration of VN, as shown in **Figure 4.7 (b)**.

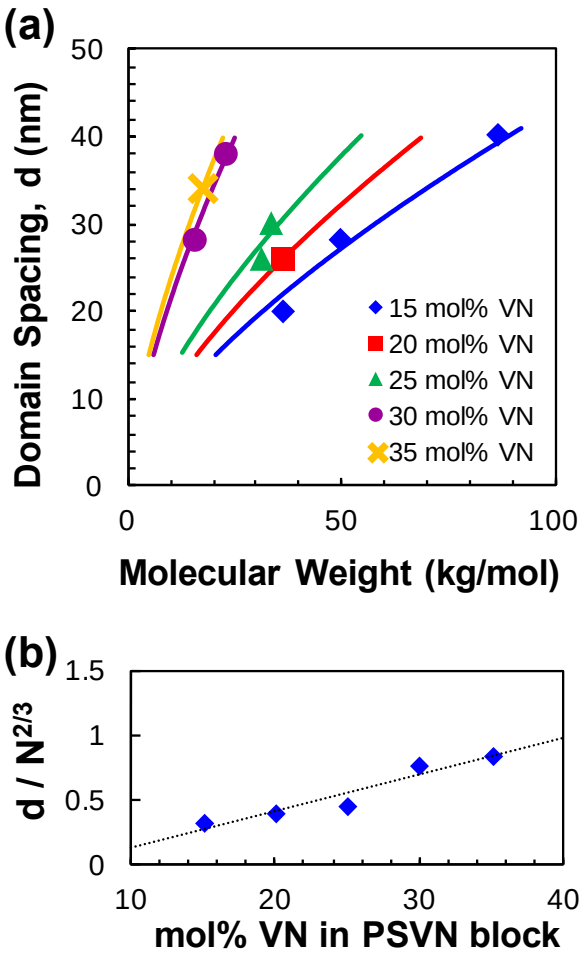

Figure 4.7 **(a)** Domain spacing 'd' of each BCP as a function of its molecular weight and VN incorporation. As VN incorporation increases, the domain spacing increases for polymers of a similar molecular weight, implying an increase in the χ parameter. The regression lines represent the scaling implied by Equation 1 with a constant χ parameter for each composition, $d \sim N^{2/3}$. **(b)** Rearranging Equation 1 gives a proportionality factor for the χ parameter, which is calculated from averaged values from (a). When plotted against VN incorporation, the increasing trend implies that the χ parameter increases as more VN is included.

To provide direct evidence that the χ parameter increases with increasing concentration of VN, two disordered samples (χ N < 10.5) with different concentrations of VN were synthesized and are summarized in the bottom two rows in **Table 4.1**. χ is a

temperature dependent parameter, and it can be described as the sum of an enthalpic (χ_H) and an entropic portions (χ_S), as shown in the following equation,[44] where A and B are empirical parameters:

$$\chi(T) = \chi_H + \chi_S = \frac{A}{T} + B \qquad \textbf{Equation 4.3}$$

Absolute intensity SAXS was used to determine χ for each sample. Scattering data was collected at several temperatures, and absolute intensity was calculated for each temperature using a pre-calibrated low density polyethylene standard for absolute intensity correction.[45] χ was an adjustable parameter in the fitting of the absolute intensity SAXS profile to Leibler's mean field theory, which was modified for dispersity and segmental volume asymmetry[46–49] (**Figure 4.8**).

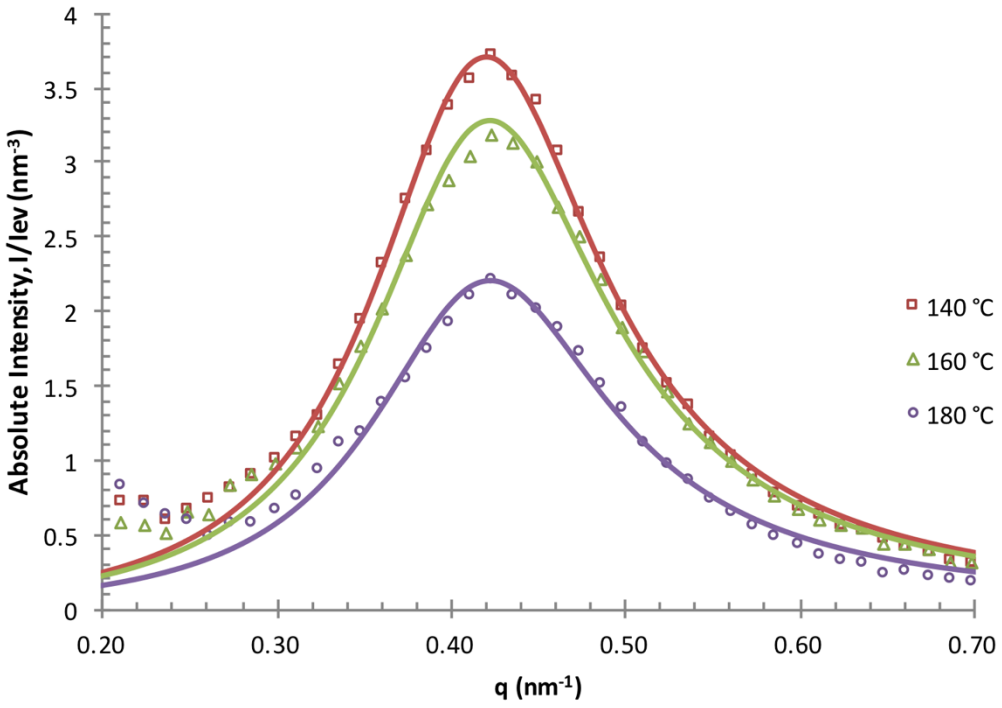

Figure 4.8 SAXS profiles for a representative sample, P($S_{83}VN_{17}$)-$PMMA_{Dis}$, near the first order peak. Scattering profiles were collected at several temperatures for the same sample, and best-fit lines were obtained by changing χ as one of the adjustable parameters using Leibler's mean-field theory.[18,46]

As shown in **Figure 4.9**, the χ parameter for all VN-containing polymers dramatically increased compared to that of PS-PMMA. **Table 4.2** summarizes the entropic and enthalpic contributions to χ for all disordered samples as well as for PS-PMMA.[18] By incorporating 29 mol% of VN in the styrenic block, the χ parameter was more than doubled as compared to PS-PMMA. The smallest domain spacing that can be achieved with P($S_{71}VN_{29}$)-PMMA is around 12.6 nm, with features sizes of about 6.3 nm. As stated previously, the smallest useable domain spacing that can be achieved with PS-PMMA is about 22 nm, with feature sizes around 11 nm. The χ parameter results also suggest that even smaller features are possible by incorporating more VN into the BCP.

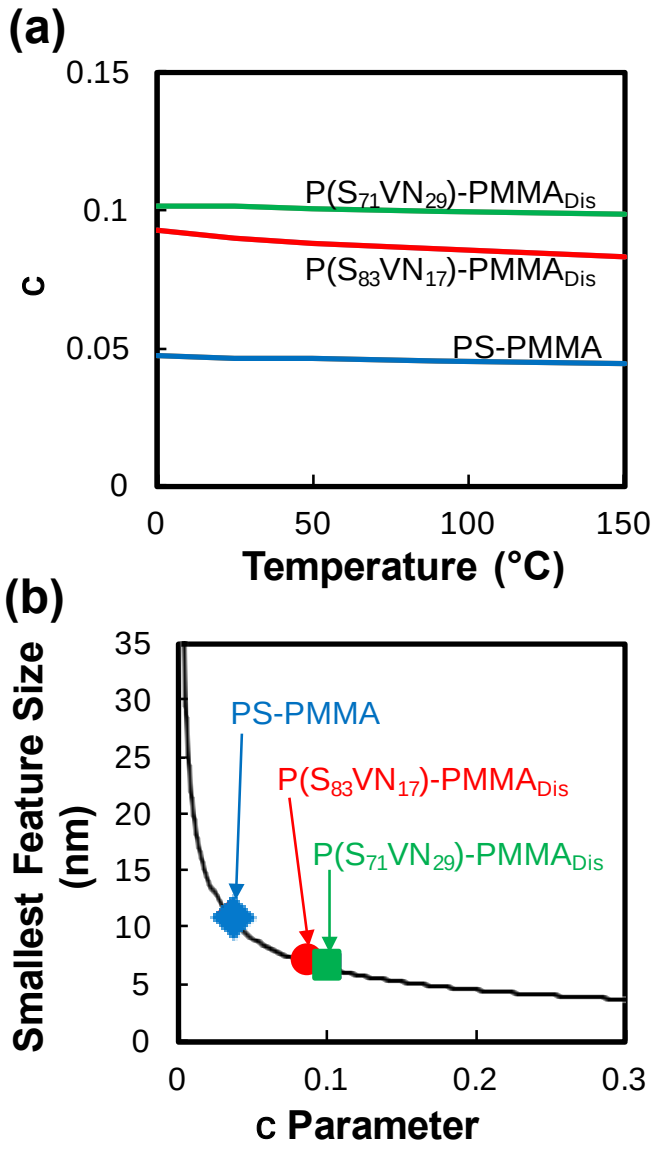

Figure 4.9 A comparison of the χ parameter of two VN-containing polymers to PS-PMMA. **(a)** A comparison of the χ parameter as a function of temperature shows that the VN-containing BCP's have much higher χ's as compared to PS-PMMA, which results in **(b)** smaller attainable features.

BCP	A	B
PS-PMMA[18]	2.85	0.037
$P(S_{83}VN_{17})$-$PMMA_{Dis}$	6.99	0.067
$P(S_{71}VN_{29})$-$PMMA_{Dis}$	2.86	0.091

Table 4.2 A and B parameters for the χ parameters of PS-PMMA and two VN-containing BCPs.

We examined the reported chemical nature of VN to explain the increase in χ with modest amounts of VN. Notably, polyvinylnaphthalene (PVN) and PS homopolymers have both been reported to form excimers upon light irradation,[50,51] which is caused by neighboring aromatic groups interacting with one another to form an electronically-excited dimer complex. Accordingly, naphthalene and benzene pendant groups in PSVN possess π-π interactions,[52] which likely are closely related to the formation of excimers. Within the context of this work, it is unreasonable to assume that every VN unit is interacting with another VN unit. Therefore, a rough calculation comparing the interaction energy of a pair of VN units to the total energy of bulk microphase separation of the PS-PMMA analogue of $P(S_{71}VN_{29})$-$PMMA_{Dis}$ was performed.

The binding energy of two VN units was estimated from a simulation for naphthalene stacking energies, which ranged from 17.4 kJ/mol for the parallel configuration to 27.6 kJ/mol for the parallel-displaced configuration.[53] To make a conservative estimation of the VN interaction, 17.4 kJ/mol or 3.47×10^{-23} kJ/pair of VN monomers was used for the following comparisons.

The total free energy of microphase separation in bulk of the PS-PMMA analogue of $P(S_{71}VN_{29})$-$PMMA_{Dis}$, wherein all VN units were replaced by styrene (PS_{100}-$PMMA_{Dis}$), was estimated using a model by D.G. Walton, et al:[54]

$$\frac{F_0}{kT} = \frac{3p}{2}\left(\frac{\chi}{2}\right)^{\frac{1}{3}} N^{\frac{1}{3}}$$ **Equation 4.4**

where F_0 is the equilibrium bulk free energy, p is the number of BCP chains in the system, and N is the normalized degree of polymerization. Using **Equation 4.4**, the energy of microphase separation in bulk for PS_{100}-$PMMA_{Dis}$ (F_0/kT) was calculated to be 9.6 x 10^{-24} kJ/chain. By comparing this energy to the interaction energy of two VN units, it is evident that the interaction energy of two VN units eclipses the energy required for microphase separation. Therefore, the observed increase in χ upon including VN in PS-PMMA would be accounted for by a small fraction of the available VN units in the PSVN block interacting with each other.

To further elaborate on the role VN self-interactions play in increasing the χ of the BCP, we revisit the original definition of χ by Flory (**Equation 4.5)**, wherein z is the lattice parameter, and k is Boltzmann's constant. χ_{AB} represents the thermodynamic contribution of energetic penalty (χ_{AB} is positive) or benefit (χ_{AB} is negative) for removing polymer segments A and B from a lattice of their peers and placing each in the position vacated by the other, i.e. an exchange energy of mixing.

$$\chi_{AB} = \frac{z\Delta w}{kT}$$ **Equation 4.5**

Δw represents the actual exchange energy for a single lattice boundary relative to the initial state,

$$\Delta w = w_{AB} - {}^1/_2\,(w_{AA} + w_{BB})$$ **Equation 4.6**

where w_{AA} and w_{BB} represent the interaction energy per mole of A and B segments in their initial, phase separated state, and w_{AB} represents the interaction energy per mole of A and B segments in contact. Due to favorable non-covalent interactions between segments, w_{AA}, w_{BB}, and w_{AB} are small negative numbers while Δw as a whole is usually positive. Therefore χ_{AB} can be increased by increasing w_{AB} (poorer chemical compatibility between

blocks) or decreasing w_{AA} (increased self-interactions in one of the blocks). We note that binding energies between aromatic groups have been computationally predicted[53] and are represented by a range of values, due to different spatial arrangements. For benzene this range is from -9 kJ/mol to -14 kJ/mol, and for naphthalene this ranges from -17 kJ/mol to -25 kJ/mol.[53] If these values were to be directly related to w_{AA} of a PSVN-PMMA BCP, where PSVN represents the *A* block, a more negative w_{AA} as VN subunits are added is fully consistent with the experimentally observed increase in χ. However, please note a predicted χ based on incorporating a composition-weighted w_{AA} is overestimated by **Equations 4.5** and **4.6**, likely due to concomitant decreases in w_{AB}, computational overpredictions of binding energy, and steric blocking of aromatic self-interactions by the polymer backbone, among other effects.

To rule out the possibility of chemical dissimilarity (increasing w_{AB}) as a major contributor to the increase in χ, polymer dewetting studies were conducted using PS and PVN as test liquids on a PMMA substrate (PMMA crosslinked mat on a Si wafer). The PVN droplets formed a larger contact angle of 15.7° (number of droplets measured, n = 23, 95% confidence interval [15.1°, 16.4°]) on the PMMA substrate than the PS droplets (contact angle 7.4°, n = 12, 95% confidence interval [6.8°, 8.1°]) (**Figure 4.10**).

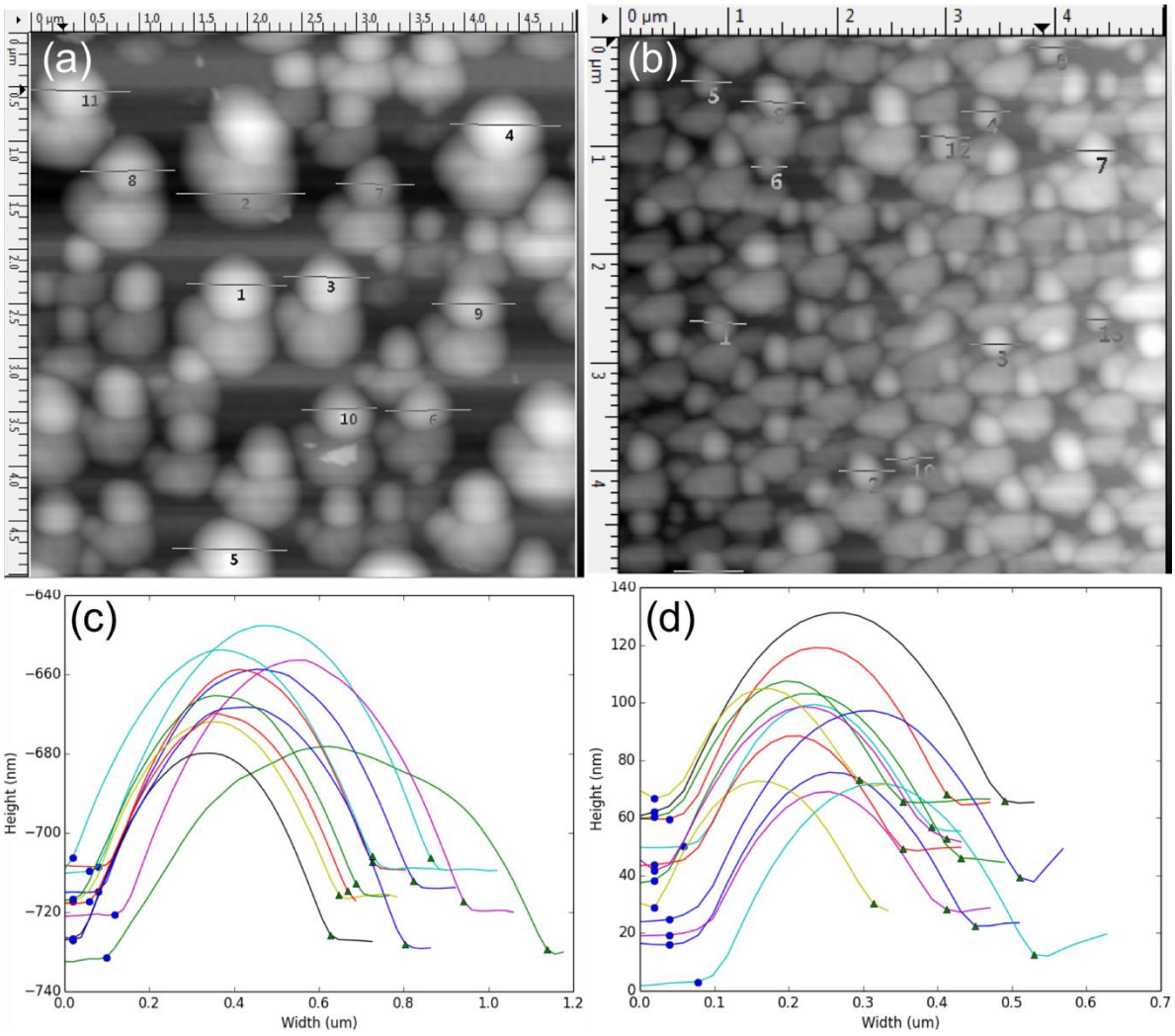

Figure 4.10 Representative AFM images of **(a)** PS and **(b)** PVN films dewetting from a crosslinked PMMA surface. Both films were annealed under vacuum at 160 °C for 96 hours. Isolated droplets of various sizes were selected to provide a comprehensive data set. A python code was written to determine the height and width of each droplet, and representative data for **(c)** PS and **(d)** PVN are shown. Dewetting contact angles were calculated by assuming spherical caps and using the equation $\cos\theta = 1–2(h/r)^2$, where h is the height of the droplet and r is half the width of the droplet.

The relative surface energies, γ_1 and γ_2, for two test liquids on the same substrate can be estimated by[55]

$$\left(\frac{\gamma_1}{\gamma_2}\right) \approx \left(\frac{\cos(\theta_2)}{\cos(\theta_1)}\right)^2 \qquad \textbf{Equation 4.7}$$

Using the experimentally determined contact angles and the reported surface energy of PS (39.4 dyn/cm),[56] the surface energy of PVN was calculated to be 40.6 dyn/cm, which falls between that of PS and PMMA (41.1 dyn/cm).[56] Since the surface energy of PVN is more like PMMA, it is not likely that the increased χ for PSVN-PMMA relative to PS-PMMA is due to increased chemical dissimilarity (w_{AB}).

4.3.3 Thin film processing

A BCP is most lithographically useful when its phase separated microdomains are oriented perpendicular to the substrate. The main incentive for choosing to study this specific BCP, PSVN-PMMA, was to investigate whether PSVN-PMMA could possess an increased χ relative to PS-PMMA while retaining the ability to orient perpendicularly via thermal annealing. **Figure 4.**11 shows representative top-down SEM micrographs of PSVN-PMMA thin films obtained after spin-coating and thermal self-assembly, and the domain sizes agreed with the SAXS results to within 1 nm. The annealing conditions were different for each sample, as summarized in **Table 4.3**. Some difficulties did arise during the annealing process, namely, dewetting at low temperatures and short annealing times. The dewetting problem was solved by annealing either in vacuum or in an enclosed oven without light. This is explained in more detail in the next chapter. Notably, a fingerprint pattern characteristic of vertically oriented lamella is present at the top surface, including $P(S_{65}VN_{35})_{7.7}$-$PMMA_{9.7}$, the sample with the highest concentration of VN.

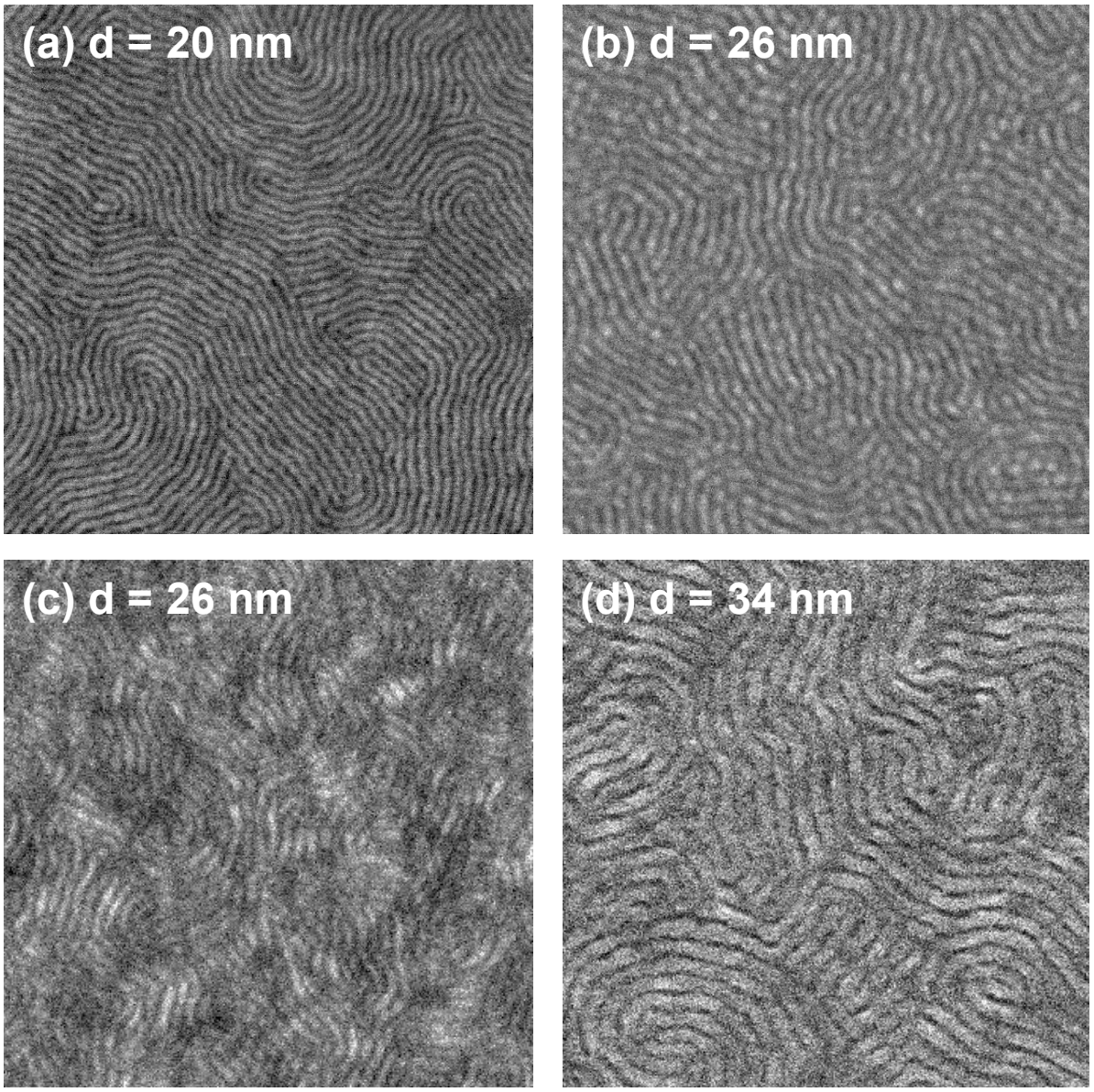

Figure 4.11 Top-down SEM images of lightly etched **(a)** $P(S_{85}VN_{15})_{17.1}$-$PMMA_{19.1}$ with a film thickness of 1.7 L_0, **(b)** $P(S_{80}VN_{20})_{15.1}$-$PMMA_{20.9}$ with a film thickness of 1.0 L_0, **(c)** $P(S_{75}VN_{25})_{12.6}$-$PMMA_{18.3}$ with a film thickness of 1.7 L_0, and **(d)** $P(S_{65}VN_{35})_{7.7}$-$PMMA_{9.7}$ with a film thickness of 1.7 L_0. All images are 1 μm x 1 μm.

Sample	mol% VN	SNT	Film thickness (in L_0)	Annealing temp (°C)	Annealing time (min)	Annealing condition
$P(S_{85}VN_{15})_{17.1}$-$PMMA_{19.1}$	15	GL57	1.7	160	120	vacuum
$P(S_{80}VN_{20})_{15.1}$-$PMMA_{20.9}$	20	GL57	1.0	160	120	vacuum
$P(S_{75}VN_{25})_{12.6}$-$PMMA_{18.3}$	25	GL54	1.7	170	4	air
$P(S_{65}VN_{35})_{7.7}$-$PMMA_{9.7}$	35	GL54	1.7	200	6	air

Table 4.3 Annealing conditions for the samples shown in Figure 4.11.

It is noteworthy that the same SNT that was used to perpendicularly orient PS-PMMA[57] was also used to successfully orient PSVN-PMMA samples. As mentioned earlier, the surface energy of PVN was calculated to be 40.6 dyne/cm based on dewetted polymer droplet contact angles. Therefore, incorporating VN into the PSVN block decreased the surface energy gap between the two blocks, allowing the BCP to easily orient with thermal annealing.

In addition, because the surface energy of PVN lies between that of PS and PMMA, increasing the concentration of VN in the PSVN block resulted in a shift in the SNT composition. For PSVN-PMMA samples with 20 mol% or less of VN in the PSVN block, GL57 (molar composition of 77 mol% styrene, 22% MMA, 1% glycidal methacrylate) was used as the SNT, whereas GL54 (molar composition of 74 mol% styrene, 25% MMA, 1% glycidal methacrylate) was used as the SNT for BCPs with 25 mol% or greater of VN in the PSVN block.

4.4 CONCLUSIONS

The addition of VN into the chemical structure of PS-PMMA to form PSVN-PMMA increased χ while retaining desirable thin film self-assembly characteristics. First, incorporating 29 mol% of VN into the PS-PMMA increased its effective χ more than twofold, and the smallest possible features formed with this BCP is 6.3 nm as compared to ~11 nm for PS-PMMA. This copolymer structure was designed to exploit naphthalene self-interactions as a means of increasing χ. Second, the surface energy of PVN is between that of PS and PMMA, so the addition of small amounts of VN into the styrenic block still enabled the self-assembled microdomains of PSVN-PMMA to be vertically oriented by thermal annealing. These two qualities, together, are greatly advantageous and suggest nanopatterning resolution in BCP lithography using a nominal "PS-PMMA" material may not be fundamentally limited by small χ.

4.5 REFERENCES

(1) Wan, L.; Ruiz, R.; Gao, H.; Patel, K. C.; Albrecht, T. R.; Yin, J.; Kim, J.; Cao, Y.; Lin, G. The Limits of Lamellae-Forming PS- B -PMMA Block Copolymers for Lithography. *ACS Nano* **2015**, *9* (7), 7506–7514.

(2) Liu, C. C.; Han, E.; Onses, M. S.; Thode, C. J.; Ji, S.; Gopalan, P.; Nealey, P. F. Fabrication of Lithographically Defined Chemically Patterned Polymer Brushes and Mats. *Macromolecules* **2011**, *44* (7), 1876–1885.

(3) Stoykovich, M. P.; Müller, M.; Kim, S. O.; Solak, H. H.; Edwards, E. W.; de Pablo, J. J.; Nealey, P. F. Directed Assembly of Block Copolymer Blends into Nonregular Device-Oriented Structures. *Science* **2005**, *308* (5727), 1442–1446.

(4) Tremblay, J.-F. AZ Readies For Chip Self-Assembly. *Chem. Eng. News* **2013**, *91* (26), 10.

(5) Mansky, P. Controlling Polymer-Surface Interactions with Random Copolymer Brushes. *Science (80-.).* **1997**, *275* (5305), 1458–1460.

(6) Han, E.; Stuen, K. O.; La, Y. H.; Nealey, P. F.; Gopalan, P. Effect of Composition of Substrate-Modifying Random Copolymers on the Orientation of Symmetric and

Asymmetric Diblock Copolymer Domains. *Macromolecules* **2008**, *41* (23), 9090–9097.

(7) Ham, S.; Shin, C.; Kim, E.; Ryu, D. Y.; Jeong, U.; Russell, T. P.; Hawker, C. J. Microdomain Orientation of PS-B-PMMA by Controlled Interfacial Interactions. *Macromolecules* **2008**, *41* (17), 6431–6437.

(8) Albert, J. N. L.; Epps III, T. H. Self-Assembly of Block Copolymer Thin Films. *Mater. Today* **2010**, *13* (6), 24–33.

(9) Xiao, S.; Yang, X.; Edwards, E. W.; La, Y.-H.; Nealey, P. F. Graphoepitaxy of Cylinder-Forming Block Copolymers for Use as Templates to Pattern Magnetic Metal Dot Arrays. *Nanotechnology* **2005**, *16* (7), S324–S329.

(10) Bang, J.; Bae, J.; Löwenhielm, P.; Spiessberger, C.; Given-Beck, S. a.; Russell, T. P.; Hawker, C. J. Facile Routes to Patterned Surface Neutralization Layers for Block Copolymer Lithography. *Adv. Mater.* **2007**, *19* (24), 4552–4557.

(11) Hawker, C. J.; Russell, T. P. Block Copolymer Lithography: Merging "Bottom-Up" with "Top-Down" Processes. *MRS Bull.* **2005**, *30* (12), 952–966.

(12) Kennemur, J. G.; Yao, L.; Bates, F. S.; Hillmyer, M. A. Sub ‐ 5 Nm Domains in Ordered Poly(cyclohexylethylene)- Block - Poly(methyl Methacrylate) Block Polymers for Lithography. **2014**.

(13) Seshimo, T.; Maeda, R.; Odashima, R.; Takenaka, Y.; Kawana, D.; Ohmori, K.; Hayakawa, T. Perpendicularly Oriented Sub-10-Nm Block Copolymer Lamellae by Atmospheric Thermal Annealing for One Minute. *Sci. Rep.* **2016**, *6* (January), 19481.

(14) Park, S. M.; Liang, X.; Harteneck, B. D.; Pick, T. E.; Hiroshiba, N.; Wu, Y.; Helms, B. A.; Olynick, D. L. Sub-10 Nm Nanofabrication via Nanoimprint Directed Self-Assembly of Block Copolymers. *ACS Nano* **2011**, *5* (11), 8523–8531.

(15) Cushen, J. D.; Bates, C. M.; Rausch, E. L.; Dean, L. M.; Zhou, S. X.; Willson, C. G.; Ellison, C. J. Thin Film Self-Assembly of Poly(trimethylsilylstyrene- B - D , L -Lactide) with Sub-10 Nm Domains. *Macromolecules* **2012**, *45* (21), 8722–8728.

(16) Matsen, M. W.; Bates, F. S. Unifying Weak- and Strong-Segregation Block Copolymer Theories. *Macromolecules* **1996**, *29* (4), 1091–1098.

(17) Fukukawa, K.; Zhu, L.; Gopalan, P.; Ueda, M.; Yang, S. Synthesis and Characterization of Silicon-Containing Block Copolymers from Nitroxide-Mediated Living Free Radical Polymerization. *Society* **2005**, 263–270.

(18) Durand, W. J.; Blachut, G.; Maher, M. J.; Sirard, S.; Tein, S.; Carlson, M. C.; Asano, Y.; Zhou, S. X.; Lane, A. P.; Bates, C. M.; Ellison, C. J.; Willson, C. G. Design of High-χ Block Copolymers for Lithography. *J. Polym. Sci. Part A Polym. Chem.* **2015**, *53* (2), 344–352.

(19) Luo, M.; Epps, T. H. Directed Block Copolymer Thin Film Self-Assembly: Emerging Trends in Nanopattern Fabrication. **2013**.

(20) Bates, C. M.; Seshimo, T.; Maher, M. J.; Durand, W. J.; Cushen, J. D.; Dean, L. M.; Blachut, G.; Ellison, C. J.; Willson, C. G. Polarity-Switching Top Coats Enable Orientation of Sub-10-Nm Block Copolymer Domains. *Science (80-.).* **2012**, *338* (6108), 775–779.

(21) Yoshida, H.; Suh, H. S.; Ramirez-Hernandez, a; Lee, J. I.; Aida, K.; Wan, L.; Ishida, Y.; Tada, Y.; Ruiz, R.; de Pablo, J.; Nealey, P. F. Topcoat Approaches for Directed Self-Assembly of Strongly Segregating Block Copolymer Thin Films. *J. Photopolym. Sci. Technol.* **2013**, *26* (1), 55–58.

(22) Zhang, J.; Clark, M. B.; Wu, C.; Li, M.; Trefonas, P.; Hustad, P. D. Orientation Control in Thin Films of a High-χ Block Copolymer with a Surface Active Embedded Neutral Layer. *Nano Lett.* **2016**, *16* (1), 728–735.

(23) Kim, S.; Nealey, P. F.; Bates, F. S. Decoupling Bulk Thermodynamics and Wetting Characteristics of Block Copolymer Thin Films. *ACS Macro Lett.* **2012**, *1* (1), 11–14.

(24) Bennett, T. M.; Pei, K.; Cheng, H.-H.; Thurecht, K. J.; Jack, K. S.; Blakey, I. Can Ionic Liquid Additives Be Used to Extend the Scope of Poly(styrene)-Block-Poly(methyl Methacrylate) for Directed Self-Assembly? *J. Micro/Nanolithography, MEMS, MOEMS* **2014**, *13* (3), 031304.

(25) Tang, C.; Hur, S. M.; Stahl, B. C.; Sivanandan, K.; Dimitriou, M.; Pressly, E.; Fredrickson, G. H.; Kramer, E. J.; Hawker, C. J. Thin Film Morphology of Block Copolymer Blends with Tunable Supramolecular Interactions for Lithographic Applications. *Macromolecules* **2010**, *43* (6), 2880–2889.

(26) Tang, C. B.; Lennon, E. M.; Fredrickson, G. H.; Kramer, E. J.; Hawker, C. J.; Chuanbing, T.; Lennon, E. M.; Fredrickson, G. H.; Kramer, E. J.; Hawker, C. J. Evolution of Block Copolymer Lithography to Highly Ordered Square Arrays. *Science (80-.).* **2008**, *322* (5900), 429–432.

(27) Han, S. H.; Pryamitsyn, V.; Bae, D.; Kwak, J.; Ganesan, V.; Kim, J. K. Highly Asymmetric Lamellar Nanopatterns via Block Copolymer. *ACS Nano* **2012**, *6* (9), 7966–7972.

(28) Vora, A.; Zhao, B.; To, D.; Cheng, J. Y.; Nelson, A. Blends of PS-PMMA Diblock Copolymers with a Directionally Hydrogen Bonding Polymer Additive. *Macromolecules* **2010**, *43* (3), 1199–1202.

(29) Sunday, D. F.; Kline, R. J. Reducing Block Copolymer Interfacial Widths through Polymer Additives. *Macromolecules* **2015**, *48* (3), 679–686.

(30) Cushen, J. D.; Wan, L.; Pandav, G.; Mitra, I.; Stein, G. E.; Ganesan, V.; Ruiz, R.; Willson, C. G.; Ellison, C. J. Ordering Poly(trimethylsilyl Styrene-Block- D,L -

Lactide) Block Copolymers in Thin Films by Solvent Annealing Using a Mixture of Domain-Selective Solvents. *J. Polym. Sci. Part B Polym. Phys.* **2014**, *52* (1), 36–45.

(31) Hiemenz, P. C.; Lodge, T. P. *Polymer Chemistry, Second Edition*; Taylor & Francis, 2007.

(32) Tsuzuki, S.; Honda, K.; Uchimaru, T.; Mikami, M. High-Level Ab Initio Computations of Structures and Interaction Energies of Naphthalene Dimers: Origin of Attraction and Its Directionality. *J. Chem. Phys.* **2004**, *120* (2), 647–659.

(33) Beckingham, B. S.; Register, R. A. Synthesis and Phase Behavior of Block-Random Copolymers of Styrene and Hydrogenated Isoprene. *Macromolecules* **2011**, *44* (11), 4313–4319.

(34) Izunobi, J. U.; Higginbotham, C. L. Polymer Molecular Weight Analysis by 1 H NMR Spectroscopy. *J. Chem. Educ.* **2011**, *88* (8), 1098–1104.

(35) Lefebvre, M. D.; Olvera de la Cruz, M.; Shull, K. R. Phase Segregation in Gradient Copolymer Melts. *Macromolecules* **2004**, *37* (3), 1118–1123.

(36) Gray, M. K.; Zhou, H.; Nguyen, S. T.; Torkelson, J. M. Synthesis and Glass Transition Behavior of High Molecular Weight styrene/4-Acetoxystyene and styrene/4-Hydroxystyrene Gradient Copolymers Made via Nitroxide-Mediated Controlled Radical Polymerization. *Macromolecules* **2004**, *37* (15), 5586–5595.

(37) Bahsteter, F.; Smid, J.; Szwarc, M. Kinetics of Anionic Polymerization and Copolymerization of the Vinylnaphthalenes and Styrene. The Intramolecular Charge-Transfer Complexes. *J. Am. Chem. Soc.* **1963**, *85* (24), 3909–3918.

(38) Moacanin, J.; Cuddihy, E.; Rembaum, A. Compatibility and Plasticization of Poly-B-Vinylnaphthalene with Polyethylene Oxide. In *Plasticization and Plasticizer Processes*; Platzer, N. A. J., Ed.; 1965; pp 159–171.

(39) Mok, M. M.; Kim, J.; Wong, C. L. H.; Marrou, S. R.; Woo, D. J.; Dettmer, C. M.; Nguyen, S. T.; Ellison, C. J.; Shull, K. R.; Torkelson, J. M. Glass Transition Breadths and Composition Profiles of Weakly, Moderately, and Strongly Segregating Gradient Copolymers: Experimental Results and Calculations from Self-Consistent Mean-Field Theory. *Macromolecules* **2009**, *42* (20), 7863–7876.

(40) Brostow, W.; Chiu, R.; Kalogeras, I. M.; Vassilikou-Dova, A. Prediction of Glass Transition Temperatures: Binary Blends and Copolymers. *Mater. Lett.* **2008**, *62* (17-18), 3152–3155.

(41) Meuler, A. J.; Ellison, C. J.; Qin, J.; Evans, C. M.; Hillmyer, M. a; Bates, F. S. Polydispersity Effects in Poly(isoprene-B-Styrene-B-Ethylene Oxide) Triblock Terpolymers. *J. Chem. Phys.* **2009**, *130* (23), 234903.

(42) Lynd, N. A.; Hillmyer, M. A. Influence of Polydispersity on the Self-Assembly of Diblock Copolymers. *Macromolecules* **2005**, *38* (21), 8803–8810.

(43) Hamley, I. W.; Castelletto, V. Small-Angle Scattering of Block Copolymers. *Prog. Polym. Sci.* **2004**, *29* (9), 909–948.

(44) Bates, F. S.; Hillmyer, M. A.; Lodge, T. P.; Bates, C. M.; Delaney, K. T.; Fredrickson, G. H. Multiblock Polymers: Panacea or Pandora's Box? *Science (80-.).* **2012**, *336* (6080), 434–440.

(45) Russell, T. P.; Lin, J. S.; Spooner, S.; Wignall, G. D. Intercalibration of Small-Angle X-Ray and Neutron Scattering Data. *J. Appl. Crystallogr.* **1988**, *21* (6), 629–638.

(46) Leibler, L. Theory of Microphase Separation in Block Copolymers. *Macromolecules* **1980**, *13* (6), 1602–1617.

(47) Sakamoto, N.; Hashimoto, T. Order-Disorder Transition of Low Molecular Weight Polystyrene-Block-Polyisoprene. 1. SAXS Analysis of Two Characteristic Temperatures. *Macromolecules* **1995**, *28* (20), 6825–6834.

(48) Zhao, Y.; Sivaniah, E.; Hashimoto, T. SAXS Analysis of the Order− Disorder Transition and the Interaction Parameter of Polystyrene-Block-Poly (Methyl Methacrylate). *Macromolecules* **2008**, *41* (24), 9948–9951.

(49) Hashimoto, T.; Bodycomb, J.; Funaki, Y.; Kimishima, K. Communications to the Editor. *Macromolecules* **1999**, 952–954.

(50) Harrah, L. Excimer Formation in Vinyl Polymers. I. Temperature Dependence in Fluid Solution. *J. Chem. Phys.* **1972**, *56* (1972), 385.

(51) Frank, C. W. Excimer Formation in Vinyl Polymers. II. Rigid Solutions of poly(2-Vinylnaphthalene) and Polystyrene. *J. Chem. Phys.* **1974**, *61* (4), 1526.

(52) Holden, D. A. Characterization of Blends of Naphthalene-Containing Polymers with Poly(alkyl Methacrylates) by Combined Steady-State Fluorescence Spectroscopy and Fluorescence Decay Measurements. *Polym. Eng. Sci.* **1988**, *28* (21), 1373–1380.

(53) Sato, T.; Tsuneda, T.; Hirao, K. A Density-Functional Study on π -Aromatic Interaction: Benzene Dimer and Naphthalene Dimer. *J. Chem. Phys.* **2005**, *123* (10).

(54) Walton, D.; Kellogg, G.; Mayes, A. A Free Energy Model for Confined Diblock Copolymers. *Macromolecules* **1994**, *27* (21), 6225–6228.

(55) Wu, S. Surface and Interfacial Tensions of Polymer Melts. II. Poly (Methyl Methacrylate), Poly (N-Butyl Methacrylate), and Polystyrene. *J. Phys. Chem.* **1970**, *I* (1960).

(56) *Polymer Handbook*; Brandrup, J., Immergut, E., Grulke, E. A., Eds.; Wiley and Sons: Hoboken, NJ, 1999.

(57) Janes, D. W.; Thode, C. J.; Willson, C. G.; Nealey, P. F.; Ellison, C. J. Light-Activated Replication of Block Copolymer Fingerprint Patterns. *Macromolecules* **2013**, *46* (11), 4510–4519.

Chapter 5: Vinylnaphthalene Degradation during Light Exposure

5.1 Introduction

Vinylnaphthalene (VN) was the enabling monomer for the work described in the previous chapter. During the course of the experiments, however, it was discovered that the incorporation of VN into polymers also caused some unforeseen difficulties, the most egregious of which was the degradation that occurred during simultaneous heating and small-angle X-ray scattering (SAXS) data collection.

In this chapter, the photochemistry of VN, with an emphasis on the degradation pathways of VN during light exposure, is described. High energy bombardment of polymers can cause chain scission and coupling reactions that invariably modify the polymer's properties. For example, many medical device polymers are sterilized by gamma irradiation. A dominance of chain scission could lead to embrittlement, while improved wear resistance may be obtained from crosslinking.[1] In addition, the free-radicals generated along the polymer backbone during X-ray exposure can react with O_2, degrading the polymer.[2] The most severe VN degradation was observed during the SAXS experiment, and that problem was eliminated by separating the thermal annealing and X-ray exposure steps, as will be discussed below.

However, thermal annealing for perpendicular orientation of block copolymer domains in thin films, as discussed in the previous chapter, also caused slight degradation of the block copolymer (BCP). This thermal annealing step was conducted in ambient laboratory conditions, where the only light exposure came from the overhead lighting. Thus, the majority of the experiments detailed in this chapter were performed with a broadband metal-halide lamp (UV) light source. The mechanism behind the degradation was determined to be the VN units interacting with oxygen, which led to crosslinking and chain scission.

5.2 Experimental Methods

5.2.1 SAXS data collection for χ

SAXS measurements were conducted on a Molecular Metrology instrument equipped with a high brilliance rotating copper anode source using Cu Kα radiation (λ= 1.5418 Å) and a gas-filled two-dimensional 120 mm multiwire detector. Horizontal focus and wavelength selection were achieved using an asymmetric cut Si(111) monochromator, and vertical focus was achieved using a single-crystal germanium mirror. Silver behenate with a primary reflection peak at 1.076 nm^{-1} was used to calibrate the beam center.

The typical SAXS procedure for χ determination involved first annealing the BCP sample in an o-ring sandwiched by two pieces of Kapton tape above the BCP's glass transition temperature to form a uniformly thick, liquid BCP sample. After cooling to room temperature to form a solid glassy sample, the sample was inserted in a heating stage (Instec HCS402 Dual Heater Microscope Hot and Cold Stage) controlled by an external temperature controller (Instec mK2000). The heating stage was mounted in the SAXS sample vacuum chamber, and the chamber was pumped down to 2-4 mTorr before data collection began. The temperature controller was used to hold the BCP sample at the set temperature while data was collected, and data was collected at four different temperatures (140 °C, 160 °C, 180 °C, 200 °C).

5.2.2 Polyvinylnaphthalene (PVN) free radical polymerization

6 g of vinylnaphthalene monomer (Acros Organics) was dissolved in THF and filtered through a basic alumina column. The filtered solution was dried under vacuum in a 500 mL round bottom flask (about 5 g of VN resulted). 250 mL of cyclohexane, about 250 mg of 2,2′-azobis(2-methylpropionitrile) (AIBN), and a stir bar were added to the flask with the VN, and a rubber septum was used to close the reactor. The solution was degassed

with argon for 20 minutes and subsequently placed in a 60 °C oil bath and left to react overnight. The reaction is summarized in **Scheme 5.1**.

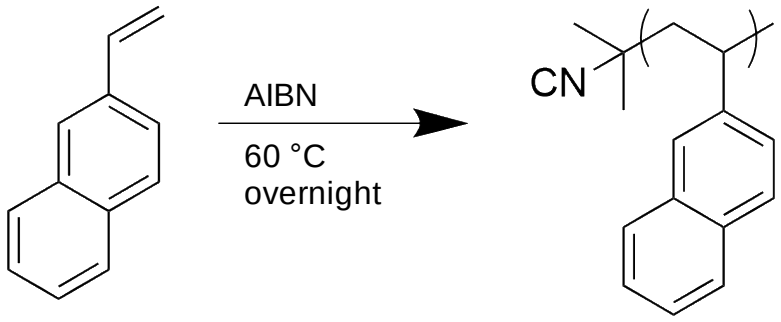

Scheme 5.1 Synthesis of PVN using free radical polymerization.

The round bottom flask was taken out of the oil bath and immediately placed in a dry ice and IPA bath to stop the reaction. After the solution was frozen, the rubber septum was removed. The reactor was then removed from the dry ice/IPA bath and left to thaw in air. The reaction solution was reduced in volume under vacuum, and the PVN was precipitated three times from THF in methanol then dried under vacuum.

5.2.3. Poly(styrene-*random*-vinylnaphthalene) (PSVN) anionic polymerization

The PSVN used in this chapter was the aliquot of $P(S_{70}VN_{30})_{7.7}$-$PMMA_{7.7}$, and the synthesis procedure is described in detail in Chapter 4.

5.2.4 UV-Vis spectroscopy

UV-Vis spectra for films were acquired using a Thermo Scientific Evolution 220 UV-visible spectrophotometer.

5.2.5 UV light exposure

A 200 W metal-halide lamp with broadband output from 300−700 nm (Optical Building Blocks Scopelite 200) was used as the light source for the light exposures. A small

amount of < 300 nm light is also present from this light source. The light intensity was 0.7 W/cm^2 at a 20 mm working distance as measured by a Coherent Field MaxII-TO radiometer with a PM10 sensor.

5.3 Results and Discussion: Poly((styrene-*random*-vinylnaphthalene)-*block*-methyl methacrylate) (PSVN-PMMA)

5.3.1 PSVN-PMMA sample damage during SAXS experiments

The SAXS procedure for collecting χ determination data for PSVN-PMMA required modification from standard operating procedures. For the numerous other BCP samples studied heretofore by other members of the group, SAXS data for χ were collected by heating the BCP sample *in-situ* in the SAXS chamber. Throughout this process, the BCP sample was bombarded with X-rays. This did not cause any problem for other samples, including PS-PMMA. However, this procedure significantly damaged the PSVN-PMMA sample, as shown in **Figure 5.1**. The sample was run through the SEC before and after the SAXS experiments (**Figure 5.2**), and a leftward shift of the elution curve indicated that crosslinking had occurred.

Figure 5.1 Photograph of PSVN-PMMA BCP sample after heating *in situ* during SAXS data collection for χ determination. The air bubbles developed during the data collection period and were not present before insertion into the SAXS sample chamber. The yellow color is from the Kapton tape.

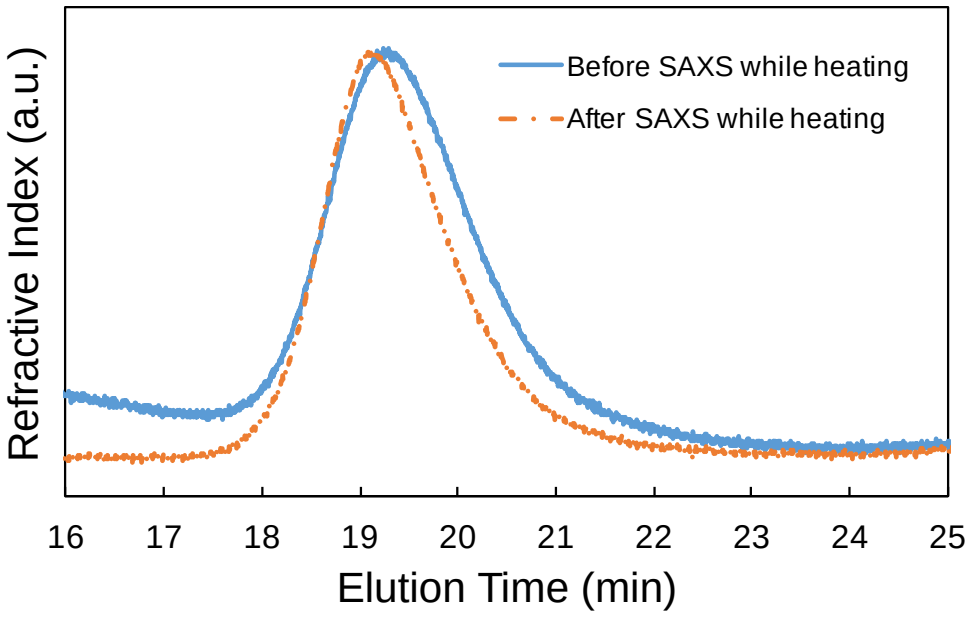

Figure 5.2 SEC traces of a PSVN-PMMA BCP before (blue line) and after (orange dashed line) a typical SAXS experiment for χ with *in situ* heating.

Because the sample was damaged during the experiment, the χ data collected did not turn out as expected. The peak is expected to broaden, decrease in intensity, and shift to the right as the temperature is increased, and as shown in **Figure 5.3**, the order of the peaks was as not typical. The peak positions shifted in both directions as temperature was increased, and the 140 °C peak was not the most intense. The temperature was ramped from lowest to highest, so it is possible that the unexpected results were a consequence of the sample degrading throughout the course of data collection (i.e. simultaneous X-ray irradiation and heating).

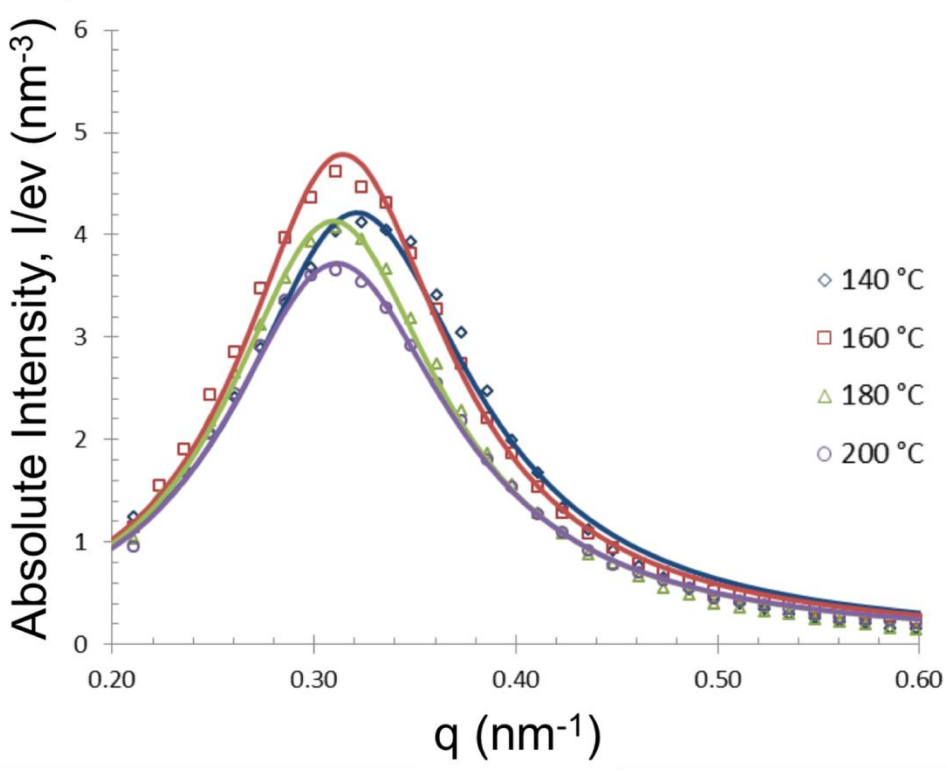

Figure 5.3 SAXS data collected at four temperatures for χ determination (open markers). χ is typically extracted from the curves fit to the collected data (colored lines), but the atypical peak heights and peak orders indicate that any extracted χ is likely inaccurate.

5.3.2 Modified χ data collection methodology

To circumvent this problem, the annealing and data collection (X-ray) steps were performed separately. In this revised experimental method, the BCP X-ray sample was still formed by heating an o-ring on a piece of Kapton tape and filling it with BCP. After the sample was satisfactorily assembled, that is, it had no air bubbles and it was approximately the thickness of the O-ring (~0.25 cm), the sample was placed into the heating stage. The heating stage was set to the first temperature at which SAXS data for χ would be collected, and the sample was annealed for 45 minutes in the lab. After 45 minutes, the sample would be quickly removed with a pair of tweezers and placed in a beaker filled with ice water. After 3-5 seconds in the ice water, the sample was quickly moved to a Dewar of liquid nitrogen to kinetically trap the BCP sample in its thermal annealing temperature state. The intermediary ice water step was necessary to prevent the sample from cracking, which resulted when the hot BCP sample was immediately cooled in the liquid nitrogen.

After the BCP sample was annealed, it was then placed in the SAXS sample holder at room temperature, and the SAXS data was collected. The BCP sample was then annealed at the second and third temperatures in the same manner, and SAXS data was collected at room temperature. In this manner, the BCP sample did not show any signs of degradation, as shown in **Figure 5.4**. The separation of heating and x-ray exposure steps significantly reduced the sample damage during SAXS measurements. This indicates the simultaneous heating and x-ray irradiations damaged PSVN-PMMA samples as shown in **Figure 5.1.**

Figure 5.4. When the high temperature annealing step and SAXS data collection step were separated, the BCP sample did not show any signs of degradation. The yellow color is from the Kapton tape.

To further confirm that each separate process was not changing the PSVN-PMMA sample, a simple SEC experiment was performed on a representative sample, $P(S_{80}VN_{20})_{15.1}$-$PMMA_{20.9}$. First, the sample was run through the SEC as is. Next, the sample was heated at 200 °C for 1 hour, which is longer than the harshest annealing conditions for the SAXS experiment. This heating procedure was performed in the lab, where there were no X-rays. After annealing, the sample was dissolved in THF and run through the SEC. The overlapping peaks from before and after the annealing process shown in **Figure 5.5** reveal that no chain scission or crosslinking occurred.

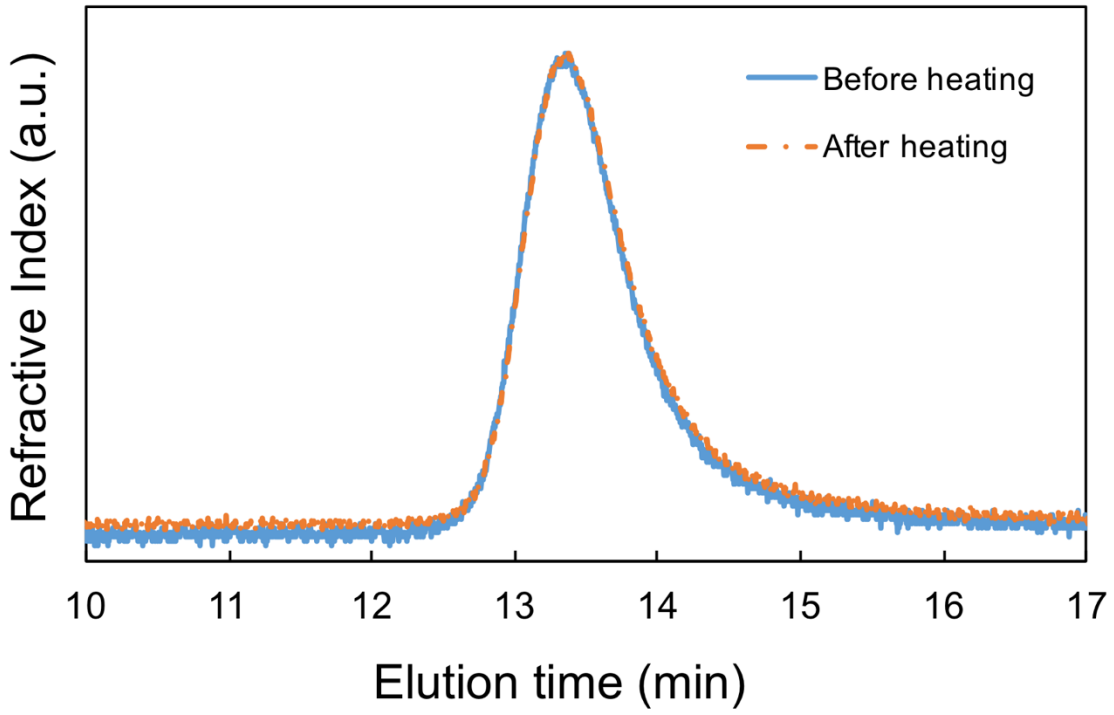

Figure 5.5 SEC trace of $P(S_{80}VN_{20})_{15.1}$-$PMMA_{20.9}$ before and after heating at 200 °C on a hot plate for 1 hour. The identical elution time and peak shape indicates that no chain scission or crosslinking occurred during the annealing process.

The same procedure was repeated with a sample of $P(S_{80}VN_{20})_{15.1}$-$PMMA_{20.9}$ that was run through a SAXS experiment without heating. Exposure to X-rays for 1 hour at room temperature also did not cause chain scission or crosslinking, as shown in **Figure 5.6**.

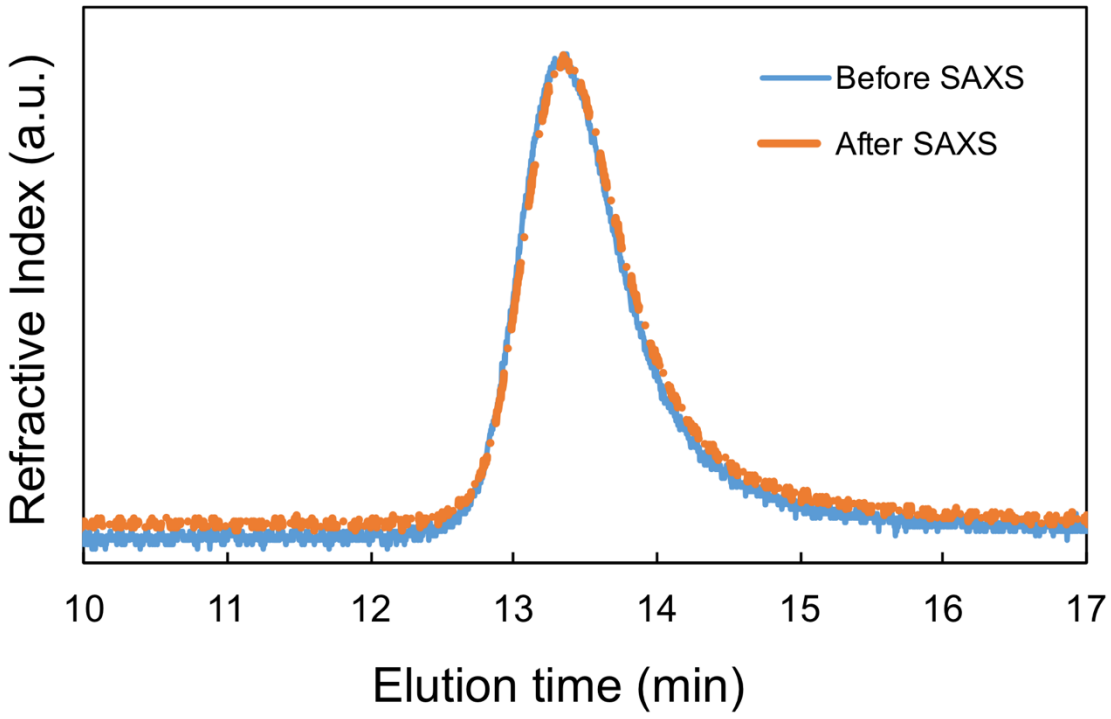

Figure 5.6 SEC trace of $P(S_{80}VN_{20})_{15.1}$-$PMMA_{20.9}$ before and after exposure to X-rays at room temperature for 60 minutes in a SAXS experiment setup. The identical elution time and peak shape indicates that no chain scission or crosslinking occurred during the data collection process.

Therefore, separating the annealing and SAXS steps allowed for the collection of SAXS data for χ determination without the formation of air bubbles in the sample. As shown in Chapter 4, this led to the successful determination of χ for PSVN-PMMA samples.

5.3.3 NMR study of PSVN degradation during SAXS

Several experiments were preformed to elucidate the mechanism behind the bubbling observed when the PSVN-PMMA sample was heated while the SAXS experiment was being run. PS-PMMA did not show any signs of degrading during SAXS when the heating element was used, and therefore, any unexpected behavior observed with

PSVN-PMMA must originate from the VN component reacting in some way. This was corroborated by **Figure 5.7**, which shows that the PSVN block was damaged (lost aromatic protons) during the simultaneous SAXS and heating experiment.

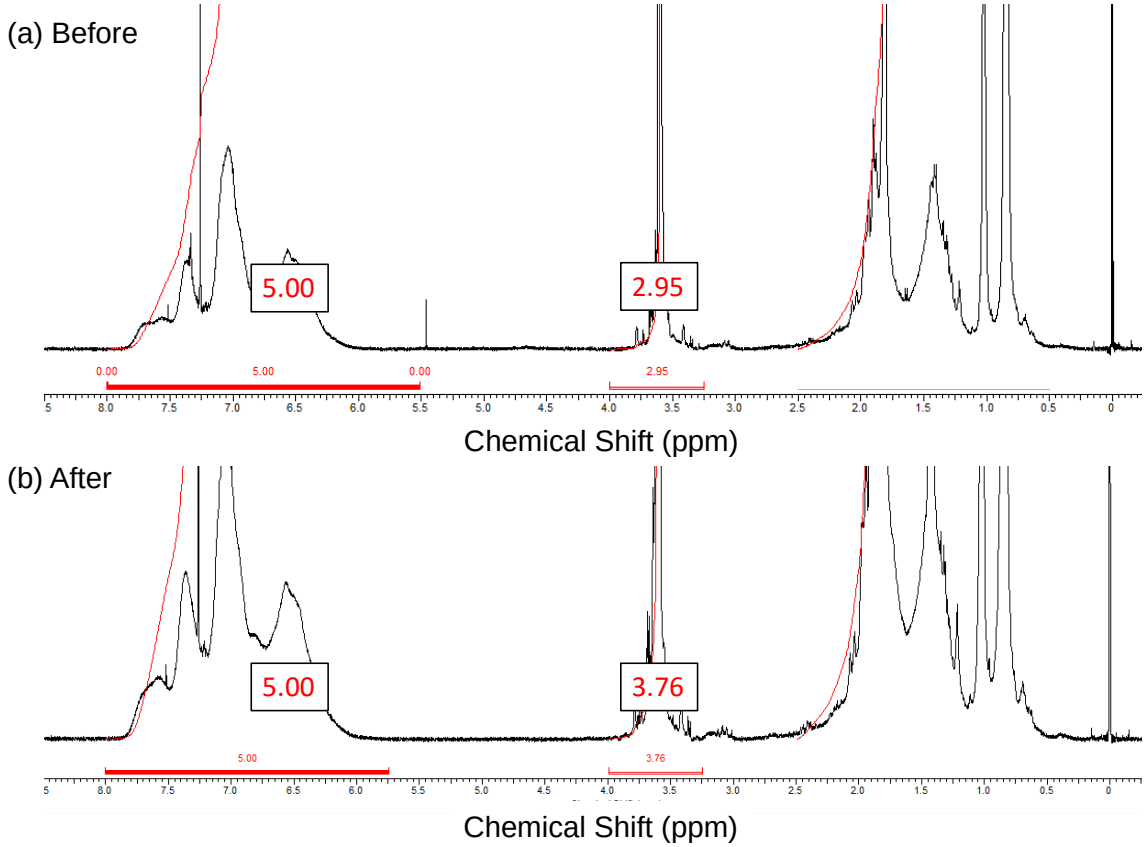

Figure 5.7 ^{1}H NMR spectra of a PSVN-PMMA sample (a) before and (b) after a typical SAXS run to collect data for χ, which involved heating the sample *in situ*. The integration of the aromatic region for both spectra have been set at 5.00. A relative increase in the methoxy integration centered at around 3.6 ppm after the experiment indicates that the PSVN block lost aromaticity during simultaneous SAXS and heating.

This is an unusual conclusion for several reasons. First, aromatic groups typically confer radiation resistance to organic molecules.[3] Second, PMMA has been shown to degrade under high-energy irradiation.[4] However, naphthalene is more reactive with singlet

oxygen than benzene,[5] and therefore, VN should be more reactive with singlet oxygen than styrene. It is hypothesized that the severe bubbling observed is due primarily to the VN degradation, although the PMMA block may have been attacked by VN degradation products and thus contributed to the bubbling. Thus, the following experiments have been conducted on either PVN or PSVN homopolymer.

5.4 Results and Discussion: Light Exposure Tests for PSVN and PVN Homopolymers

It should be emphasized that the following experiments were conducted using a UV light source, not X-rays. Therefore, while the conclusions may help explain some of the unusual behavior in the SAXS, a direct comparison cannot be made. However, the BCP also showed signs of dewetting under moderate thermal annealing conditions (temperatures under 200 °C for 5 minutes). These thermal annealing experiments were carried out under ambient conditions, and as laboratory light does emit some UV,[6] the following UV light exposure experiments can explain some of the deleterious effects.

To corroborate the NMR findings that the aromaticity in the PSVN block decreased after simultaneous X-ray irradiation and heating, we conducted a simple UV-Vis experiment on a PSVN homopolymer. As shown in **Figure 5.8**, in general aromatic systems the absorbance peak shifts towards shorter wavelengths as the conjugated nature of the system is reduced.

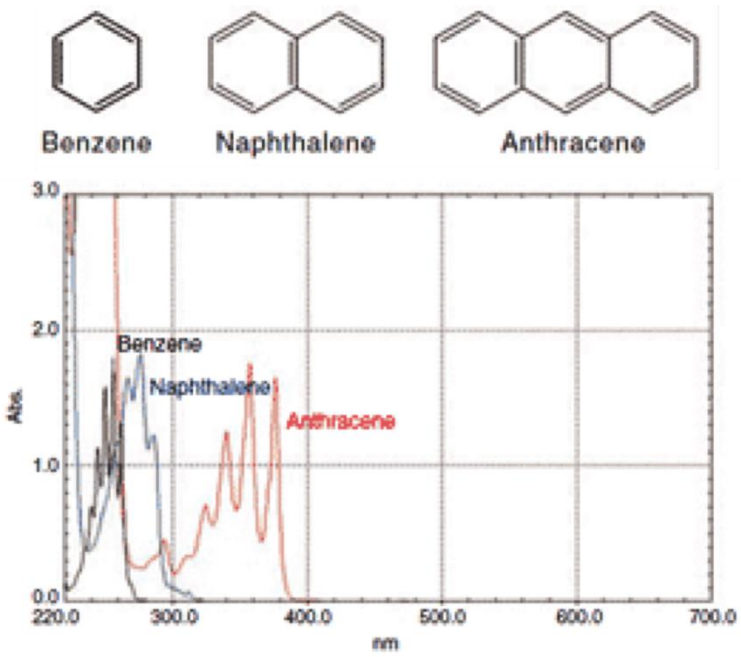

Figure 5.8 Chemical structures and UV-Vis absorption spectra data for benzene, naphthalene, and anthracene. As the size of the conjugated system increases, so does the wavelength of the absorption peak. Reproduced from [7].

A thin film of PVN homopolymer (not PSVN homopolymer) was spin coated onto a quartz substrate under ambient conditions and exposed to UV light. UV-Vis absorbance data were taken after various intervals of light exposure (i.e., varied light dosage), as shown in **Figure 5.9**. As the dosage increased, the absorbance peak shifted toward lower wavelengths, suggesting that conjugated π-electrons are being disrupted in the VN rings (i.e. less conjugation upon light exposure).

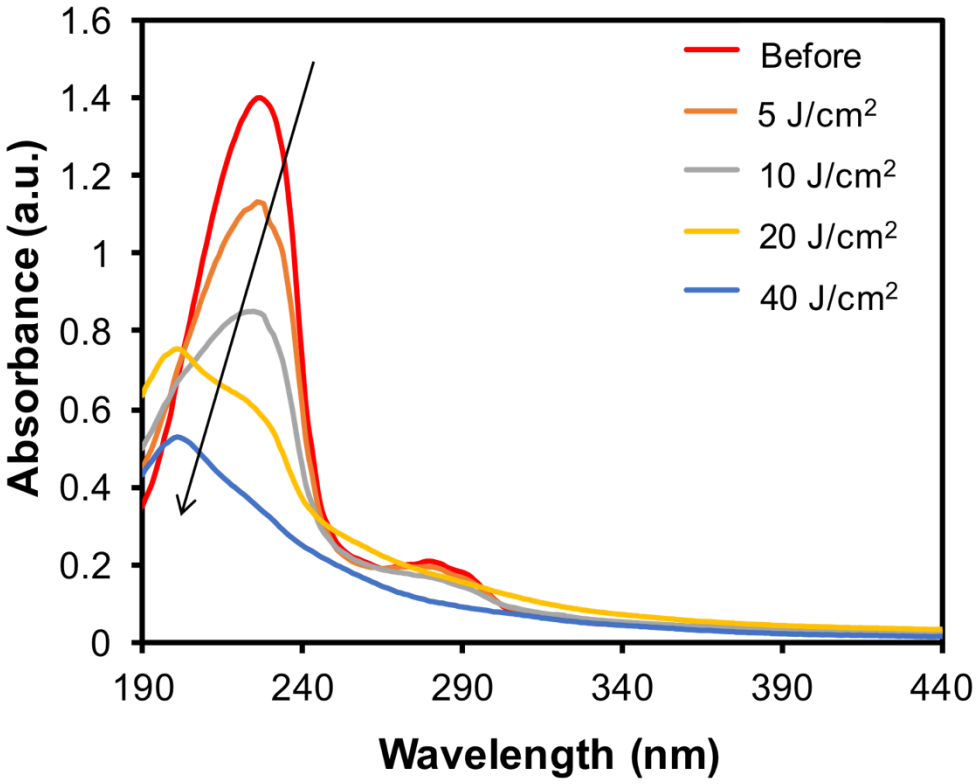

Figure 5.9 UV-Vis data for a PVN homopolymer sample before exposure (red line) and after various doses of UV light. The arrow indicates the trend of the peak as dose increased.

After the UV-Vis studies, attempts to clean the quartz wafer revealed that the PVN film had crosslinked during the course of the UV exposure, as shown in **Figure 5.10**. The wafer was soaked in a THF bath for 2 days then sonicated for 1 hour, and the crosslinked film still remained. To further confirm the crosslinking, 4 mg of PVN was placed in a scintillation vial, and exposed to 10 J/cm^2 of light. 2 mL of THF was added to the exposed polymer and the solution was run through the SEC. The leftward shift of the SEC peak after exposure confirmed that crosslinking occurred, as shown in **Figure 5.11**.

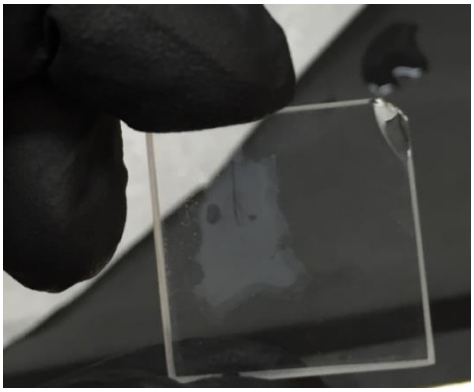

Figure 5.10 Photo of the quartz wafer used for UV-Vis studies after soaking in THF bath for 2 days and sonicating for 1 hour. The cloudy portion is the crosslinked PVN film.

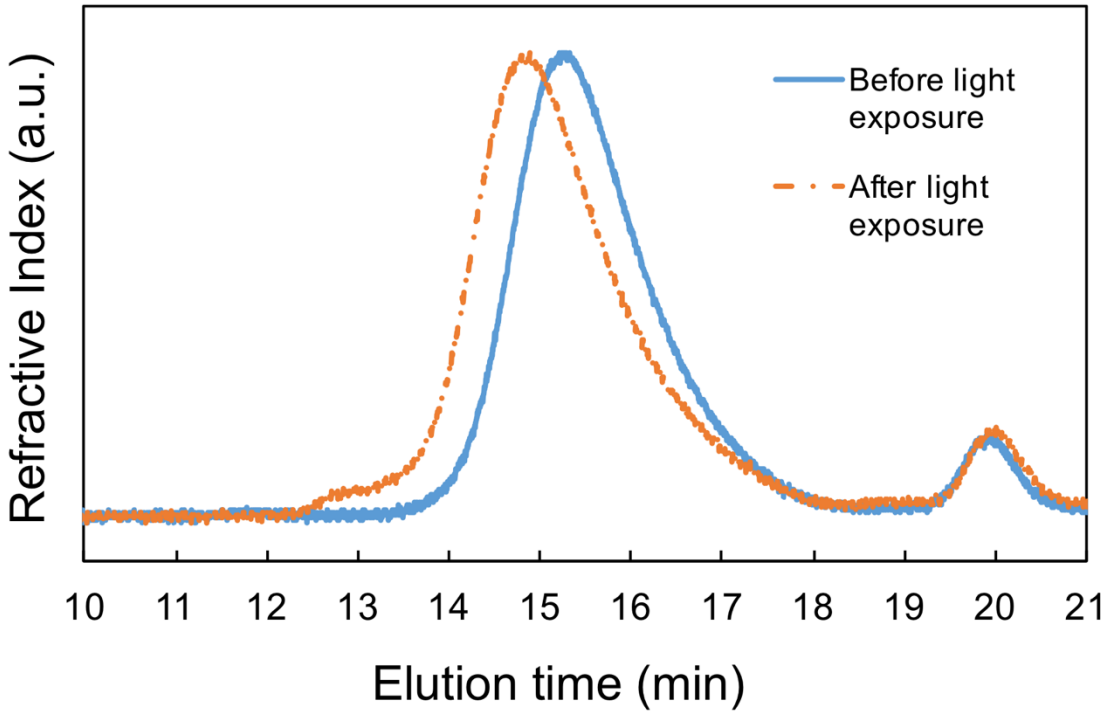

Figure 5.11 SEC trace of PSVN homopolymer before (blue) and after (orange) UV light exposure without heating.

Two hypotheses were formulated to explain the observed PVN thin film crosslinking, and both hypotheses were derived from the behavior of anthracene upon UV irradiation. Anthracene, a compound similar to naphthalene, is known to photodimerize upon UV light exposure. As shown in **Scheme 5.2(a)**, anthracene can dimerize when exposed to UV light with a wavelength of 365 nm.[8,9] The photodimer can be broken either by heat[10] or by irradiation with 303 nm light.[9] Due to structural/ chemical similarities, the first hypothesis was that the naphthalene could also photodimerize and possibly crosslink the polymer chains, as proposed in **Scheme 5.2(b)**.

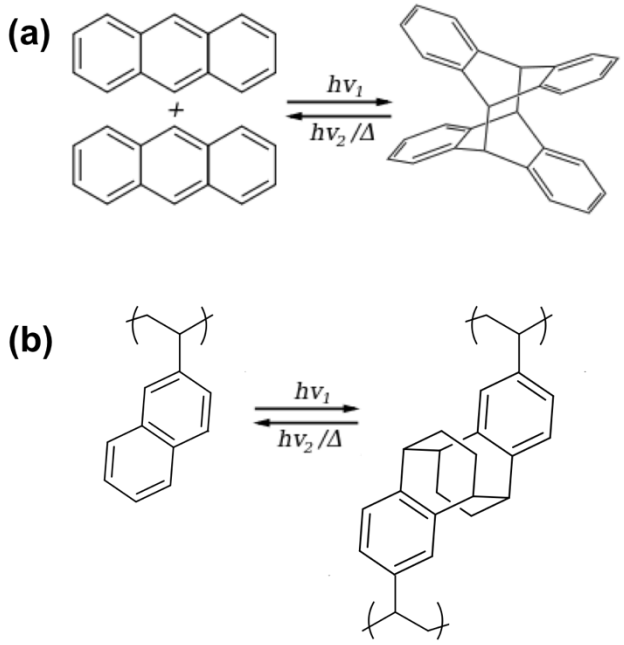

Scheme 5.2 (a) Reversible photodimerization of anthracene. Irradiation by 365 nm light can dimerize anthracene, and the photodimer can be reversed by either heat or by irridation by 303 nm light. (b) Proposed dimerization reaction by vinylnaphthalene.

This hypothesis was tested by heating an exposed film (total exposure dose 10 J/cm^2) at 160 °C for periods of time up to 2 hours to see whether heating resulted in the

recovery of conjugated bonds (see **Scheme 5.2(a)**). The absorbance was monitored by UV-Vis. As shown in **Figure 5.12**, heating for up to 2 hours did not change the UV-Vis spectrum significantly. The original peak at higher wavelengths (**Figure 5.9**, before exposure, red line) was never recovered, indicating that conjugation was not regained. This result suggests that this first hypothesis is not correct, and the observed PVN thin film crosslinking is not due to photodimerization.

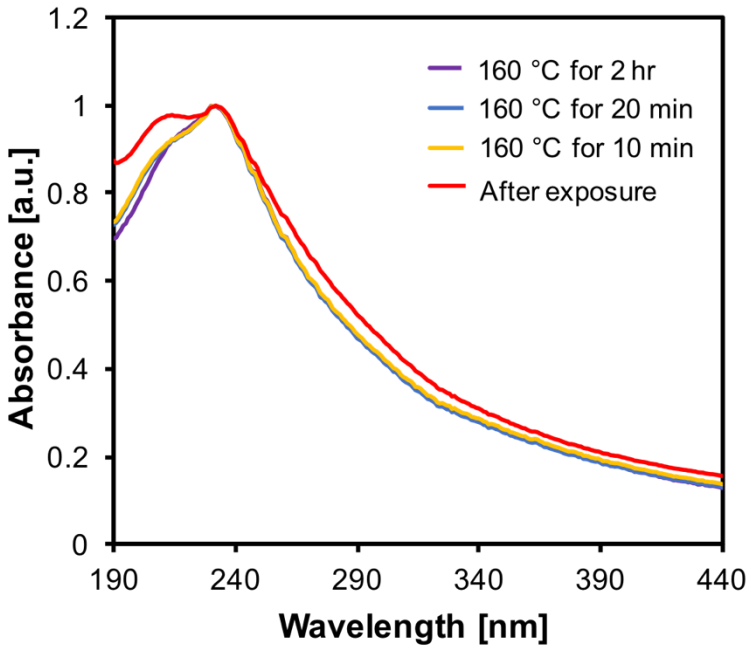

Figure 5.12 UV-Vis data for a PVN thin film after exposure to 10 mJ/cm^2 of light exposure and subsequent heating at 160 C for up to 2 hours. The spectrum shape was not drastically changed after 2 hours of heating, suggesting that the PVN thin film did not undergo any further changes. In turn, this indicates that the crosslinking observed in the PVN thin film was not due to photodimerization of the naphthalene units.

The second hypothesis for explaining the crosslinking in the PVN thin film upon UV light exposure is the formation of an intermediate endoperoxide compound, which decomposes to form radicals upon exposure to light and heat.[11] The formed radicals may

then react with nearby polymer chains to crosslink the film. Oxygen is required to form endoperoxide; small amounts of oxygen may have been trapped in the BCP sample because the sample was assembled under ambient air conditions.

The first test was designed to determine whether an oxygen-containing intermediate is formed. A PVN thin film was irradiated under a nitrogen atmosphere under otherwise identical conditions. As illustrated below in **Figure 5.13**, the UV-Vis spectra did not change significantly. Also, the film was readily washed off with THF, indicating that crosslinking did not occur. Thus, oxygen appears to be a key component to the crosslinking reaction.

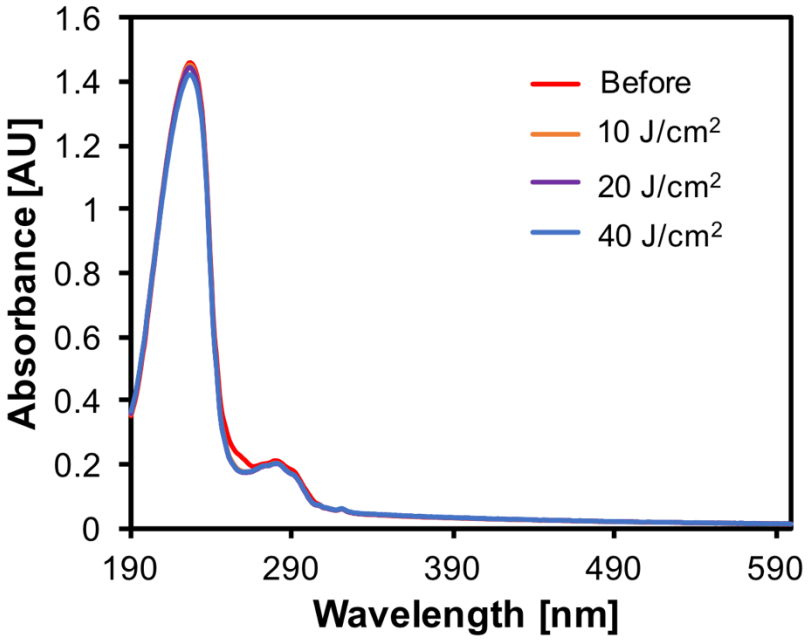

Figure 5.13 UV-Vis data for a PVN homopolymer sample before exposure (red line) and after various doses of light exposure under a nitrogen atmosphere.

A contrast curve for PVN and PS homopolymers was created as an aid to elucidate the molecular actions during light exposure in an ambient air atmosphere (**Figure 5.14**). Various doses of UV were exposed onto polymer films and then they were subsequently

washed with good solvents. The contrast curves shown in **Figure 5.14** were constructed by measuring film thicknesses before and after the solvent wash step using ellipsometry. PS showed negligible amounts of crosslinking (gel fraction of about 0%), while the PVN gel fraction increased to a maximum of about 60% at about 20 W/cm^2 of light exposure, then decreased thereafter. The increase in gel fraction is hypothesized to be due to endoperoxide forming upon heating in the presence of oxygen, decomposing to form radicals, and these radicals attacking other VN units to crosslink. At the same time, the extensive light exposure is causing the polymer backbone to simultaneously undergo chain scission. It is hypothesized that the crosslinking reaction dominates at first, then chain scission dominates, leading to the observed contrast curve. Neither PVN nor PS exhibited a significant gel fraction when the identical procedure was carried out in a nitrogen atmosphere.

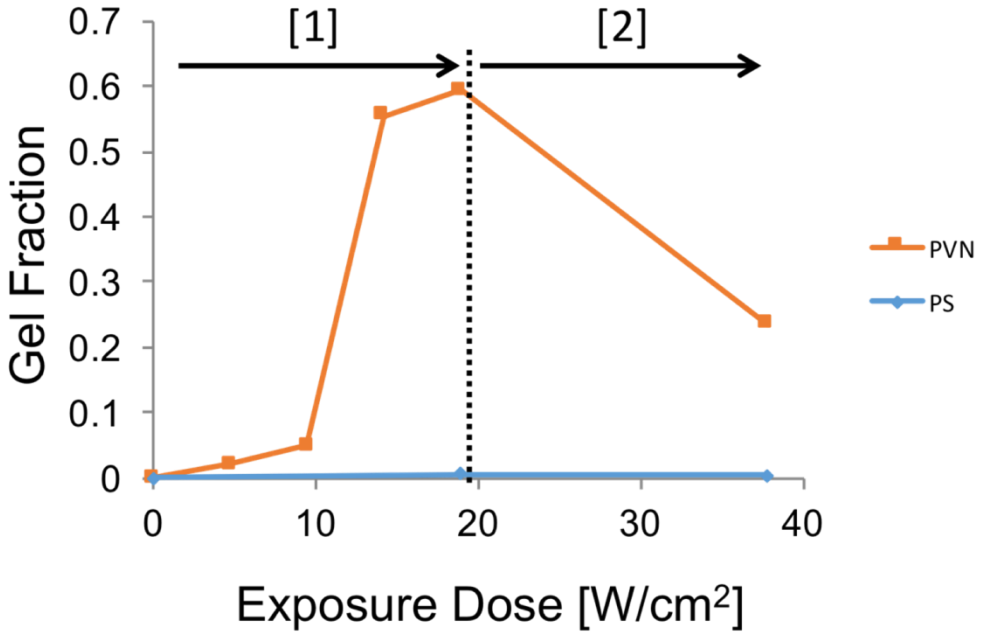

Figure 5.14 Contrast curve for PS and PVN homopolymers under ambient conditions. For PVN, the gel fraction increased until a maximum of about 60% after 20 W/cm^2 of exposure [1], then decreased afterwards [2]. It is hypothesized that PVN is crosslinking in section [1], and chain scission is occurring in section [2].

The photochemistry experiments outlined heretofore have supported the hypothesis that the crosslinking is due to oxygen interacting with the VN units of the polymer chain. Thus, the thin film annealing experiments outlined in the previous chapter were performed either in an enclosed oven in air (no light), or in a vacuum chamber (no light or oxygen). Perpendicular features observed with the samples were annealed under these conditions, as shown in the previous chapter. In addition, after these experiments, all PSVN-PMMA samples were stored in glass jars wrapped with aluminum foil to prevent degradation.

I posit that a similar mechanism leads to the degradation of the BCP samples when they were heated during the SAXS experiments. While UV light can excite O_2 to singlet oxygen, which can then react with VN to form an intermediate endoperoxide radical that

can cause subsequently promote crosslinking or chain scission,[12,13] X-rays can produce free radicals and ionic species, which can then lead to indiscriminate backbone chain scission and aromatic crosslinking.[3]

Separating the heating and exposure steps solved the degradation issue because the incident beam area of the X-ray beam is very small, and the BCP is kinetically frozen below its glass transition temperature. When the sample was heated during exposure, the ionization products were both more likely to form and free to diffuse within the liquid BCP sample, wreaking havoc on the polymer structure.[14] When the sample was kept at room temperature during exposure, the ionization products could not diffuse within the solid BCP matrix. Upon the subsequent thermal annealing step, the small amount of ionization products produced during the exposure could diffuse through the sample, but because the incident beam area is so small, the effects on the total BCP sample were negligible.

5.4 CONCLUSIONS

The degradation of the PSVN-PMMA sample during SAXS data collection to determine the χ parameter was likely caused by the X-rays ionizing the small amount of oxygen in the BCP sample. When the BCP sample was heated in situ, the ionization products had the mobility to diffuse during the exposure, causing massive amounts of the sample to decompose. When the heating and exposure steps were separated, the problem was mitigated, and χ SAXS data was successfully taken, as shown in Chapter 4.

UV exposure of PVN in the presence of oxygen caused an intermediate endoperoxide compound to form. During UV light exposure, the PVN thin film first crosslinked, then experienced chain scission. To prevent these detrimental reactions, thin film annealing was successfully performed in completely enclosed ovens or in a vacuum oven.

5.5 ACKNOWLEDGEMENTS

I would like to acknowledge my lab mate and good friend, Chae Bin Kim, for his invaluable advice and experimental help in collecting the data reported in this chapter.

5.6 REFERENCES

(1) McCalden, R. W.; MacDonald, S. J.; Rorabeck, C. H.; Bourne, R. B.; Chess, D. G.; Charron, K. D. Wear Rate of Highly Cross-Linked Polyethylene in Total Hip Arthroplasty. A Randomized Controlled Trial. *J. Bone Joint Surg. Am.* **2009**, *91* (4), 773–782.

(2) Davies, K. J. a. Protein Damage and Degradation by Oxygen Radicals. *J. Biol. Chem.* **1987**, *262* (20), 9914–9920.

(3) Reichmanis, E.; Frank, C. W.; O'Donnell, J. H.; Hill, D. J. T. Radiation Effects on Polymeric Materials. In *Irradiation of Polymeric Materials*; 1993; Vol. 527, pp 1–8.

(4) Coffey, T.; Urquhart, S. G.; Ade, H. Characterization of the Effects of Soft X-Ray Irradiation on Polymers. *J. Electron Spectrosc.* **2002**, *122* (1), 65–78.

(5) Chien, S. H.; Cheng, M. F.; Lau, K. C.; Li, W. K. Theoretical Study of the Diels-Alder Reactions between Singlet (1Δg) Oxygen and Acenes. *J. Phys. Chem. A* **2005**, *109* (33), 7509–7518.

(6) Scientific Committee on Emerging and Newly Identified Health Risks. *Light Sensitivity*; 2008.

(7) Shimadzu. The Relationship Between UV-VIS Absorption and Structure of Organic Compounds http://www.shimadzu.com/an/uv/support/uv/ap/apl.html (accessed Jan 1, 2016).

(8) O'Donnell, M. Photodimerization of Solid Anthracene. *Nature* **1968**, *218*, 460–461.

(9) Tomlinson, W. J.; Chandross, E. a; Fork, R. L.; Pryde, C. a; Lamola, a a. Reversible Photodimerization: A New Type of Photochromism. *Appl. Opt.* **1972**, *11* (3), 533–548.

(10) Breton, G. W.; Vang, X. Photodimerization of Anthracene : A [4 S + 4 S] Photochemical Cycloaddition. *J. Chem. Educ.* **1998**, *75* (1), 81–82.

(11) Turro, N. J.; Chow, M.; Rigaudyo, J. Mechanism of Thermolysis of Endoperoxides of Aromatic Compounds. Activation Parameters, Magnetic Field, and Magnetic Isotope Effectst. *J. Am. Chem. Soc.* **1981**, *103* (4), 7218–7224.

(12) Lauer, A.; Dobryakov, A. L.; Kovalenko, S. a; Fidder, H.; Heyne, K. Dual Photochemistry of Anthracene-9,10-Endoperoxide Studied by Femtosecond Spectroscopy. *Phys. Chem. Chem. Phys.* **2011**, *13* (19), 8723–8732.

(13) Balta, D. K.; Arsu, N.; Yagci, Y.; Sundaresan, A. K.; Jockusch, S.; Turro, N. J. Mechanism of Photoinitiated Free Radical Polymerization by Thioxanthone-Anthracene in the Presence of Air. *Macromolecules* **2011**, *44* (8), 2531–2535.

(14) Kim, C. Bin; Janes, D. W.; McGuffin, D. L.; Ellison, C. J. Surface Energy Gradient Driven Convection for Generating Nanoscale and Microscale Patterned Polymer Films Using Photosensitizers. *J. Polym. Sci. Part B Polym. Phys.* **2014**, *52* (18), 1195–1202.

Chapter 6: Future Works

As previous chapters in this document have demonstrated, block copolymers are an attractive, potential solution for manufacturing the nanoimprint templates necessary for implementing bit pattern magnetic recording, which could carry the hard disk drive industry to areal densities of 5 Tbit/in^2 and beyond.[1] Many of the other patterning alternatives that can achieve such small features (5-10 nm),[2] such as EUV,[3] require immense capital investment in the form of tools whose arrival have been delayed almost a decade.[4] In comparison, BCPs are cost-effective because each thin film is spin coated out of a dilute solution, and 1 L of BCP solution requires only 10 g of BCP.

Not every BCP is lithographically useful; as mentioned in the introduction, there are some minimum criteria that should be satisfied in order for a BCP to be lithographically useful:

6. Form a lithographically useful morphology
7. Form features that are small enough to be useful for applications
8. Perpendicular domain orientations in thin films
9. Etch selectivity and resistance for ease of pattern transfer
10. Ability to be aligned over large areas

So far, in this dissertation, four BCPs were assessed for their potential industrial usefulness: poly(trimethylsilyl styrene-*block*-lactide) (PTMSS-PLA), poly(trimethylsilyl styrene-*block*-isoprene) (PTMSS-PI), poly(pentamethydisilyl styrene-*block*-ethyl glycolide) (PDSS-PEGL), and poly((styrene–*random*-vinylnaphthalene)-*block*-methyl methacrylate) (PSVN-PMMA). While each aforementioned BCP has its strengths and improved upon existing BCPs, none of the four hit all five minimum criteria. To that end, this chapter

provides some ideas for future work that may increase the industrial worth of these materials.

6.1 Directed Self-Assembly

Directed self-assembly (DSA) has been demonstrated many times in the literature[5–7] to successfully align BCP domains to form device-useful structures over a large area. However, none of the BCPs described in this dissertation have been aligned, and this is a crucial step if any of these polymers are to be industrially useful. Thus, the next step in demonstrating the viability of these BCPs is DSA for all of these polymers.

There are two common routes for DSA, chemoepitaxy and graphoepitaxy, and mentioned in Chapter 1. Many members of this project have successfully demonstrated chemoepitaxy for other silicon-containing polymers,[8,9] and it is an ongoing area of investigation. While PSVN-PMMA has not been aligned by DSA, its cousin, PS-PMMA, has been successfully aligned by many DSA strategies.[10] Thus, the next step for assessing the lithographic usefulness of PSVN-PMMA is testing whether the strategies and conditions that worked for DSA of PS-PMMA can be adopted for PSVN-PMMA. As demonstrated in Chapter 4, the same SNTs that were used to perpendicularly orient PS-PMMA could also be used to orient some PSNV-PMMA. Therefore, it is hoped that the DSA conditions for PS-PMMA could provide a good starting point, if not the entire solution, for DSA of PSVN-PMMA.

After finding the correct conditions for DSA of the polymers studied in this dissertation, defect density is the next major concern in terms of industrial implementation of BCP lithography.[11] For example, for the HDD industry, the read/write head must be able to find the next bit based on the location of any arbitrary bit, and the acceptable defect density for the final magnetic disk is less than 1 in 1000 bits.[10] Fine-tuning the DSA

conditions to reduce defectivity can be an iterative process with much trial and error, such as selecting the best brush chemistry for chemoepitaxy and the best trench depth for graphoepitaxy.[12] One ongoing area of research for chemoepitaxy is optimizing the e-beam writing conditions and pattern multiplication processes such that low defect BCP patterns can be assembled on the least number of e-beam-patterned lines.[13] Because the e-beam write step is the most time-consuming and expensive part of this process, optimizing this step has the greatest impact on increasing throughput.

6.2 Increasing Etch Contrast and Resistance of PSVN-PMMA

While PSVN-PMMA can be perpendicularly oriented with only thermal annealing and can form smaller features than PS-PMMA, no etch studies have yet been conducted on this BCP. A longtime collaborator of the group, Stephen Sirard of Lam Research Corporation, has demonstrated fantastic etch results for PS-PMMA,[14] and I hope that the recipe can be tailored for PSVN-PMMA.

In Chapter 5, it was demonstrated that the VN moiety could form endoperoxide upon UV (254 nm) exposure and subsequent heating in the presence of oxygen, which leads to an interesting opportunity. Drawing inspiration from the many silicon-containing BCPs that have been studied within the group, the etch contrast between the PSVN block and the PMMA block can be increased by incorporating silicon into the PSVN block via surface chemistry. Incorporating silicon onto the PSVN block would also serve to increase the etch resistance of the remaining block after PMMA is removed. After the PSVN-PMMA is perpendicularly oriented in thin films, the BCP can be heated to form endoperoxides or other oxidative functional groups at the surface of the PSVN regions, and silicon-containing brushes can be selectively grafted to the PSVN by forming a covalent bond with the oxygen containing functional groups.

Some preliminary work shows that this is a feasible method of introducing silicon to the PSVN block after the BCP has been oriented in a thin film. Water contact angle measurements were taken on as-spun PVN thin films, light exposed PVN thin films, and light exposed PVN thin films after various silane treatments. The silanes were spin coated on the exposed PVN thin films, washed with toluene, and heated for 1 minute at 120 °C. As shown in **Figure 6.1**, the water contact angle of PVN changed after light exposure. After grafting trimethylchlorosilane and (3-aminopropyl)triethoxysilane (APTES) on two different exposed samples, the water contact angle changed significantly, indicating that the chemical makeup of the thin film surface was indeed modified.

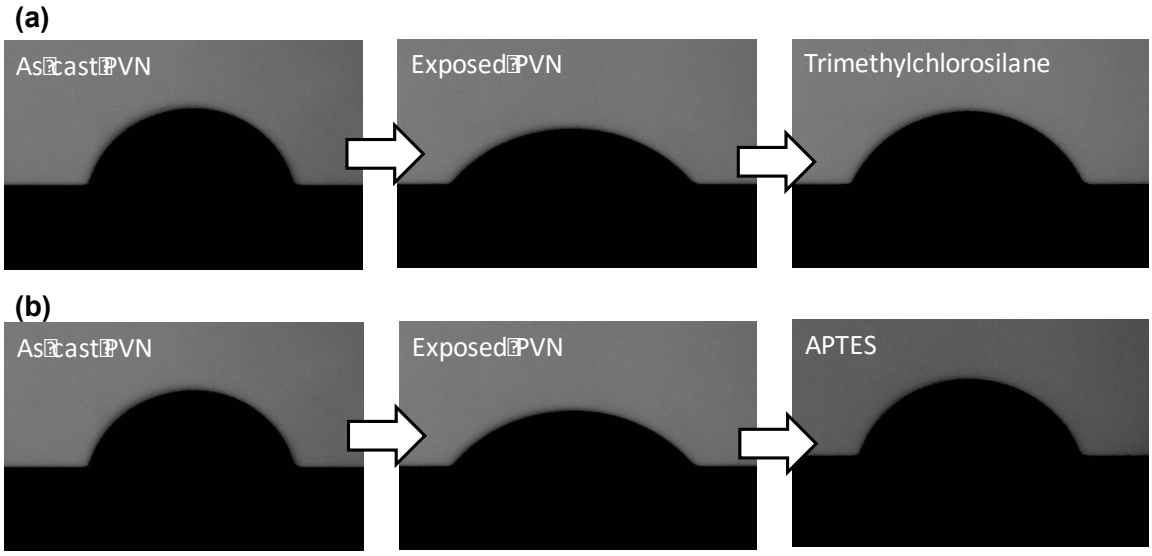

Figure 6.1 Water contact angle images of as cast PVN thin film, exposed PVN thin film, and exposed PVN thin film with grafted (a) trimethylchlorosilane and (b) APTES.

Many additional tests will need to be conducted to determine the feasibility of this proposal. First, water contact angle is a poor quantitative measurement of surface grafting. However, as a first test, it is sufficient to provide qualitative proof that this avenue may be worth pursuing. Next, these preliminary experiments used pure PVN homopolymer, which

presents the maximum grafting sites for silanes. When used on BCP thin films, where VN accounts for as little as 7 mol% of the BCP, the results may be vastly different. Further experiments are needed to optimize grafting density on BCP thin films. Finally, a monolayer of silicon on the surface of the BCP thin film may not be sufficient to provide suitable etch contrast between the two blocks because the inorganic etch barrier takes a few seconds to form, during which time 5 nm or more of the thin film is etched away. In this case, the endoperoxides could be exploited to initiate other secondary reactions or polymerizations, of which silane grafting is an example. Using the endoperoxide as an initiation site could also increase the silicon density at the top of the BCP, providing enhanced etch contrast.

6.3 Doping Small Molecules into PSVN-PMMA

A quick, interesting possible avenue of investigation would be ascertaining whether doping small amounts of pyrene or graphene into the PVN block of PSVN-PMMA could induce phase transitions and increase the effective χ parameter. This is inspired by a study by Aissou et al. that demonstrated doping small amounts of bipyridine into a sugar-*block*-polystyrene BCP induces phase transitions of the BCP.[19] For example, if introducing a low concentration of a small molecule into the PSVN block of a disordered PSVN-PMMA BCP could induce order, even smaller features could be realized.

However, doping small molecules into the BCP could also selectively plasticize the block it prefers, which could drastically change the surface energy of that block. In addition, doping of small molecules could also change the etch properties of the block it prefers, which might be detrimental or advantageous for the intended application. Therefore, careful proof of concept experiments should be designed and conducted before investing copious time and energy pursuing this path.

6.4 Introducing Self-Interaction in the PMMA Block of PSVN-PMMA

PSVN-PMMA demonstrated that enhancing the self-interaction of one block of a BCP is a viable strategy for increasing the BCP's χ parameter. A potential future project could investigate how increasing self-interaction of both blocks affects the χ parameter of the BCP. For example, many studies have shown that introducing hydrogen bonding in a block affects the microphase segregation behavior of the BCP.[15,16] Therefore, an interesting future work could involve including hydrogen bonding in the PMMA block.

Many groups have studied poly(styrene-*block*-methacrylic acid) (PS-PMAA) in the context of micelles for drug delivery applications.[17,18] Drawing inspiration from their work, small amounts of MAA could be included in the PMMA block of PSVN-PMMA to introduce self-interaction in that block, as shown in **Figure 6.2**. However, because PS-PMAA readily forms micelles in solution, there is likely a maximum amount of MAA that can be incorporated in PMMA. Above that maximum amount, the BCP will likely not dissolve in common spin coating solvents, as it will form micelles instead.

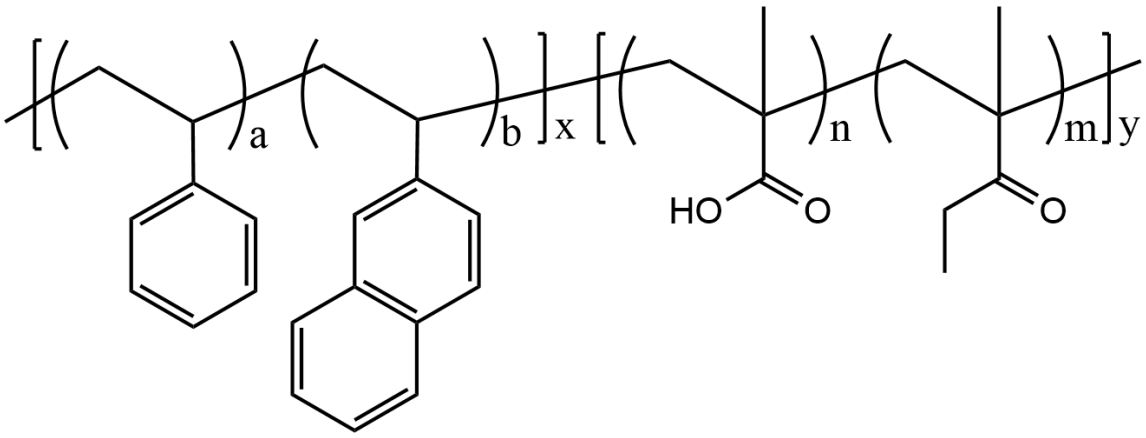

Figure 6.2 Proposed BCP that incorporates self-interaction into both blocks.

Therefore, the first test will be to try to incorporate a modest amount of PMAA into the PMMA block of PS-PMMA (around 20 mol%) to see whether this poly(styrene-*block*-(methyl methacrylate-*random*-methacrylic acid)) (PS-PMMAMAA) will form micelles in toluene or other common spin coating solvents, such as cyclopentanone, MIBK, PGMEA, α-methylene-γ-butyrolactone, and dioxane. If this PS-PMMAMAA cannot be dissolved in spin coating solvents, it cannot be used for thin film applications, rendering it useless for the application at hand.

Provided the BCP can be spin coated, the next step would be to determine its χ parameter. If there is an increase compared to PS-PMMA, the PMMAMAA block can be added to the PSVN block to create PSVN-PMMAMAA, which would possess self-interactions in both blocks: π interactions in the PSVN block and hydrogen bonding interactions in the PMMAPMAA block. These effects should both theoretically increase the χ parameter of the BCP. It would be interesting to see how the effects on the χ parameter add up: would the increase from the PSVN π interaction add linearly to the expected increase from the PMMAMAA hydrogen bonding? Or would there be some sort of synergistic effect that leads to exponential increase in χ when both blocks have self-interaction? Conversely, would the self-interactions of the two blocks somehow cancel each other out in some way?

Finally, the thin film performance of the proposed PSVN-PMMAMAA BCP must be evaluated. As mentioned before, one of the main advantages of PS-PMMA is its simple orientation procedure by simply thermal annealing. If the proposed BCP can no longer be oriented by thermal annealing, there is little advantage to choosing to work with a PS-PMMA-derivative BCP as opposed to working with another high-χ BCP, such as one that can be oriented with top coats.

6.5 REFERENCES

(1) Richter, H. J.; Dobin, A. Y.; Gao, K.; Heinonen, O.; Van De Veerdonk, R. J.; Lynch, R. T.; Xue, J.; Weller, D. K.; Asselin, P.; Erden, M. F.; Brockie, R. M. Recording on Bit-Patterned Media at Densities of 1Tb/in2 and beyond. *INTERMAG 2006 - IEEE Int. Magn. Conf.* **2006**, *42* (10), 721.

(2) Shiroishi, Y.; Fukuda, K.; Tagawa, I.; Iwasaki, H.; Takenoiri, S.; Tanaka, H.; Mutoh, H.; Yoshikawa, N. Future Options for HDD Storage. *IEEE Trans. Magn.* **2009**, *45* (10), 3816–3822.

(3) Wagner, C.; Harned, N. EUV Lithography: Lithography Gets Extreme. *Nat. Photonics* **2010**, *4* (1), 24–26.

(4) Martini, M. The long and tortuous path of EUV lithography to full production.

(5) Stoykovich, M. P.; Kang, H.; Daoulas, K. C.; Liu, G.; Liu, C. C.; De Pablo, J. J.; Müller, M.; Nealey, P. F. Directed Self-Assembly of Block Copolymers for Nanolithography: Fabrication of Isolated Features and Essential Integrated Circuit Geometries. *ACS Nano* **2007**, *1* (3), 168–175.

(6) Hu, H.; Gopinadhan, M.; Osuji, C. O. Directed Self-Assembly of Block Copolymers: A Tutorial Review of Strategies for Enabling Nanotechnology with Soft Matter. *Soft Matter* **2014**, *10* (22), 3867–3889.

(7) Luo, M.; Epps, T. H. Directed Block Copolymer Thin Film Self-Assembly: Emerging Trends in Nanopattern Fabrication. **2013**.

(8) Maher, M. J.; Rettner, C. T.; Bates, C. M.; Blachut, G.; Carlson, M. C.; Durand, W. J.; Ellison, C. J.; Sanders, D. P.; Cheng, J. Y.; Willson, C. G. Directed Self-Assembly of Silicon-Containing Block Copolymer Thin Films. *ACS Appl. Mater. Interfaces* **2015**, *7* (5), 3323–3328.

(9) Cushen, J.; Wan, L.; Blachut, G.; Maher, M. J.; Albrecht, T. R.; Ellison, C. J.; Willson, C. G.; Ruiz, R. Double-Patterned Sidewall Directed Self-Assembly and Pattern Transfer of Sub-10 Nm PTMSS-B-PMOST. *ACS Appl. Mater. Interfaces* **2015**, *7* (24), 13476–13483.

(10) Wan, L.; Ruiz, R.; Gao, H.; Patel, K. C.; Albrecht, T. R.; Yin, J.; Kim, J.; Cao, Y.; Lin, G. The Limits of Lamellae-Forming PS- B -PMMA Block Copolymers for Lithography. *ACS Nano* **2015**, *9* (7), 7506–7514.

(11) Bencher, C.; Smith, J.; Miao, L.; Cai, C.; Chen, Y.; Cheng, J. Y.; Sanders, D. P.; Tjio, M.; Truong, H. D.; Holmes, S.; Hinsberg, W. D. Self-Assembly Patterning for Sub-15nm Half-Pitch : A Transition from Lab to Fab. *Spie* **2011**, *7970*, 79700F – 79700F – 9.

(12) Trombly, D. M.; Pryamitsyn, V.; Ganesan, V. Surface Energies and Self-Assembly of Block Copolymers on Grafted Surfaces. *Phys. Rev. Lett.* **2011**, *107* (14), 1–5.

(13) Cheng, J. K.; Rettner, C. T.; Sanders, D. P.; Kim, H. C.; Hinsberg, W. D. Dense Self-Assembly on Sparse Chemical Patterns: Rectifying and Multiplying Lithographic Patterns Using Block Copolymers. *Adv. Mater.* **2008**, *20* (16), 3155–3158.

(14) Sirard, S.; Azarnouche, L.; Gurer, E.; Durand, W.; Maher, M.; Mori, K.; Blachut, G.; Janes, D.; Asano, Y.; Someya, Y.; Hymes, D.; Graves, D.; Ellison, C. J.; Willson, C. G. Interactions between Plasma and Block Copolymers Used in Directed Self-Assembly Patterning. **2016**, *9782*, 97820K.

(15) Han, S. H.; Pryamitsyn, V.; Bae, D.; Kwak, J.; Ganesan, V.; Kim, J. K. Highly Asymmetric Lamellar Nanopatterns via Block Copolymer. *ACS Nano* **2012**, *6* (9), 7966–7972.

(16) Tang, C.; Hur, S. M.; Stahl, B. C.; Sivanandan, K.; Dimitriou, M.; Pressly, E.; Fredrickson, G. H.; Kramer, E. J.; Hawker, C. J. Thin Film Morphology of Block Copolymer Blends with Tunable Supramolecular Interactions for Lithographic Applications. *Macromolecules* **2010**, *43* (6), 2880–2889.

(17) Erhardt, R.; Zhang, M.; Böker, A.; Zettl, H.; Abetz, C.; Frederik, P.; Krausch, G.; Abetz, V.; Müller, A. H. E. Amphiphilic Janus Micelles with Polystyrene and Poly(methacrylic Acid) Hemispheres. *J. Am. Chem. Soc.* **2003**, *125* (11), 3260–3267.

(18) Qin, A.; Tian, M.; Ramireddy, C.; Webber, S. E.; Munk, P. Polystyrene-Poly(methacrylic Acid) Block Copolymer Micelles. *Macromolecules* **1994**, *27* (1), 120–126.

(19) Aissou, K.; Otsuka, I.; Rochas, C.; Fort, S.; Halila, S.; Borsali, R. Nano-Organization of Amylose-B-Polystyrene Block Copolymer Films Doped with Bipyridine. *Langmuir* **2011**, *27* (7), 4098–4103.

References

(1) Moore, G. E. Cramming More Components onto Integrated Circuits. *Electronics* **1965**, *38* (5), 114–117.

(2) Walter, C. Kryder's Law. *Scientific American*. 2005.

(3) Dobisz, E. A.; Bandic, Z. Z.; Tsai-Wei Wu; Albrecht, T. Patterned Media: Nanofabrication Challenges of Future Disk Drives. *Proc. IEEE* **2008**, *96* (11), 1836–1846.

(4) Wood, R. The Feasibility of Magnetic Recording at 1 Terabit per Square Inch. *IEEE Trans. Magn.* **2000**, *36* (1), 917–923.

(5) Weller, D.; Moser, A. Thermal Effect Limits in Ultrahigh-Density Magnetic Recording. *IEEE Trans. Magn.* **1999**, *35* (6), 4423–4439.

(6) Alcorn, P. Toshiba Achieves Record Areal Density in 2.5-Inch HDDs.

(7) Ross, C. A. Patterned Magnetic Recording Media. *Annu. Rev. Mater. Res.* **2001**, *31*, 203–235.

(8) ASTC. ASTC Technology Roadmap.

(9) Wood, R. *Shingled Magnetic Recording and Two-Dimensional Magnetic Recording*; 2010.

(10) Krishnan, A. R.; Radhakrishnan, R.; Vasic, B. Read Channel Modeling for Detection in Two-Dimensional Magnetic Recording Systems. *IEEE Trans. Magn.* **2009**, *45* (10), 3679–3682.

(11) Chan, K. S.; Radhakrishnan, R.; Eason, K.; Elidrissi, M. R.; Miles, J. J.; Vasic, B.; Krishnan, A. R. Channel Models and Detectors for Two-Dimensional Magnetic Recording. *IEEE Trans. Magn.* **2010**, *46* (3 PART 1), 804–811.

(12) Hwang, E.; Negi, R.; Kumar, B. V. K. V. Signal Processing for Near 10 Tbit/in<formula Formulatype="inline"> <img src="/images/tex/732.gif" alt="^{2}"> </formula> Density In<newline/> Two-Dimensional Magnetic Recording (TDMR). *IEEE Trans. Magn.* **2010**, *46* (6), 1813–1816.

(13) Wood, R.; Williams, M.; Kavcic, A.; Miles, J. The Feasibility of Magnetic Recording at 10 Terabits per Square Inch on Conventional Media. *IEEE Trans. Magn.* **2009**, *45* (2), 917–921.

(14) Amer, A.; Holliday, J.; Long, D. D. E.; Miller, E. L.; Pâris, J. F.; Schwarz, T. Data Management and Layout for Shingled Magnetic Recording. *IEEE Trans. Magn.* **2011**, *47* (10), 3691–3697.

(15) Hall, D.; Marcos, J. H.; Coker, J. D. Data Handling Algorithms for Autonomous Shingled Magnetic Recording HDDs. *IEEE Trans. Magn.* **2012**, *48* (5 PART 1), 1777–1781.

(16) Shimpi, A. L. Seagate to Ship 5TB HDD in 2014 using Shingled Magnetic Recording http://www.anandtech.com/show/7290/seagate-to-ship-5tb-hdd-in-2014-using-shingled-magnetic-recording/.

(17) Gasior, G. Shingled platters breathe helium inside HGST's 10TB hard drive.

(18) Gibson, G.; Ganger, G. *Principles of Operation for Shingled Disk Devices*; 2011.

(19) Rottmayer, R. E.; Batra, S.; Buechel, D.; Challener, W. A.; Hohlfeld, J.; Kubota, Y.; Li, L. L. L.; Lu, B. L. Bin; Mihalcea, C.; Mountfield, K.; Pelhos, K.; Peng, C. P. C.; Rausch, T.; Seigler, M. A.; Weller, D.; Yang, X. Y. X. Heat-Assisted Magnetic Recording. *IEEE Trans. Magn.* **2006**, *42* (10), 2417–2421.

(20) Kryder, M. H.; Gage, E. C.; McDaniel, T. W.; Challener, W. A.; Rottmayer, R. E.; Ganping Ju; Yiao-Tee Hsia; Erden, M. F. Heat Assisted Magnetic Recording. *Proc. IEEE* **2008**, *96* (11), 1810–1835.

(21) Pan, L.; Bogy, D. B. Data Storage: Heat-Assisted Magnetic Recording. *Nat. Photonics* **2009**, *3* (4), 189–190.

(22) Stipe, B. C.; Strand, T. C.; Poon, C. C.; Balamane, H.; Boone, T. D.; Katine, J. a.; Li, J.-L.; Rawat, V.; Nemoto, H.; Hirotsune, A.; Hellwig, O.; Ruiz, R.; Dobisz, E.; Kercher, D. S.; Robertson, N.; Albrecht, T. R.; Terris, B. D. Magnetic Recording at 1.5 Pb m−2 Using an Integrated Plasmonic Antenna. *Nat. Photonics* **2010**, *4* (7), 484–488.

(23) Shilov, A. Hard Disk Drives with HAMR Technology Set to Arrive in 2018 http://www.anandtech.com/show/9866/hard-disk-drives-with-hamr-technology-set-to-arrive-in-2018.

(24) Shiroishi, Y.; Fukuda, K.; Tagawa, I.; Iwasaki, H.; Takenoiri, S.; Tanaka, H.; Mutoh, H.; Yoshikawa, N. Future Options for HDD Storage. *IEEE Trans. Magn.* **2009**, *45* (10), 3816–3822.

(25) Richter, H. J.; Dobin, A. Y.; Gao, K.; Heinonen, O.; Van De Veerdonk, R. J.; Lynch, R. T.; Xue, J.; Weller, D. K.; Asselin, P.; Erden, M. F.; Brockie, R. M. Recording on Bit-Patterned Media at Densities of 1Tb/in2 and beyond. *INTERMAG 2006 - IEEE Int. Magn. Conf.* **2006**, *42* (10), 721.

(26) Yang, X.; Xu, Y.; Seiler, C.; Wan, L.; Xiao, S. Toward 1Tdot ⁄ in.2 Nanoimprint Lithography for Magnetic Bit-Patterned Media: Opportunities and Challenges. *J. Vac. Sci. Technol. B* **2008**, *26* (2008), 2604–2610.

(27) Ruiz, R.; Kang, H.; Detcheverry, F. A.; Dobisz, E.; Kercher, D. S.; Albrecht, T. R.; de Pablo, J. J.; Nealey, P. F. Density Multiplication and Improved Lithography by Directed Block Copolymer Assembly. *Science (80-.).* **2008**, *321* (5891), 936–939.

(28) Ruiz, R.; Dobisz, E.; Albrecht, T. R. Rectangular Patterns Using Block Copolymer Directed Assembly for High Bit Aspect Ratio Patterned Media. *ACS Nano* **2011**, *5* (1), 79–84.

(29) Wan, L.; Ruiz, R.; Gao, H.; Patel, K. C.; Lille, J.; Zeltzer, G.; Dobisz, E. a.; Bogdanov, A.; Nealey, P. F.; Albrecht, T. R. Fabrication of Templates with Rectangular Bits on Circular Tracks by Combining Block Copolymer Directed Self-Assembly and Nanoimprint Lithography. *J. Micro/Nanolithography, MEMS, MOEMS* **2012**, *11* (3), 031405–1.

(30) Pease, B. R. F.; Chou, S. Y. Lithography and Other Patterning Techniques for Future Electronics. *Proc. IEEE* **2008**, *96* (2).

(31) Neisser, M.; Wurm, S. ITRS Lithography Roadmap: 2015 Challenges. *Adv. Opt. Technol.* **2015**, *4* (4), 235–240.

(32) Bates, C. M.; Maher, M. J.; Janes, D. W.; Ellison, C. J.; Willson, C. G. Block Copolymer Lithography. *Macromolecules* **2014**, *47* (1), 2–12.

(33) Ji, S.; Liu, C.-C.; Liu, G.; Nealey, P. F. Molecular Transfer Printing Using Block Copolymers. *ACS Nano* **2010**, *4* (2), 599–609.

(34) Stoykovich, M. P.; Nealey, P. F. Block Copolymers and Conventional Lithography. *Mater. Today* **2006**, *9* (9), 20–29.

(35) Cushen, J. D.; Otsuka, I.; Bates, C. M.; Halila, S.; Fort, S.; Rochas, C.; Easley, J. A.; Rausch, E. L.; Thio, A.; Borsali, R.; Willson, C. G.; Ellison, C. J. Oligosaccharide/silicon-Containing Block Copolymers with 5 Nm Features for Lithographic Applications. *ACS Nano* **2012**, *6* (4), 3424–3433.

(36) Park, S.; Lee, D. H.; Xu, J.; Kim, B.; Hong, S. W.; Jeong, U.; Xu, T.; Russell, T. P. Macroscopic 10-Terabit-per-Square-Inch Arrays from Block Copolymers with Lateral Order. *Science* **2009**, *323* (February), 1030–1033.

(37) Kennemur, J. G.; Yao, L.; Bates, F. S.; Hillmyer, M. A. Sub‐5 Nm Domains in Ordered Poly(cyclohexylethylene)- Block - Poly(methyl Methacrylate) Block Polymers for Lithography. **2014**.

(38) Lee, J.; Kim, K.; Park, W. I.; Kim, B.-H.; Park, J. H.; Kim, T.-H.; Bong, S.; Kim, C.-H.; Chae, G.; Jun, M.; Hwang, Y.; Jung, Y. S.; Jeon, S. Uniform Graphene Quantum Dots Patterned from Self-Assembled Silica Nanodots. *Nano Lett.* **2012**, *12* (12), 6078–6083.

(39) Cochran, E. W.; Garcia-Cervera, C. J.; Fredrickson, G. H. Stability of the Gyroid Phase in Diblock Copolymers at Strong Segregation. *Macromolecules* **2006**, *39* (7), 2449–2451.

(40) Fredrickson, G. H.; Bates, F. S. Dynamics of Block Copolymers: Theory and Experiment. *Annu. Rev. Mater. Sci.* **1996**, *26* (1), 501–550.

(41) Matsen, M. W.; Bates, F. S. Unifying Weak- and Strong-Segregation Block Copolymer Theories. *Macromolecules* **1996**, *29* (4), 1091–1098.

(42) Park, M. Block Copolymer Lithography: Periodic Arrays of 1011 Holes in 1 Square Centimeter. *Science (80-.).* **1997**, *276* (5317), 1401–1404.

(43) Albert, J. N. L.; Epps III, T. H. Self-Assembly of Block Copolymer Thin Films. *Mater. Today* **2010**, *13* (6), 24–33.

(44) Mansky, P. Controlling Polymer-Surface Interactions with Random Copolymer Brushes. *Science (80-.).* **1997**, *275* (5305), 1458–1460.

(45) Park, S.; Kim, B.; Xu, J.; Hofmann, T.; Ocko, B. M.; Russell, T. P. Lateral Ordering of Cylindrical Microdomains Under Solvent Vapor. *Macromolecules* **2009**, *42* (4), 1278–1284.

(46) Maher, M. J.; Bates, C. M.; Blachut, G.; Sirard, S.; Self, J. L.; Carlson, M. C.; Dean, L. M.; Cushen, J. D.; Durand, W. J.; Hayes, C. O.; Ellison, C. J.; Willson, C. G. Interfacial Design for Block Copolymer Thin Films. *Chem. Mater.* **2014**, *26* (3), 1471–1479.

(47) Bates, C. M.; Seshimo, T.; Maher, M. J.; Durand, W. J.; Cushen, J. D.; Dean, L. M.; Blachut, G.; Ellison, C. J.; Willson, C. G. Polarity-Switching Top Coats Enable Orientation of Sub-10-Nm Block Copolymer Domains. *Science (80-.).* **2012**, *338* (6108), 775–779.

(48) Durand, W. J.; Blachut, G.; Maher, M. J.; Sirard, S.; Tein, S.; Carlson, M. C.; Asano, Y.; Zhou, S. X.; Lane, A. P.; Bates, C. M.; Ellison, C. J.; Willson, C. G. Design of High-χ Block Copolymers for Lithography. *J. Polym. Sci. Part A Polym. Chem.* **2015**, *53* (2), 344–352.

(49) Wu, S. Surface and Interfacial Tensions of Polymer Melts. II. Poly (Methyl Methacrylate), Poly (N-Butyl Methacrylate), and Polystyrene. *J. Phys. Chem.* **1970**, *I* (1960).

(50) Asakawa, K.; Hiraoka, T.; Hieda, H.; Sakurai, M.; Kamata, Y.; Naito, K. Nano-Patterning for Patterned Media Using Block-Copolymer. *J. Photopolym. Sci. Technol.* **2002**, *15* (3), 465–470.

(51) Jung, Y. S.; Ross, C. A. Orientation-Controlled Self-Assembled Nanolithography Using a Polystyrene-Polydimethylsiloxane Block Copolymer. *Nano Lett.* **2007**, *7* (7), 2046–2050.

(52) Stoykovich, M. P.; Kang, H.; Daoulas, K. C.; Liu, G.; Liu, C. C.; De Pablo, J. J.; Müller, M.; Nealey, P. F. Directed Self-Assembly of Block Copolymers for Nanolithography: Fabrication of Isolated Features and Essential Integrated Circuit Geometries. *ACS Nano* **2007**, *1* (3), 168–175.

(53) Yang, X. M.; Peters, R. D.; Nealey, P. F.; Solak, H. H.; Cerrina, F. Guided Self-Assembly of Symmetric Diblock Copolymer Films on Chemically Nanopatterned Substrates. *Macromolecules* **2000**, *33* (26), 9575–9582.

(54) Kim, S. O.; Solak, H. H.; Stoykovich, M. P.; Ferrier, N. J.; De Pablo, J. J.; Nealey, P. F. Epitaxial Self-Assembly of Block Copolymers on Lithographically Defined Nanopatterned Substrates. *Nature* **2003**, *424* (6947), 411–414.

(55) Bita, I.; Yang, J. K. W.; Jung, Y. S.; Ross, C. a; Thomas, E. L.; Berggren, K. K. Graphoepitaxy of Self-Assembled Block Copolymers on Two-Dimensional Periodic Patterned Templates. *Science* **2008**, *321* (5891), 939–943.

(56) Somervell, M.; Gronheid, R.; Hooge, J.; Nafus, K.; Delgadillo, P. R.; Thode, C.; Younkin, T.; Matsunaga, K.; Rathsack, B.; Scheer, S.; Nealey, P. Comparison of Directed Self-Assembly Integrations. *Adv. Resist Mater. Process. Technol. XXIX* **2012**, *8325*, 83250G (14 pp.).

(57) Albrecht, T. R.; Bedau, D.; Dobisz, E.; Gao, H.; Grobis, M.; Hellwig, O.; Kercher, D.; Lille, J.; Marinero, E.; Patel, K.; Ruiz, R.; Schabes, M. E.; Wan, L.; Weller, D.; Wu, T.-W. Bit Patterned Media at 1 Tdot/in<formula Formulatype="inline"><tex Notation="TeX">^{2}</tex></formula> and Beyond. *IEEE Trans. Magn.* **2013**, *49* (2), 773–778.

(58) Cheng, J. Y.; Ross, C. A.; Thomas, E. L.; Smith, H. I.; Vancso, G. J. Fabrication of Nanostructures with Long-Range Order Using Block Copolymer Lithography. *Appl. Phys. Lett.* **2002**, *81* (19), 3657–3659.

(59) Wang, J.; Chen, W.; Russell, T. P. Ion-Complexation-Induced Changes in the Interaction Parameter and the Chain Conformation of PS-B-PMMA Copolymers. *Society* **2008**, 4904–4907.

(60) Wan, L.; Ruiz, R.; Gao, H.; Patel, K. C.; Albrecht, T. R.; Yin, J.; Kim, J.; Cao, Y.; Lin, G. The Limits of Lamellae-Forming PS- B -PMMA Block Copolymers for Lithography. *ACS Nano* **2015**, *9* (7), 7506–7514.

(61) Ting, Y.-H.; Park, S.-M.; Liu, C.-C.; Liu, X.; Himpsel, F. J.; Nealey, P. F.; Wendt, A. E. Plasma Etch Removal of Poly(methyl Methacrylate) in Block Copolymer Lithography. *J. Vac. Sci. Technol. B Microelectron. Nanom. Struct.* **2008**, *26* (5), 1684.

(62) Liu, C. C.; Nealey, P. F.; Ting, Y. H.; Wendt, A. E. Pattern Transfer Using Poly(styrene-Block-Methyl Methacrylate) Copolymer Films and Reactive Ion Etching. *J. Vac. Sci. Technol. B* **2007**, *25* (6), 1963–1968.

(63) Chiang, W.-Y.; Lin, Y.-C. Synthesis and Characterization of Novel Copolymers with the Trimethylsilyl Group for Deep-UV Photoresists. *J. Appl. Polym. Sci.* **2002**, *83* (13), 2791–2798.

(64) Vert, M.; Schwach, G.; Engel, R.; Coudane, J. Something New in the Field of PLA / GA Bioresorbable Polymers? *J. Control. Release* **1998**, *53* (May 1997), 85–92.

(65) Zalusky, A. S.; Olayo-Valles, R.; Wolf, J. H.; Hillmyer, M. a. Ordered Nanoporous Polymers from Polystyrene-Polylactide Block Copolymers. *J. Am. Chem. Soc.* **2002**, *124* (43), 12761–12773.

(66) Dechy-Cabaret, O.; Martin-Vaca, B.; Bourissou, D. Controlled Ring-Opening Polymerization of Lactide and Glycolide. *Chem. Rev.* **2004**, *104* (12), 6147–6176.

(67) Wikimedia Commons. Lactide Stereoisomers Structural Formulae.

(68) Cushen, J. D.; Bates, C. M.; Rausch, E. L.; Dean, L. M.; Zhou, S. X.; Willson, C. G.; Ellison, C. J. Thin Film Self-Assembly of Poly(trimethylsilylstyrene- B - D , L -Lactide) with Sub-10 Nm Domains. *Macromolecules* **2012**, *45* (21), 8722–8728.

(69) Cushen, J. D. High Interaction Parameter Block Copolymers for Advanced Lithography, University of Texas at Austin, 2013.

(70) Cushen, J. D.; Wan, L.; Pandav, G.; Mitra, I.; Stein, G. E.; Ganesan, V.; Ruiz, R.; Willson, C. G.; Ellison, C. J. Ordering Poly(trimethylsilyl Styrene-Block- D,L -Lactide) Block Copolymers in Thin Films by Solvent Annealing Using a Mixture of Domain-Selective Solvents. *J. Polym. Sci. Part B Polym. Phys.* **2014**, *52* (1), 36–45.

(71) Cushen, J. D.; Bates, C. M.; Rausch, E. L.; Dean, L. M.; Zhou, S. X.; Willson, C. G.; Ellison, C. J. Thin Film Self-Assembly of Poly(trimethylsilylstyrene-B-D,L-Lactide) with Sub-10 Nm Domains. *Macromolecules* **2012**, *45* (21), 8722–8728.

(72) De Jong, S. J.; Arias, E. R.; Rijkers, D. T. S.; Van Nostrum, C. F.; Kettenes-Van den Bosch, J. J.; Hennink, W. E. New Insights into the Hydrolytic Degradation of Poly(lactic Acid): Participation of the Alcohol Terminus. *Polymer (Guildf).* **2001**, *42* (7), 2795–2802.

(73) Kim, S.; Nealey, P. F.; Bates, F. S. Decoupling Bulk Thermodynamics and Wetting Characteristics of Block Copolymer Thin Films. *ACS Macro Lett.* **2012**, *1* (1), 11–14.

(74) Hirao, A.; Loykulnant, S.; Ishizone, T. Recent Advance in Living Anionic Polymerization of Functionalized Styrene Derivatives. *Prog. Polym. Sci.* **2002**, *27* (8), 1399–1471.

(75) Worsfold, D. J.; Bywater, S. ANIONIC POLYMERIZATION OF ISOPRENE. *Can. J. Chem.* **1964**, *42* (12), 2884–2892.

(76) Zhang, J.; Clark, M. B.; Wu, C.; Li, M.; Trefonas, P.; Hustad, P. D. Orientation Control in Thin Films of a High-χ Block Copolymer with a Surface Active Embedded Neutral Layer. *Nano Lett.* **2016**, *16* (1), 728–735.

(77) Han, E.; Stuen, K. O.; La, Y. H.; Nealey, P. F.; Gopalan, P. Effect of Composition of Substrate-Modifying Random Copolymers on the Orientation of Symmetric and Asymmetric Diblock Copolymer Domains. *Macromolecules* **2008**, *41* (23), 9090–9097.

(78) Durand, W. J. Design, Synthesis, and Engineering of Advanced Materials for Block Copolymer Lithography, 2015.

(79) Huang, E.; Pruzinsky, S.; Russell, T. P.; Mays, J.; Hawker, C. J. Neutrality Conditions for Block Copolymer Systems on Random Copolymer Brush Surfaces. *Macromolecules* **1999**, *32* (16), 5299–5303.

(80) Koneripalli, N.; Singh, N.; Levicky, R.; Bates, F. S.; Gallagher, P. D.; Satija, S. K. Confined Block Copolymer Thin Films. *Macromolecules* **1995**, *28*, 2897–2904.

(81) Rafiee, J.; Mi, X.; Gullapalli, H.; Thomas, A. V.; Yavari, F.; Shi, Y.; Ajayan, P. M.; Koratkar, N. a. Wetting Transparency of Graphene. *Nat. Mater.* **2012**, *11* (3), 217–222.

(82) Ma, S. J.; Mannino, S. J.; Wagner, N. J.; Kloxin, C. J. Photodirected Formation and Control of Wrinkles on a Thiol − Ene Elastomer. *ACS Macro Lett.* **2013**, *2*, 474–477.

(83) Stafford, C. M.; Harrison, C.; Beers, K. L.; Karim, A.; Amis, E. J.; VanLandingham, M. R.; Kim, H. C.; Volksen, W.; Miller, R. D.; Simonyi, E. E. A Buckling-Based Metrology for Measuring the Elastic Moduli of Polymeric Thin Films. *Nat. Mater.* **2004**, *3* (8), 545–550.

(84) Liu, C. C.; Han, E.; Onses, M. S.; Thode, C. J.; Ji, S.; Gopalan, P.; Nealey, P. F. Fabrication of Lithographically Defined Chemically Patterned Polymer Brushes and Mats. *Macromolecules* **2011**, *44* (7), 1876–1885.

(85) Stoykovich, M. P.; Müller, M.; Kim, S. O.; Solak, H. H.; Edwards, E. W.; de Pablo, J. J.; Nealey, P. F. Directed Assembly of Block Copolymer Blends into Nonregular Device-Oriented Structures. *Science* **2005**, *308* (5727), 1442–1446.

(86) Tremblay, J.-F. AZ Readies For Chip Self-Assembly. *Chem. Eng. News* **2013**, *91* (26), 10.

(87) Ham, S.; Shin, C.; Kim, E.; Ryu, D. Y.; Jeong, U.; Russell, T. P.; Hawker, C. J. Microdomain Orientation of PS-B-PMMA by Controlled Interfacial Interactions. *Macromolecules* **2008**, *41* (17), 6431–6437.

(88) Xiao, S.; Yang, X.; Edwards, E. W.; La, Y.-H.; Nealey, P. F. Graphoepitaxy of Cylinder-Forming Block Copolymers for Use as Templates to Pattern Magnetic Metal Dot Arrays. *Nanotechnology* **2005**, *16* (7), S324–S329.

(89) Bang, J.; Bae, J.; Löwenhielm, P.; Spiessberger, C.; Given-Beck, S. a.; Russell, T. P.; Hawker, C. J. Facile Routes to Patterned Surface Neutralization Layers for Block Copolymer Lithography. *Adv. Mater.* **2007**, *19* (24), 4552–4557.

(90) Hawker, C. J.; Russell, T. P. Block Copolymer Lithography: Merging "Bottom-Up" with "Top-Down" Processes. *MRS Bull.* **2005**, *30* (12), 952–966.

(91) Seshimo, T.; Maeda, R.; Odashima, R.; Takenaka, Y.; Kawana, D.; Ohmori, K.; Hayakawa, T. Perpendicularly Oriented Sub-10-Nm Block Copolymer Lamellae by Atmospheric Thermal Annealing for One Minute. *Sci. Rep.* **2016**, *6* (January), 19481.

(92) Park, S. M.; Liang, X.; Harteneck, B. D.; Pick, T. E.; Hiroshiba, N.; Wu, Y.; Helms, B. A.; Olynick, D. L. Sub-10 Nm Nanofabrication via Nanoimprint Directed Self-Assembly of Block Copolymers. *ACS Nano* **2011**, *5* (11), 8523–8531.

(93) Fukukawa, K.; Zhu, L.; Gopalan, P.; Ueda, M.; Yang, S. Synthesis and Characterization of Silicon-Containing Block Copolymers from Nitroxide-Mediated Living Free Radical Polymerization. *Society* **2005**, 263–270.

(94) Luo, M.; Epps, T. H. Directed Block Copolymer Thin Film Self-Assembly: Emerging Trends in Nanopattern Fabrication. **2013**.

(95) Yoshida, H.; Suh, H. S.; Ramirez-Hernandez, a; Lee, J. I.; Aida, K.; Wan, L.; Ishida, Y.; Tada, Y.; Ruiz, R.; de Pablo, J.; Nealey, P. F. Topcoat Approaches for Directed Self-Assembly of Strongly Segregating Block Copolymer Thin Films. *J. Photopolym. Sci. Technol.* **2013**, *26* (1), 55–58.

(96) Bennett, T. M.; Pei, K.; Cheng, H.-H.; Thurecht, K. J.; Jack, K. S.; Blakey, I. Can Ionic Liquid Additives Be Used to Extend the Scope of Poly(styrene)-Block-Poly(methyl Methacrylate) for Directed Self-Assembly? *J. Micro/Nanolithography, MEMS, MOEMS* **2014**, *13* (3), 031304.

(97) Tang, C.; Hur, S. M.; Stahl, B. C.; Sivanandan, K.; Dimitriou, M.; Pressly, E.; Fredrickson, G. H.; Kramer, E. J.; Hawker, C. J. Thin Film Morphology of Block Copolymer Blends with Tunable Supramolecular Interactions for Lithographic Applications. *Macromolecules* **2010**, *43* (6), 2880–2889.

(98) Tang, C. B.; Lennon, E. M.; Fredrickson, G. H.; Kramer, E. J.; Hawker, C. J.; Chuanbing, T.; Lennon, E. M.; Fredrickson, G. H.; Kramer, E. J.; Hawker, C. J. Evolution of Block Copolymer Lithography to Highly Ordered Square Arrays. *Science (80-.).* **2008**, *322* (5900), 429–432.

(99) Han, S. H.; Pryamitsyn, V.; Bae, D.; Kwak, J.; Ganesan, V.; Kim, J. K. Highly Asymmetric Lamellar Nanopatterns via Block Copolymer. *ACS Nano* **2012**, *6* (9), 7966–7972.

(100) Vora, A.; Zhao, B.; To, D.; Cheng, J. Y.; Nelson, A. Blends of PS-PMMA Diblock Copolymers with a Directionally Hydrogen Bonding Polymer Additive. *Macromolecules* **2010**, *43* (3), 1199–1202.

(101) Sunday, D. F.; Kline, R. J. Reducing Block Copolymer Interfacial Widths through Polymer Additives. *Macromolecules* **2015**, *48* (3), 679–686.

(102) Hiemenz, P. C.; Lodge, T. P. *Polymer Chemistry, Second Edition*; Taylor & Francis, 2007.

(103) Tsuzuki, S.; Honda, K.; Uchimaru, T.; Mikami, M. High-Level Ab Initio Computations of Structures and Interaction Energies of Naphthalene Dimers: Origin of Attraction and Its Directionality. *J. Chem. Phys.* **2004**, *120* (2), 647–659.

(104) Beckingham, B. S.; Register, R. A. Synthesis and Phase Behavior of Block-Random Copolymers of Styrene and Hydrogenated Isoprene. *Macromolecules* **2011**, *44* (11), 4313–4319.

(105) Izunobi, J. U.; Higginbotham, C. L. Polymer Molecular Weight Analysis by 1 H NMR Spectroscopy. *J. Chem. Educ.* **2011**, *88* (8), 1098–1104.

(106) Lefebvre, M. D.; Olvera de la Cruz, M.; Shull, K. R. Phase Segregation in Gradient Copolymer Melts. *Macromolecules* **2004**, *37* (3), 1118–1123.

(107) Gray, M. K.; Zhou, H.; Nguyen, S. T.; Torkelson, J. M. Synthesis and Glass Transition Behavior of High Molecular Weight styrene/4-Acetoxystyene and styrene/4-Hydroxystyrene Gradient Copolymers Made via Nitroxide-Mediated Controlled Radical Polymerization. *Macromolecules* **2004**, *37* (15), 5586–5595.

(108) Bahsteter, F.; Smid, J.; Szwarc, M. Kinetics of Anionic Polymerization and Copolymerization of the Vinylnaphthalenes and Styrene. The Intramolecular Charge-Transfer Complexes. *J. Am. Chem. Soc.* **1963**, *85* (24), 3909–3918.

(109) Moacanin, J.; Cuddihy, E.; Rembaum, A. Compatibility and Plasticization of Poly-B-Vinylnaphthalene with Polyethylene Oxide. In *Plasticization and Plasticizer Processes*; Platzer, N. A. J., Ed.; 1965; pp 159–171.

(110) Mok, M. M.; Kim, J.; Wong, C. L. H.; Marrou, S. R.; Woo, D. J.; Dettmer, C. M.; Nguyen, S. T.; Ellison, C. J.; Shull, K. R.; Torkelson, J. M. Glass Transition Breadths and Composition Profiles of Weakly, Moderately, and Strongly Segregating Gradient Copolymers: Experimental Results and Calculations from Self-Consistent Mean-Field Theory. *Macromolecules* **2009**, *42* (20), 7863–7876.

(111) Brostow, W.; Chiu, R.; Kalogeras, I. M.; Vassilikou-Dova, A. Prediction of Glass Transition Temperatures: Binary Blends and Copolymers. *Mater. Lett.* **2008**, *62* (17-18), 3152–3155.

(112) Meuler, A. J.; Ellison, C. J.; Qin, J.; Evans, C. M.; Hillmyer, M. a; Bates, F. S. Polydispersity Effects in Poly(isoprene-B-Styrene-B-Ethylene Oxide) Triblock Terpolymers. *J. Chem. Phys.* **2009**, *130* (23), 234903.

(113) Lynd, N. A.; Hillmyer, M. A. Influence of Polydispersity on the Self-Assembly of Diblock Copolymers. *Macromolecules* **2005**, *38* (21), 8803–8810.

(114) Hamley, I. W.; Castelletto, V. Small-Angle Scattering of Block Copolymers. *Prog. Polym. Sci.* **2004**, *29* (9), 909–948.

(115) Bates, F. S.; Hillmyer, M. A.; Lodge, T. P.; Bates, C. M.; Delaney, K. T.; Fredrickson, G. H. Multiblock Polymers: Panacea or Pandora's Box? *Science.* **2012**, *336* (6080), 434–440.

(116) Russell, T. P.; Lin, J. S.; Spooner, S.; Wignall, G. D. Intercalibration of Small-Angle X-Ray and Neutron Scattering Data. *J. Appl. Crystallogr.* **1988**, *21* (6), 629–638.

(117) Leibler, L. Theory of Microphase Separation in Block Copolymers. *Macromolecules* **1980**, *13* (6), 1602–1617.

(118) Sakamoto, N.; Hashimoto, T. Order-Disorder Transition of Low Molecular Weight Polystyrene-Block-Polyisoprene. 1. SAXS Analysis of Two Characteristic Temperatures. *Macromolecules* **1995**, *28* (20), 6825–6834.

(119) Zhao, Y.; Sivaniah, E.; Hashimoto, T. SAXS Analysis of the Order− Disorder Transition and the Interaction Parameter of Polystyrene-Block-Poly (Methyl Methacrylate). *Macromolecules* **2008**, *41* (24), 9948–9951.

(120) Hashimoto, T.; Bodycomb, J.; Funaki, Y.; Kimishima, K. Communications to the Editor. *Macromolecules* **1999**, 952–954.

(121) Harrah, L. Excimer Formation in Vinyl Polymers. I. Temperature Dependence in Fluid Solution. *J. Chem. Phys.* **1972**, *56* (1972), 385.

(122) Frank, C. W. Excimer Formation in Vinyl Polymers. II. Rigid Solutions of poly(2-Vinylnaphthalene) and Polystyrene. *J. Chem. Phys.* **1974**, *61* (4), 1526.

(123) Holden, D. A. Characterization of Blends of Naphthalene-Containing Polymers with Poly(alkyl Methacrylates) by Combined Steady-State Fluorescence Spectroscopy and Fluorescence Decay Measurements. *Polym. Eng. Sci.* **1988**, *28* (21), 1373–1380.

(124) Sato, T.; Tsuneda, T.; Hirao, K. A Density-Functional Study on π -Aromatic Interaction: Benzene Dimer and Naphthalene Dimer. *J. Chem. Phys.* **2005**, *123* (10).

(125) Walton, D.; Kellogg, G.; Mayes, A. A Free Energy Model for Confined Diblock Copolymers. *Macromolecules* **1994**, *27* (21), 6225–6228.

(126) *Polymer Handbook*; Brandrup, J., Immergut, E., Grulke, E. A., Eds.; Wiley and Sons: Hoboken, NJ, 1999.

(127) Janes, D. W.; Thode, C. J.; Willson, C. G.; Nealey, P. F.; Ellison, C. J. Light-Activated Replication of Block Copolymer Fingerprint Patterns. *Macromolecules* **2013**, *46* (11), 4510–4519.

(128) McCalden, R. W.; MacDonald, S. J.; Rorabeck, C. H.; Bourne, R. B.; Chess, D. G.; Charron, K. D. Wear Rate of Highly Cross-Linked Polyethylene in Total Hip Arthroplasty. A Randomized Controlled Trial. *J. Bone Joint Surg. Am.* **2009**, *91* (4), 773–782.

(129) Davies, K. J. A.; Delsignore, M. E. Protein Damage and Degradation by Oxygen Radicals. *J. Biol. Chem.* **1987**, *262* (20), 9908–9913.

(130) Reichmanis, E.; Frank, C. W.; O'Donnell, J. H.; Hill, D. J. T. Radiation Effects on Polymeric Materials. In *Irradiation of Polymeric Materials*; 1993; Vol. 527, pp 1–8.

(131) Coffey, T.; Urquhart, S. G.; Ade, H. Characterization of the Effects of Soft X-Ray Irradiation on Polymers. *J. Electron Spectrosc.* **2002**, *122* (1), 65–78.

(132) Chien, S. H.; Cheng, M. F.; Lau, K. C.; Li, W. K. Theoretical Study of the Diels-Alder Reactions between Singlet (1Δg) Oxygen and Acenes. *J. Phys. Chem. A* **2005**, *109* (33), 7509–7518.

(133) Scientific Committee on Emerging and Newly Identified Health Risks. *Light Sensitivity*; 2008.

(134) Shimadzu. The Relationship Between UV-VIS Absorption and Structure of Organic Compounds http://www.shimadzu.com/an/uv/support/uv/ap/apl.html (accessed Jan 1, 2016).

(135) O'Donnell, M. Photodimerization of Solid Anthracene. *Nature* **1968**, *218*, 460–461.

(136) Tomlinson, W. J.; Chandross, E. a; Fork, R. L.; Pryde, C. a; Lamola, a a. Reversible Photodimerization: A New Type of Photochromism. *Appl. Opt.* **1972**, *11* (3), 533–548.

(137) Breton, G. W.; Vang, X. Photodimerization of Anthracene : A [4 S + 4 S] Photochemical Cycloaddition. *J. Chem. Educ.* **1998**, *75* (1), 81–82.

(138) Turro, N. J.; Chow, M.; Rigaudyo, J. Mechanism of Thermolysis of Endoperoxides of Aromatic Compounds. Activation Parameters, Magnetic Field, and Magnetic Isotope Effectst. *J. Am. Chem. Soc.* **1981**, *103* (4), 7218–7224.

(139) Lauer, A.; Dobryakov, A. L.; Kovalenko, S. a; Fidder, H.; Heyne, K. Dual Photochemistry of Anthracene-9,10-Endoperoxide Studied by Femtosecond Spectroscopy. *Phys. Chem. Chem. Phys.* **2011**, *13* (19), 8723–8732.

(140) Balta, D. K.; Arsu, N.; Yagci, Y.; Sundaresan, A. K.; Jockusch, S.; Turro, N. J. Mechanism of Photoinitiated Free Radical Polymerization by Thioxanthone-Anthracene in the Presence of Air. *Macromolecules* **2011**, *44* (8), 2531–2535.

(141) Kim, C. Bin; Janes, D. W.; McGuffin, D. L.; Ellison, C. J. Surface Energy Gradient Driven Convection for Generating Nanoscale and Microscale Patterned Polymer Films Using Photosensitizers. *J. Polym. Sci. Part B Polym. Phys.* **2014**, *52* (18), 1195–1202.

(142) Wagner, C.; Harned, N. EUV Lithography: Lithography Gets Extreme. *Nat. Photonics* **2010**, *4* (1), 24–26.

(143) Martini, M. The long and tortuous path of EUV lithography to full production.

(144) Hu, H.; Gopinadhan, M.; Osuji, C. O. Directed Self-Assembly of Block Copolymers: A Tutorial Review of Strategies for Enabling Nanotechnology with Soft Matter. *Soft Matter* **2014**, *10* (22), 3867–3889.

(145) Maher, M. J.; Rettner, C. T.; Bates, C. M.; Blachut, G.; Carlson, M. C.; Durand, W. J.; Ellison, C. J.; Sanders, D. P.; Cheng, J. Y.; Willson, C. G. Directed Self-Assembly of Silicon-Containing Block Copolymer Thin Films. *ACS Appl. Mater. Interfaces* **2015**, *7* (5), 3323–3328.

(146) Cushen, J.; Wan, L.; Blachut, G.; Maher, M. J.; Albrecht, T. R.; Ellison, C. J.; Willson, C. G.; Ruiz, R. Double-Patterned Sidewall Directed Self-Assembly and Pattern Transfer of Sub-10 Nm PTMSS-B-PMOST. *ACS Appl. Mater. Interfaces* **2015**, *7* (24), 13476–13483.

(147) Bencher, C.; Smith, J.; Miao, L.; Cai, C.; Chen, Y.; Cheng, J. Y.; Sanders, D. P.; Tjio, M.; Truong, H. D.; Holmes, S.; Hinsberg, W. D. Self-Assembly Patterning for Sub-15nm Half-Pitch : A Transition from Lab to Fab. *Spie* **2011**, *7970*, 79700F – 79700F – 9.

(148) Trombly, D. M.; Pryamitsyn, V.; Ganesan, V. Surface Energies and Self-Assembly of Block Copolymers on Grafted Surfaces. *Phys. Rev. Lett.* **2011**, *107* (14), 1–5.

(149) Cheng, J. K.; Rettner, C. T.; Sanders, D. P.; Kim, H. C.; Hinsberg, W. D. Dense Self-Assembly on Sparse Chemical Patterns: Rectifying and Multiplying Lithographic Patterns Using Block Copolymers. *Adv. Mater.* **2008**, *20* (16), 3155–3158.

(150) Sirard, S.; Azarnouche, L.; Gurer, E.; Durand, W.; Maher, M.; Mori, K.; Blachut, G.; Janes, D.; Asano, Y.; Someya, Y.; Hymes, D.; Graves, D.; Ellison, C. J.; Willson, C. G. Interactions between Plasma and Block Copolymers Used in Directed Self-Assembly Patterning. **2016**, *9782*, 97820K.

(151) Aissou, K.; Otsuka, I.; Rochas, C.; Fort, S.; Halila, S.; Borsali, R. Nano-Organization of Amylose-B-Polystyrene Block Copolymer Films Doped with Bipyridine. *Langmuir* **2011**, *27* (7), 4098–4103.

(152) Erhardt, R.; Zhang, M.; Böker, A.; Zettl, H.; Abetz, C.; Frederik, P.; Krausch, G.; Abetz, V.; Müller, A. H. E. Amphiphilic Janus Micelles with Polystyrene and Poly(methacrylic Acid) Hemispheres. *J. Am. Chem. Soc.* **2003**, *125* (11), 3260–3267.

(153) Qin, A.; Tian, M.; Ramireddy, C.; Webber, S. E.; Munk, P. Polystyrene-Poly(methacrylic Acid) Block Copolymer Micelles. *Macromolecules* **1994**, *27* (1), 120–126.